USE OF ULTRA-HIGH-PERFORMANCE FIBER-REINFORCED CONCRETE (UHP-FRC) FOR FAST AND SUSTAINABLE REPAIR OF PAVEMENT

and

A NEW SUSTAINABLE STRUCTURAL MEMBER WITH ULTRA-HIGH-PERFORMANCE FIBER-REINFORCED CONCRETE (UHP-FRC) AND FIBER-REINFORCED POLYMER (FRP) REINFORCEMENT

by

ASHISH KARMACHARYA

Presented to the Faculty of the Graduate School of

The University of Texas at Arlington in Partial Fulfillment

of the Requirements

for the Degree of

MASTER OF SCIENCE IN CIVIL ENGINEERING

THE UNIVERSITY OF TEXAS AT ARLINGTON

MAY 2019

Acknowledgements

Foremost, I would first like to thank my advisor, Dr. Shih-Ho Chao, ACI member and Professor at the University of Texas, Arlington, TX. He has provided continuous support, motivation, and guidance for driving me into research for my thesis throughout my Master's program in the University of Texas at Arlington. It would not have been possible without his guidance and continuous encouragement. I hope that my research will contribute to the field of structural engineering and my research in the field of UHPFRC will contribute to the betterment of this field.

I am very much thankful to graduate students Venkata Rahul Chandra and Nisarg Patel for their help in casting and specimen preparation. I would like to express my gratitude to Dr. Seyed Mohsen Shahandashti and Binaya Pudasaini for sharing the information on "Preliminary cost comparison between conventional and UHP-FRC based airport pavement repair methods." I would also like to thank all the members of Dr. Chao's research group Shuveksha Tuladhar, Nga Thuy Phan, Ghassan Sulaiman Almasabha, Seyed Missagh Shamshiri Guilvayi, Dr. Kyoung-Sub Park, Bhupendra Raj Acharya, Ahmed Abdullah Alateeq, Dr. Chatchai Jiansinlapadamrong, Dr. Young-Jae Choi, Ra'ed Al-Mazaidh for the support. I would also like to acknowledge the UTA CELB technicians, Timothy Andrew Kruzic and Maziar Mahdavi, for the technical support in the lab.

I am greatly indebted to my father Uttam Krishna Karmacharya and my mother Manju Maiya Shrestha for their utmost support, cooperation and understanding during my entire study period in UTA. My special thanks to my girlfriend, Subhechha Shrestha for her unconditional love, support, and encouragement throughout my time at UTA. Last but not the least, I would like to extend my deepest gratitude to all my friends and colleagues for their constant encouragement.

April 19, 2019

Abstract

USE OF ULTRA-HIGH-PERFORMANCE FIBER-REINFORCED CONCRETE (UHP-FRC) FOR FAST AND SUSTAINABLE REPAIR OF PAVEMENT

and

A NEW SUSTAINABLE STRUCTURAL MEMBER WITH ULTRA-HIGH-PERFORMANCE FIBER-REINFORCED CONCRETE (UHP-FRC) AND FIBER-REINFORCED POLYMER (FRP) REINFORCEMENT

Ashish Karmacharya, MS

The University of Texas at Arlington, 2019

Supervising Professor: Shih-Ho Chao

The first part of this research presents a new methodology, which enables streets, roads, highways, bridges, and airfields to use an advanced fiber-reinforced concrete material, which can delay or prevent the deterioration of these transportation infrastructure when subjected to traffic and environmental loadings. The major problem of concrete is its considerable deterioration and limited service life due to its brittleness and limited durability. As a result, it requires frequent repair and eventual replacement, which consumes more natural resources. Ultra-high-performance fiber-reinforced concrete (UHP-FRC) introduces significant enhancement in the sustainability of concrete structures due to its dense microstructure and damage-tolerance characteristics. These characteristics can significantly reduce the amount of repair, rehabilitation, and maintenance work, thereby giving the transportation infrastructure a longer service life. This research addresses the strong need to develop fast and sustainable UHP-FRC materials for pavement repair that can be easily cast onsite without special treatments. This avoids any major changes to current concrete production practice and accelerates the use of UHP-FRC materials. This research investigated a new method for concrete repair by combining precast UHP-FRC panels with a small quantity of cast-in-place UHP-FRC for pavement repair without any dowel bars. In this method, a precast UHP-FRC panel is used

along with cast-in-place UHP-FRC. The vertical repair surfaces of the existing concrete are roughened on site. The outer edges of the UHP-FRC precast panel are roughened before they are brought to the site (no dowel bars are needed). The depth of the precast UHP-FRC panel is the same as the existing pavement thickness. Only a small cast-in-place UHP-FRC joint (one to two inches wide) is done onsite. The roughened precast UHP-FRC panel is placed in the repair area and cast-in-place UHP-FRC is cast into the joint. Experimental results showed that using a roughened surface (up to about CSP 5) provides a very large bond resistance, which is enough to prevent faulting.

For the second part, the research looks into a highly sustainable and efficient reinforced concrete structural members for future infrastructure by utilizing emerging high-performance materials. These materials include ultra-high-performance fiber-reinforced concrete (UHP-FRC) and corrosion resistant high-strength fiber-reinforced polymer (FRP) bars. Four small-scale UHP-FRC specimens were tested under large displacement reversals to prove the proposed new design concept by fully utilizing these ultra-high-performance materials. Micro steel fibers were used for three specimens and ultra-high molecular weight polyethylene fibers was used for one specimen. One specimen with MMFX high-strength steel rebars (100 ksi as per ASTM A1035, 2016), one with high-strength GFRP (glass, 90 ksi) rebars and two with BFRP (basalt) rebars were tested. The beams had a reinforcement ratio of 14% to 15%. The test results conclude that the beams could sustain very large cyclic drift ratios without major damage in the UHP-FRC material, which provided ample shear strength and confinement to the reinforcement throughout the testing. Even with the high amount of reinforcement, UHP-FRC's superior ductility provided a very stable cyclic behavior up to very large drift ratios. The specimens also exhibited self-centering ability, which considerably reduces the residual displacement after being subject to large displacements. The test results also showed that the high damage resistant and self-centering characteristics of the proposed UHP-FRC columns can provide excellent resilience for building structures.

Table of contents

List of illustrations

List of Tables

Chapter 1

Organization of Thesis

This thesis is made up of two different research projects and is organized into two major parts. The organization of the report is discussed in this chapter.

Part I will be covered in Chapter 2 through Chapter 6 and will discuss the use of ultra-high-performance fiber-reinforced concrete (UHP-FRC) for fast and sustainable repair of pavement. Chapter 2 will present a literature review on UHP-FRC, pavement types and repair techniques. Chapter 3 will discuss the experimental program which includes the new proposed design method, trial mix design, slant shear test and punch test. Chapter 4 will present the experimental results of the trial mix design, slant shear test and punch test. Chapter 5 will present the life-cycle cost analysis, preliminary cost comparison, field installation and performance monitoring to the proposed UHP-FRC pavement repair method. Finally, Chapter 6 will provide the summary, conclusion and recommendation of the part I of the project.

Part II will be covered in Chapter 7 through Chapter 10 and will describe a new sustainable structural member with UHP-FRC and fiber-reinforced polymer (FRP) reinforcement. Chapter 7 will present a literature review on UHP-FRC, ASTM A1035/A1035M and FRP reinforcing bars. Chapter 8 will discuss the experimental testing program which includes the specimen design, discussion of fibers and UHP-FRC mix design, specimen preparation and instrumentation. Chapter 9 will present the experimental results of the tested UHP-FRC specimens and the summary, conclusion and recommendation of the part II of the project will be discussed in Chapter 10.

Chapter 2

Part I: USE OF ULTRA-HIGH-PERFORMANCE FIBER-REINFORCED CONCRETE (UHP-FRC) FOR FAST AND SUSTAINABLE REPAIR OF PAVEMENT

2.1. Introduction

Statistical data shows that in industrially developed countries, about 50% of total construction costs are related to repair, replacement, and maintenance of existing structures that have deteriorated or been damaged by environmental stress, structural loading, or other effects *(Mehta and Monteiro, 2014)*. Durability issues of structures can lead to a significantly higher life-cycle cost in comparison to the initial construction cost. Transportation infrastructure can quickly deteriorate due to overloading by increasing traffic, climate change, and other environmental loads. For example, climate change such as summer heat waves, droughts, and flooding can have major impacts on the pavement maintenance and rehabilitation costs. These extreme events are likely to occur in greater frequency and intensity in the future as the global temperature continues to rise. Rainfall changes can alter moisture balances and influence pavement deterioration. In addition, temperature can also affect the aging of bitumen resulting in an increase in cracking of the pavement surface, with a consequent loss of waterproofing. The result is that surface water can enter the pavement causing rapid loss of surface condition. Changes in temperature and rainfall patterns can interact when higher temperatures increase cracking. Pavement maintenance and rehabilitation budget can considerably increase in the coming years considering both the influences of climate change and transport demand changes. Deficiencies in conventional concrete and its subsequent

impact on the environment calls for a much more durable material that will last longer under environmental stress, thereby contributing to the conservation of natural resources and the protection of the ecosystem.

Many solutions have been proposed for enhancing the sustainability of concrete, and the use of ultra-high-performance fiber-reinforced concrete (UHP-FRC) is a promising one. UHP-FRC has recently attracted the attention of researchers and practitioners not only because of its high compressive strength but also because of its excellent environmental resistance *(Graybeal and Tanesi, 2007)*. The porous nature of conventional concrete can be improved by reducing dimensions of microcracking (or defects) in the concrete resulting in enhanced compressive strength *(Horii and Nemat, 1985)* and delayed liquid ingress. This is achieved in UHP-FRC through a very low water to cementitious material ratio (w/cm) and dense particle packing, which leads to almost no shrinkage or creep (which significantly reduces prestress losses and long-term deformations). Furthermore, the addition of fibers (typically 2 to 4 percent by volume of concrete) not only improves the brittleness of concrete by increasing the tensile cracking resistance, post-cracking strength, ductility, and energy absorption capacity (*Figure 2-1*), but also improves the ability of concrete to resist negative environmental effects. Its high-early strength and durability allow for fast reopening of traffic to areas previously closed by repair and fewer detours due to less need for future repairs.

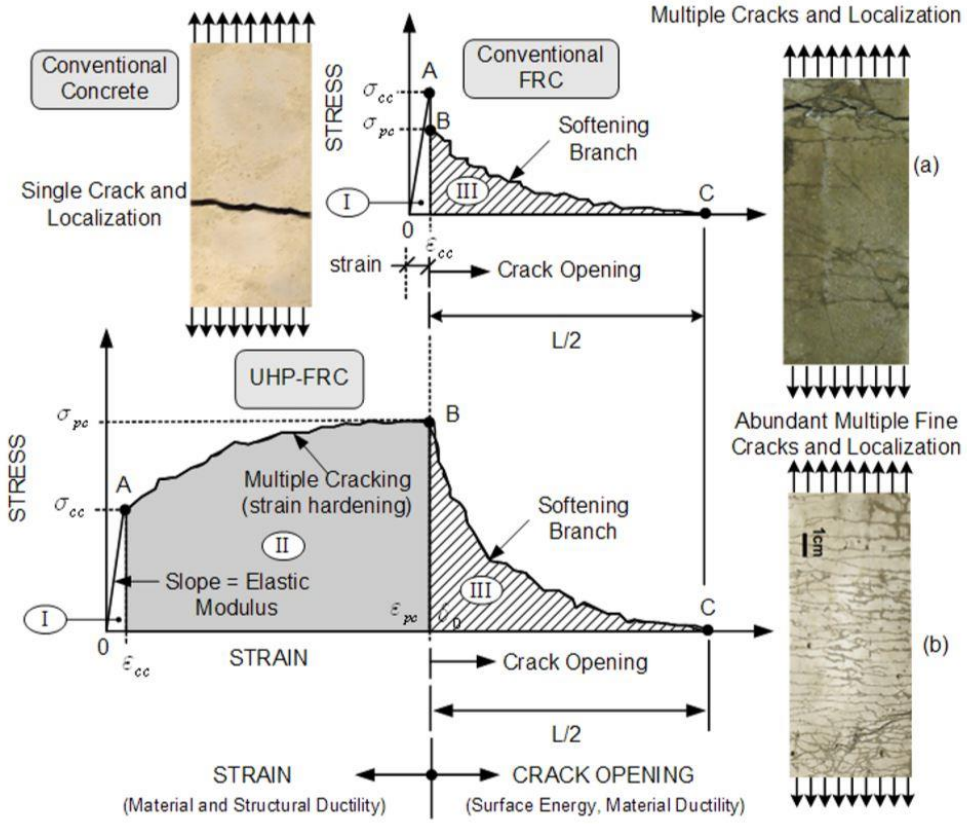

Figure 2- 1 Ductile (tensile strain-hardening) behavior of UHP-FRC (Chao, 2008).

This project offers a new methodology, which will enable the transportation infrastructure to use an advanced fiber-reinforced concrete material, UHP-FRC, that can delay or prevent the deterioration of transportation infrastructure when subjected to traffic and environmental loadings. The major problem of concrete is the considerable deterioration and consequent repair work needed due to its brittleness and limited durability. The consequence of concrete deterioration and short service life requires frequent repair and eventual replacement, which consumes more natural resources.

2.2. Literature review

2.2.1. Pavement Types

Rigid pavement and flexible pavement are two different types of pavements. Flexible pavements deflect or flex under loading. They are surfaced by bituminous or asphalt materials. Depending on the volume of traffic, flexible pavements can be either in the form of pavement surface treatments for lower

traffic volume or hot-mix asphalt (HMA) surface courses for higher traffic volume. In this type of pavement, the load is distributed over a small area due to its flexible nature. Load is transferred to the subgrade by the combination of different layers.

Rigid pavements are firm and do not deform under loading. They exhibit higher elastic modulus than the flexible pavements. They are made up of a plain concrete (PC) surface course and might have steel reinforcement bars to reduce or eradicate the joints. Due to their stiff nature, they distribute the load over a wide area of subgrade. Most of the structural capacity is provided by the concrete slab.

Broadly, rigid pavements can be classified into three different types: jointed plain concrete pavement (JPCP), continuously reinforced concrete pavement (CRCP) and jointed reinforced concrete pavement (JRCP) as shown in *Figure 2-2*. They are discussed below:

2.2.1.1. Continuously Reinforced Concrete Pavement (CRCP):

Continuously reinforced concrete pavement (CRCP) is comprised of continuous, longitudinal reinforcing steel of about 0.6–0.7 percent of the cross-section pavement area with the reinforcements placed at mid-depth. No. 5, and No. 6 bars are generally used. Transverse joints are absent in this type of rigid pavement. In the new CRCP, restraint stresses and tensile stresses are developed because of volumetric changes due to cement hydration, thermal effects and external drying. These stresses increase rapidly in the early stages. This causes full depth transverse cracks dividing the pavement into short, individual slabs. The continuous reinforcements act as an internal restraint in CRCP *(Roesler et al., 2016)*. The reinforcement steel bars permit the formation of contraction cracks at small intervals but is designed to limit the cracks to 0.02 inches (0.5 mm). This aids in the transfer of load to the adjacent slabs through aggregate interlock and prevents spalling and water penetration.

2.2.1.2. Jointed Plain Concrete Pavement (JPCP):

Jointed plain concrete pavement (JPCP) consists of plain concrete slabs without any reinforcing steel. It uses contraction joints for crack control. The transverse joint spacing is determined from temperature and moisture stress considerations, and is typically limited to 20 ft (6.1 m). The spacing is selected to prevent any intermediate cracking between the joints. The joint spacing is typically between 12 ft (3.7 m) and 20 ft (6.1 m). The spacing is limited by the nature of the concrete. Due to the limited tensile

capacity of plain concrete, slabs greater than 20 ft usually break in the middle. The load transfer at the joint takes place from aggregate interlock and the dowel bar action of the smooth bars *(*pavementinteractive.org,2018*)*. Unlike the CRCP where transverse cracks are created throughout the slab due to the developed tensile stresses, the location of cracks are directed using timely sawing in JPCP.

2.2.1.3. Jointed Reinforced Concrete Pavement (JRCP):

Jointed reinforced concrete pavement (JRCP) consists of concrete pavement reinforced with wire mesh reinforcement of about 0.2% of the cross-sectional area of the concrete *(Roesler et al., 2016)*. It uses contraction joints and reinforcing steel for crack control. The cracking due to the restraint stresses is limited by the reinforcing steel or the steel meshes. The interval for the transverse contraction joints is longer than for JPCP and ranges from 25 ft (7.6 m) to 50 ft (15.2 m). Load transfer is achieved in the transverse joints by means of dowel bars *(*pavementinteractive.org,2018*)*.

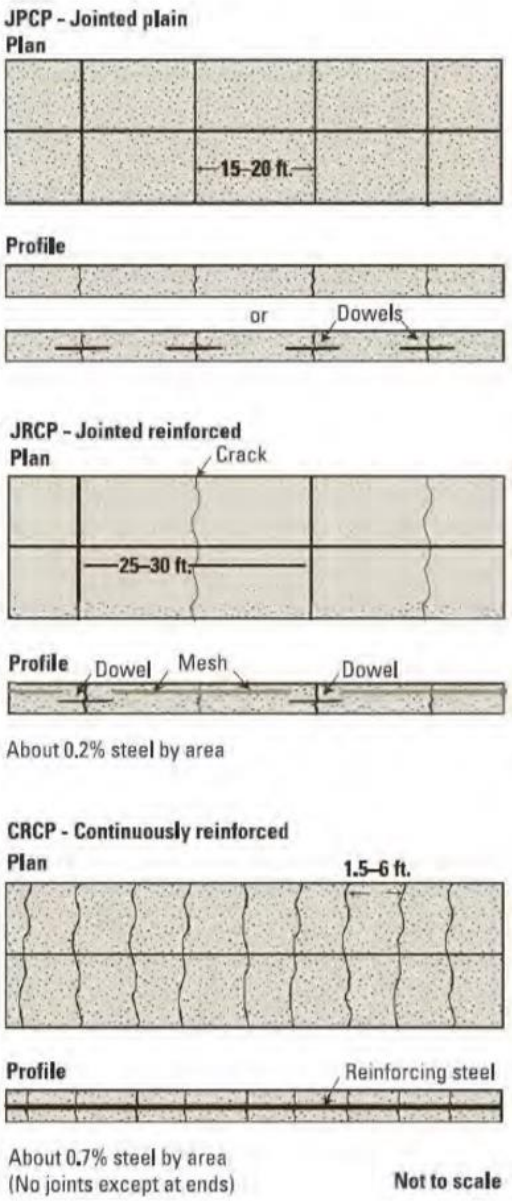

Figure 2- 2. Three common rigid pavement types (Roesler et al., 2016).

2.2.2. Rigid Pavement Rehabilitation Techniques

Major rehabilitation activities are defined as "*any work that is undertaken to significantly extend the service life of an existing pavement through the principles of resurfacing, restoration, and/or reconstruction*." *(AASHTO, 1993)*. The first step of the rehabilitation process is the evaluation of the pavement condition. In this phase, the problems existing in the pavement are identified. The types and the causes of the distress

and the level of deterioration in the pavement is determined. The major factors which need to be considered during the consideration of major rehabilitation strategies are as follows *(AASHTO, 1993)*:

- Selection of a major rehabilitation category that may or may not involve an overlay (resurfacing).
- Decision to use new or recycled materials or a combination of both.
- Decision choosing the type of rehabilitation method to be employed which includes full reconstruction, partial reconstruction, a full overlay or a combination of reconstruction and overlay.
- Determination of the optimum rehabilitation technique through life-cycle cost analysis of several possible rehabilitation methods.

Depending on the joint/crack distress seen, the following repair and preventive methods can be adopted for rehabilitation purposes (Table 2-1):

Table 2- 1 Possible repair and preventive methods for different kinds of distresses for rigid pavements.*

Joint/Crack distress	#	Repair Methods	#	Preventive Methods
Pumping	1	Subseal	1	Reseal joints
			2	Restore load transfer
			3	Subdrainage
			4	Edge support (PCC shoulder/edge beam)
Faulting	1	Grind	1	Subseal
	2	Structural overlay	2	Reseal joints
			3	Restore load transfer
			4	Subdrainage
			5	Edge support
Slab cracking	1	Full-depth repair	1	Subseal loss of support
	2	Replace/recycle lane	2	Restore load transfer
			3	Structural overlay
Joint or crack spalling	1	Full-depth repair	1	Reseal joints
	2	Partial-depth repair		
Blow-up	1	Full-depth repair	1	Pressure relief joint
			2	Resealing joints/cracks
Punchouts	1	Full-depth repair	1	Polymer or epoxy grouting
			2	Subseal loss of support
			3	Rigid shoulders

*From AASHTO Design Guide for Design of Pavement Structures, Vol. 1, Table 4.1 *(AASHTO, 1993)*.

Among the different possible major rehabilitation techniques, this research looks into the full-depth pavement repair of rigid pavements; jointed plain concrete pavement (JPCP) and continuously reinforced concrete pavement (CRCP) shown in *Figure 2-3*.

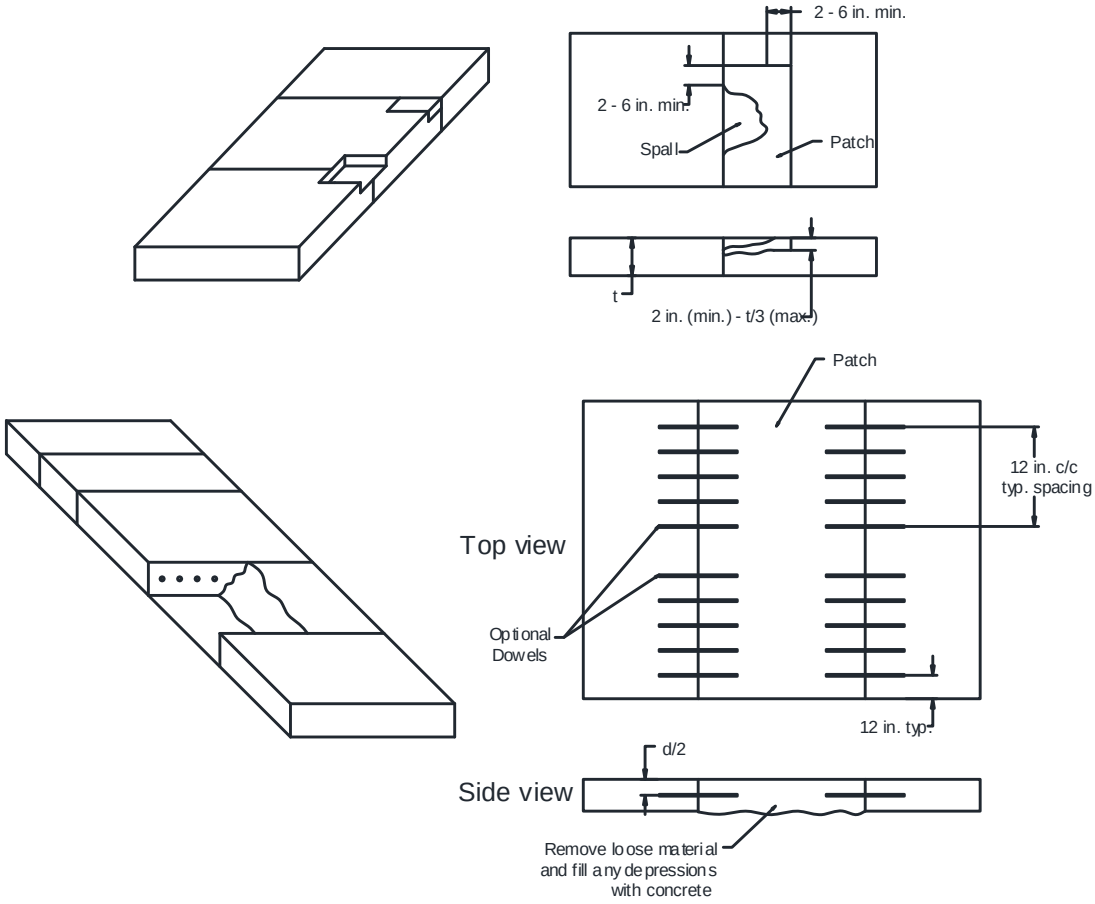

Figure 2- 3. Partial and full-depth patches.

2.2.2.1. Full-depth Repair:

This repair method is a rehabilitation technique that is commonly used for the restoration of structural integrity and provides a smooth vehicular movement in the pavement. This is done for the full-depth and full-width across the lane. Transverse cracks, which extend throughout the depth of the slab, need to be treated with full-depth repair. The full-depth cracks are created due to temperature/moisture variations and wheel-load stresses. Shattered slabs and corner breaks also require full-depth repair. These distresses are caused due to pavement design issues and construction issues. This method of pavement rehabilitation can be used in all types of pavement.

Portland cement concrete is used for full-depth repair purposes. Depending on the project requirements, it is possible to achieve very early opening time. By changing the constituents of the concrete mixture, very high early strength can be achieved. This involves reducing the water to cement ratio, using well-graded aggregates, accelerating admixtures, and increasing the cement content.

Full-depth Repair of Jointed Concrete Pavement:

The pavement joint is a major factor which influences the performance of jointed concrete pavement. Deficient joints with insufficient load transfer generated distress such as spalling, rocking of the patch, faulting and corner breaks. The transfer of load across the patched joint interface can be achieved by one or a combination of tie bars, dowel bars, undercutting and aggregate interlock. In the case of jointed concrete pavements, full-depth repair is suitable for distresses such as blow-ups, corner breaks, durability "D" cracking (caused by the freezing and thawing aggregate problem), and distress caused by insufficient load transfer across the joint and excessive spalling.

Full-depth Repair of Continuously Reinforced Concrete Pavement:

This involves cast-in-place concrete repair requiring the full-depth repair of CRCP. For adequate transfer of load, the reinforcing steel must be extended for sufficient length into the repair. It should be tied or welded to the reinforcement added in the repair for adequate bond development; moreover, the repair face needs to be vertical. Full-depth repair is applicable to CRCP in cases such as blow-ups, punchouts, durability "D" cracking, and construction joint problems.

Full-depth Repair Procedure:

The procedure of the full-depth pavement repair is described below *(ACPA, 1995; FHWA, 2005)*:

1. The first step for full depth repair is identifying the location of distress and selection of boundaries. It should include all the areas showing distress including the ones not visible from the surface to avoid pavement failures in the future. Appropriate load transfer across the repair joints is essential to ensure the performance of the repair.
2. Then, a diamond-blade saw is used to cut full depth transverse cuts to isolate the deteriorated concrete. The deteriorated concrete is then removed using either the lift-out method or the breakup method. Among them, the lift-out method is favored as it is quick and does not disturb the subgrade.

3. After that the repair area is prepared. Any disturbed base, subbase and subgrade materials should be removed and replaced with concrete. The repair area should be free of moisture before new materials are added.
4. Load transfer across the repair joint is fundamental. The depth of the holes should be 10 in. *(Stacks, 2018)* to make sure sufficient bond develops between concrete and the dowel bars. The holes should be cleaned properly and absent of moisture, dust and oil. The holes are then filled with epoxy and dowels are inserted. At least four dowel bars should be used for each wheel path. For CRCP, continuity of the longitudinal reinforcements at the transverse joint must be sustained. To maintain continuity, a minimum of 33 times the diameter of the transverse reinforcing steel *(Stacks, 2018)* should be provided as the embedment length to prevent reinforcement pullout.
5. The next step is the pouring of the concrete. Hand vibrators are used to consolidate the concrete. The surface is then textured comparable to the surrounding concrete. The concrete is covered properly to prevent the loss of moisture. The concrete must be properly cured to avoid map cracking due to excessive evaporation and large temperature gradient.
6. Finally, the transverse and longitudinal joints are sawed, formed, and then sealed. The objective of doing so is to reduce spalling and infiltration of water.
7. The pavement can be reopened for traffic when the concrete reaches a compressive strength of 2000 lb/in^2 (13,780 kPa).

2.2.2.2. Partial-Depth Repair:

Surface defects and shallow joint spalling is treated by partial-depth pavement repair. This method of repair is selected when the distress does not extend through the full-depth of the slab and the load transfer mechanisms across the joint are operative. Partial-depth repair is used to deal with distress in the pavement such as localized scaling, early stages of “D” cracking and low spalling.

The choice of material for the partial-depth repair relies primarily on the required opening time of the project. The curing time, ambient temperature, cost and performance and the repair size are also important factors in the determination of materials used. Partial-depth repair materials can broadly be classified into cementitious, polymer-based and bituminous materials. Among them cementitious materials,

which includes the Portland cement concrete, is the most commonly used. As with the full-depth repair, the constituents can be altered to obtain the required properties. However, it exhibits similar durability issues.

Procedure for Partial-Depth Repair:

Partial-depth pavement repair encompasses the following steps *(FHWA, 2005)*:

1. The first step is to identify the extent of distress and the limit of repair. The area is marked to include all deterioration.
2. Then, the deteriorated concrete is removed. The perimeter of the marked area is saw-cut to a minimum depth of 1-1/2 inches, and then the damaged concrete is chipped off to uncover sound concrete within.
3. To ensure a good bond development between the old concrete and the new concrete interface, the old concrete exposed surface should be cleaned with water to remove any dust before casting the new concrete.
4. After that, the repair materials are placed. Precautions needed to ensure a good bond development should be adopted. In the case of ready-mix concrete, the repair surface should be saturated with water without ponding before the concrete is placed.
5. Finally, the surface is finished to bring the repair surface to the same elevation as the pavement surface. The texture of the repaired surface is also matched to the surrounding concrete. The repaired concrete should be properly cured to prevent excessive volume changes due to drying shrinkage.

2.2.2.3. Precast Concrete Pavement Repair at Full-depth

Precast concrete pavement uses precast panels for accelerated pavement repair and rehabilitation. The precast panels used in this method of concrete repair are cast off site, transported to the repair site and installed. Because of being prepared in a controlled environment with better curing conditions, the concrete quality of the precast slab is significantly better than the cast-in-place concrete. Moreover, this method of concrete repair needs minimum curing time before it can be opened for traffic significantly reducing the opening time.

Precast concrete pavement repair is carried out for the full-lane replacement of fractured slab and for full-depth repair of cracked slabs or slabs with deteriorated joints. The repair is always carried out for the full-lane width. In one method of repair, the dowel bars are installed in the precast concrete panel. Slots for the dowel bars are cut into the existing pavement. The precast panel is put in place and the slots are filled with fast-setting patching material. The second method is similar to the method of cast-in-place, full-depth repair; the dowel bars are fixed in the existing pavement by the process of drilling and grouting with epoxy. Slots are fabricated in the precast concrete panel in the transverse side on the bottom side. The precast panels are then put in place and the slots and the perimeter joint is filled with fast setting grout.

2.2.2.4. Comparison of Rigid Pavement Repair Alternatives

The pavement design alternatives can broadly be categorized into three types: rigid pavements using conventional mix concrete, rigid pavements using rapid-setting concrete and rigid pavements using precast panels. Choice of the alternatives depends on the requirements of the project. It also depends on other parameters such as the available curing time, the ambient temperature, the material cost and the desired performance. Each of the three types of pavement mentioned above has its own advantages and disadvantages which must be considered with respect to the project requirements before making the choice for a certain type. The pros and cons of each alternative are discussed below *(FAA, 2007)*:

Conventional Rigid Pavement Repair:

The primary advantage of conventional rigid pavement is its high final strength. Conventional concrete has been in use for a very long time. As a result, contractors and workers have the tools, equipment and necessary experience required for working with conventional concrete. Conventional concrete has well defined specification, testing methods and proven design ensuring the quality of the mix. Compared to rapid set and precast panels, it is easier to work with this type of concrete and the materials are readily available in the market. Also, the cost estimates can be done with a reasonable degree of accuracy. The cost of using conventional mix is lower over using rapid-set and precast panels. It results in a pavement with low maintenance and longer life span compared to the other two.

The major disadvantage of this rigid pavement is a longer reopening time. This mix requires considerable construction as well as curing time, which leads to a very long downtime. Also, if the concrete used for the repair does not meet the determined specification, the concrete has to be removed and placed again.

Accelerated Early Strength Gaining Rigid Pavement Repair:

In this type of Portland cement concrete (PCC) the concrete mixture is tailored to obtain very high early strength. This involves reducing the water to cement ratio, using well-graded aggregate, accelerating admixtures and increasing the cement content. The early strength gain is mostly dependent in the properties of the cement and the additives used. The high early strength provides the required compressive strength within a few hours. This allows for the opening of the pavement for driving with minimum downtime. Although the reduced downtime is a huge benefit, the cost of using this type of concrete is high. It has a lower final strength. Mixes for high early-strength concrete present problems such as poorly formed air voids, less homogeneous paste and increased microcracking, alkali silica reaction (ASR), and a high degree of scaling *(Van Dam et al., 2005)*. This affects the long-term serviceability of the pavement and imparts a shorter life span than the regular conventional mix. A very low setting time of the concrete poses many difficulties in the use of this alternative. It requires a larger work force and precise scheduling. Also, inexperienced contractors not accustomed to working with this type of concrete make it arduous. The concrete has low workability and has an increased safety risk to workers because of the caustic nature of some accelerants. If the specifications are not met, the concrete has to be removed and redone which takes additional time and money.

Precast Rigid Pavement Repair:

Using precast slabs permits rapid repair of pavement. The panels are fabricated off site in a controlled environment. This ensures good quality of concrete. The strength can further be improved by prestressing them.

Despite the merits, using precast panels for pavement repair poses some challenges. The cost of using precast panels is high. Inexperience of the contractors and workers with this type of pavement repair makes the process arduous. Also, transporting the precast panels from the precast plant to the site and positioning of the precast panels in place is difficult. The edges of the precast panels are likely to get damaged and this process of repair may require power grouting or lifting screw jacks *(Tayabji et al., 2013)*.

2.2.3. Characteristics of UHP-FRC

In a prior National Science Foundation-sponsored research project, the research team developed a highly flowable UHP-FRC mix by using currently available materials on the U.S. market. FRC was

invented many decades ago; however conventional FRC only enhances the post-cracking ductility and its compressive strength is close to that of plain concrete (3 to 5 ksi). In other words, conventional FRC does not change the micro-structure of concrete but just the tensile capacity after concrete cracks. On the other hand, UHP-FRC's compressive strength is about 22–30 ksi (six times higher than conventional concrete) with a post-cracking tensile strain up to 0.6% without strength degradation. The one-day strength was approximately 12 ksi, which is more than twice that of the ultimate long-term strength of conventional concrete.

UHP-FRC has very high durability due to its dense microstructure *(Ahlborn, 2011)*. Micro high-strength steel fibers were incorporated in the concrete mix to enhance its ductility and toughness. The excellent flowability of UHP-FRC was achieved by introducing a pozzolanic material (fly ash), which has a spherical shape. Its shape allows all the particles to roll over thereby increasing the flowability during the mixing state. The scientific basis of this invention is due to the fact that the void (or defect) dimensions and entrapped air are critical factors in determining concrete strength. The voids can be minimized by high packing density, induced by combined mixing of big- and small-sized particles, e.g., coarse and fine sands, cement, glass powder, and silica fume, to achieve ultra-high compressive strength. This approach is based on the fundamental particle-stacking theory, as briefly illustrated by *Figure 2-4 (Aghdasi et al., 2016)*. Filling the interstitial voids with smaller particles can increase the packing density of the primary particles. There are two different ways to fill these voids—with a single large particle or with many small particles. In our approach, both void filling methods were combined to reach the highest concrete strength. Therefore, the combined particles are a primary particle (biggest size particle), a secondary small particle (filling voids in the middle of primary particles) and micro-sized particles. The void size was further reduced by reducing the water to a cementitious materials ratio down to about 0.2. A high-range water reducer was used to assist flowability during the mixing process. Because the process simply relies on particle packing and chemical admixture, no special treatment and mixing technique is needed to produce UHP-FRC; hence, it is suitable not only for precast but also on-site casting applications. The high compressive/tensile ductility, and excellent flowability have been experimentally verified as shown in *Figure 2-5*.

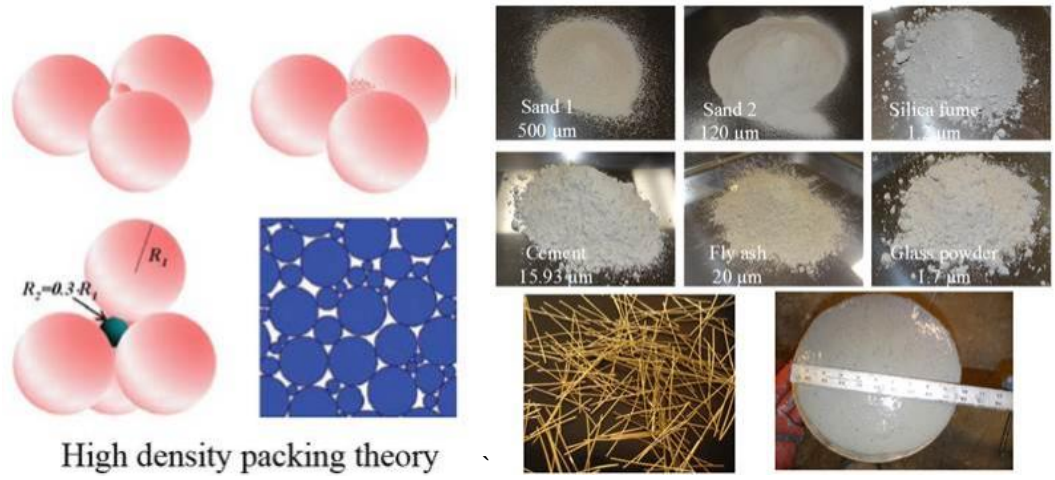

Figure 2- 4 Fundamental concept of UHP-FRC and materials (Aghdasi et al., 2016).

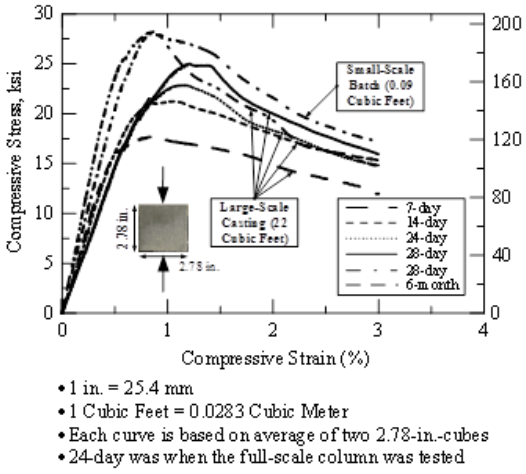

(a)

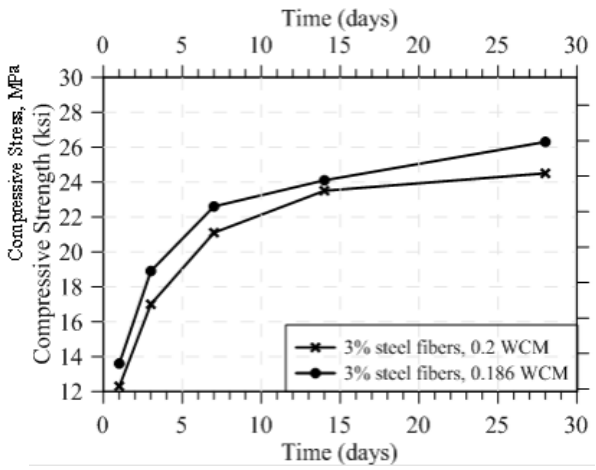

(b)

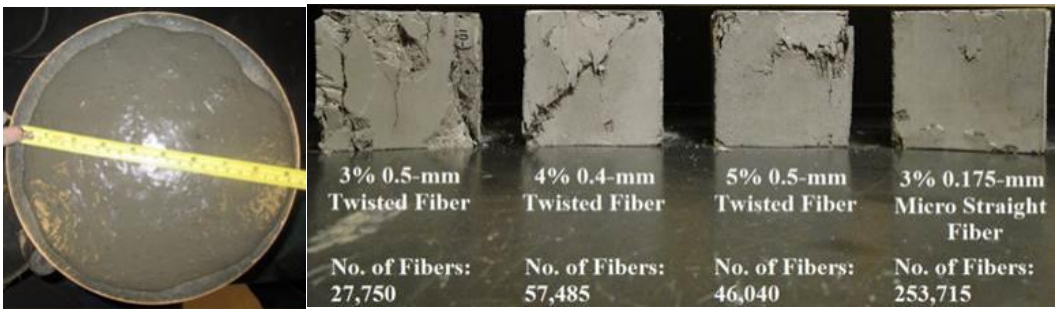

(c) (d)

Figure 2- 5 Features of UHP-FRC used for this study: (a) compressive stress-strength curves, (b) compressive strength development versus time, (c) flowability, and (d) improved compressive ductility with 3% micro straight steel fibers (Aghdasi et al., 2016).

UHP-FRC was developed by changing the porous nature of conventional concrete through reducing dimensions of microcracking (or defects) in the concrete. This is achieved in UHP-FRC through a very low water to cementitious materials ratio (0.18 to 0.25) and a dense particle packing *(*Aghdasi et al., 2016*)*, which leads to almost no shrinkage or creep, making it very suitable for concrete members under long-term compression. The consequences of a very dense microstructure and low-water ratio results in enhanced compressive strength and delayed liquid ingress. Furthermore, the addition of steel or synthetic fibers improves the brittle nature of concrete by increasing the tensile cracking resistance, post-cracking strength, ductility, and energy absorption capacity. In terms of corrosion resistance, research has indicated that UHP-FRC has a much greater durability than conventional concrete due to its very dense microstructure (*Graybeal and Tanesi, 2007).* This dense microstructure impedes the conductive chloride ions from coming into direct contact with the steel reinforcing bars, which protects the reinforcing bars from corrosion. Table 2-2 provides a comparison between typical conventional concrete and UHP-FRC.

Table 2- 2 Comparison of typical conventional concrete and UHP-FRC (UT Arlington test data except Rapid Chloride Penetration Test)

Properties of Concrete	**Conventional Concrete**	**UHP-FRC**
Ultimate Compressive Strength	< 8,000 psi (55 MPa)	18,000 to 30,000 psi (124 to 207 MPa)
Early (24-hour) compressive strength	< 3000 psi (21 MPa)	10,000 – 12,000 psi (69 to 83 MPa)
Flexural Strength	< 670 psi (4.6 MPa)	2,500 to 6,000 psi (17 to 41 MPa)
Shear strength	< 180 psi (1.2 MPa)	> 600 psi (4.1 MPa)
Direct Tension	< 450 psi (3 MPa)	up to 1,450 psi (10 MPa)
Rapid Chloride Penetration Test *(Ahlborn et al., 2011)*	2000-4000 Coulombs passed	Negligible (< 100 Coulombs passed)

Ductility	Negligible	High ductility
Ultimate Compressive Strain, ε_{cu}	0.003	0.015 to 0.03
Confining	Negligible	High confining capability

2.2.4. Prior UHP-FRC Research

In a prior NSF research, UHP-FRC was used in a full-scale earthquake-resistant column. The high toughness and strength of the UHP-FRC was utilized and the operation successfully accomplished mixing and pouring at a 1-cubic yard scale, demonstrating applications for potential large-scale construction (*Figure 2-6*). The column was constructed at University of Texas at Arlington's (UTA) Civil Engineering Lab Building (CELB) and transported by a flatbed truck to the Multi-Axial Sub-assemblage Testing (MAST) facility at the University of Minnesota for testing. The testing results are shown in the *Figure 2-7* below. UHP-FRC column had extremely high damage tolerance capability as compared to conventional reinforced concrete columns when subjected to severe earthquake motions.

(a) (b)

(c)

Figure 2- 6 UHP-FRC (a) pouring, (b) completed section, and (c) final casting.

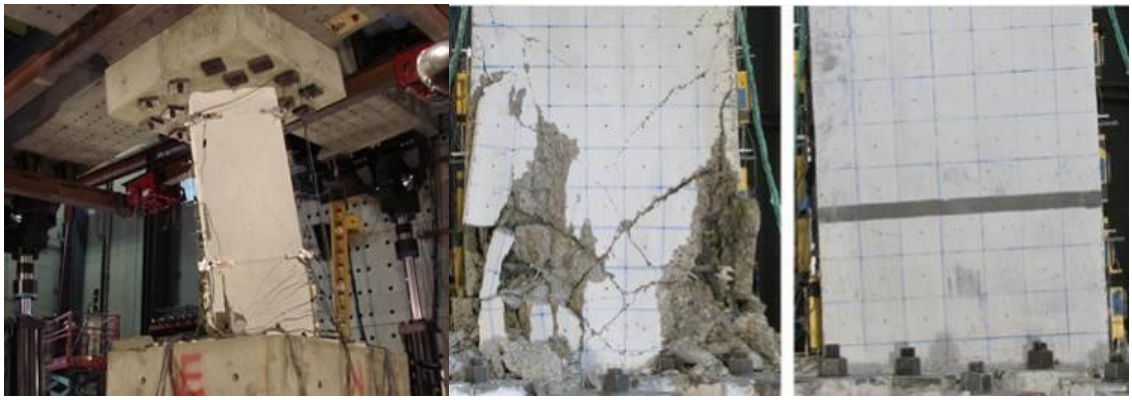

(a) (b) (c)

Figure 2- 7 Experimental testing at NSF MAST laboratory (a) Test setup, (b) conventional reinforced concrete column, and (c) UHP-FRC concrete column.

The applications of UHP-FRC in precast products was also explored by the UTA's research team. One of the applications included the concrete sandwich façade panel discussed above. In conventional panels, concrete is reinforced with steel reinforcing bars, and the panel is typically 8 to 12 inches thick. The use of UHP-FRC eliminated all reinforcing bars and the thickness was reduced 50%, which translates into a 50% weight reduction. The load test showed (*Figure 2-8*) that the cracking resistance of a UHP-FRC

façade panel was three times that of the conventional reinforced concrete façade panel even when there were no reinforcing bars in the UHP-FRC façade panel. This test result was very promising because it exhibited the high cracking resistance and durability of UHP-FRC façade panels with reduced weight, cost in labor, transportation, and installation.

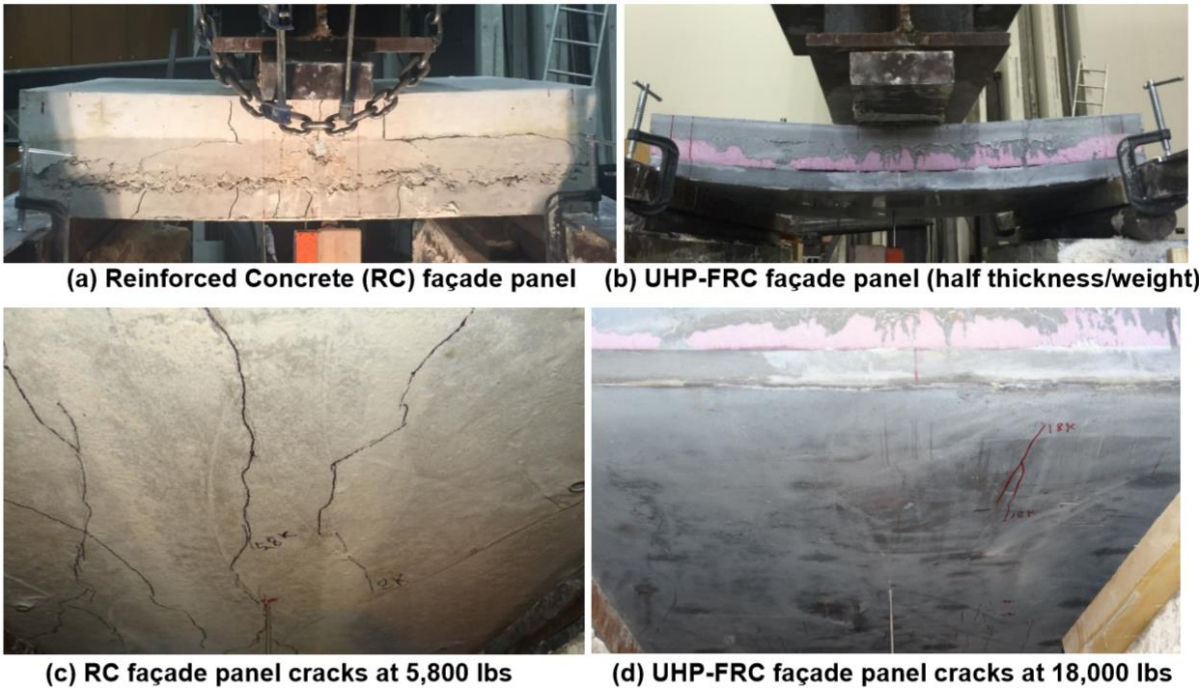

Figure 2- 8 Load testing of RC and UHP-FRC façade panels at UTA CELB.

The advantages of UHP-FRC materials are:

1. High-strength and high durability as compared conventional concrete pavement: the ultrahigh strength and dense microstructure of UHP-FRC allows much thinner and durable pavement and complete removal of conventional reinforcement. The high durability comes from a very dense microstructure due to dense particle packing design and low water ratio used. This leads to a very low permeability (about 1% of conventional concrete) which in turn leads to a very durable concrete material *(Ahlborn et al., 2011)*.
2. UHP-FRC also serves an excellent option for urgent repair which allows minimal downtime due to its high early strength (one-day strength about 10 ksi) (*Figure 2-5b*).
3. UHP-FRC's high damage tolerance capability can significantly reduce the number of joints as well as any pop out of concrete after cracking (*Figure 2-7*). UHP-FRC can take much greater

compression/tension and its ductility allows it to accommodate large deformation due to temperature change (*Figure 2-9*), which permits the use of jointless pavement.

4. UHP-FRC's high cracking resistance (*Figure 2-8*) and high strength allows much sustainable pavement and lower life-cycle costs due to considerably reduced repair needs.

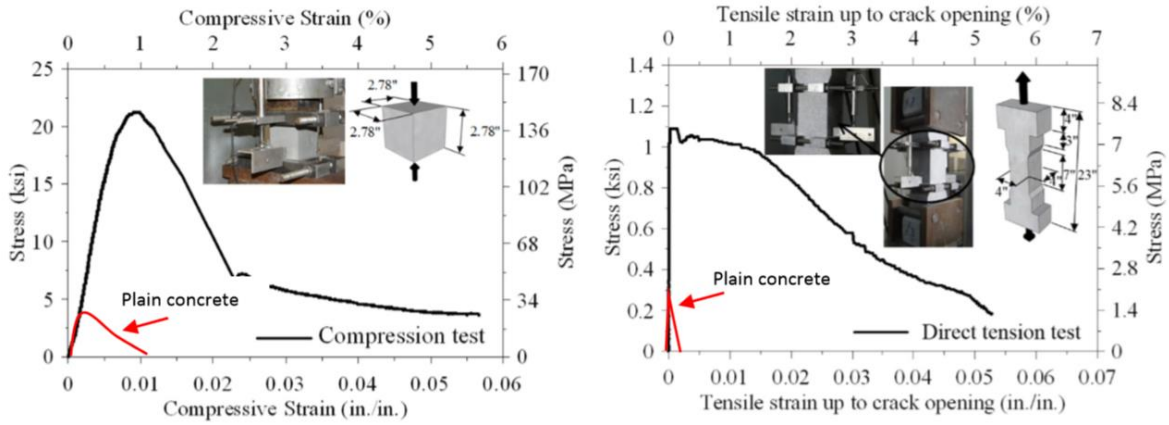

Figure 2- 9 Typical compressive stress-strain of UHP-FRC/plain concrete (left); and direct tension test response for UHP-FRC/plain concrete (right) (Kaka, 2017).

While UHP-FRC can significantly enhance the load-carrying capacity and durability of repaired pavement, a sound pavement joint between the existing concrete and UHP-FRC needs to provide adequate transfer of loads. Load transfer can be obtained by using dowel bars or by cohesion/aggregate interlock. A prior research carried out by our research team *(Palacios, 2015; Waweru, 2015)* using large-scale push-off test (*Figure 2-10*) with various magnitudes of surface roughness (*Figure 2-11*) indicated that a rougher surface is able to provide strong interface shear resistance of approximately 0.2 ksi. The results also indicated that dowel bars are effective only when certain slip of the interface occurs. Therefore, the cohesion/aggregate interlock is the primary resistance before slip occurs. Considering the high shear resistance (in the range of 0.2 ksi), it is possible for the joints to provide sufficient strength by using a roughened surface.

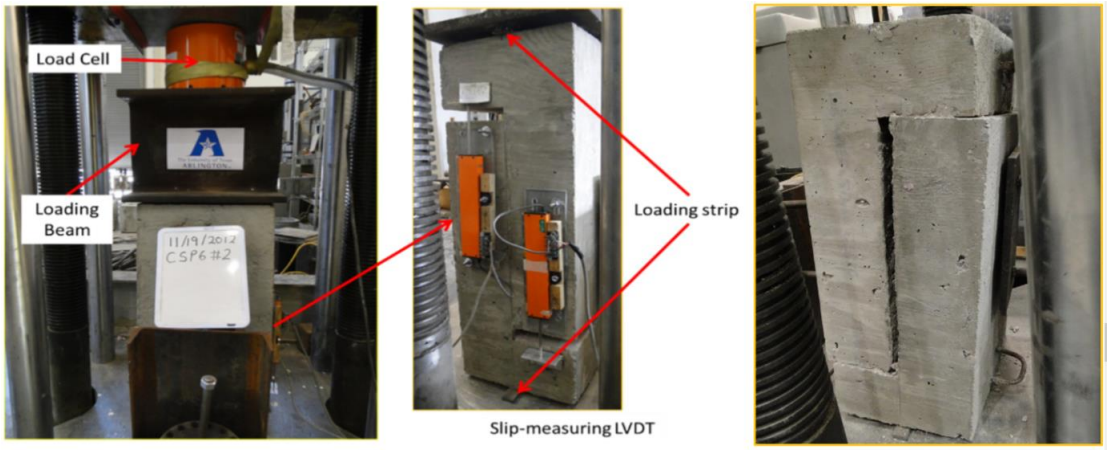

Figure 2- 10 Push-off test setup (Palacios, 2015; Waweru, 2015).

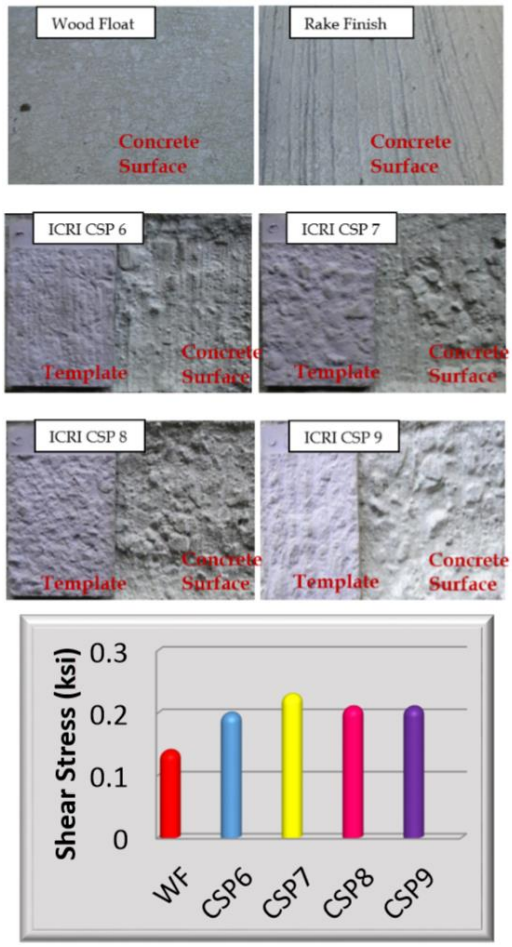

Figure 2- 11 Surface roughness and the corresponding cohesion/aggregate interlock resistance.

2.2.5. UHP-FRC in Repair

Overlay in pavements and bridge decks repair is the majority transportation infrastructure applications of UHP-FRC to UHP-FRC overlay shows greater bond strength between the substrate concrete and the UHP-FRC overlay than that of the substrate concrete. UHP-FRC also exhibits a significant increase in flexural strength and toughness, post cracking tensile capacity, high resistance to environmental and chemical attack, and negligible permeability *(Khayat and Valipour, 2014) (Muñoz, 2012) (Shann, 2012) (Sarkar, 2010)*.

UHP-FRC has been used in limited pavement and deck repair. UHP-FRC was used successfully in a pilot project for the repair and upgrade of an existing reinforced concrete motorway bridge in a high-level road network in Austria *(Hadl et al., 2015)*. Toppings and deck panels using UHP-FRC were employed in the rehabilitation of the orthotropic bridge deck, in the Netherlands *(Buitelaar, 2004) (Yuguang et al., 2008)*. Log Cezsoski Bridge in Slovenia used UHP-FRC in bridge deck overlay *(Sajna et al., 2012)*.

There is almost no literature review regarding the use of UHP-FRC in pavement repair *(Russell and Graybeal, 2013)* similar to the one proposed in this study.

Chapter 3

Part I: Experimental Program

3.1. Methodology

The primary purpose of this research was to investigate the advantages of using UHP-FRC over conventional concrete in pavement repair. For this, the first part of this research involved trials with different constituents and mix proportions. This research focused on delineating the behavior of UHP-FRC when used as a repair material in the full- and partial-depth repair of pavement. Thus, a proper understanding of the shear transfer across the interface between the old concrete and new UHP-FRC repair material was necessary. In this study, the research team used slant shear test (SST) and punch test to examine the interface shear strength.

3.1.1. Trial Mix

In this phase, varying proportions of individual components and different kinds of fibers were tried to obtain the desired compressive strength of UHP-FRC. Steel fibers (*Figure 3-1*) have been used in UHP-FRC as they provide great mechanical properties to the concrete mix. However, steel fibers may not be suitable for pavements because of liability issue concerns. In this regard, synthetic fibers (*Figure 3-1*) can serve as a better alternative. The mechanical properties of the fibers used are shown in Table 3-1.

Figure 3- 1 Micro steel fiber (left) and ultra-high molecular weight polyethylene fiber (right).

Table 3- 1 Mechanical properties of the fibers used.

	Length in.(mm)	Diameter in.(mm)	Tensile strength ksi (MPa)
Micro short steel fiber	0.51 (13)	0.008 (0.21)	399 (2750)
UHMW Polyethylene fiber	0.5 (13)	0.00006 (0.0015)	375 (2580)

3.1.2. Slant Shear Test (SST)

SST is an ASTM standard testing method *(ASTM, 2013)* and adequate to predict the strength of concrete-to-concrete interfaces in shear. However, while ASTM C882 requires the SST specimen be made of two equal sections of a 75×150-mm (3×6-in.) cylinder, each section had a diagonally cast bonding area at a 30° angle from the vertical position. Extensive numerical finite element simulations carried out by Santos *(Santos, 2009)*, suggested a prismatic SST specimen with a 150×150×560 mm^3 (5.9×5.9×22 in^3) with a shear plane at a 30-degree angle from the vertical position (*Figure 3-2*). The optimal geometry for SST specimens was determined based on: a) obtaining an acceptable stress distribution along the interface, b) adopting a single geometry for all slant shear specimens, only varying the shear plane angle and the corresponding total height *(Santos, 2009)*. The following geometry with a cross section of 150×150 mm^2 (5.9×5.9 in^2) will be used in this research. Different concrete surface profiles (CSP) as defined by the International Concrete Repair Institute (ICRI) were used. CSP are numbered from 1 to 9 in with the surface CSP9 being the roughest and CSP1 the least rough.

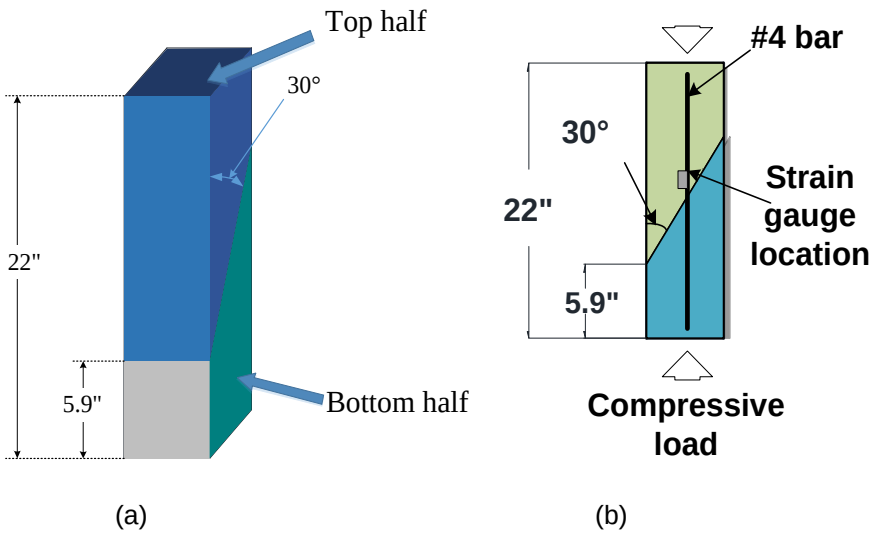

Figure 3- 2 (a) Slant shear test specimen and (b) slant shear specimen showing rebar and strain gauge location.

3.1.2.1 Specimen Preparation

Three types of specimens were prepared. In the first type, the inclined surface of the bottom half was cut smooth. Then, vertical holes were drilled parallel to the long face of the specimen.

1. A wood support (*Figure 3-3*) was prepared to provide an incline casting surface at an angle of 30°. The mold was placed on the support with its back face resting on the inclined support as shown below. Then, the bottom half of the mold was cast, covered by plastic sheeting and cured at normal room temperature for a minimum of six days.

Figure 3- 3 Mold placement and casting for bottom half of slant shear specimen.

2. The specimen was demolded and the inclined surface was cut to a smooth surface using a concrete saw (*Figure 3-4a*). This step is necessary to simulate the actual saw cutting in the field repair. This cutting results in a smooth surface of the inclined plane (*Figure 3-4b*).

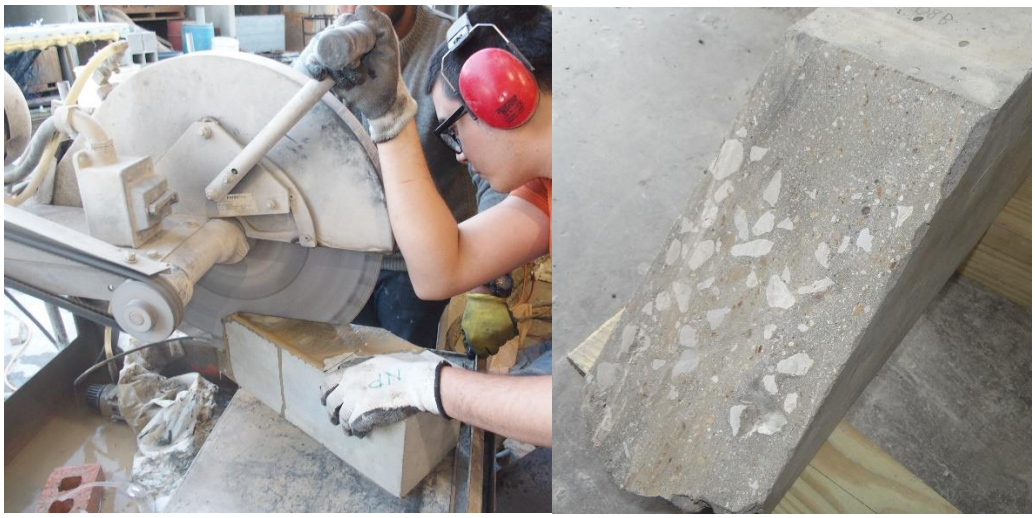

(a) (b)

Figure 3- 4 (a) Using concrete saw to smooth cut the incline surface and (b) smooth cut surface after sawing.

3. The next step is to treat the inclined surface of the bottom half as per specimen requirement for the top half. Based on the type of specimen to be prepared, the following steps should take place.
   a. To prepare a specimen with a smooth surface and an embedded reinforcement bar:
      i. First, vertical holes were drilled parallel to the long face of the bottom half (*Figure 3-5a, 3-5b*) to a depth of 8 inches. Then the holes were cleaned of dust. For this, a blow-out gun (*Figure 3-5c*) is used to blow-out the hole twice followed by brushing out the hole twice. Then the hole is blown out two more times. This ensures that maximum bonding can be obtained while anchoring the rebar.

(a) (b)

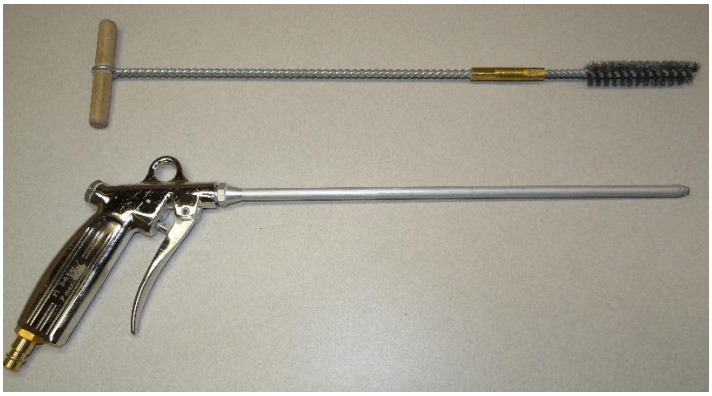

(c)

Figure 3- 5 (a) Drilling of holes in bottom half, (b) finished holes in two specimen bottom halves, and (c) manual brush and blow-out air pump used for specimen preparation.

ii. Then, epoxy is inserted in the drilled hole and a rebar is embedded into the drilled hole with a slight twisting motion. Once the epoxy is set, the strain gauge is installed on the rebar one inch away from the interface as shown in *Figure 3-6*.

(a) (b)

Figure 3- 6 (a) No. 4 rebar anchored in bottom half and (b) strain gauge installed in rebar.

b. To prepare the specimen with the roughened surface, the surface was roughened using a pneumatic needle scaler (*Figure 3-7a*) to desired concrete surface preparation level as shown in *Figure 3-7*.

(a)

(b) (c)

Figure 3- 7 (a) Pneumatic needle scaler used for surface roughening. The saw cut inclined surface (b) before and (c) after roughening.

c. For the specimen with the smooth surface without any embedded rebar, the saw cut surface is left as it is.

4. The prepared specimen is then positioned in the mold in the orientation shown in *Figure 3-8*; then, the top half of the material is cast, after which the specimen is covered with plastic sheeting and cured at room temperature.
5. The specimen is then demolded and tested.

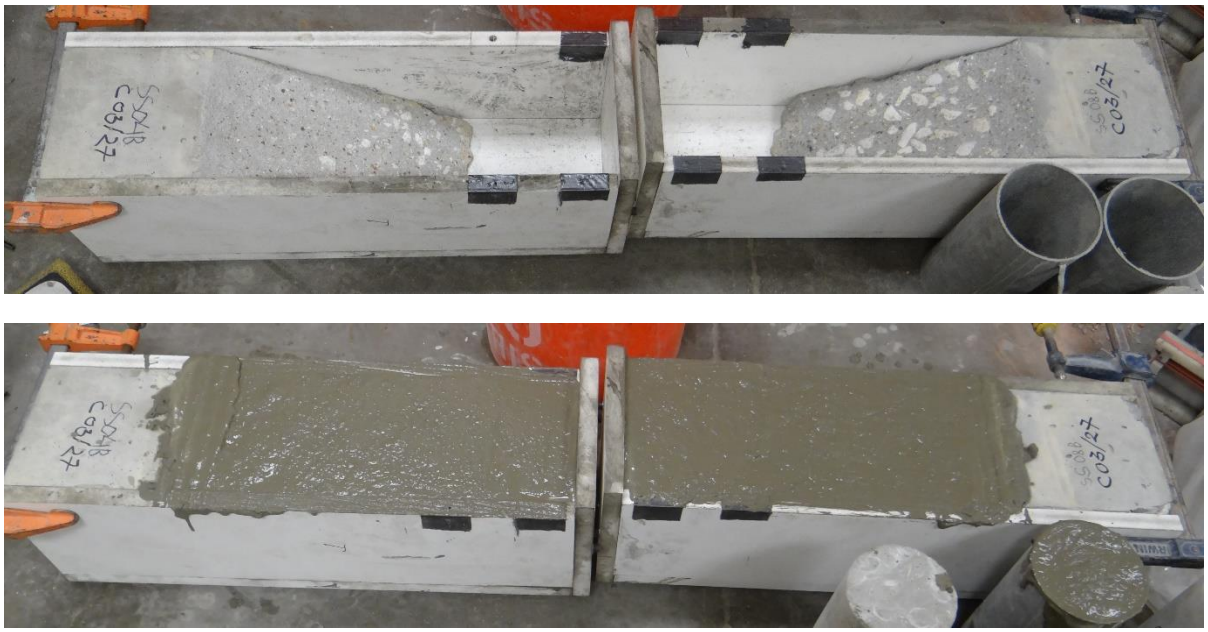

Figure 3- 8 Casting of top half of the slant shear specimen with PC with roughened surface (CSP **7).**

3.1.2.2 Testing

A specimen was prepared in two stages. The bottom half represents the existing concrete of the pavement and the concrete in the upper half represents the new repair pavement concrete. Molds and support were fabricated to allow the preparation of such a specimen. The bottom concrete was cast using the concrete mix of 1:1:2 with a water-to-cement ratio of 0.5. Curing was performed under ambient temperature, and the cast concrete was covered with plastic sheets. The cylinder tests of the concrete mix provided a 6-day compressive strength of 2960 psi. The bottom half was left to cure for a minimum of 6 days before additional casting was done on top of it. The top half was cast for different concrete mixes and tested in one day. Tests were done using a loading rate of 0.02 in/min. Displacement control was chosen

over load control to incorporate the post-peak data for the slant shear tests for the specimens with a rebar embedded on it. The same displacement control loading was adopted for other slant shear specimens to maintain uniformity for all the specimens. Tests were done in a Tinius Olsen SuperL universal testing machine located in the Civil Engineering Laboratory Building (CELB) at UTA. Depending on the top half of the slant shear specimen, the test setup consists of a load cell, a strain gauge and two linear variable differential transformers (LVDTs).

The LVDT was used to measure the vertical deformation and the load cell was used to measure the applied vertical load. The strain gauge (when used) was placed 1 inch above the interface which gave the value of the strain in the reinforcement bar. All sensors were connected to the DAQ box and the data was recorded. The test setup is shown in *Figure 3-9*.

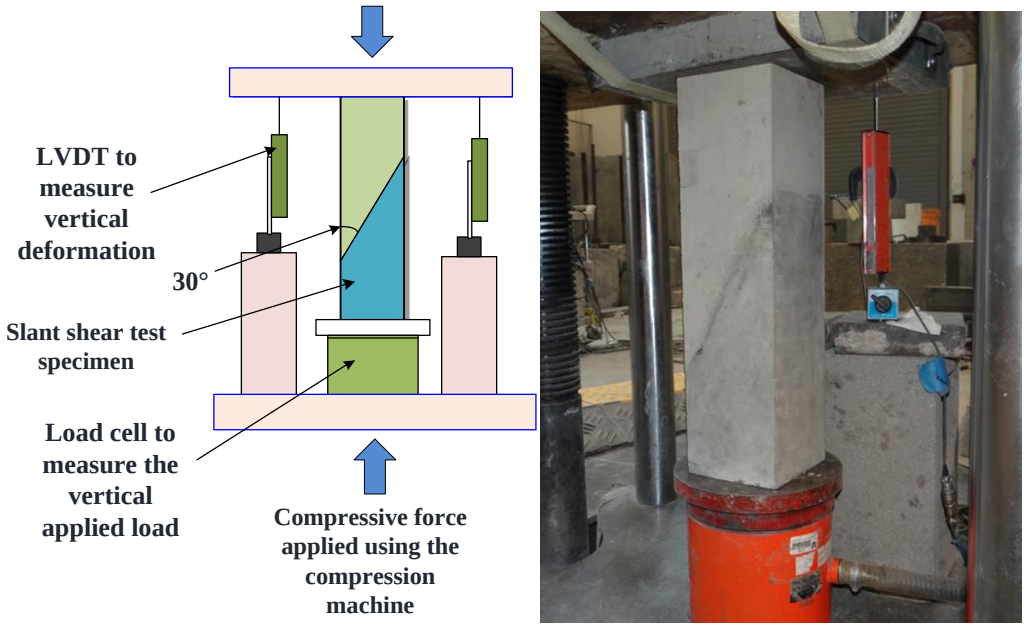

Figure 3- 9 Slant shear test setup.

The shear stress was obtained from the recorded peak's longitudinal load using the formulae presented below:

$$V = P\ cos30° \qquad [3\text{-}1]$$

where:

V = Shear force, and

P = Vertical applied load.

$$s = d/cos30° \quad [3\text{-}2]$$

where:

s = Deformation along slip, and

d = Vertical deformation.

$$\tau = V/A_{inclined} \quad [3\text{-}3]$$

where:

τ = Shear stress, and

$A_{inclined}$ = Inclined area.

The following formula was used to calculate the rebar force:

$$A_{eff} = A_{rebar} \times sin30° \quad [3\text{-}4]$$

where:

A_{eff} = Effective area of rebar = 0.2 in^2, and

A_{rebar} = Area of No. 4 rebar = 0.2 in^2.

$$T = \varepsilon \times E_{rebar} \times A_{eff} \quad [3\text{-}5]$$

where:

T = Rebar force,

E = Strain in rebar, and

E_{rebar} = Modulus of elasticity of rebar = 29000 ksi.

3.1.3. Punch Test

3.1.3.1. Necessity of Punch Test

The vertical force applied in the slant shear specimen can be divided into two components, the shear force component (P cos30°) acting parallel to the inclined interface and the normal component (P sin30°) acting normal to the inclined surface as shown in *Figure 3-10*. The normal component (P sin30°) generates a frictional force (μ P sin30°) which provides additional resistance. This along with the shear

strength of the interface provides a combined resistance which causes the overestimation of the shear capacity of the interface.

$$V_n = cA_{cv} + \mu P_n \qquad [3\text{-}6]$$

where:

V_n = Shear capacity of the interface,

$C\ A_{cv}$ = cohesion and/or aggregate interlock which is a function of the surface properties, and

$\mu\ P_n$ = friction component resulted due to the normal component of the applied vertical load.

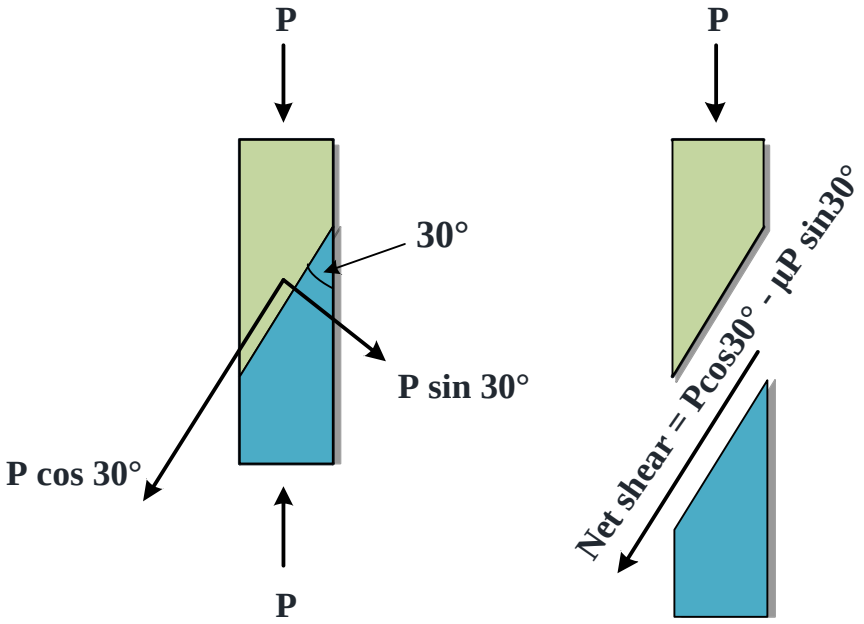

Figure 3- 10 Forces transfer in a slant shear test specimen.

Therefore, a punch test was necessary in this project.

3.1.3.2. Punch Test Specimen

The punch test for conventional concrete was designed on the basis of the actual repair practices used in the field (*Figure 3-11*).

Figure 3- 11 Conventional concrete repair.

A new method for concrete repair was proposed combining the features of precast UHP-FRC with cast-in-place repair of pavement without any dowel bars (*Figure 3-12*). In this method, a precast UHP-FRC panel is used along with cast-in-place UHP-FRC. The vertical repair surfaces of the existing concrete are roughened on site. The outer edges of the UHP-FRC precast slabs are roughened before brought to the site (no dowel bars are needed). The depth of the precast UHP-FRC is same as the existing pavement slab thickness. Only a small cast-in-place UHP-FRC joint (one to two inches wide) is done onsite. The roughened precast UHP-FRC slab is placed in the repair area and UHP-FRC is cast in the joint. Note that a prior case study for airfield pavement indicated that a 6,000-ft taxiway reconstruction was done by using precast panels with only overnight closures, compared with a 90-day closure for conventional methods *(Switzer et al., 2003)*.

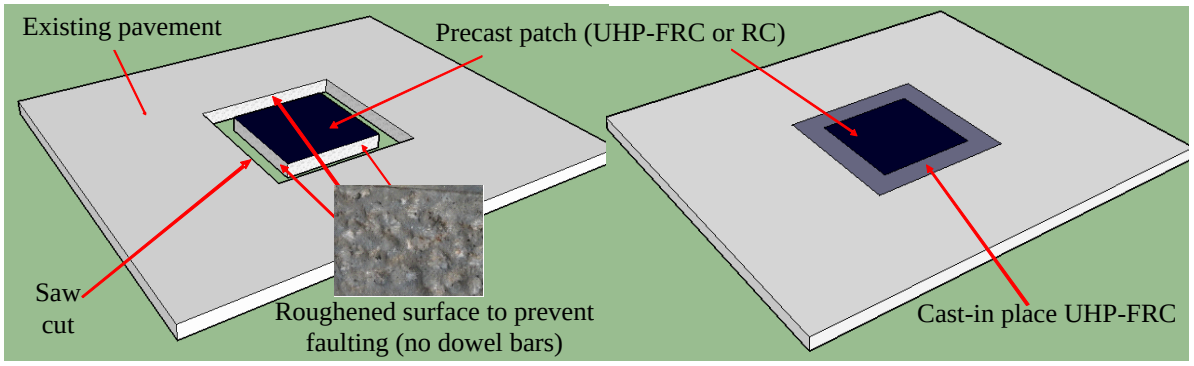

Figure 3- 12 Proposed method for UHP-FRC pavement repair.

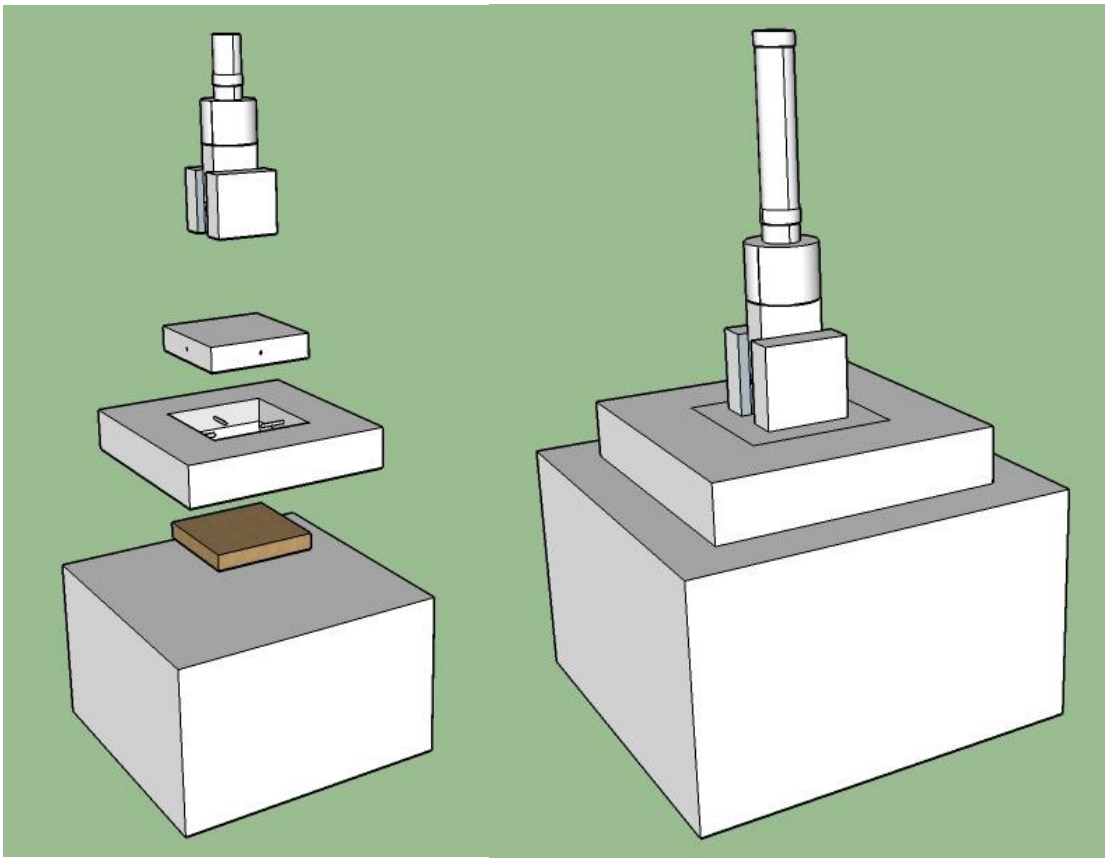

(a) (b)

Figure 3- 13 Punch test setup (a) exploded view and (b) normal view.

The proposed idea was verified by the punch test shown in *Figure 3-13*. Two punch specimens were designed to compare the interface shear capacity between the existing concrete pavement and the repair concrete material. Both specimens consist of an outer hollow slab with external dimensions of 50 × 28 in^2 (1270 × 711 mm^2) and internal hollow section with dimensions of 30 ×10 in^2 (762 × 254 mm^2) with a total depth of 10 inches (254 mm). The depth of the inner repair slab for both the specimens was selected as 4 inches (101 mm).

The first specimen was prepared to simulate the actual repair methods used in practice. Four No. 4 rebars of 17 inches (432 mm) were used as dowel bars with 8.5 inches (216 mm) embedded in the outer hollow slab and remaining in the inner cast-in place slab as shown in *Figure 3-14*. The rebars were positioned at a depth of 2 inches (51 mm) from the top surface (mid depth of the repair cast in place concrete slab). Strain gauges were placed in each dowel bar one inch from the interface.

For the second specimen, UHP-FRC was used. A precast UHP-FRC slab with dimensions of 26 × 6 × 4 in^3 (660 × 152 × 102 mm^3) was placed in the middle of the repair area and the remaining area was filled with cast-in-place UHP-FRC (*Figure 3-15*). The primary purpose of using the UHP-FRC precast panel is to significantly reduce the required volume of UHP-FRC to be cast on site. This would make it more convenient and further aid in reducing the curing time of the cast-in-place UHP-FRC pavement repair.

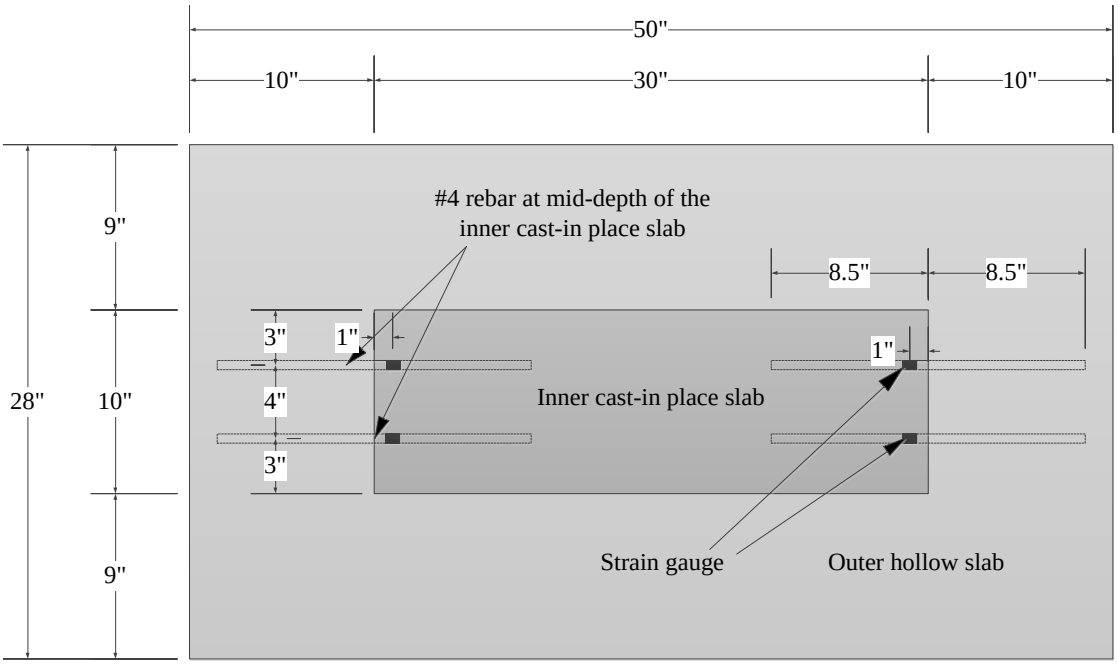

Figure 3- 14 Specimen details for punch test specimen with No. 4 rebars and cast-in-place PC.

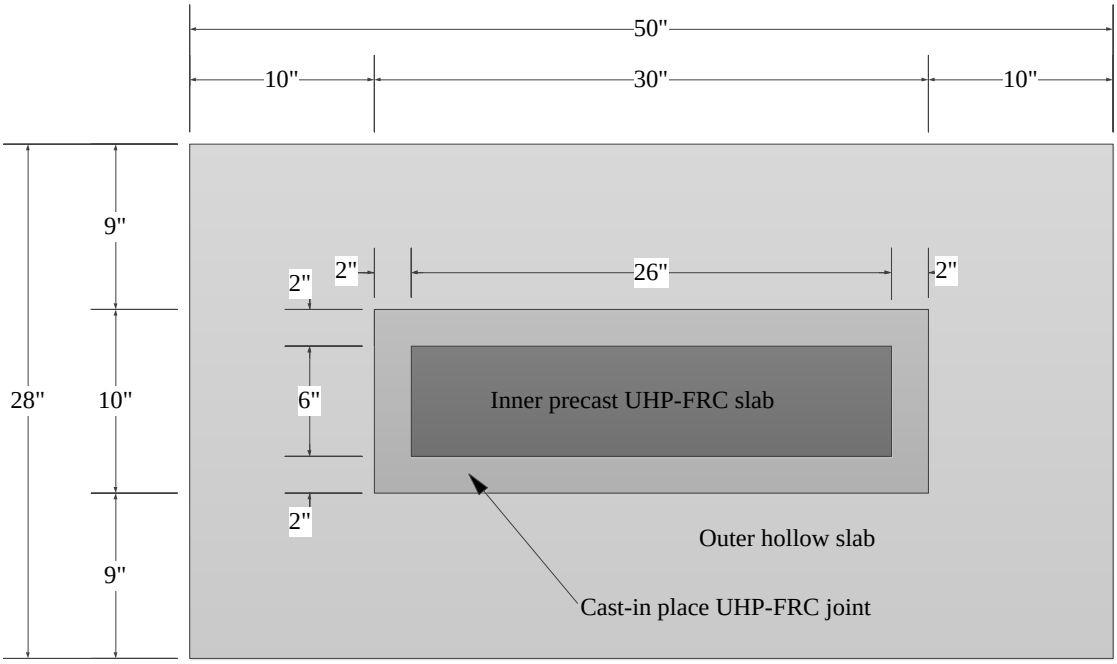

Figure 3- 15 Specimen details for punch test specimen with an inner precast UHP-FRC slab and a cast-in-place UHP-FRC joint.

The preparation of formwork, mixing, and casting of the outer hollow slab is presented below from *Figures 3-16 and 3-17*. The concrete surface after the removal of the specimen from the formwork is shown in *Figure 3-18*.

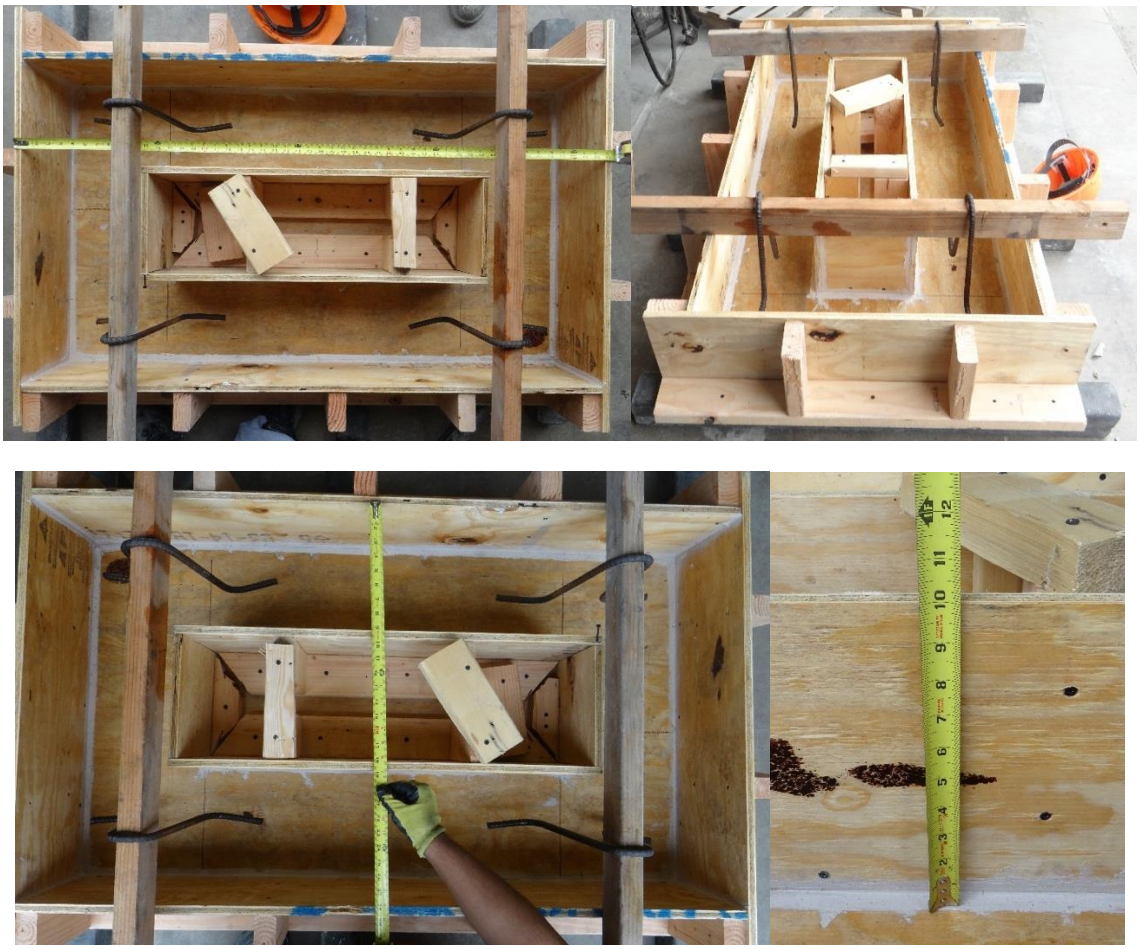

Figure 3- 16 Formwork for the outer hollow slab.

Figure 3- 17 In-lab concrete mixing is shown in top photo and casting for the outer hollow slab is shown in the bottom photo.

Figure 3- 18 Concrete surface roughness (cast in contact with wood formwork).

3.1.3.3. Punch Test Specimen Preparation

Preparation of punch specimen with dowel bars and cast-in-place PC:

1. Holes 8.5 inches (216 mm) deep (*Figure 3-19*) were drilled in the outer hollow slab at a depth of 2 inches (51 mm) from the top surface. Then the hole was blown out twice, brushed out twice, and blown out twice again. Epoxy was then put in the hole and a rebar was inserted with a slight twisting motion. *Figure 3-20* shows the specimen after the insertion of rebar.

(a) (b)

Figure 3- 19 (a) Drilling in the outer hollow slab for rebar placement and (b) rebar length inside the newly repaired concrete.

Figure 3- 20 Outer hollow slab showing embedded rebar location.

2. Then, the strain gauges were installed one inch from the interface as shown in *Figure 3-21*.

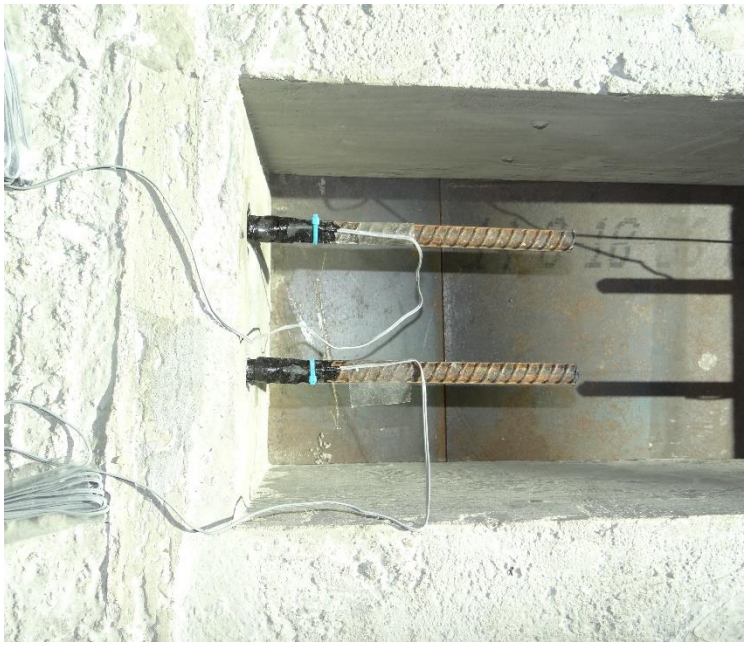

Figure 3- 21 Strain gauges installed on the rebar 1 inch from the interface.

3. The outer hollow slab with the rebar installed with the strain gauge was setup on the compression machine on a steel support.

4. The hollow portion was filled with 6 inches of sand and slightly compacted to provide a firm base for casting 4 inches (102 mm) of cast-in-place plain concrete as shown in *Figure 3-22*.

Figure 3- 22 Placing and compacting the sand in the hollow portion of the slab to provide a firm support for casting 4 inches of cast-in-place PC.

5. Finally, PC is cast in place on the sand (*Figure 3-23*).

Figure 3- 23 Cast in place PC punch test specimen.

Preparation of punch specimen with UHP-FRC:

1. First, the precast UHP-FRC precast panel was cast (*Figure 3-24*). After casting, the concrete was heated using heaters to provide an average temperature of 100°F.

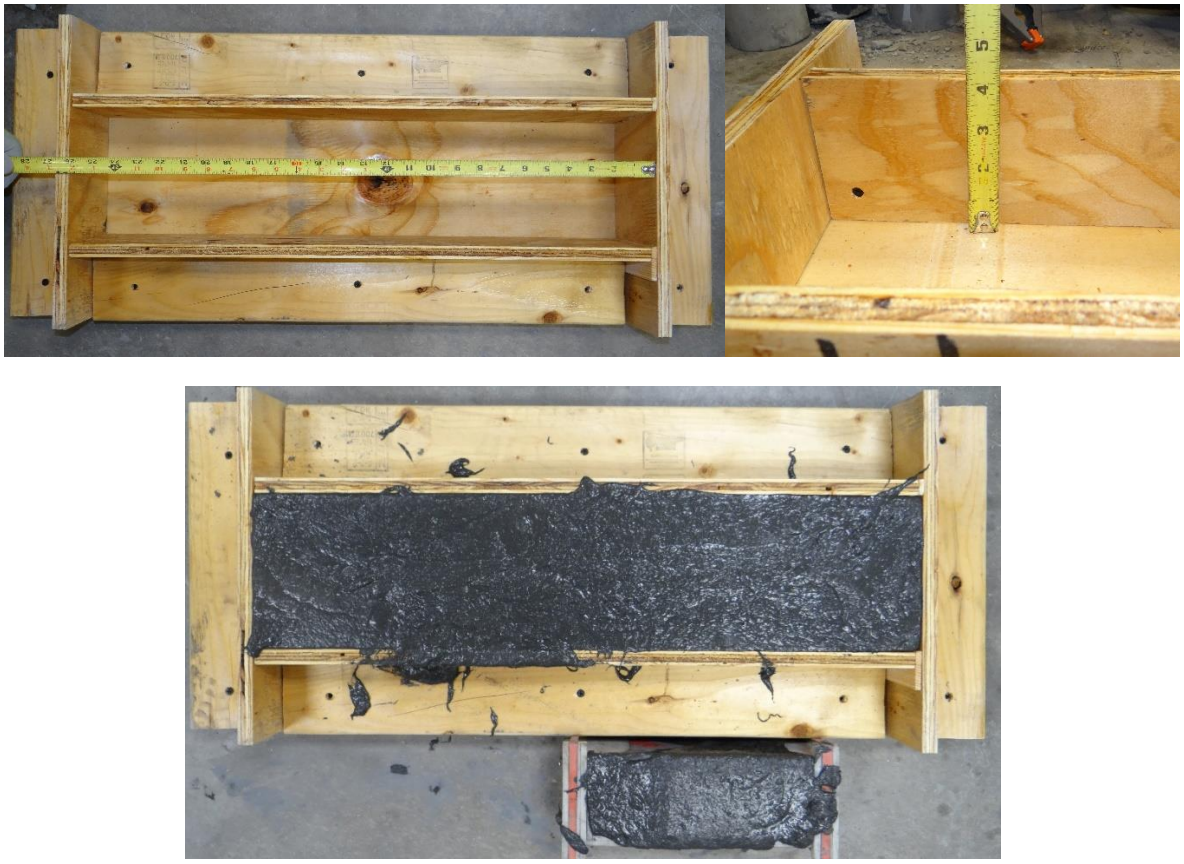

Figure 3- 24 Formwork and casting of the UHP-FRC precast panel.

2. Then, the inner surface of the hollow slab was roughened to a depth of 4 inches from the top. A pneumatic needle scaler was used to get a CSP 5 roughness level (*Figure 3-25*).

Figure 3- 25 Roughened surface of inner wall of the outer hollow slab with a depth of 4 inches with a roughness level of CSP 5.

3. After that, the outer slab was placed on steel supports in the compression machine. Sand was filled and compacted in the bottom 6 inches of the hollow portion, which provided a depth of 4 inches from the top for placement of the UHP-FRC precast panel and UHP-FRC casting (*Figure 3-26*).

Figure 3- 26 The 4-inch casting surface level obtained after placement and compaction of sand in the hollow portion.

4. The UHP-FRC precast panel was placed in the center of the hollow part as shown in *Figure 3-27* and UHP-FRC was cast in place in the joint between the precast UHP-FRC panel and the outer hollow slab (*Figure 3-28*).

Figure 3- 27 Placement of precast UHP-FRC panel into hollow portion of outer hollow slab.

Figure 3- 28 Cast in place UHP-FRC between the precast UHP-FRC slab and outer hollow slab.

5. Finally, the cast in place UHP-FRC is heated using a combination of lamps to obtain an average temperature of 100 °F (*Figure 3-29*).

Figure 3- 29 The cast-in-place UHP-FRC repair joint heated to an average temperature of 100 °F using a combination of heaters.

3.1.3.4. Testing

The specimen was tested one day after casting of the hollow portion of the outer hollow slab (PC and UHP-FRC). The tests were done using Tinius Olsen SuperL universal testing machine located in the Civil Engineering Laboratory Building (CELB) at UTA. Tests were done using a loading rate of 0.02 in./min. Displacement control was chosen over load control to incorporate the post-peak data for the punch specimens. Similar to the slant shear test, LVDT was used to measure the vertical deformation and a load cell was used to measure the applied vertical load. The strain gauge (when used) was placed one inch above the interface, which gave the value of strain in the reinforcement bar. All the sensors were connected to the DAQ box and the data was recorded. Uniform loading was applied in the central 18 × 9 in^2 area using two 9 × 9 × 2 in^3 square steel plates. A 0.5-in.-thicksteel plate was placed on top of these two steel plates[2] to keep the plates stationary throughout the loading to assure uniform application. The test setup is shown below in *Figure 3-30*.

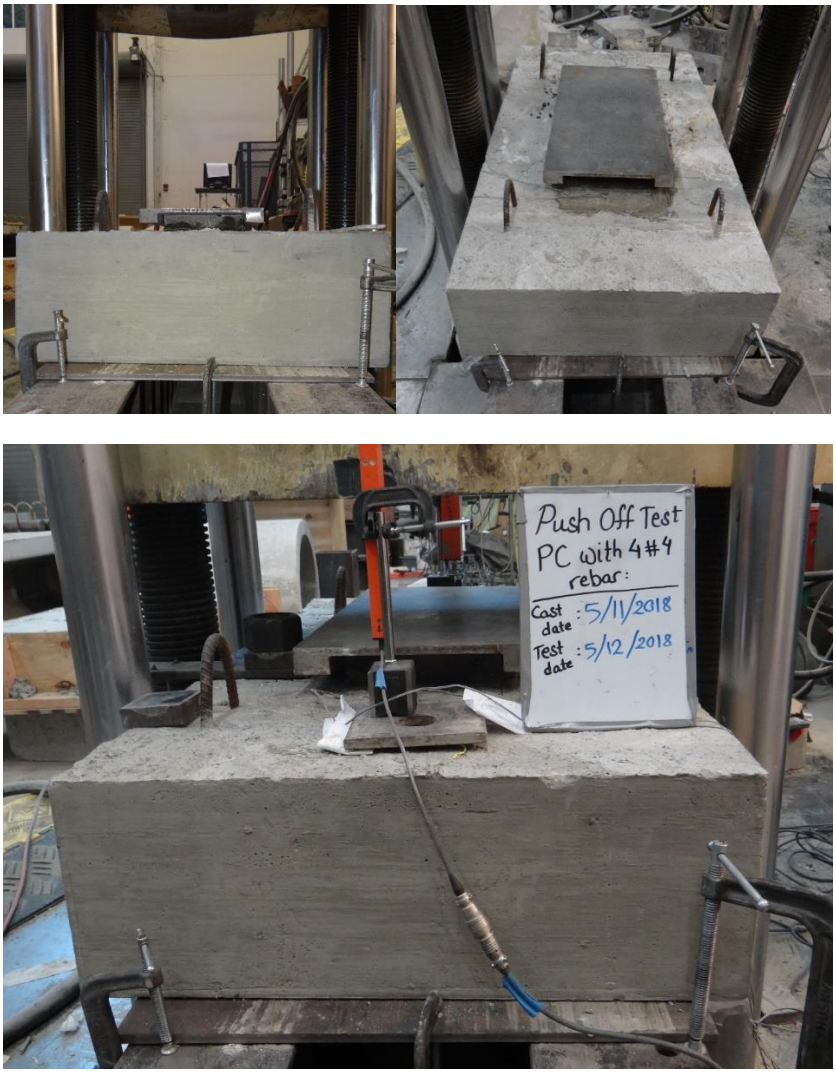

Figure 3- 30 Test setup for the punch test.

Chapter 4

Part I: Experimental results

4.1 Trial Mix

The results of the trial mix are presented in Table 4-1. *Figures 4-1 to 4–12* show the stress vs. strain graphs of the trial specimens in Table 4-1.

Table 4- 1 Trial mix design.

Trial Mix	Description	Peak load			Average Peak Load	Average compressive strength	Age of concrete
		Sample 1	Sample 2	Sample 3			
		kips	kips	kips	kips	ksi	days
1	CL Mix 0.75% LFB: Long polyethylene fiber (LFB)	137.4	148.5	132.7	139.6	18.06	28
2	No GP, 20% Imerfill, Long PE: Glass powder (GP) Polyethylene fiber (PE)	119.2	124.9	125.5	123.2	15.94	28
3	No GP, Long PE	137.8	130.5	133.2	133.8	17.32	28
4	30% FA, LPE 0.75%: Fly ash (FA)	125.6	136.8	119.3	127.3	16.47	14
5	30% FA, LPE 0.1%, SPE 0.65%: Long Polyethylene fiber (LPE)	114.2	119.8	119.4	117.8	15.24	14

	Short Polyethylene fiber (SPE)						
6	30% FA, LPE 0.1%, SPE 0.65%	120.5	115.0	128.7	121.4	15.71	28
7	30% FA, LPE 0.25%, SPE 0.5%	120.0	115.5	-	117.8	15.24	14
8	30% FA, LPE 0.25%, SPE 0.5%	132.1	118.2	-	125.2	16.19	28
9	30% FA, LPE 0.25%, SPE 0.5%(greased)	87.8	-	-	87.8	11.36	14
10	30% FA, LPE 0.75%	121.1	154.4	129.5	135.0	17.47	28
11	3% Steel (greased)	133.1	-	-	133.1	17.22	17
12	20% FA, PE 0.75%	120.4	126.2	115.0	120.6	15.6	14
13	20% FA, PE 0.75%: 150°F	67.4	76.0	84.6	76.0	9.84	1
14	20% FA, PE 0.75%: 100°F	51.8	55.2	52.9	53.3	6.90	1

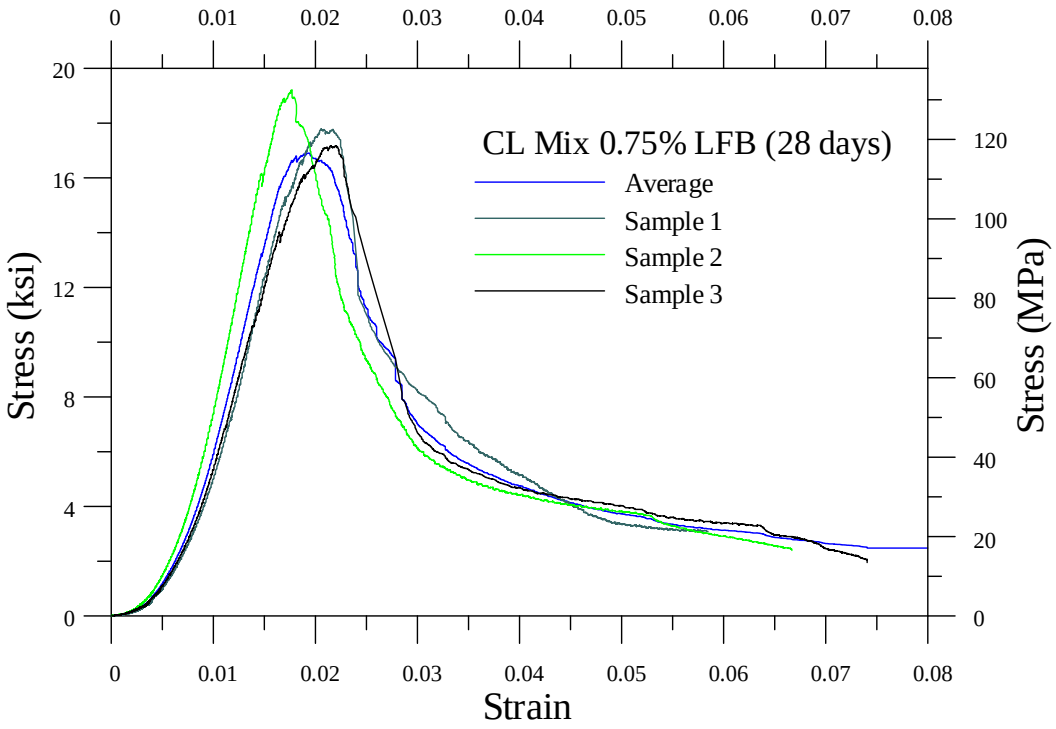

Figure 4- 1 Stress vs. strain (Trial Mix 1: CL mix 0.75% LFB for 28 days).

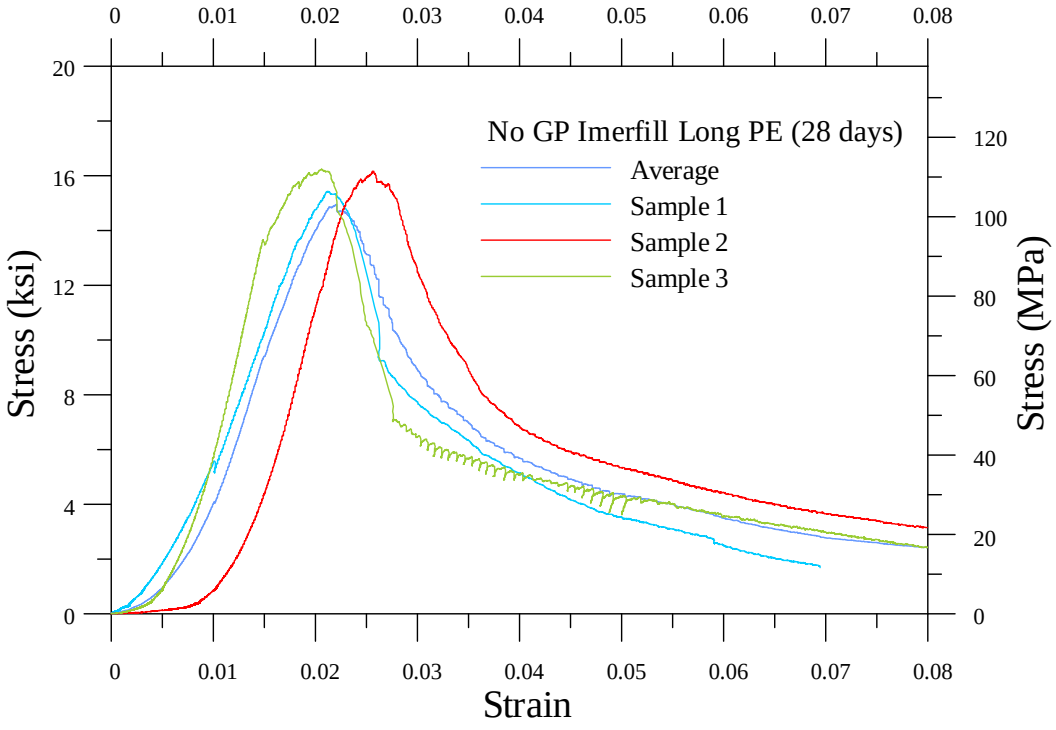

Figure 4- 2 Stress vs. strain (Trial Mix 2: No GP, Imerfill, long PE for 28 days).

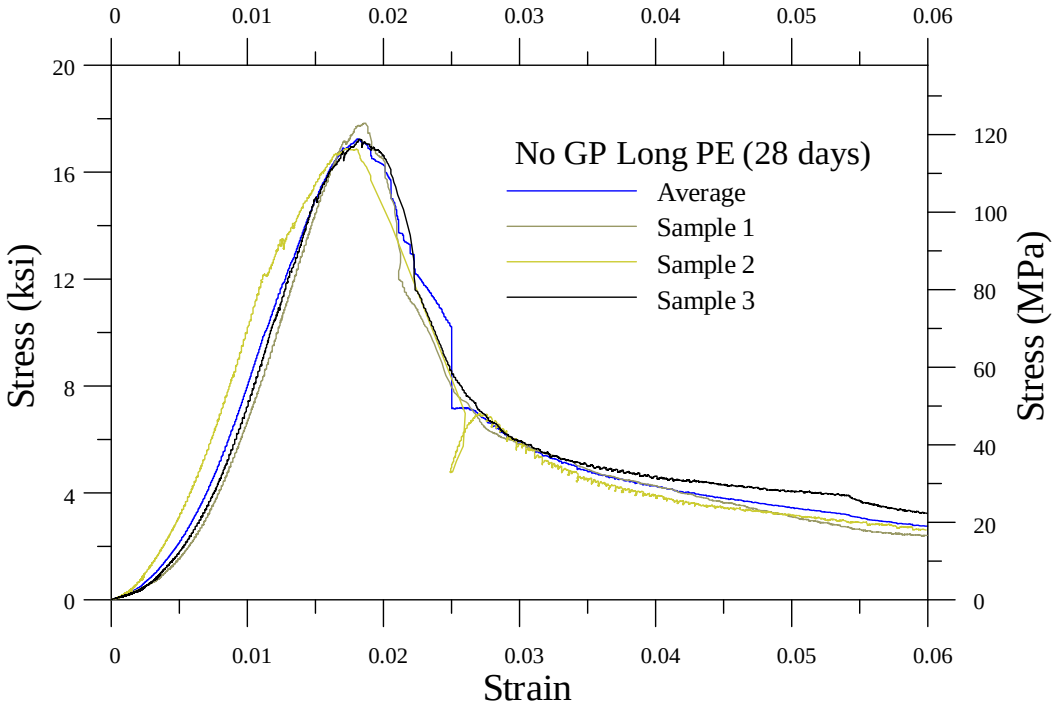

Figure 4- 3 Stress vs. strain (Trial Mix 3: No GP, long PE for 28 days).

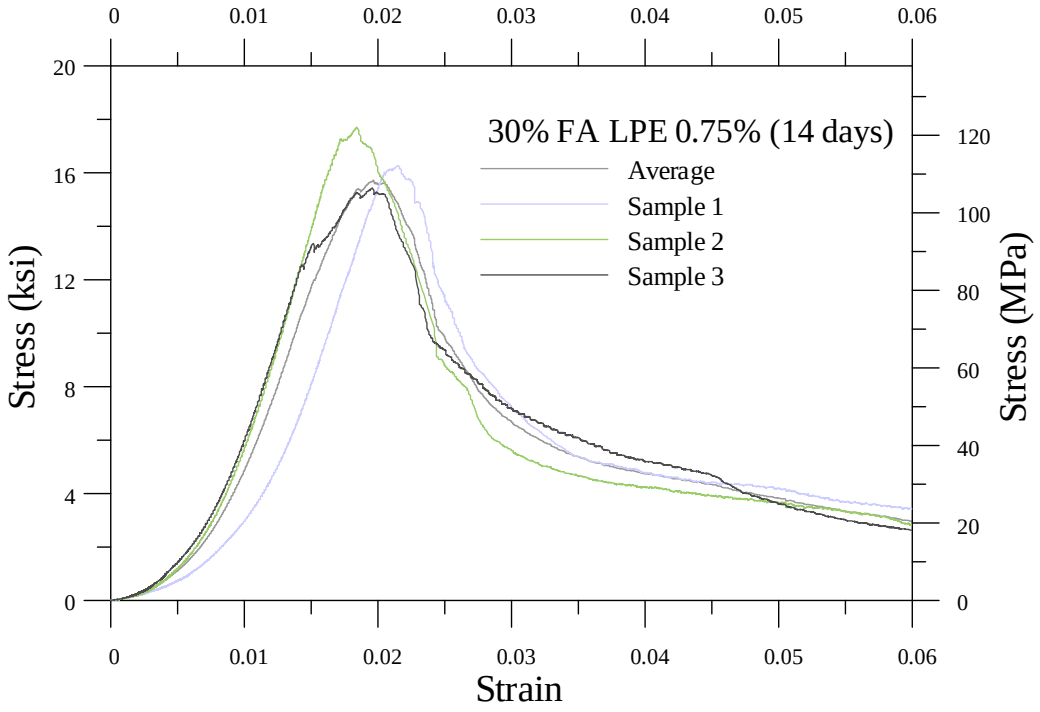

Figure 4- 4 Stress vs. strain (Trial Mix 4: 30% FA, long PE 0.75% for 14 days).

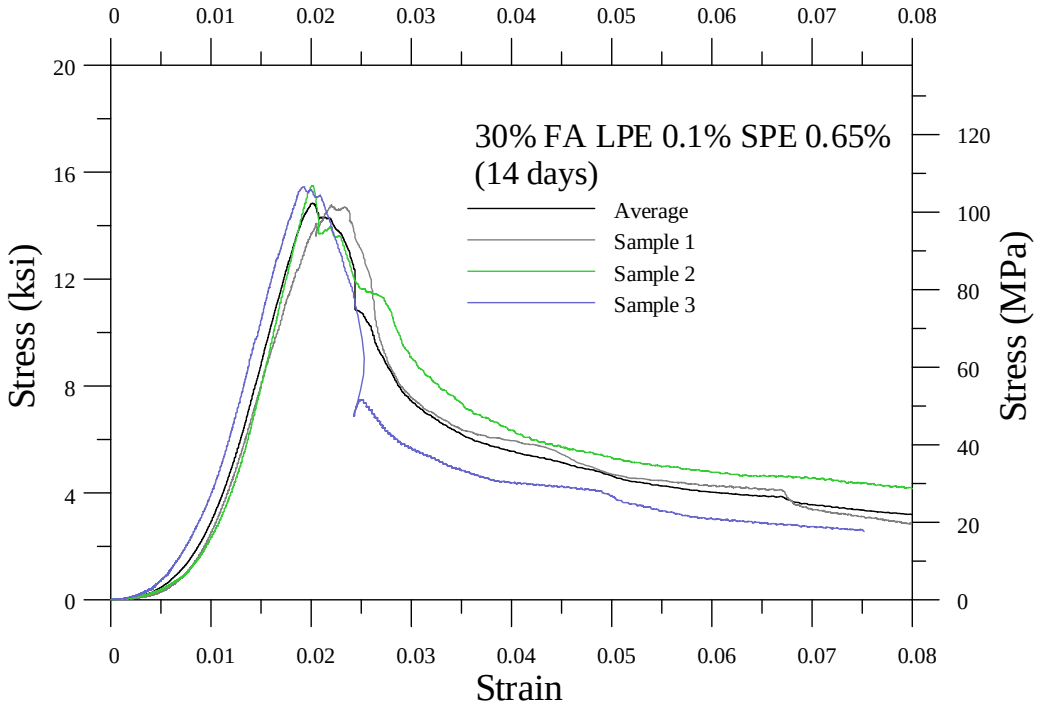

Figure 4- 5 Stress vs. strain (Trial Mix 5: 30% FA, long PE 0.1%, short PE 0.65% for 14 days).

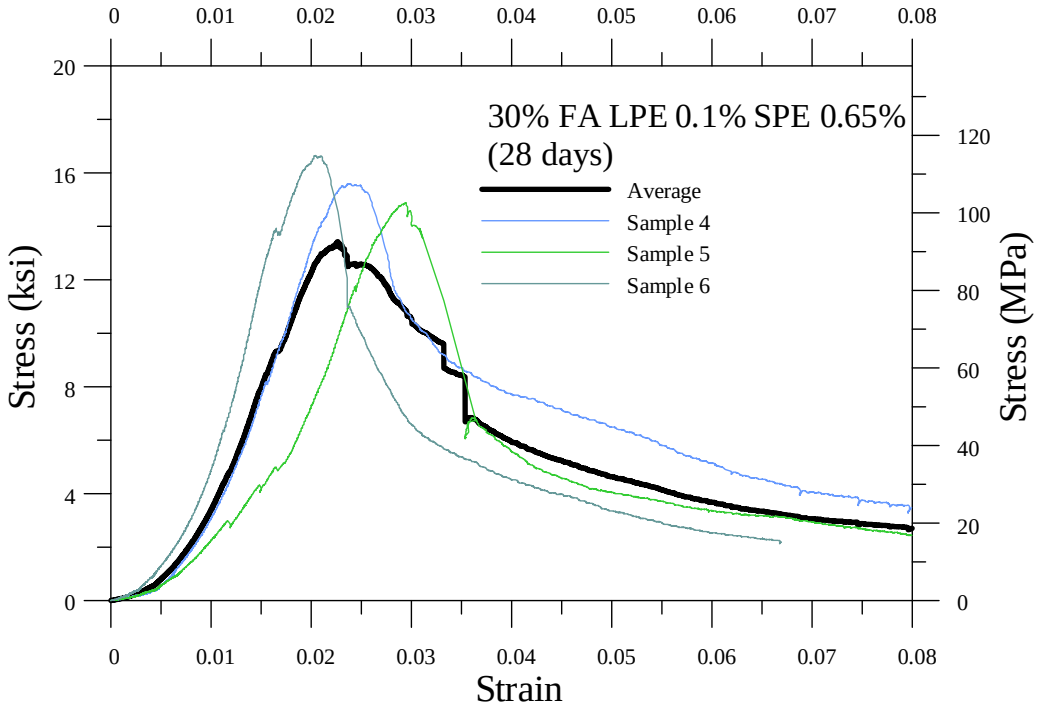

Figure 4- 6 Stress vs. strain (Trial Mix 6: 30% FA long PE 0.1% short PE 0.65% for 28 days).

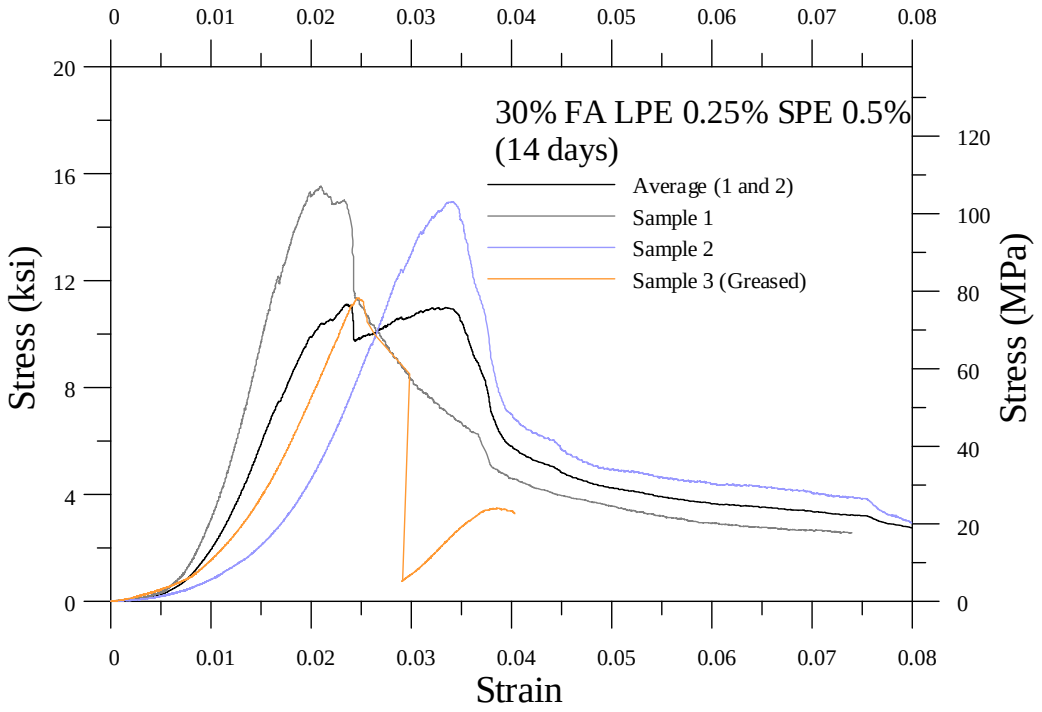

Figure 4- 7 Stress vs. strain (Trial Mix 7: 30% FA long PE 0.25% short PE 0.5% for 14 days).

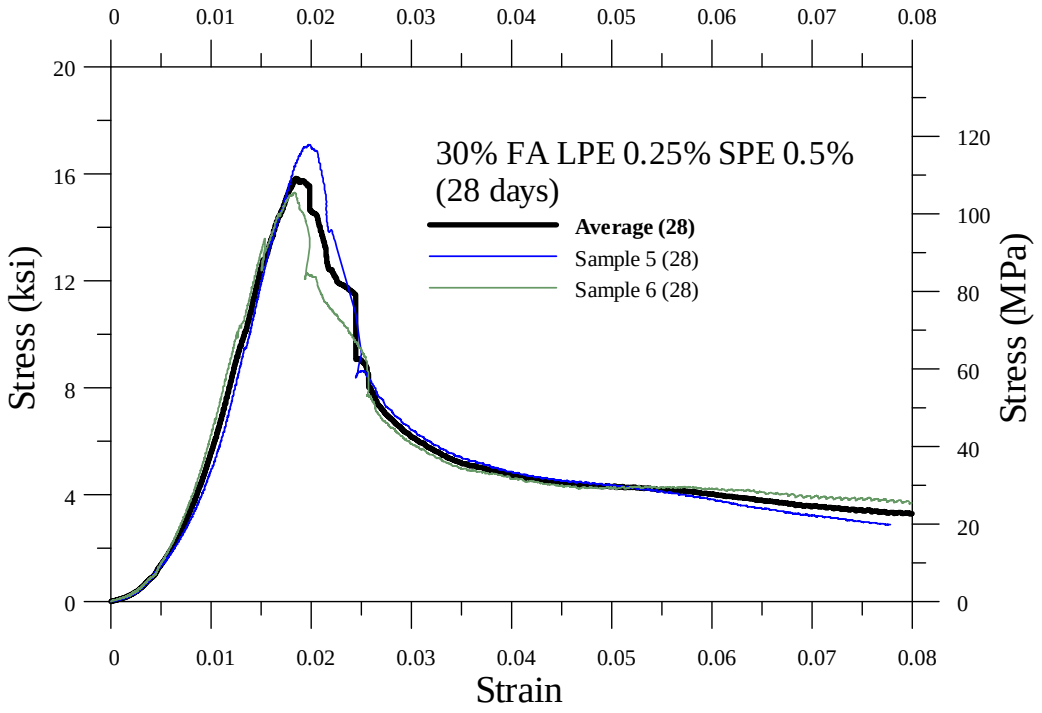

Figure 4- 8 Stress vs. strain (Trial Mix 8: 30% FA long PE 0.25% short PE 0.5% for 28 days).

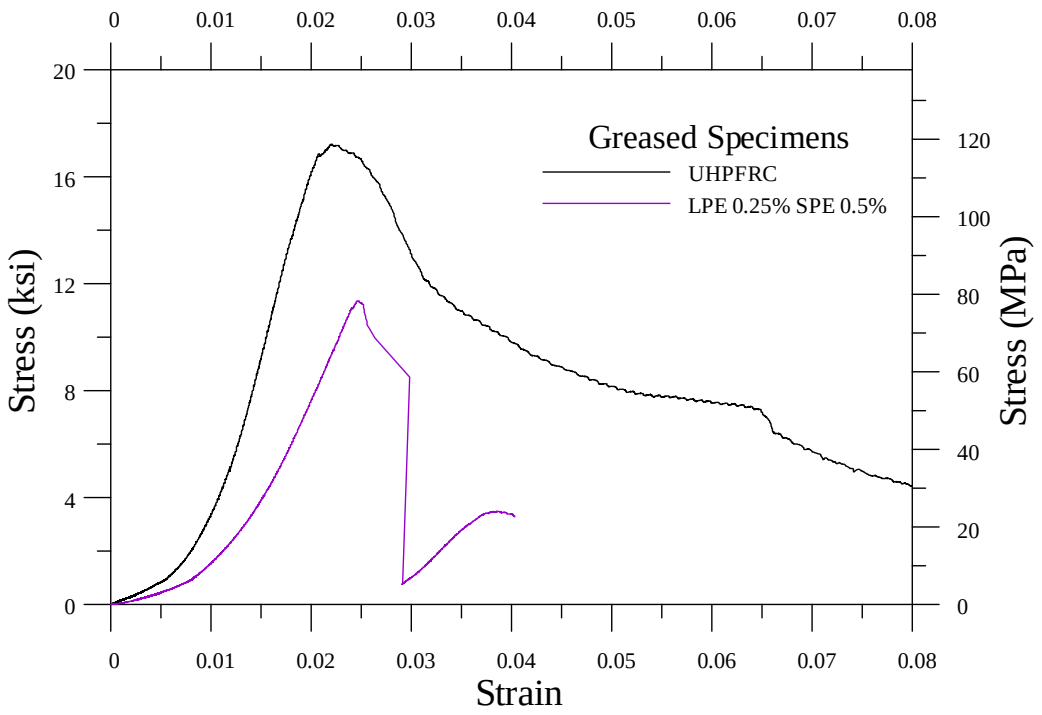

Figure 4- 9 Stress vs. strain (Trial Mix 9 and 11: greased specimens).

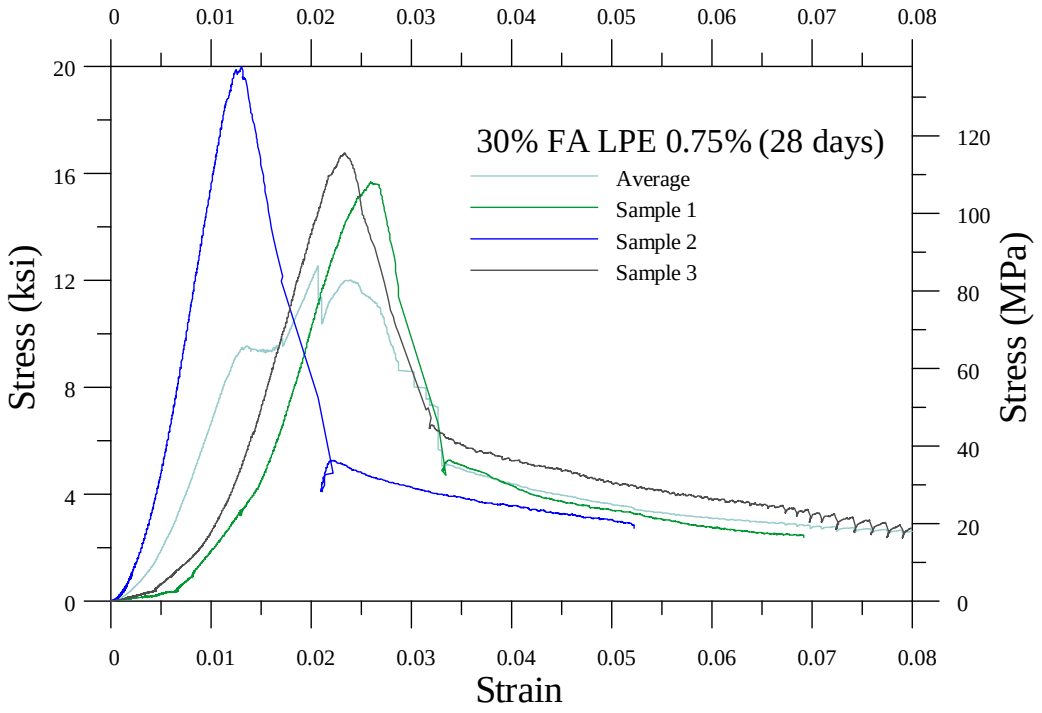

Figure 4- 10 Stress vs. strain (Trial Mix 10: 30% FA long PE 0.75% for 28 days).

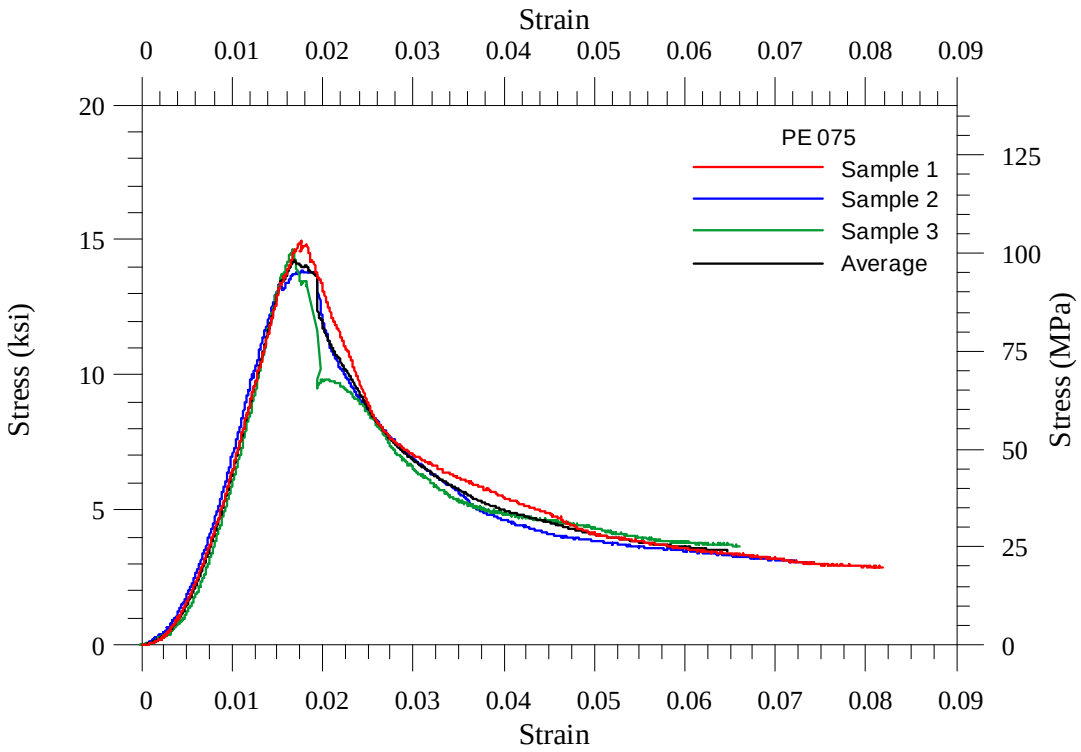

Figure 4- 11 Stress vs. strain (Trial Mix 12: 20% FA PE 0.75%).

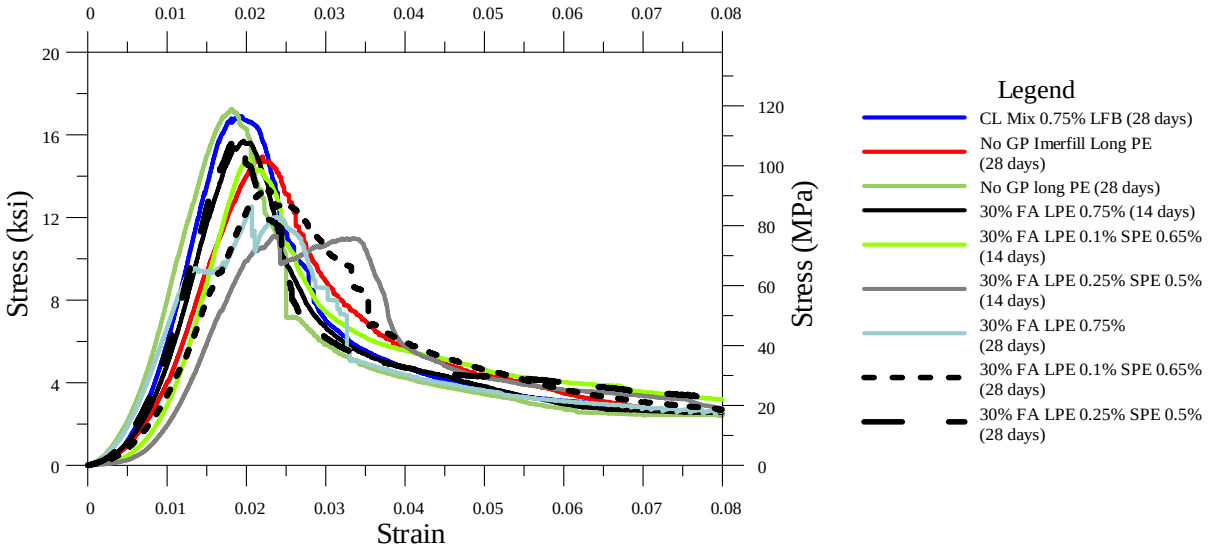

Figure 4- 12 Stress vs. strain (combined).

Among the different mixes that were tried during this phase, based on economics and consistency of the mix, the concrete consisting of 0.75% per unit volume polyethylene fibers was selected. The mix was cured at a temperature of 150 °F and gained a one-day compressive strength of 9.84 ksi. The same UHP-

FRC mix was used for the slant shear testing. However, in the UHP-FRC punch test specimen, the heating setup was able to maintain an average temperature of 100 °F. This resulted in a one-day compressive strength of 6.9 ksi.

4.2 Experimental results for Slant Shear Test

A total of 12 slant shear specimens were prepared. However, 5 specimens did not meet the surface roughness criteria and hence the test results were discarded. The test results for the slant shear tests are presented in the Table 4-2.

Table 4- 2 Slant shear test results.

Specimen Top Half	Days	Peak vertical load (kips)	Shear stress (psi)	Average shear stress (psi)
PC with smooth surface (saw cut)	1	36.6	455	455
PC with surface roughened (roughness level CP7)	1	50.4	625	598
		45.7	570	
PC with #4 rebar and smooth surface (saw cut)	1	44.1	550	609
		52.3	650	
		50.4	625	
UHP-FRC with surface roughened (roughness level CP5)	1	81.9	1019	1019

4.2.1 Strain (PC with Dowel Bars)

Figure 4-13 shows the vertical applied load versus strain in reinforcement and vertical applied load versus deformation along slip plane obtained from the slant shear test data.

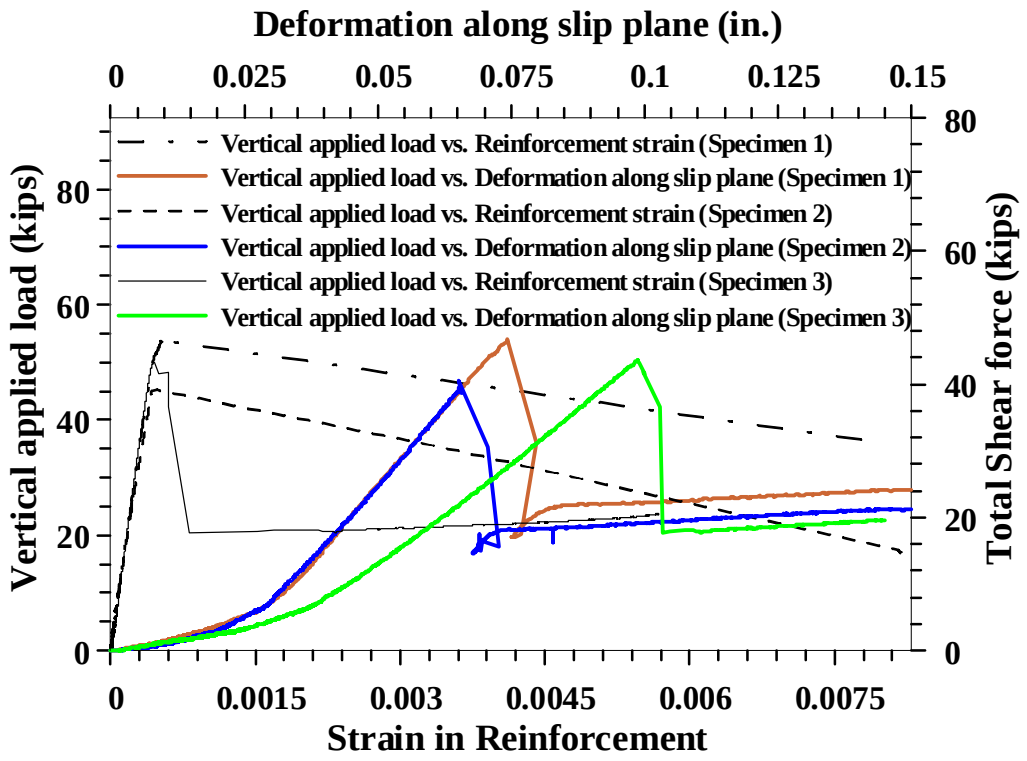

Figure 4- 13 Vertical applied load vs. strain in reinforcement and vertical applied load vs. deformation along the slip plane for SST test specimen with a smooth surface and rebar.

From the graph (Figure 4-13) above, it was observed that, from Equation 5:

Rebar force = 0.0006 ×29000 ksi × 0.2 in^2 × sin (30°)

= 1.74 kips

This value of rebar force is very low. This suggests that the force developed in the rebar is not very significant at the instant of peak vertical applied load.

4.2.2 UHP-FRC test specimens

The specimens were tested one day after casting of the top half of the slant shear specimen. A pneumatic surface scaler (*Figure 4-14b*) was used to approximate ICRI's CSP 5 (*Figure 4-14c*) and no dowel bars were used. The UHP-FRC slant shear specimens (*Figure 4-14c*) were cured at 150 °F in an oven and after one day, the compressive strength was 10.95 ksi.

For the slant shear specimen, a peak applied vertical load of 81 kips was recorded. This corresponds to a shear force of 71 kips, which is 50% higher than that of conventional pavement repair. A post-test UHP-FRC specimen is shown in *Figure 4-15*.

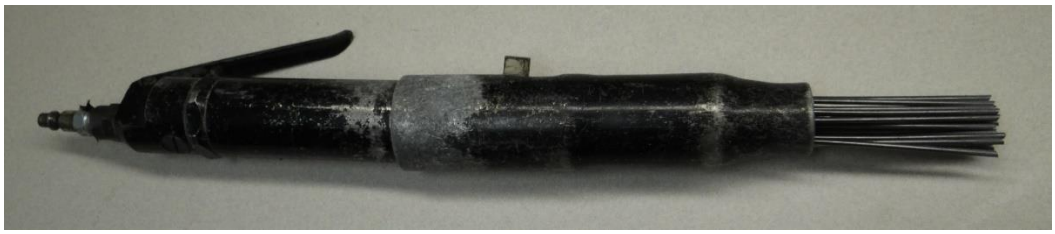

(a)

(b) (c)

Figure 4- 14 (a) A pneumatic needle scaler used to roughen the specimen, (b) roughened surface for the bottom half of the UHP-FRC specimen roughened by using the pneumatic scaler to approximately measure ICRI's CSP 5, and (c) results of the UHP-FRC slant shear test.

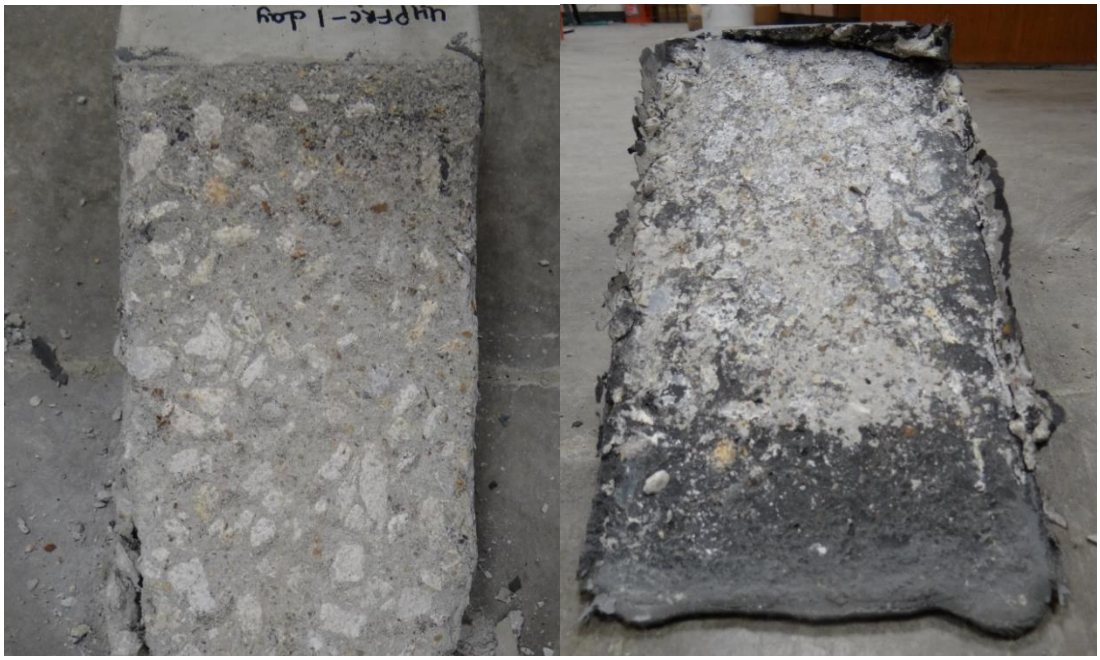

(a) (b)

Figure 4- 15 Post-test pictures of slant shear specimen. (a) Lower part: plain concrete and (b) Upper part: UHP-FRC.

4.2.3 Main Findings

The following are the findings of the slant shear tests:

- From the slant shear tests, it was observed that the peak shear stress for UHP-FRC is 167% of the shear stress recorded for the Portland cement concrete (PCC). Hence, UHP-FRC shows a significantly better interface bond strength than PCC.
- For the slant shear specimen with a smooth interface embedded with a No. 4 dowel bar, it is seen that the strain in the rebar is significantly lower when the peak value of the vertical load is reached. The strain in the rebar increased gradually and then yielded after the peak vertical load was achieved. This implies that the rebar does not contribute to bond strength development at peak load.
- The peak vertical load values for the PC does not show much variation for different levels of concrete surface preparation. Previous research carried out using large scale push off tests *(Palacios, 2015; Waweru, 2015)* with various magnitudes of surface roughness indicated that a

rougher surface can provide strong interface shear resistance. This contradicts the data obtained from the slant shear test. Hence, a different test method is necessary for accurate representation of the interface bond strength between the existing concrete and the new repair concrete. For this purpose, further test results are necessary using the punch tests to determine the exact values of shear strength.

4.3 Experimental results for Punch Test

The results of the punch test are summarized in the Table 4-3 below:

Table 4- 3 Results for punch test specimens.

Punch specimen	Peak applied vertical load (kips)	Vertical deformation at peak (in)	Shear stress (psi)	Remarks
PC with dowel bars and interface surface smooth	39.3	0.027	120	
UHP-FRC without dowel bars and interface roughness CSP 5	51.3	0.054	160	30% more

4.3.1 Observed Cracking (PC with Dowel Bars)

The specimen reached a peak load of 39.3 kips at a vertical deformation of 0.027 in. The loading behavior is shown in the *Figure 3-30*. The nature of the vertical load vs. vertical deformation and vertical load vs reinforcement strain obtained is similar to the nature of the graph obtained from the slant shear tests. The loading curve shows no development of strain in the rebar at the peak load. The graph shows a significant drop in the vertical applied load after the peak. The load then increases gradually in proportion to the increase in reinforcement strain till the rebar yields, which is followed by the sudden drop in the load. The vertical deformation corresponding to the drop in the load by the yielding of rebar is 0.1 inch.

The vertical applied load vs strain of reinforcement is represented by the dashed line and the vertical applied load vs vertical deformation is represented by the solid line in *Figure 4-16* shown below.

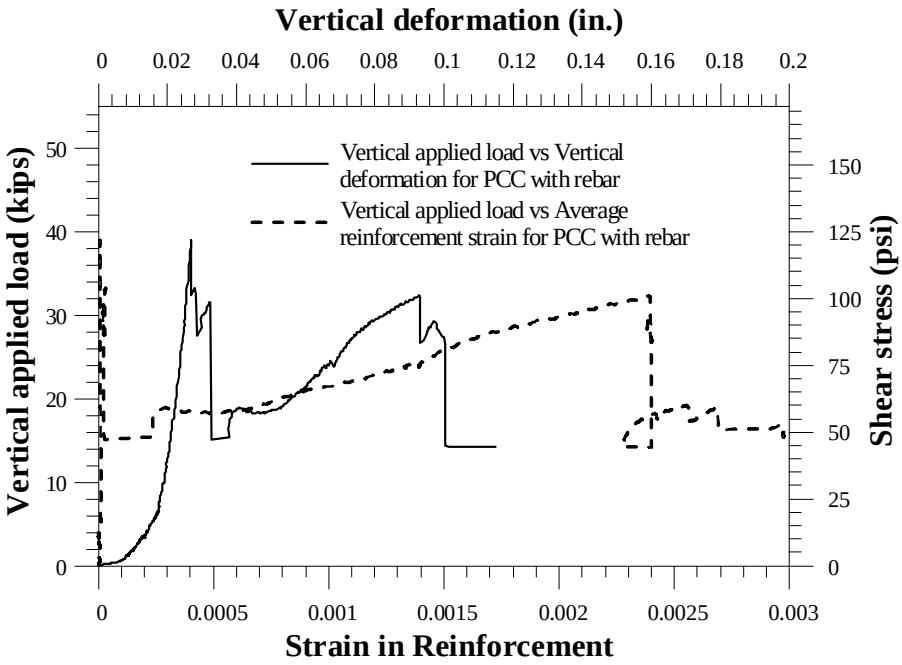

Figure 4- 16 Vertical applied load vs strain in reinforcement and vertical applied load vs. vertical deformation for PC concrete repair with dowel bars.

The following figures (*Figure 4-17 to 4-21*) show the test specimen before and after the completion of the tests.

Figure 4- 17 Punch test setup for PC specimen with dowel bars.

Figure 4- 18 Cracks observed at the interface between repair cast in place PC and the old concrete (outer hollow slab) post peak.

Figure 4- 19 Cracks seen in the outer slab initiating from the interface with the loading plates.

Figure 4- 20 Cracks seen at mid-span of the longer dimension extending throughout the depth of the slab.

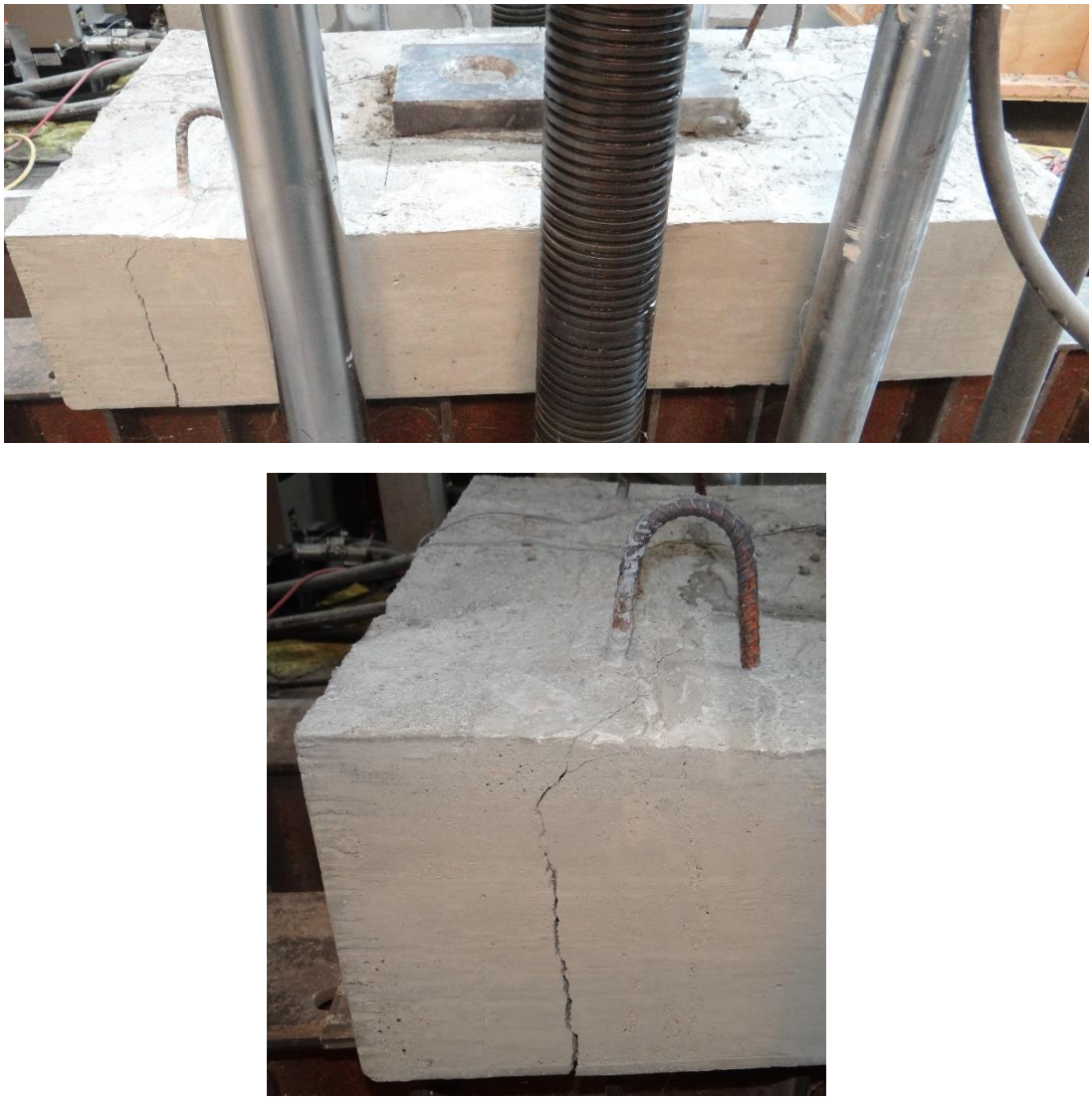

Figure 4- 21 Throughout cracks observed near the slab ends propagating from the corner of the inner slabs.

4.3.2 Observed Cracking (UHP-FRC)

The specimen reached a peak vertical load of 51.3 kips at a vertical deformation of 0.054 in. The specimen maintained the peak vertical load until a vertical deformation of 0.1 in. was reached. It was then followed by a gradual decrease in the vertical applied load with an increase in vertical deformation. No cracks were observed before the peak vertical load was reached.

Figure 4-22 presents the vertical applied load vs. vertical deformation for the UHP-FRC punch specimen.

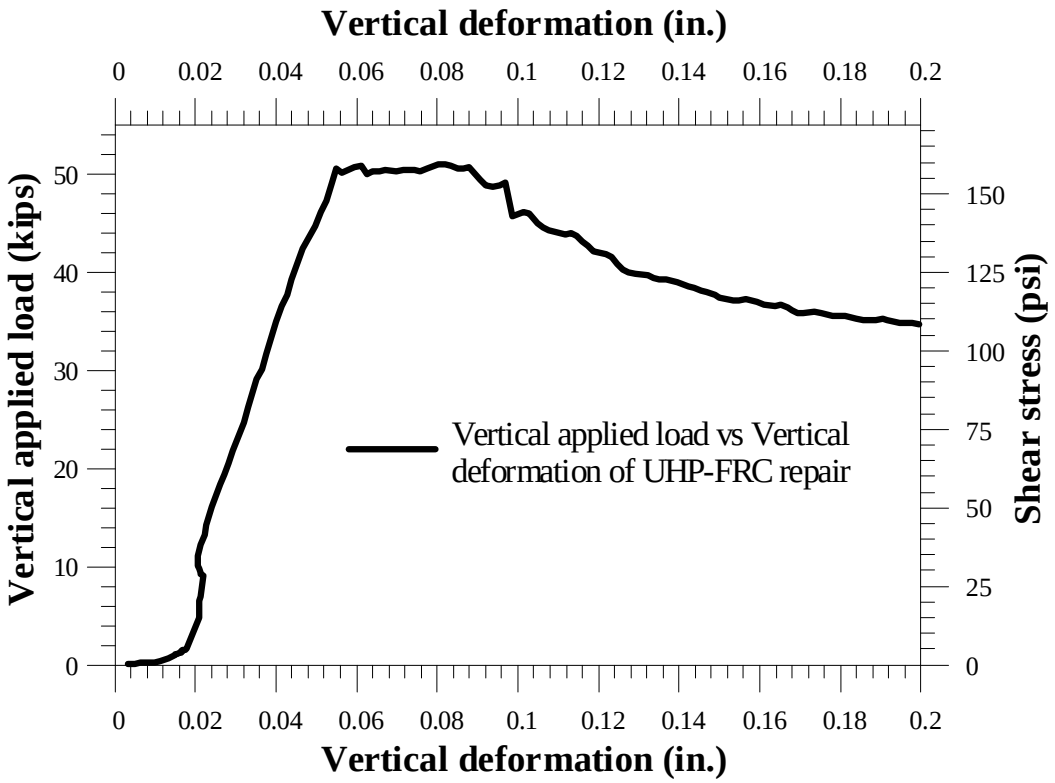

Figure 4- 22 Vertical applied load vs. vertical deformation of UHP-FRC punch test specimen.

Figures 4-23 to 4-28 show the test specimen before and after the completion of the tests.

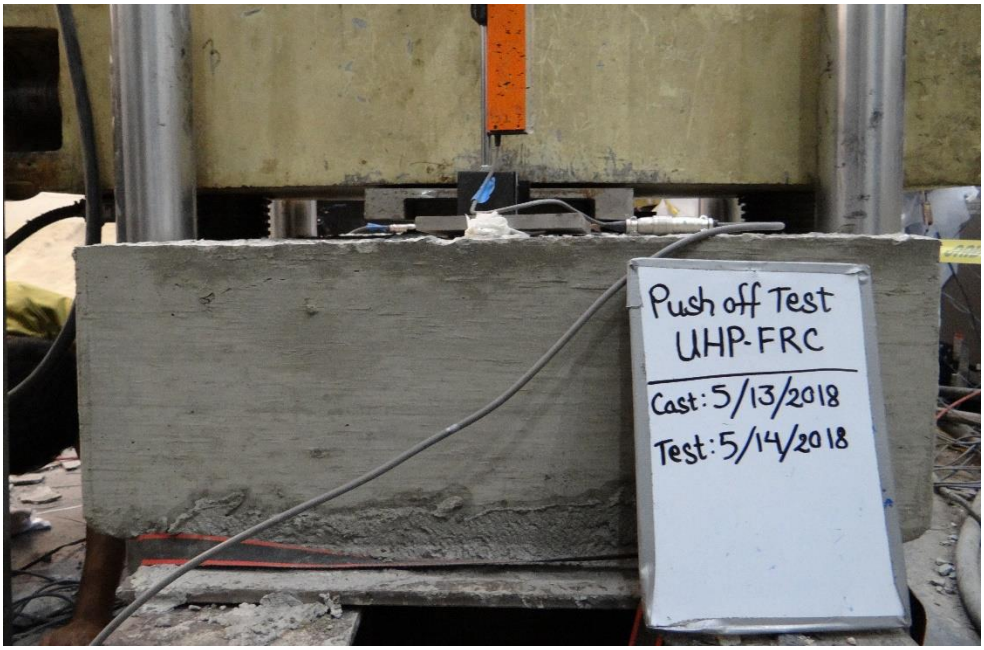

Figure 4- 23 Punch test setup for specimen with UHP-FRC precast slab and cast-in-place joint.

Figure 4- 24 Interface cracks observed in the UHP-FRC punch test specimen after peak.

Figure 4- 25 Initiation of cracks from the corner of the repair joint at 44 kips of the post peak vertical load.

Figure 4- 26 Interface crack caused due to vertical slip and cracks observed on the outer support slab.

Figure 4- 27 Vertical deformation of the central repair slab and cracks propagating from the corner of the repair slab into the supporting outer slab.

Figure 4- 28 Cracks at the mid-span and the edge of the support outer slab.

4.3.3 Main Findings

The following are the finding of the punch test:

- The No. 4 dowel bars showed no strain when the peak vertical load was reached. This implies that the dowel bars had no contribution to the interface bond strength unless significant interface slip was reached.
- The UHP-FRC punch test specimen consisting of precast UHP-FRC panels and a cast-in-place UHP-FRC joint shows 30% greater peak vertical load than that of the cast-in-place PC punch test specimen with dowel bars.
- The PC punch test specimen exhibits a rapid strength drop (*Figure 4-16*) after reaching the peak load while the UHP-FRC specimen maintained the peak vertical load up to a significant vertical deformation followed by a gradual decrease in the load. This ductility allows force redistribution in the actual pavement should the load exceed the capacity of the UHP-FRC strip used for repair.
- The outer hollow slab was not reinforced and showed significant cracking during the test.

Chapter 5

Life-Cycle Cost Analysis, Cost Comparison, Field Installation and Performance Monitoring

5.1 Life-cycle Cost Analysis (LCCA)

The life-cycle cost of cast in place (CIP) concrete pavement repair is compared with the proposed ultra-high- performance fiber-reinforced concrete (UHP-FRC) pavement repair.

The considerations considered while performing the LCCA are presented below:

- Panel thickness of 10 in. for both the scenarios were considered.
- Days required for each section in construction scheduling for CIP pavement repair was taken to be 7 days and 1 day for UHP-FRC pavement repair (similar to precast pavement repair) for every component. *(Menard, 2010)*
- The lane being repaired was closed for the entire duration of the scheduled pavement repair process.
- The user cost associated was assumed to be constant throughout the analysis period for simplicity.
- The LCCA was performed on a single lane (width of 12 ft and depth of 10 in.) for 1-mile length.
- Material cost for CIP pavement repair was taken as $\$250/yd^3$.
- Material cost for UHP-FRC pavement repair was taken as $\$1500/yd^3$.
- Maintenance strategy of CIP concrete pavement repair *(PennDOT, 2018)* was used. The maintenance interval for UHP-FRC repair was taken as double than the CIP concrete pavement repair owing to its increased durability.
- A 100 years analysis period was taken.
- Total cost for cast in place pavement repair was taken as $917,123 per lane mile (1997-2001 data form INDOT Contracts Division).
- Work zone cost and circuitry costs from the FHWA Interim Technical Bulletin *(Walls III and Smith, 1998)* were used after some modifications.
- Crash costs were ignored to simplify the calculations.
- The annual traffic growth rate for the analysis period was assumed to be 3%.

5.1.1 Calculation data and graphs:

The calculated agency costs and user costs associated with the conventional cast in place concrete pavement repair and the proposed UHP-FRC pavement repair method are presented in the Table 5-1 below.

Table 5- 1 The agency and user costs associated with the CIP concrete pavement repair and the proposed UHP-FRC pavement repair method

	Cast in Place Concrete Pavement repair			UHP-FRC pavement repair		
Years	Agency cost	User cost	Sum	Agency cost	User cost	Sum
	×1000	×1000	×1000	×1000	×1000	×1000
0	$917	$313	$1,230	$2,995	$45	$3,039
10	$64	$421	$485			
20				$64	$81	$145
15	$92	$488	$580			
25	$92	$656	$748			
30				$92	$109	$201
35	$92	$881	$974			
40	$64	$1,022	$1,086			
45	$92	$1,184	$1,277			
50	$917	$1,373	$2,290	$92	$196	$289
60	$64	$1,845	$1,909			
65	$92	$2,139	$2,232			
70				$92	$354	$447
75	$92	$2,875	$2,967			
80				$64	$476	$540
85	$92	$3,864	$3,956			
90	$64	$4,479	$4,543	$92	$640	$732
95	$92	$5,193	$5,285			

100	$0	$0	$0	$0	$0	$0

The data for the conventional CIP concrete repair in the Table 5-1 are converted to net present values for a varying discount rates starting from 1% to 6% with 1% increments and are presented in the Table 5-2 below.

Table 5- 2 Net present value with varying discount rates for CIP pavement repair

Years	Total cost ×1000	Net Present Value (NPV) × 1000					
		i=1%	i=2%	i=3%	i=4%	i=5%	i=6%
0	$1,230	$1,230	$1,230	$1,230	$1,230	$1,230	$1,230
10	$485	$485	$398	$361	$328	$298	$271
15	$580	$476	$431	$373	$322	$279	$242
25	$748	$645	$456	$357	$281	$221	$174
35	$974	$722	$487	$346	$247	$177	$127
40	$1,086	$766	$492	$333	$226	$154	$106
45	$1,277	$858	$524	$338	$219	$142	$93
50	$2,290	$1,464	$851	$522	$322	$200	$124
60	$1,909	$1,161	$582	$324	$181	$102	$58
65	$2,232	$1,228	$616	$327	$174	$94	$51
75	$2,967	$1,479	$672	$323	$157	$76	$38
85	$3,956	$1,785	$735	$321	$141	$63	$28
90	$4,543	$1,950	$764	$318	$133	$56	$24
95	$5,285	$2,158	$805	$319	$127	$51	$21
100	$0	$0	$0	$0	$0	$0	$0
	Total x 1000	$16,406	$9,043	$5,791	$4,089	$3,143	$2,586

The data for the proposed UHP-FRC pavement repair in the Table 5-1 are converted to net present values for a varying discount rates starting from 1% to 6% with 1% increments and are presented in the Table 5-3 below.

Table 5- 3 Net present value with varying discount rates for UHP-FRC pavement

Years	Total cost ×1000	Net Present Value (NPV) × 1000					
		i=1%	i=2%	i=3%	i=4%	i=5%	i=6%
0	$3,039	$3,039	$3,039	$3,039	$3,039	$3,039	$3,039
20	$145	$119	$97	$80	$66	$55	$45
30	$201	$149	$111	$83	$62	$47	$35
50	$289	$175	$107	$66	$41	$25	$16
70	$447	$223	$112	$56	$29	$15	$8
80	$540	$244	$111	$51	$23	$11	$5
90	$732	$299	$123	$51	$21	$9	$4
100	$0	$0	$0	$0	$0	$0	$0
	Total x1000	$4,248	$3,701	$3,426	$3,281	$3,200	$3,152

The net present values for corresponding values of discount rates for the conventional CIP pavement repair method and proposed UHP-FRC pavement repair are summarized and compared in the Table 5-4 below.

Table 5- 4 Comparison of results of LCCA between CIP concrete pavement repair and proposed UHP-FRC repair for varying discount rates for the 100-year analysis period

Discount rate	CIP concrete pavement repair	Proposed UHP-FRC pavement repair	Remarks
i%	Total × 1000	Total × 1000	
1%	$16,406	$4,248	26%
2%	$9,043	$3,701	41%
3%	$5,791	$3,426	59%
4%	$4,089	$3,281	80%
5%	$3,143	$3,200	102%

6%	$2,586	$3,152	122%

The above Table 5-4 is presented in a graphical format in the *Figure 5-1* below.

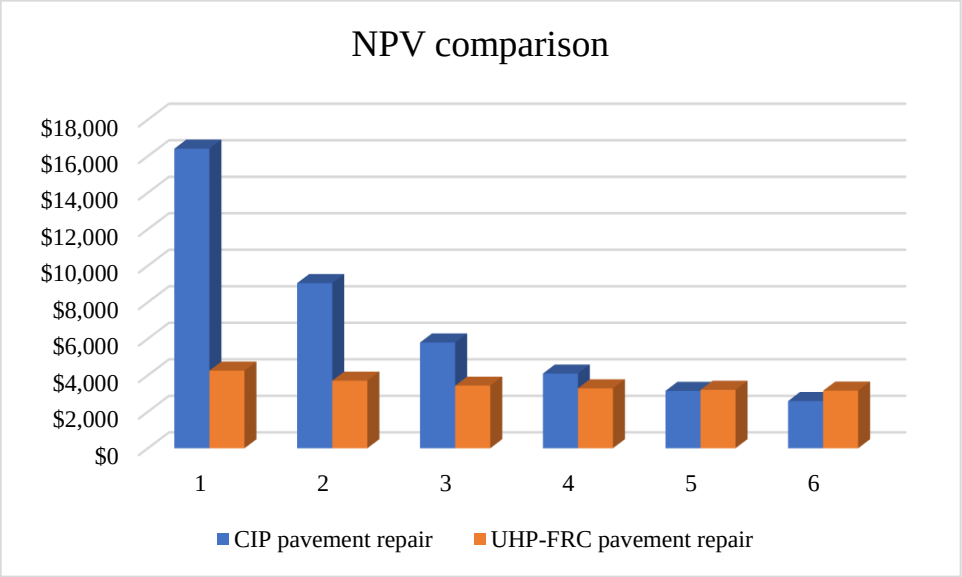

Figure 5- 1 Comparison of net present value of the two alternatives; the horizontal axis represents the discount rate in percentage and the vertical axis represents the net present value in thousands (× 1000).

5.1.2 Findings:

The findings of the LCCA are presented below:

- It was observed that the initial construction cost of the proposed UHP-FRC pavement repair method was higher than the CIP pavement repair method.
- The conventional CIP pavement repair method employs maintenance activities at shorter intervals as compared to the UHP-FRC pavement repair method. This results in an increased user costs during the analysis period for the conventional CIP concrete pavement repair method. Also, the shorter construction time for the UHP-FRC pavement repair method (1 day) further reduces the user costs.
- For low values of discount rates (<5%), the net present value of the conventional CIP pavement repair method is higher than the proposed UHP-FRC pavement repair method.

5.2 Preliminary cost comparison between conventional and UHP-FRC based airport pavement repair methods

5.2.1 Assumptions

1) The length and the width of repair are taken as 22 feet and 18 feet, respectively. The depth of repair is taken as 17 inches.
2) The repair section is assumed to be a part of a critical runway in DFW airport (e.g. 18R/36L in 1990 based on McNerney and Harrison 1998).
3) The entire runway has to be closed during the repair time due to safety considerations. Hence, the repair time is taken equal to the runway closure time.
4) Labor costs and equipment costs are assumed equal for both the repair methods. Hence, it is not considered here for the comparison.

5.2.2 Cast In Place using Conventional Concrete and Construction

Material Costs: $250/yd^3 (Chao 2018)

Repair Time: 7 days (Chao 2018)

5.2.3 UHP-FRC Based Pavement Repair (Precast panel with minimal Casting In Place)

Material Cost for UHP-FRC pavement: $1500/yd^3 (Chao 2018)

Repair Time: 1 Day (Chao 2018)

5.2.4 DFW Airport Runway Closure Costs

At Dallas/Fort Worth International Airport, the Air Transport Association (ATA) estimated the cost of closing runway 18R/36L in 1990 could be as high as $131,000 per day (McNerney and Harrison 1998). For this analysis, the same closure cost is used and adjusted for inflation using the historical cost indices given in 2019 RSMeans Heavy Construction Costs Book (Gordian 2019).

Historical Cost Index for July 1990 = 41.50 (Gordian 2019)

Historical Cost Index for January 2019 = 100.00 (Gordian 2019)

Runway Closure Cost for the DFW Airport for 2018 = $131,000 * 100.00/41.50 = $315,662.65

5.2.5 Cost for The Airport Pavement Repair

Volume of Concrete Used for Repair (V_{conc}) = 22 ft x 18 ft x 17 in = 20.78 yd^3

Conventional Method

Material Costs = V_{conc} x $ 250 per yd^3 = $ 5,194.45

Airport Closure Costs = 7-days x $ 315,662.65 per day= $ 2,209,638.55

$$\mathbf{CLM_{Conventional} = Material\ Costs + Airport\ Closure\ Costs = \$\ 2{,}214{,}833.00}$$

UHP-FRC Based Method

Material Costs = V_{conc} x $1500 per yd^3 = $ 31,166.69

Airport Closure Costs = 1-day x $ 315,662.65 per day = $ 315,662.65

$$\mathbf{CLM_{UHP-FRC} = Material\ Costs + Airport\ Closure\ Costs = \$\ 346{,}829.34}$$

5.2.6 Conclusion

The cost of a typical airport runway repair using conventional approach is approximately $2,214,833.00 while the same using UHP-FRC based method is approximately $ 346,829.34.

5.3 Field Installation

A proof-of-concept of using sustainable UHP-FRC for pavement repair was done at the Dallas/Fort Worth (DFW) International Airport. The pavement repair using the new concept was performed in Taxiway P (1162' S of EJ Center Line) of the DFW International Airport as shown in *Figure 5-2*.

Figure 5- 2 Location of the pavement repair pilot program carried out at the DFW International Airport

Both precast and onsite casting of the UHP-FRC were carried out during the duration of the project and the dowel bars were completely eliminated. A pavement panel of 22 ft (6.7 m) by 18 ft (5.5 m) and 17 in. (43 cm) deep was removed repaired using the proposed method. High-shear mixer (*Figure 5-3*) was used for UHP-FRC mixing. All the dry materials were collected, and the mix was prepared (*Figure 5-4*) on the outskirts of the airport. The repair was carried out using three precast UHP-FRC panels with a cast in place UHP-FRC joint 4 in. (101 mm) wide in-between them. Formwork were initially constructed for preparing the precast UHP-FRC panels (*Figure 5-5*). Leveling screws were preinstalled before the casting of the precast UHP-FRC panels to aid the leveling process. UHP-FRC was prepared in batches and was

poured into each panel in turns (*Figure 5-6*). Samples of 2.74 in.(70 mm) cubes were collected for the purpose of compression tests (*Figure 5-7*). The panels along with the samples were cured in the same environment for consistent results (*Figure 5-8*). The precast panels reached a compressive strength of 5,000 psi (34 MPa) in 16 hours.

The panels were then demolded the outer surface of the precast panels were roughened to a level of ICRI CSP 5 (*Figure 5-9*). Simultaneously, the deteriorated taxiway panel was removed and the inner surfaces were roughened onsite to the roughness level of CSP 5. The precast UHP-FRC panels were then transferred the site (*Figure 5-10*) and leveled using the leveling screws. Finally, the interface joint was filled with 4 in. (102 mm) of cast in place UHP-FRC (*Figure 5-11 and 5-12*). The ends of the leveling screws coming out from the surface were cut off and the specimen was covered for curing.

Figure 5- 3 High-shear mixer used for the UHP-FRC mixing.

(a) (b)

Figure 5- 4 (a)Separation of the dry materials for individual batches (b) UHP-FRC mixing

Figure 5- 5 Formwork the casting of precast UHP-FRC panels with the leveling screws installed

Figure 5- 6 Pouring UHP-FRC for the precast UHP-FRC panel

Figure 5- 7 Collection of UHP-FRC samples for compressive testing

Figure 5- 8 Covering up of the UHP-FRC panel for curing

Figure 5- 9 Roughening of the UHP-FRC precast panels

Figure 5- 10 Placement of the pre-cast UHP-FRC in the repair site

Figure 5- 11 Pouring of UHP-FRC cast-in-place joint

Figure 5- 12 The pavement after pouring of cast-in-place UHP-FRC joint

5.4 Performance Monitoring

Load testing was done after two days of casting of UHP-FRC joints. 100 passes using 58,000 lbf (258 kN) vehicle was done on the repair site (*Figure 5-13*). The pavement showed satisfactory behavior.

Figure 5- 13 Load testing of the UHP-FRC pavement repair site

Chapter 6

Part I: Summary, Conclusions and Recommendations

6.1 Summary

Durability issues with conventional plain concrete has led to significant higher life-cycle costs in comparison to construction costs. Repair, replacement and maintenance of the existing structures are estimated to increase by 30% owing to the change in climatic conditions and transportation demand changes.

Ultra-high-performance fiber-reinforced concrete (UHP-FRC) with its high compressive strength and excellent environmental resistance and durability provides a solution to make the infrastructure more economical and sustainable. UHP-FRC has a high early strength gain which drastically reduces the downtime of traffic after pavement repair. Also, the presence of fibers imparts tensile cracking resistance, post-cracking strength, ductility and energy absorption capacity.

The first phase of this research focused on the material development needed to tailor the UHP-FRC previously developed at UT-Arlington for the needs of pavement construction and repair. In the second phase, a slant shear test was used to quantify the interface shear capacity of existing plain concrete and UHP-FRC repair. Although simple, slant shear test overestimates the shear capacity due to the presence of a frictional force developed as a result of a normal component of the applied load. As a result, in the third phase, a new punch test was developed. This punch test incorporates a specimen much like an actual pavement repair situation with vertical interfaces between the existing plain concrete and the repair materials for accurate determination of the interface shear capacity. The test data indicated that the interface shear strength of UHP-FRC is much higher than that of conventional concrete.

Test results for both the slant shear test and punch test indicated that the dowel bars do not participate in the load transfer at peak load. A certain value of vertical deformation after the initial slip is required before the dowel bars can start accepting load. Hence, it is possible to remove the dowel bars from the pavement repair and use a roughened interface to enhance the bond between the interfaces. This significantly reduces the repair time and makes the repair process simple and convenient.

In the punch test, a new idea of pavement repair was tested for the UHP-FRC: A precast UHP-FRC panel was used for the full depth repair and the joint was sealed using cast-in-place UHP-FRC. By

using this approach, good quality can be achieved using the precast panel. Furthermore, the subsequent reduction of cast-in-place UHP-FRC not only minimizes the volume but also reduces the on-site time. This makes the process very convenient.

6.2 Conclusions

The conclusions drawn from data collected during this research are presented below:

1. Conventional concrete pavement repair uses a saw cut to remove the damaged portion and leaves a smooth surface at the cut surface. It then uses dowel bars to engage the new and existing concrete pavement to transfer the force and prevent faulting between the interface; however, experimental tests showed that the rebars used as dowel bars to prevent faulting do not play a major role in the interface load transfer at the peak load. A certain vertical deformation of the pavement (i.e., damage or faulting) is required before the rebar can start carrying the load. From this observation it can be concluded that the replacement of dowel bars by a roughened interface is feasible. This research showed that using a roughened surface (up to CSP4 or CSP 5) provides a very large bond resistance which is enough to prevent faulting. Replacing dowel bars by roughening the surface can eliminate the preparation time for dowel bars (drilling holes and waiting epoxy to harden). While drilling holes takes may take less time than that for roughening the surface, the curing time for epoxy can take several hours.
2. The slant shear test overestimates the shear capacity due to the influence of a frictional force resulting from the normal component of the applied vertical force (Table 4-2). As a result, a new test, the punch test, was developed in this research to obtain a more realistic shear capacity of the interface.
3. From the peak load values obtained from the slant shear test and the punch test, the bond strength of UHP-FRC is substantially greater than plain concrete.
4. A new method for concrete repair was developed and is proposed, which combines the features of precast UHP-FRC with cast-in-place repair of pavement without any dowel bars (*Figure 3-12*). In this method, a precast UHP-FRC panel is used along with cast-in-place UHP-FRC. The vertical

repair surfaces of the existing concrete are roughened on site. The outer edges of the UHP-FRC precast slabs are roughened before they are brought to the site (no dowel bars are needed). The depth of the precast UHP-FRC is the same as the existing pavement slab thickness. Only a small cast-in-place UHP-FRC joint (one to two inches wide) is done onsite. The roughened precast UHP-FRC slab is placed in the repair area and UHP-FRC is cast in the joint.

5. This proposed method has several advantages over the conventional repair methods: (1) pavement reconstruction using precast panels need only overnight closures, compared with a long-term closure for conventional methods *(Switzer et al., 2003)*; (2) The largest portion of the repair is precast, which provides higher quality control than cast-in-place concrete; (3) a limited amount of cast-in-place UHP-FRC is used and dowel bars are eliminated, which reduces the work and labor, as well as the downtime; 4) UHP-FRC can gain high early strength in a few hours, which can accelerate the repair work.
6. From the LCCA it can be concluded that although the initial capital cost of the proposed UHP-FRC pavement repair method is higher than the cast-in place pavement repair method, using the UHP-FRC pavement repair method can be much cost-effective when life-cycle period is considered.

6.3 Recommendations

The recommendations from this study are:

1. The UHP-FRC mixes (obtained from trial testing) were able to reach a high early strength. A one-day compressive strength is approximately 10 ksi. Also, the mix with 0.75% by volume of ultra-high molecular weight polyethylene (PE) fibers provided a consistent strength. Hence, the ratio of 0.75% by volume is recommended.
2. During the trial mixing it was observed that a curing temperature of 150 °F resulted in higher early strength gain of the UHP-FRC. Temperature curing is recommended for the cast-in-place UHP-FRC joints should a high early compressive strength, such as 2500 psi, is needed within 4 to 5 hours.

3. A large-scale proof-of-concept test for an actual pavement replacement or repair is recommended to identify any potential onsite problems that a contractor may have. This test can facilitate the wide applications of the proposed sustainable pavement repair method.

Chapter 7

Part II: A NEW SUSTAINABLE STRUCTURAL MEMBER WITH ULTRA-HIGH-PERFORMANCE FIBER-REINFORCED CONCRETE (UHP-FRC) AND FIBER-REINFORCED POLYMER (FRP) REINFORCEMENT:

Literature review

7.1 Ultra-High-Performance Fiber-Reinforced Concrete (UHP-FRC)

Ultra-high-performance fiber-reinforced concrete (UHP-FRC) is a new generation of fiber-reinforced concrete which has ultra-high compressive strength (18–30 ksi; 10 to 12 ksi after 24 hours.) and ductility. A concrete with only ultra-high compressive strength is not suitable for structural application, even reinforced with mild reinforcing steel, as the very brittle nature can cause potential issues such as abrupt unpredictable failures and a minimum capability of stress redistribution. UHP-FRC was developed by changing the porous nature of conventional concrete through reducing dimensions of microcracking (or defects) in the concrete. This is achieved in UHP-FRC through a very low water to cementitious materials ratio (0.18 to 0.25) and a dense particle packing, which leads to almost no shrinkage or creep, making it very suitable for concrete members under long-term compression. The consequences of a very dense microstructure and low-water ratio results in enhanced compressive strength (Horii and Nemat-Nasser, 1985) and delayed liquid ingress (FHWA 2011). Furthermore, the addition of steel or synthetic fibers (typically less than 3% by volume of concrete) improves the brittle nature of concrete by increasing the tensile cracking resistance, post-cracking strength, ductility, and energy absorption capacity. In terms of corrosion resistance, research has indicated that UHP-FRC has a much greater durability than conventional concrete due to its very dense microstructure (Ahlborn et al 2011). This dense microstructure impedes the conductive chloride ions from coming into direct contact with the steel reinforcing bars, which protects the reinforcing bars from corrosion. Table 7-1 provides a comparison between typical conventional concrete and UHP-FRC.

Table 7- 1 Comparison of typical conventional concrete and UHP-FRC (all data from UT Arlington research except Rapid Chloride Penetration Test)

Properties of Concrete	Conventional Concrete	UHP-FRC
Ultimate Compressive Strength	< 8,000 psi (55 MPa)	18,000 to 30,000 psi (124 to 207 MPa)
Early (24-hour) compressive strength	< 3000 psi (21 MPa)	10,000 – 12,000 psi (69 to 83 MPa)
Flexural Strength	< 670 psi (4.6 MPa)	2,500 to 6,000 psi (17 to 41 MPa)
Shear strength	< 180 psi (1.2 MPa)	> 600 psi (4.1 MPa)
Direct Tension	< 450 psi (3 MPa)	up to 1,450 psi (10 MPa)
Rapid Chloride Penetration Test*	2000-4000 Coulombs passed	Negligible (< 100 Coulombs passed)
Ductility	Negligible	High ductility
Ultimate Compressive Strain, ε_{cu}	0.003	0.015 to 0.03
Confining	Negligible	High confining capability

* Ahlborn et al 2011

Fiber-reinforced concrete (FRC) has been used for many decades; however, conventional FRC only enhances the post-cracking ductility, and its compressive strength is close to that of plain concrete (5 to 8 ksi). In other words, conventional FRC does not fundamentally change the micro-structure of concrete, but it has a greater residual tensile capacity and ductility after cracking. Research (Aviram et al., 2010) shows that even a high-performance FRC column (an FRC with tensile strain-hardening behavior) has essentially the same failure mode as that of an RC column after FRC is crushed, which eventually leads to rebar buckling and fracture (*Figure 7-1*).

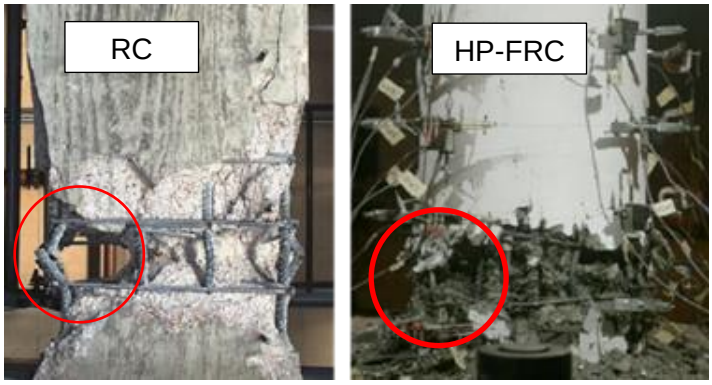

Figure 7- 1 Failure pattern of RC column (Bae, 2005) and HPFRC Column (Aviram et al., 2010) with a specified compressive strength of 8 ksi

7.1.1 Mechanical properties

7.1.1.1 Compression

UHPC without fibers: In the absence of a particular mix proportion, the mechanical properties of UHPC varies based on the composition of the mix. Typically, UHPC mix without fibers has a characteristic compressive strength of higher than 22 ksi (150 MPa), with a high modulus of elasticity in the range of 6,500 ksi to 8,000 ksi (45 GPa to 55 GPa) and exhibiting extremely brittle failure after peak strength. Similar to conventional and high strength concretes, an increase in compressive strength results to the increase in brittleness in UHPC. The increased density of the hardened paste results in the higher modulus of the elasticity as seen in the *Figure 7-2*. The explosive nature of UHPC prevented the recording of the post-peak curve.

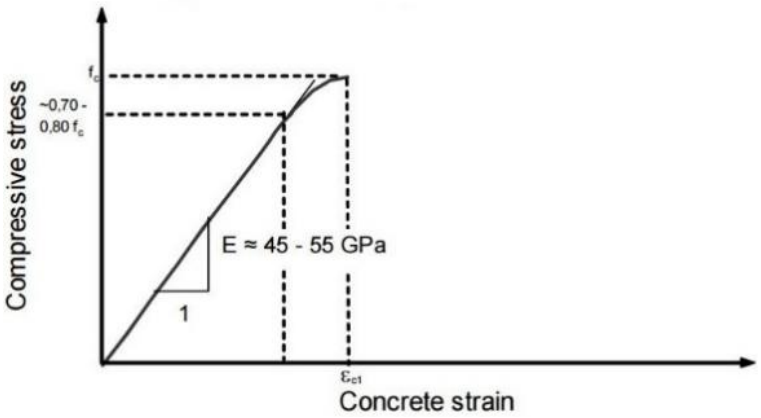

Figure 7- 2 Compressive stress behavior of UHPC without fibers (Fehling el al., 2004)

UHPC with fibers: Addition of fibers to the matrix decreases the brittleness and increases the maximum usable compressive strain. Addition of fibers slightly increase in the compressive strength. Addition of fibers up to a volume fraction of 4% increased the compressive strength by 5-10% (Neilson, 1995 and Behloul, 1996). The UHPC matrix with fibers shows more distinct non-linear behavior before the peak compressive strength as compared to UHPC without fibers. The UHPC mix introduced by Parham et al., 2016 showed ultimate compressive strength at a strain of approximately 1.2-1.4% as shown in *Figure 7-3* below.

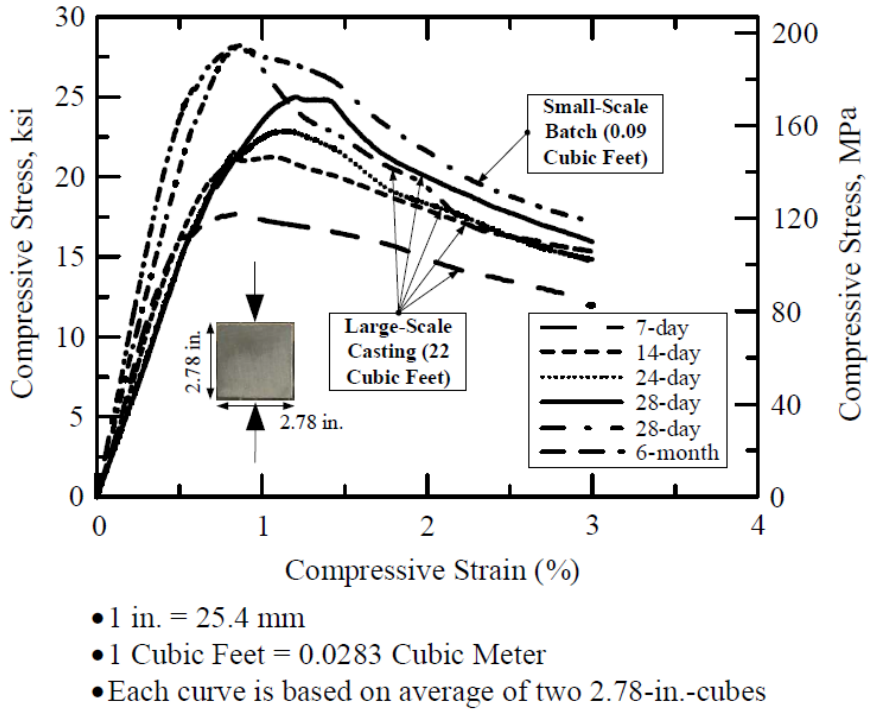

Figure 7- 3 Compressive stress-strain behavior of UHP-FRC (Parham et al., 2016)

7.1.2 UHP-FRC Design recommendation

At the present, there is no design guidelines and recommendation in the United States which are generally accepted. There are design guidelines and recommendations for UHP-FRC in Australia, France and Japan but they are limiting in the use of UHP-FRC's compressive ductility. This results to a very conservative design. Compressive stress-strain model for ultimate limit state and serviceability limit state design recommended by AFGC and JSCE uses a linear constitutive law with a yield plateau. The

compressive stress-strain relationship as per AFGC recommendation is given below in *Figure 7-4*. Professor Franz-Josef Ulm at MIT proposed the only design recommendations for UHP-FRC in the United States which was used for the first time in the design of the Cat Point Creek Bridge in Virginia (Davilla, 2007).

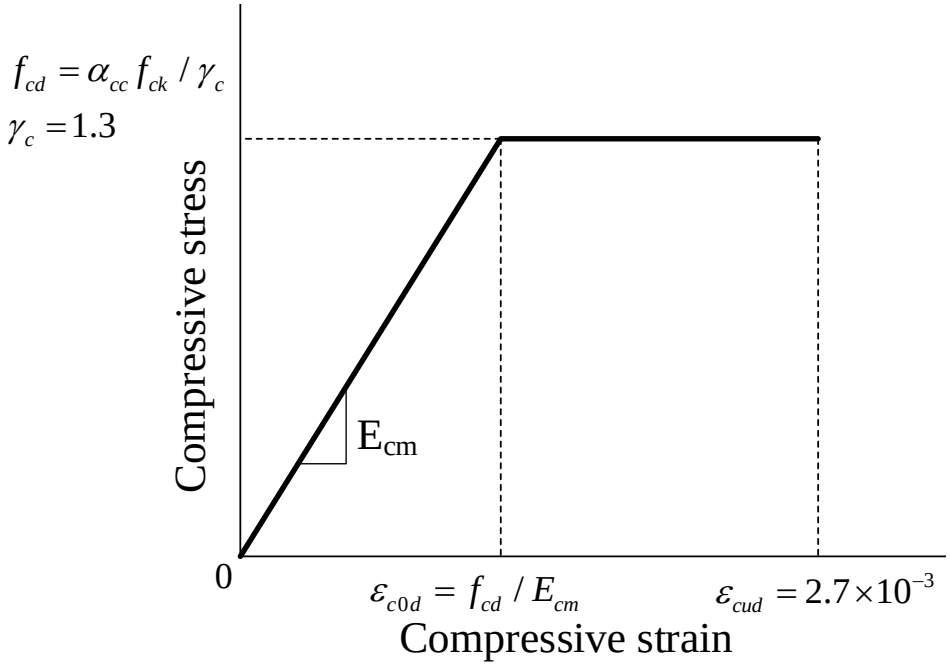

Figure 7- 4 UHP-FRC stress-strain relationship (AFGC, 2013)

7.2 High Strength Steel Reinforcement

7.2.1 ASTM A1035 Reinforcement

ASTM A1035 reinforcement has low carbon content and high chromium content as compared to ASTM A615/A615M steel. This makes the ASTM A1035 reinforcements high-strength and more corrosion resistant (ACI, 2010a). This reinforcement has seen its major use in bridge decks subjected to de-icing salts (Seliem et al., 2008; Shahrooz et al., 2011).

7.2.1.1 Tensile properties

The stress-strain curves for ASTM A1035/A1035M bars in Grades 100 (690) and 120 (830), ASTM A615/A615M bars in Grades 60 (420) and 75 (520) and ASTM A706/A706M bars are shown in the *Figure 7-5*.

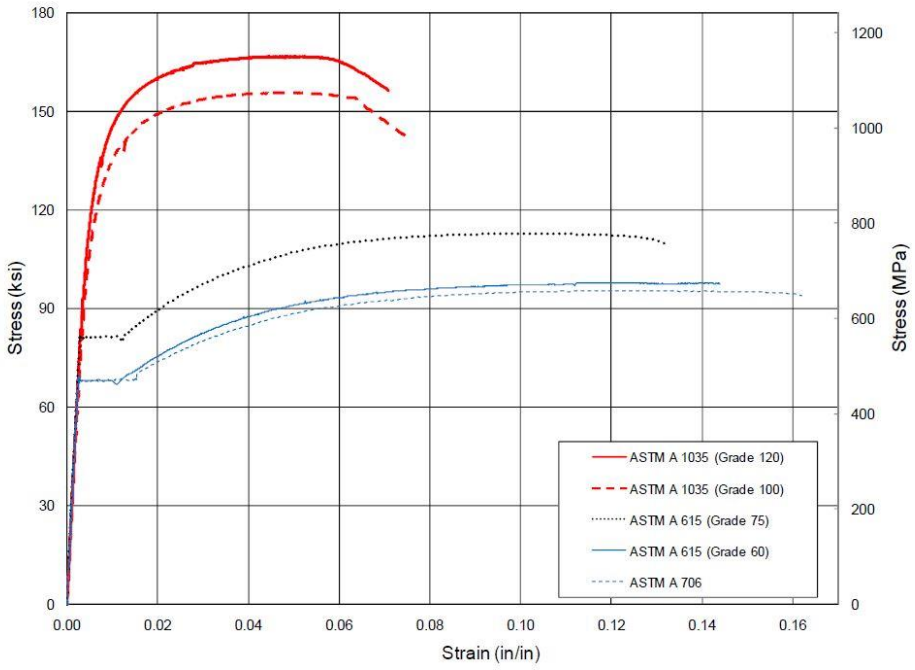

Figure 7- 5 Stress-strain curves for different grades of steel reinforcing bars (WJE, 2008)

ASTM A1035/A1035M bars have higher tensile strength but no well-defined yield point. The proportionate limit of ASTM 1035/A1035M bars is at a stress of 60,000 to 80,000 psi (410 to 550 MPa) which is similar to the yield stress of ASTM A615/A615M Grade 60 (420) and ASTM 706/A706M bars (WJE, 2008). The strain at peak tensile stress for ASTM A615/A615M Grade 60 (420) steel lies at 0.07 to 0.10, and for ASTM A706/A706M steel is within 0.10 to 0.14. For ASTM A1035/A1035M steel, the ultimate strain at fracture ranges from 0.08 to 0.13, while for ASTM A615/A615M Grade 60 (420) and ASTM A706/A706M steel ranges from 0.09 to 0.12 and 0.14 to 0.20 respectively. The modulus of elasticity is observed to be 29,000 ksi (200,000 MPa) for ASTM A1035/A1035M bars similar to the other steel (WJE, 2008). From actual testing, the yield strength of the ASTM A1035/A1035M bars obtained from 0.2% offset method (*Figure 7-6*) is more than 115,000 psi (790 MPa) for Grade 100 (690) bars and 125,000 psi (850 MPa) for Grade 120 (830) bar.

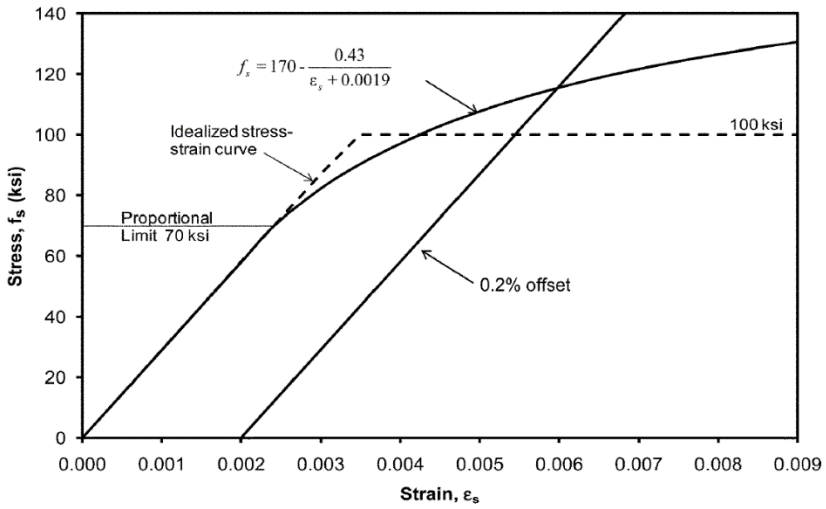

Figure 7- 6 Approximated nonlinear stress-strain relationship of ASTM A1035/A1035M Grade 100 (690) steel and idealized bilinear elastic-plastic stress-strain relationship for simplified design (ACI ITG-6R-10)

The tensile strength for ASTM A1035/A1035M Grade 100 (690) bar and Grade 120 (830) bar exceeds 155,000 psi (1070 MPa) and 160,000 psi (1100 MPa) respectively. The following equations 5-1 to 5-3 are based on a proportional limit of 70,000 psi (480 MPa) and an assumed tensile strength of 150,000 psi (1030 MPa) at a strain of 0.02.

Approximate lower bound of stress-strain curves of Grade 100 (690) are represented by following equations:

$f_s = 29{,}000\varepsilon_s$ (ksi) for $0 \le \varepsilon_s \le 0.0024$ Eq. (5-1)

$f_s = 170 - \frac{0.43}{\varepsilon_s + 0.0019}$ (ksi) for $0.0024 \le \varepsilon_s \le 0.02$ Eq. (5-2)

$f = 150$ (ksi) for $0.02 \le \varepsilon_s \le 0.06$ Eq. (5-3)

Aforementioned equations in SI units:

$f_s = 200{,}000\varepsilon_s$ (MPa) for $0 \le \varepsilon_s \le 0.0024$ Eq. (5-1M)

$f_s = 1170 - \frac{2.96}{\varepsilon_s + 0.0019}$ (MPa) for $0.0024 \le \varepsilon_s \le 0.02$ Eq. (5-2M)

$f = 1040$ (MPa) for $0.02 \le \varepsilon_s \le 0.06$ Eq. (5-3M)

Table 7- 2 Specified tensile and yield strengths (ACI ITG-6R-10)

Bar type	Tensile strength, minimum, psi (MPa)	Yield strength[a]		Stress corresponding to prescribed strain	
		Minimum, psi (MPa)	Maximum, psi (MPa)	Minimum stress, psi (MPa)	Strain, %
ASTM A615/A615M Grade 60	90,000 (620)	60,000 (420)	—	60,000 (420)[b]	0.35[b]
ASTM A615/A615M Grade 75	100,000 (690)	75,000 (520)	—	75,000 (520)[b]	0.35[b]
ASTM A615/A615M Grade 80	105,000 (725)	80,000 (550)	—	80,000 (550)[b]	0.35[b]
ASTM A706/A706M Grade 60	80,000 (550)[c]	60,000 (420)	78,000 (540)	60,000 (420)[b]	0.35[b]
ASTM A706/A706M Grade 80	100,000 (690)[c]	80,000 (550)	98,000 (675)	80,000 (550)[b]	0.35[b]
ASTM A1035/A1035M Grade 100	150,000 (1030)	100,000 (690)	—	80,000 (550)	0.35
ASTM A1035/A1035M Grade 120	150,000 (1030)	120,000 (830)	—	90,000 (620)	0.35

[a] Observed yield point for ASTM A615/A615M and ASTM A706/A706M bars, and yield strength according to 0.2% offset method for ASTM A1035/A1035M bars.

[b] Applicable to ASTM A615/A615M and ASTM A706/706M bars only when steel bar tested does not exhibit a well-defined yield point.

[c] Tensile strength for ASTM A706/A706M bars should also be not less than 1.25 times actual yield strength.

Table 7- 3 Representative chemical composition of rebar

Element	Bar type		
	ASTM A1035/A 1035M	ASTM A615/A615M	ASTM A706/A706M
	Maximum content, %		
Carbon	0.15	b	0.30
Chromium	8.0 to 10.9[a]	—	— [c]
Manganese	1.50	b	1.50[c]
Nitrogen	0.05	—	—
Phosphorus	0.035	0.06	0.035
Sulphur	0.045	b	0.045
Silicon	0.50	—	0.50

7.2.1.2 Flexural design

ACI ITG-6R-10 suggests limiting the strain developed in the longitudinal reinforcement to 0.015 to prevent excessive cracking and deflection. A practical design can be performed through a nonlinear flexural analysis by considering force equilibrium and strain compatibility using equations 5-1 and 5-2 and considering the limiting strain of 0.015.

A simplified flexural design method for ASTM A1035/A1035M bars was put forward by Mast et al. (2008). He proposed using stress-strain behavior comprising of a linear elastic portion followed by a plastic yield plateau *(Figure 7-7)* similar to ASTM A615/A615M Grades 60 (420) and 75 (520) bars.

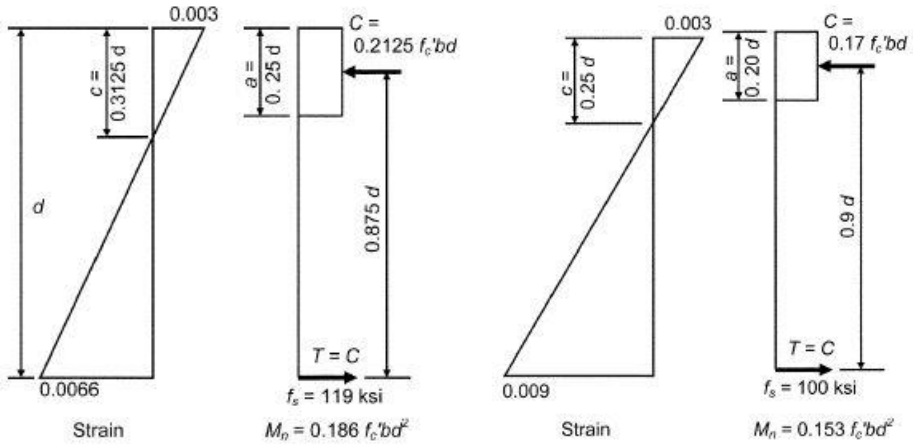

(a) (b)

Figure 7- 7 (a) Behavior based on Eq. (2-2) (b) Behavior based on simplified method (Tension controlled strain limits with $f_C^{'}=5ksi$ and $\beta=0.8$)

Table 7- 4 Comparison of design methods using ASTM A 1035/A1035M Grade 100 (690) steel (in.-lb units) (ACI ITG-6R-10)

	Using Eq. 2-1 and 2-2	Simplified method
Tension-controlled strain limit	0.0066	0.009
Steel tensile stress f_s, ksi	119	100
Neutral axis depth c, in.	$0.3125d$	$0.25d$
Stress block depth $a=\beta_1 c$, in.	$0.3125\beta_1 d$	$0.25\beta_1 d$
Compression force C, kip	$0.85 f_c^1 ab$	$0.85 f_c^1 ab$
Steel area $A_s = C / f_s$, in.^{2}	$0.85(f_c^1/119)(0.3125\beta_1 d)b$	$0.85(f_c^1/100)(0.25\beta_1 d)b$
Tension-controlled reinforcement ratio $\rho_t = A_s / bd$	$0.002232 f_c^1 \beta_1$	$0.002125 f_c^1 \beta_1$
$T = C = A_s f_s = \rho_t bd f_s$, kip	$0.2656 f_c^1 \beta_1 bd$	$0.2125 f_c^1 \beta_1 bd$
Lever arm = $d - a/2$, in.	$d(1-0.156\beta_1)$	$d(1-0.125\beta_1)$
M_n for $f_c^1 = 22$ ksi; $\beta_1 = 0.8$, kip-in.	$0.232 f_c^1 bd^2$	$0.191 f_c^1 bd^2$

Table 7- 5 Comparison of design methods using ASTM A 1035/A1035M Grade 100 (690) steel (SI units) (ACI ITG-6R-10)

	Using Eq. 2-1 and 2-2	Simplified method
Tension-controlled strain limit	0.0066	0.009
Steel tensile stress f_s, MPa	820	690
Neutral axis depth c, mm	$0.3125d$	$0.25d$
Stress block depth $a = \beta_1 c$, mm	$0.3125\beta_1 d$	$0.25\beta_1 d$
Compression force C, N	$0.85 f_c^1 ab$	$0.85 f_c^1 ab$
Steel area $A_s = C / f_s$, mm²	$0.85(f_c^1 / 820)(0.3125\beta_1 d)b$	$0.85(f_c^1 / 690)(0.25\beta_1 d)b$
Tension-controlled reinforcement ratio $\rho_t = A_s / bd$	$0.0003239 f_c^1 \beta_1$	$0.0003079 f_c^1 \beta_1$
$T = C = A_s f_s = \rho_t bdf_s$, N	$0.2656 f_c^1 \beta_1 bd$	$0.2125 f_c^1 \beta_1 bd$
Lever arm = $d - a/2$, mm	$d(1-0.156\beta_1)$	$d(1-0.125\beta_1)$
M_n for $f_c^1 =$ ksi; $\beta_1 = 0.8$, N-mm	$0.232 f_c^1 bd^2$	$0.191 f_c^1 bd^2$

7.2.1.3 Tension and Compression-Control

ACI 318 defines tension-controlled sections as the flexural members having a net tensile strain of 0.05 in the extreme tension reinforcement. This is based on the ASTM A615/A615m Grade 60 (420) and Grade 75 (720) bars. Behavior similar to the members designed using ACI 318 with Grades 60 (420) and 75 (720) was found using the simplified model for ASTM A1035/A1035M bar at a tension-controlled strain limit of 0.0066 (Mast et al., 2008). The strain limit was modified to 0.009 to balance for the actual stress at nominal strength being higher than the assumed 100,000 psi (690 MPa).

ACI 318 defines compression-controlled sections as the flexural members having the net tensile strain at balanced strain condition. For a yield strength of 100,000 psi (690 MPa) and modulus of elasticity of 29,000 ksi (200,000 MPa), the compression-controlled strain limit is 0.00345. (ACI ITG-6R-10).

7.3 Fiber-Reinforced Polymer (FRP) reinforcement

Corrosion is an issue of concern in non-pre-stressed and prestressed steel in reinforced concrete structures exposed to aggressive environments. Composite materials such as fiber-reinforced polymer

(FRP) bars are a suitable alternative to steel reinforcing bars when reinforced concrete is exposed to deicing salts, built in or close to seawater, subjected to other corrosive agents, required to maintain low electric conductivity or electromagnetic neutrality, or required to meet weight limits (FRP is about 75% lighter than steel). Fiber reinforced polymers uses a polymeric resin system reinforced with fibers. Hence. the properties of FRP is a combination of the properties of the resin matrix and the fibers used *(Figure 7-8)*. Fibers are typically aramid, basalt, carbon or glass and the polymer is usually an epoxy, phenol formaldehyde resin, polyester thermosetting plastic or vinyl ester.

Aramid fiber reinforced polymer (ARFP), carbon fiber reinforced polymer (CFRP) and glass fiber reinforced polymer (GFRP) are the most commonly used FRP composites. Aramid fibers are a synthetic aromatic-polyamide material. Aramid fibers are lighter than carbon and glass fibers with similar mechanical properties and are more suitable for prestressed concrete structures than for reinforced concrete ones. Carbon fibers are manufactured by heat treatment processes such as carbonization and graphiting. CFRP shows suitable mechanical properties; in spite of this, the fibers are electrically conductive which might result in the formation of galvanic cells on contact with a metallic substrate. Glass fibers are manufactured by extruding silica dioxide and exhibit favorable mechanical properties; however, they are vulnerable to creep- and moisture-induced damage. Basalt fibers are a mineral-based inorganic product and were recently introduced to the structural engineering community (NCHRP, 2017). Basalt fibers are chemically inert and demonstrate good acidic and thermal resistance. The properties and costs of basalt fibers are similar to those of glass fibers.

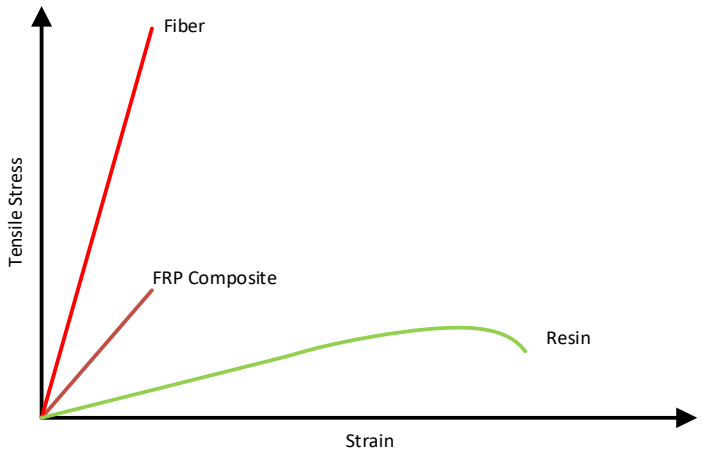

Figure 7- 8 Properties of FRP composite (SP system)

7.3.1 Tensile and compressive behavior

The tensile behavior of FRP bars are controlled by the properties of the fiber and resin, fiber volume fraction and the fiber geometry and orientation within the matrix (SP system). FRP materials are anisotropic in nature and show elastic behavior until failure. As a result, this lack of ductility should be taken into considerations while designing concrete structures reinforced with FRP bars. *Figure 7-9* shows the typical behavior of the FRP bars. FRP bars shows higher tensile strength than steel bars but the tensile modulus of FRP bars is significantly lower than steel counterparts, as small as 20% (ACI.1R-15, 2015). Typical mechanical properties of FRP bars are presented in Table 7-6.

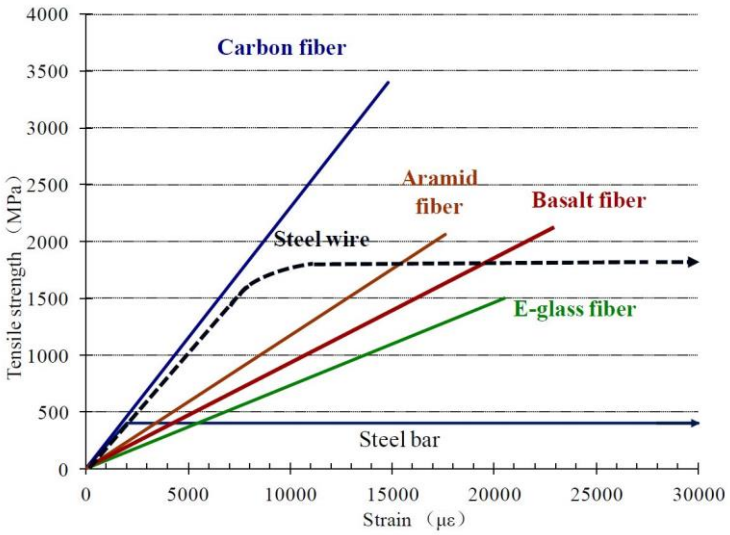

Figure 7- 9 Tensile stress strain relationship for FRP bars (Wu et al., 2012)

Table 7- 6 Typical mechanical properties of FRP bars (NCHRP, 2017)

Type	Density lb/in3 (g/cm3)	Tensile strength ksi (MPa)	Tensile modulus ksi (GPa)	Elongation at break (%)
Aramid	0.052 (1.45)	525-533 (3,600-3,620)	18,000-19,000 (127-131)	2.5-2.8
Carbon	0.064-0.078 (1.77-2.16)	275-640 (1,900-4,410)	32000-110,000 (220-758)	0.32-2.0
Glass	0.09-0.092	500-625	10,500-12,600	4.8-5.0

	(2.49-2.54)	(3,450-4,300)	(72.4-86.9)	

7.3.2 Flexural design

Design of reinforced concrete members with FRP reinforcements is similar to the design of steel-reinforced concrete members. However, unlike steel, the FRP bars do not exhibit ductility. Hence, the failure of reinforced concrete due to rupture of FRP bars before concrete crushing is sudden, destructive and not desirable. It is preferable for FRP-reinforced concrete members to fail in compression rather than the rupture of FRP bars (Nanni, 1993). Either of the above-mentioned method of failure for FRP-reinforced structural members; tension-controlled or compression-controlled failure, will not provide ductility to the structure. Therefore, in the absence of ductility ACI 440.1R (2015) suggests a more conservative design for FRP-reinforced members than for the steel-reinforced members. If high strength concrete is used with the FRP reinforcement bars, stiffness of the cracked section is increased but it reduces the deformability of the flexural member compared to normal strength concrete (ACI 440.1R-15, 2015). The balanced FRP reinforcement ratio can be computed from equation 5-4.

$$\rho_{fb} = 0.85\beta_1 \frac{f_c^{'}}{f_{fu}} \frac{E_f \varepsilon_{cu}}{E_f \varepsilon_{cu} + f_{fu}} \qquad \text{Eq. (7-4)}$$

For compression-control: $\rho_f < \rho_{fb}$

For tension-controlled: $\rho_f > \rho_{fb}$

Equilibrium equations and strain compatibility can be used for the calculation of the nominal flexural strength of FRP-reinforced concrete flexural members (*Figure 7-10*).

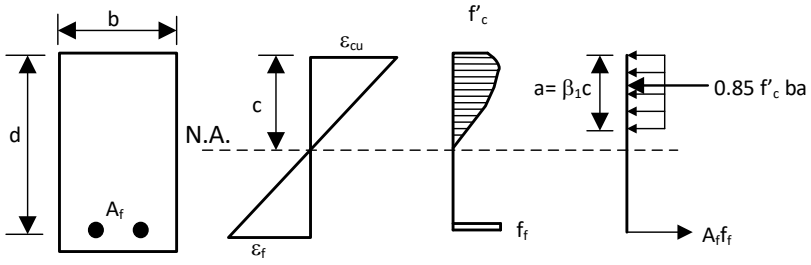

(a) Failure governed by concrete crushing

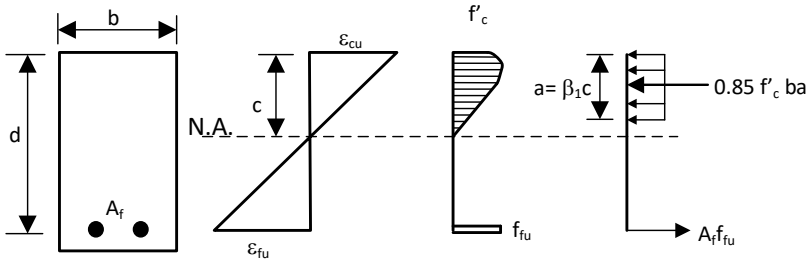

(b) Balanced failure condition

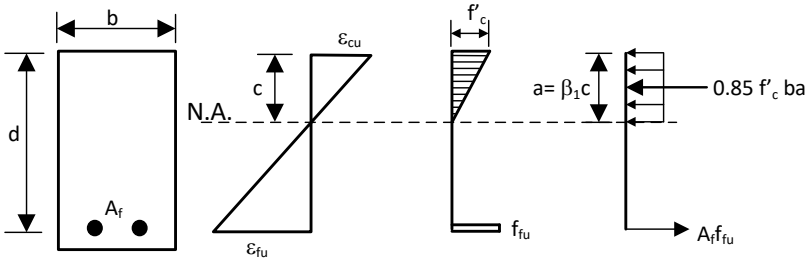

(c) Failure governed by FRP rupture (concrete stress maybe nonlinear)

Figure 7- 10 Stress-strain distribution at ultimate conditions (ACI 440.1R-15, 2015)

7.3.3 Nominal Flexural Strength

7.3.3.1 Compression-controlled ($\rho_f > \rho_{fb}$)

Crushing of concrete is the controlling limit state. In this case, the stress distribution in the concrete can be approximated with the ACI rectangular stress block. Force equilibrium and strain compatibility gives us the following equation 5-5 to calculate nominal flexural strength.

$$M_n = A_f f_f \left(d - \frac{a}{2} \right) \qquad \text{Eq. (7-5)}$$

7.3.3.2 Tension-controlled ($\rho_f < \rho_{fb}$)

Rupture of FRP reinforcement is the controlling limit state. Force equilibrium and strain compatibility gives us the following equation 5-6 to calculate nominal flexural strength.

$$M_n = A_f f_{fu} \left(d - \frac{a}{2} \right) \qquad \text{Eq. (7-6)}$$

7.3.4 Shear design

The shear design for FRP-reinforced concrete members is similar to the steel-reinforced concrete members. However, issues related to FRP reinforcements such as low modulus of elasticity, low transverse shear resistance, lack of ductility needs to be considered. ACI 318 suggests using a strength reduction factor of 0.75 for FRP reinforcement similar to steel-reinforced concrete. The nominal shear strength of the reinforced concrete section is the sum of the shear resistance provided by the concrete and the shear reinforcement (ACI 318).

Due to the lower axial stiffness for the FRP reinforcements, a cross section with FRP flexural reinforcements after cracking has a smaller depth to the neutral axis as compared to the steel-reinforced section with equal areas of longitudinal reinforcement. The depth of the compression zone is reduced, and the crack width are wider. This reduces the contribution of the aggregate interlock and compression zone in the shear resistance. Earlier research on shear capacity of flexural concrete members without shear reinforcement has shown that shear strength of concrete depends on stiffness of flexural reinforcement (Nagasaka et al., 1993; Sonobe et al., 1997; Michaluk et al., 1998; Tureyen and Frosch 2002). There is lack of study regarding the involvement of FRP reinforcement bars in the dowel action. However, it can be assumed that the contribution is less than comparable area of steel owing to the lower axial stiffness of the FRP rebars.

7.3.5 High strength to weight ratio

Specific weight of FRP is less than 2 (SP systems) compared to nearly 8 for steel (*Figure 7-11*). This makes FRP 75% lighter than steel. This results in the FRP having a very high strength to weight ratio

compared to metals. Hence, the potential of FRP bars in reinforced concrete structures is very great (El-Sayed et al. 2006a, b; Mukherjee and Arwikar, 2005).

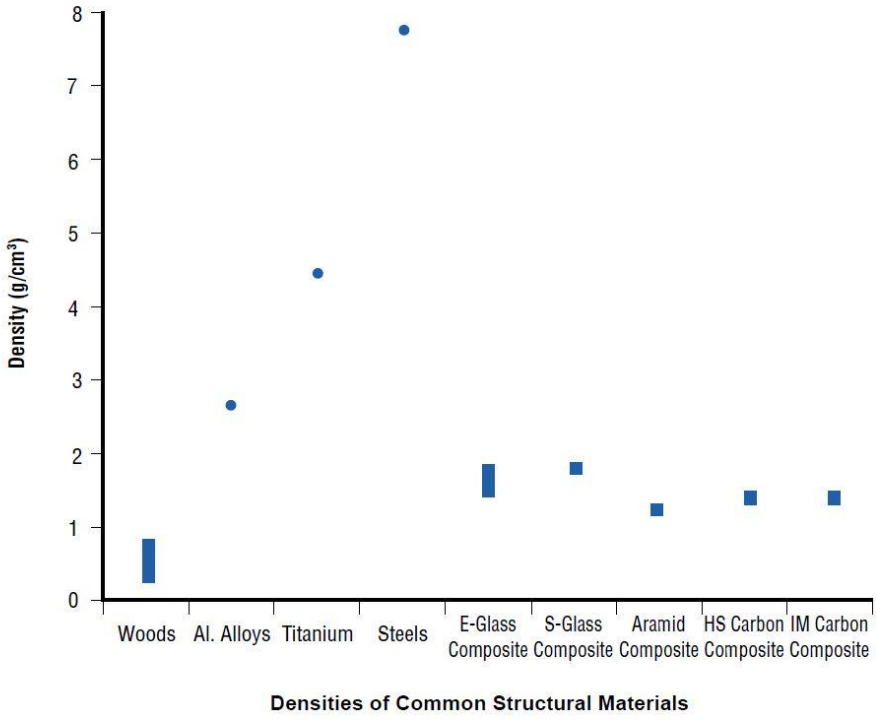

Figure 7- 11 Densities of common structural materials (SP systems)

7.4 Previous UHP-FRC research

The potential of using the superior mechanical properties of UHP-FRC to improve the low damage resistant ability of conventional concrete was demonstrated in a pilot study where a full-scale ACI 318-compliant RC column (ACI 318, 2014) and a UHP-FRC column were tested under large axial load and displacement reversals up to failure (Chao et al., 2016; Palacios et al., 2017). Both columns had the same reinforcement details with ASTM A706 Grade 60 rebars. Although the UHP-FRC column could have had a smaller cross section by utilizing its high compressive strength, a column's cross-sectional dimension is usually controlled by the stiffness requirement of the structure; therefore, both column specimens used the same dimensions. Both columns were fabricated at UT Arlington's Civil Engineering Laboratory Building (CELB) and tested at the MAST laboratory at the University of Minnesota (*Figure 7-12*). The UHP-FRC

material used in the experiment was developed at UT Arlington based on a dense particle-packing concept (Aghdasi et al., 2016).

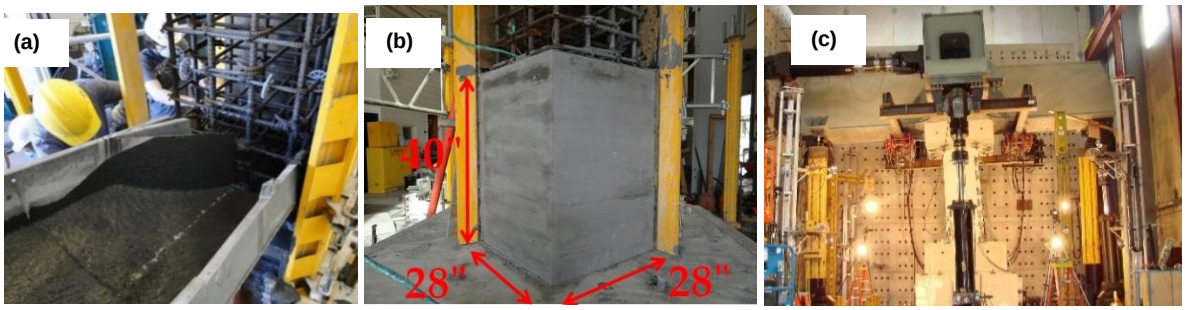

Figure 7- 12 (a) UHP-FRC casting at UT Arlington CELB, (b) completed UHP-FRC at the plastic hinging zone of the specimen, and (c) experimental testing at MAST laboratory at the University of Minnesota

The hysteresis responses for both column specimens are shown in *Figure 7-13a*. For the RC column with normal strength concrete (5 ksi), the first observable flexural cracks were seen at 0.5% drift ratio, and the first longitudinal bar yielded at 0.75% drift ratio. The failure of the RC column started with concrete crushing at the corners of the columns at 1.0% drift ratio. Soon after the crushing, a decrease in strength was observed at 1.38% drift ratio. As the cyclic reversals continued, the concrete cover was eventually lost, followed by the bulging and opening of the transverse reinforcement, and then the buckling and fracture of the longitudinal reinforcement. This deterioration resulted in a significant decrease in strength and eventual failure of the RC column. On the other hand, the UHP-FRC column maintained strength up to nearly 4% drift ratio. Note that ACI 374-13 (ACI, 2013) requires that for frame buildings, the maximum story drift ratio should be kept within 4% to meet the “Collapse Prevention” performance level requirement. To meet the “Life Safety” performance level requirement, a structure should not have a strength degradation of up to 2% story drift ratio. *Figure 7-13a* shows that the UHP-FRC column was able to maintain nearly full peak strength up to 4% story drift ratio, and it had no strength degradation up to approximately 2.5% story drift ratio. Note that while the axial load ratio ($P_u/A_g f'_c$) for the RC column was 0.3, it dropped to 0.06 for the UHP-FRC column due to the high compressive strength of UHP-FRC. This smaller axial load ratio in the UHP-FRC column minimized the influence of the axial load effect at the post-elastic stage, which is very beneficial for columns.

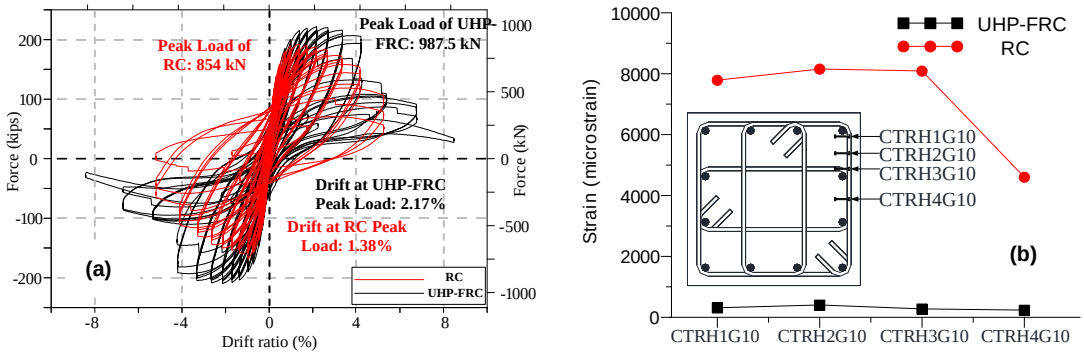

Figure 7- 13 Comparison of UHP-FRC and RC columns: (a) hysteresis loops and (b) confinement characteristic

The use of UHP-FRC significantly changes the failure mechanism observed in conventional RC columns due to its high strength and high compressive ductility. There was no visible concrete damage observed in the plastic hinge region of the UHP-FRC column throughout the test (*Figure 7-14*). This allowed longitudinal reinforcement to be fully utilized to its ultimate tensile capacity without buckling. Furthermore, strain data of transverse reinforcement in the UHP-FRC region only indicated minor strains of less than 50% yielding, suggesting that transverse reinforcement may be significantly reduced in UHP-FRC columns allowing for less congestion and greater ease of construction. *Figure 7-13* compares both specimens, at the same lateral load of 190 kips, with embedded concrete gauges at a cross-section10 inches above the footing. It shows that the measured concrete tensile strains in the UHP-FRC column is significantly lower than those in the RC column, which illustrates the great confinement provided by UHP-FRC material. *Figure 7-14* compares both columns at 2.75% and 5.25% drift ratios showing significant concrete crushing and bar buckling in the RC column with no visible damage detected in the UHP-FRC column. The ultimate failure of the UHP-FRC column was due to the low-cycle fatigue of the longitudinal reinforcement at the interface between the footing and the column section. Inside the UHP-FRC column, ultrasonic tomography showed that the internal cracking of the UHP-FRC column was much less than that of RC column (Choi et al., 2018). These pilot test results show the great resilience capability of columns made of UHP-FRC materials.

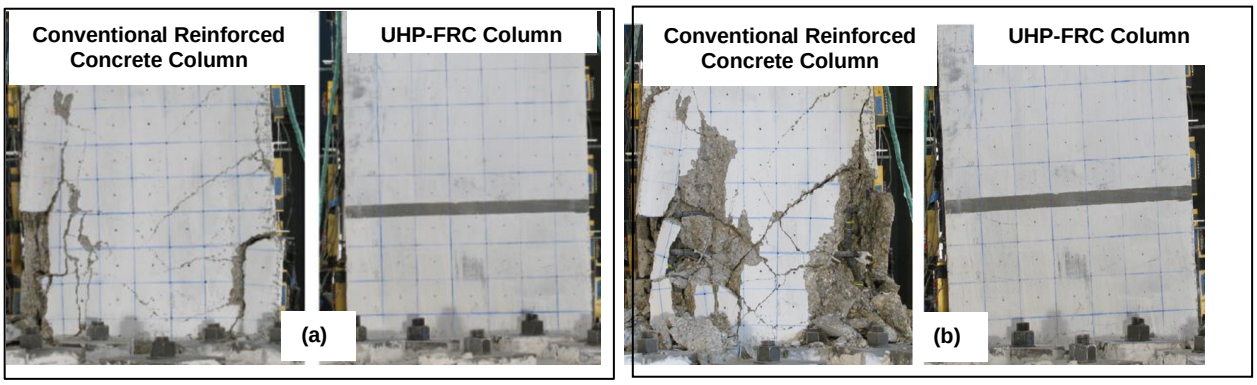

Figure 7- 14 Experimental test results (a) at 2.75% drift ratio and (b) at 5.25% drift ratio (Palacios et al., 2017)

7.5 Ductile-Concrete Strong-Reinforcement (DCSR) Design Concept

The research objective is to develop highly sustainable and efficient reinforced concrete structural members. UHP-FRC offers a new way to design reinforced concrete flexural members due to its superior mechanical properties as compared to conventional concrete. For plain concrete, the compressive strain at this level of stress is 0.003. AASHTO LRFD (2017) and ACI 318 (ACI, 2014) uses 0.003 as the design maximum strain at the crushing of concrete (*Figure 7-15*). Due to this small strain capacity of plain concrete, only a small amount of longitudinal reinforcement could be used to ensure that the flexural member is tension-controlled. For a tension-controlled beam section, the tensile strain in the extreme tension reinforcement (closest to the tension face) is sufficiently large (≥ 0.005); therefore, the beam shows a large deflection as a warning before failure occurs.

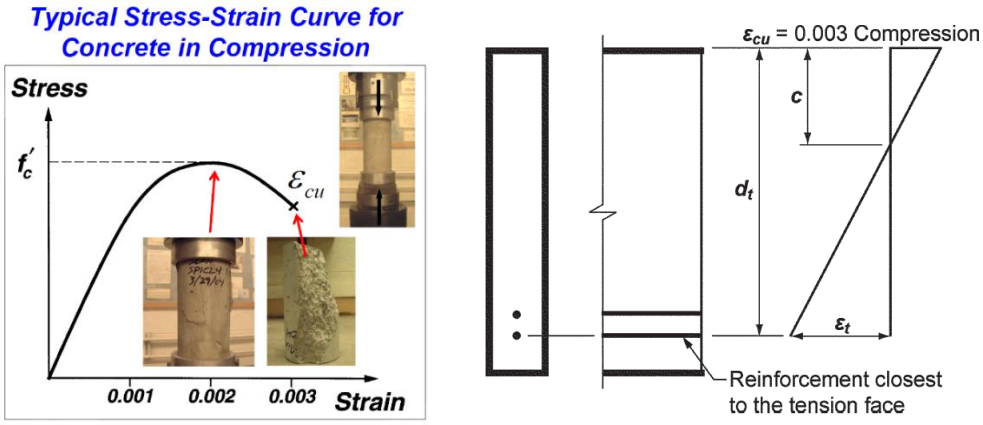

Figure 7- 15 Typical compressive stress-strain response of conventional concrete and maximum usable strain allowed by AASHTO and ACI 318

Figure 7-16 shows typical compressive and tensile stress-strain relations of UHP-FRC materials (Aghdasi et al., 2016). The maximum usable compressive strain (at a post-peak stress of approximately 80% of the peak stress), ε_{cu}, is approximately 0.015. If the concrete compressive strain can be five times greater, the beam could be more efficiently utilized by placing a considerably higher amount of longitudinal reinforcement while still maintaining tension-controlled behavior.

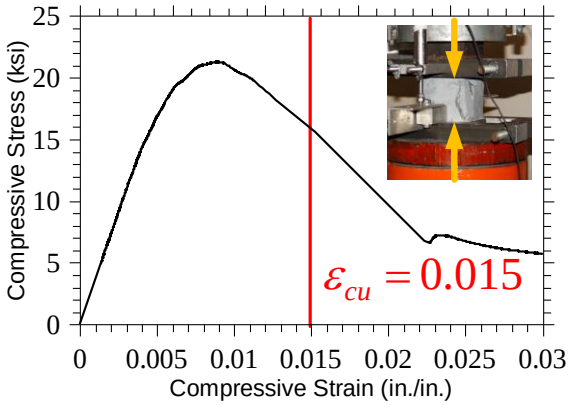

Figure 7- 16 Typical compressive stress-strain response of UHP-FRC

The proposed DCSR design concept is to use UHP-FRC as the ductile element and fiber-reinforced polymer (FRP) bars as the elastic element, which is opposite to conventional RC where the steel bars are the ductile element and the concrete is the brittle element. Using high-strength FRP bars can reduce reinforcement congestion, while achieving high structural efficiency in members (that is, high flexural strength with a relatively smaller cross-section). Keeping FRP bars elastic will also reduce the bond demand and the residual deformation (i.e., self-centering) once a member experiences large deformation under overloading. In addition, FRP bars are a suitable alternative to steel reinforcing bars when reinforced concrete is exposed to deicing salts, built in or close to seawater, subjected to other corrosive agents, required to maintain low electric conductivity or electromagnetic neutrality, or required to meet weight limits (FRP is about 75% lighter than steel). The high shear strength of UHP-FRC allows partial or total elimination of shear reinforcement.

7.5.1 Previous test results (Kaka, 2017)

ACI 440 (2015) suggests a very conservative design for concrete members reinforced with FRP bars because both concrete and FRP bars are brittle materials. However, combining UHP-FRC (very

ductile) and FRP bars can provide an excellent solution for concrete structures, which require both ductility and corrosion-free characteristics. Four beam specimens were designed and tested as a part of the experimental program. Main parameters to be investigated include: 1) type of FRP bars (glass fiber, carbon fiber, and basalt fiber). 2) fiber types for UHP-FRC: high-strength micro steel fibers and ultra-high-molecular-weight polyethylene (PE) fibers, and 3) shear reinforcement (steel, FRP).

7.5.1.1 Beam details (Monotonic Loading)

In the previous test (Kaka, 2017) two beams were tested verify the new DCSR design concept. One UHP-FRC beam reinforced with BFRP (basalt) bars were tested along with an RC specimen with conventional steel. The BFRP bars had an ultimate tensile strength of approximately 125 ksi and an ultimate tensile strain of 0.017 to 0.025. The RC beam was designed to have the highest amount of longitudinal reinforcement while still maintaining tension-controlled behavior, according to ACI 318 and AASHTO LRFD provisions. Thus, the extreme tensile reinforcement reached 0.005 strain when the maximum concrete strain was 0.003 (*Figure 7-17a*). This led to the use of nine Grade 60 No. 5 rebars. Design compressive strength of the RC beams was 5,000 psi. For the UHP-FRC beam, the design compressive strength of UHP-FRC was 22,000 psi, and the maximum usable compressive strain, ε_{cu}, was taken as 0.015. A lower bound BFRP rupture strain of 0.014 was used for design (*Figure 7-17b*). This led to a higher amount of high-strength reinforcement. No shear reinforcement was used in UHP-FRC beam (*Figure 7-18*). Design summary is given in *Table 7-7*.

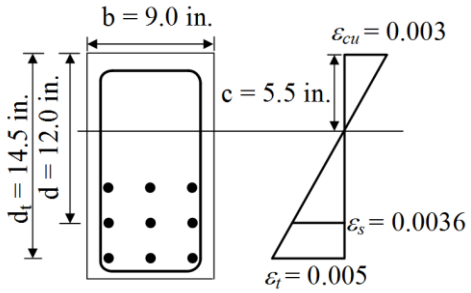

(a)

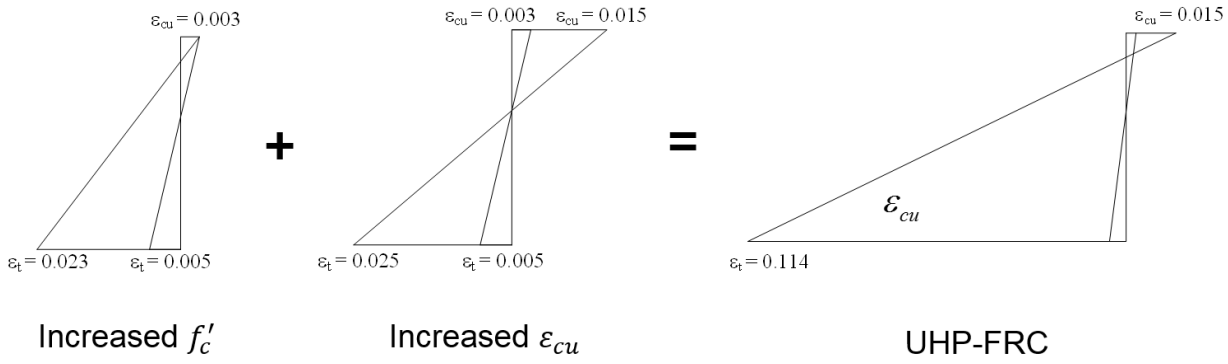

(b)

Figure 7- 17 Strain profile of (a) RC (Gr. 60 steel rebars); (b) UHP-FRC (BFRP bars)

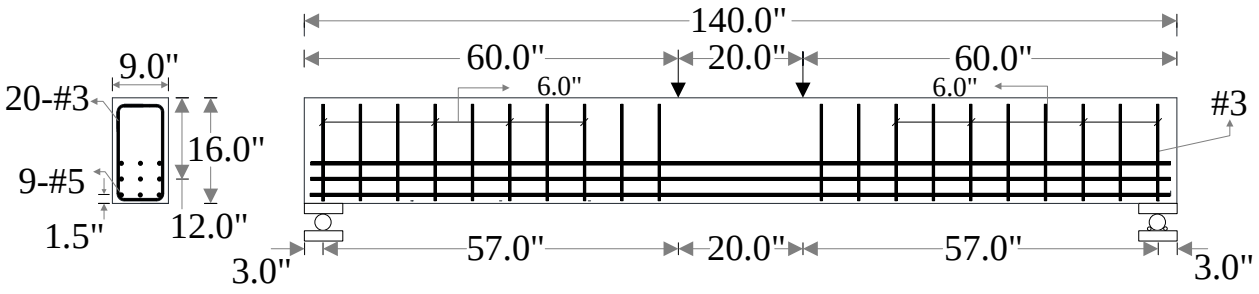

(a) RC (Gr. 60 mild steel rebars)

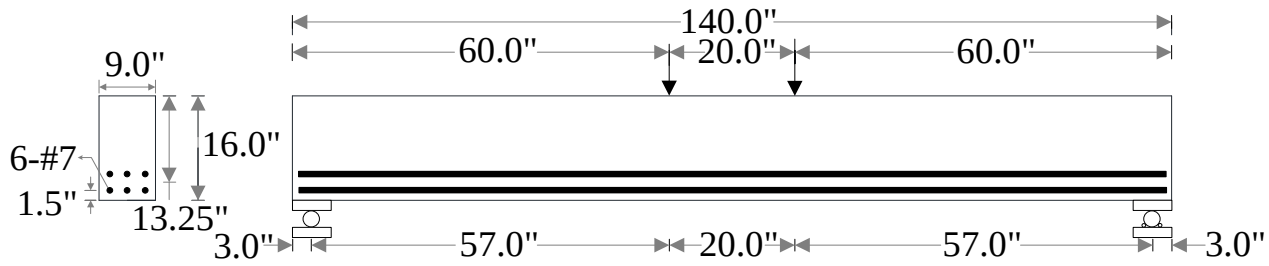

(b) UHP-FRC (BFRP bars; no shear reinforcement)

Figure 7- 18 Reinforcement details: (a) conventional RC beam; (b) UHP-FRC beam with BFRP bars (no shear reinforcement)

Table 7- 7 Design summary of RC and UHP-FRC beams

Specimen	Effective depth (d) in. (mm)	a/d	ρ (%)	β_1	Target Compressive Strength psi (MPa)	Measured compressive strength psi (MPa)
RC #1 (Grade 60 steel)	12 (305)	4.75	2.58	0.8	5000 (35)	5000 (35)
UHP-FRC #4 (BFRP)	13.25 (336.55)	4.3	3.02	0.65	22000 (152)	18500 (128)

Figure 7-19 shows the test results which indicate that the UHP-FRC beam has a much higher stiffness and a strength three times that of conventional RC beam. The UHP-FRC beam also have an excellent ductility, allowing a large deformation or warning sign to occur before failure. As shown in *Figure 7-20*, compared to RC beam, UHP-FRC beam shows high damage resistant capability even beyond ultimate loads. UHP-FRC beam's behavior was controlled by flexure even no shear reinforcement was used.

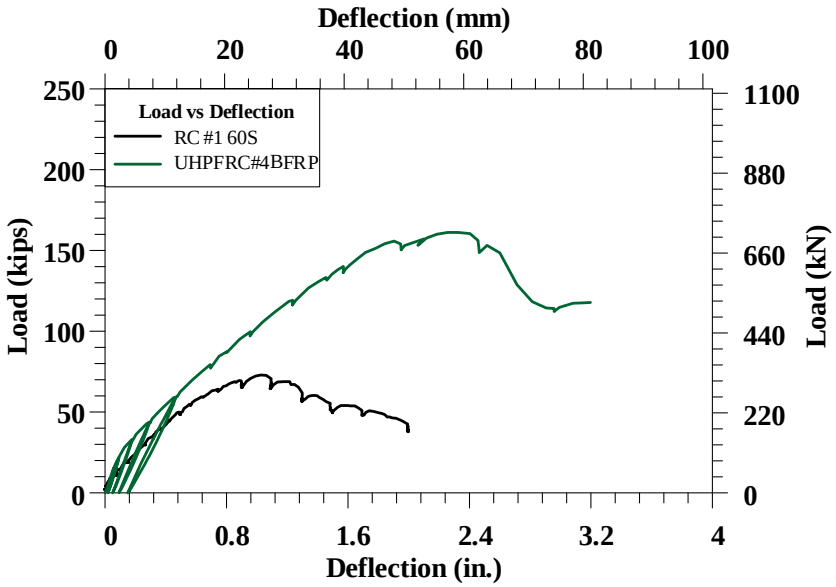

Figure 7- 19 Responses of RC and UHP-FRC beam with FRP bars

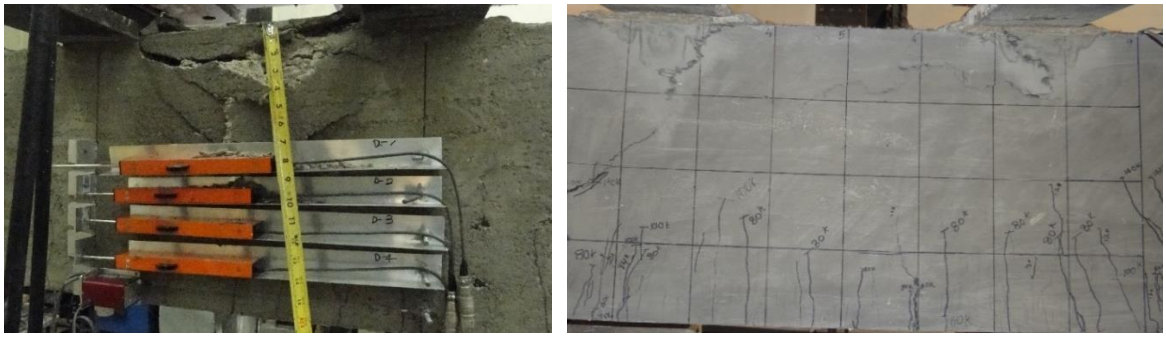

(a) **(b)**

Figure 7- 20 Damage at end of testing: (a) RC beam; (b) UHP-FRC (with BFRP bars) beam without shear reinforcement

Chapter 8

Part II: Experimental Program

The primary purpose of this research is to develop the next-generation highly corrosive-resistant and structurally efficient structural members by utilizing the high durability, compressive ductility, cracking resistance, and shear strength of UHP-FRC as well as the corrosion resistant high-strength fiber-reinforced polymer (FRP) bars. The research focused on using high-strength reinforcement to reduce reinforcement congestion while achieving a high structural efficiency in members (that is, high flexural strength with a relative smaller cross section).

8.1 Specimen design

A total of four beams were designed and tested under reversed cyclic loading. Their design parameters are presented in Table 8-1. All UHP-FRC specimens were tested under large displacement reversals to prove the proposed new DCSR design concept by fully utilizing these ultra-high-performance materials. Micro steel fibers were used for three specimens and ultra-high molecular weight polyethylene fibers was used for one specimen. One specimen with high strength corrosion resistant MMFX steel rebars (100 ksi as per ASTM A1035, 2016), one with high-strength GFRP (glass, 104 ksi) rebars and two with BFRP (basalt, 145.8 ksi) (Table 8-2) were tested. The beams had a reinforcement ratio of 14% to 15%. The cross-section details along with the detailed side view of the specimens are presented below from *Figure 8-1 to Figure 8-5*. A shorter effective span was chosen for the specimens UHP-FRC #3 and UHP-FRC #4 to reduce the shear span to depth ratio for the remaining beams. This was done to observe any possible changes in the dominant mode of failure of the specimen.

Table 8- 1 Design summary of specimens

Specimen	Effective depth (d), in. (mm)	Width of compression face (b), in. (mm)	ρ (%)	Reinforcement type	Fiber type	Effective span, in. (mm)
UHP-FRC #1	4.311 (109)	6 (152)	15.5	MMFX	Steel (V_f=3%)	49.5 (1257)
UHP-FRC #2	6.375 (162)	6 (152)	13.9	GFRP	Steel (V_f=3%)	49.5 (1257)
UHP-FRC #3	5.35 (136)	8 (203)	14.8	BFRP	PE (V_f=0.75%)	34 (864)
UHP-FRC #4	5.35 (136)	8 (203)	14.8	BFRP	Steel (V_f=3%)	34 (864)

Table 8- 2 Reinforcement details (as mentioned by the suppliers)

Reinforcement type	Diameter in. (mm)	Tensile strength ksi (MPa)
MMFX	1.125 (29)	100 (690)
GFRP	0.75 (19)	104 (717)
BFRP	1.00 (25)	145.8 (1005)

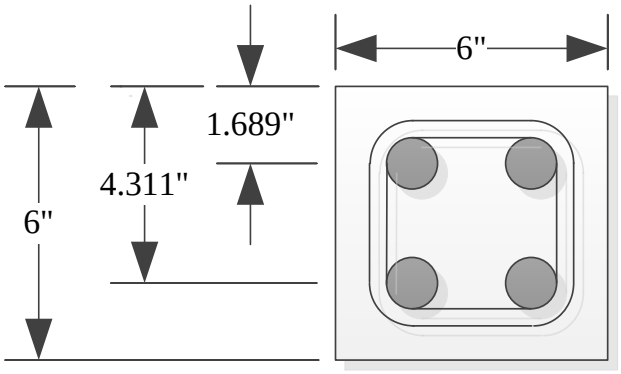

Figure 8- 1 Cross section of MMFX Beam (UHP-FRC #1)

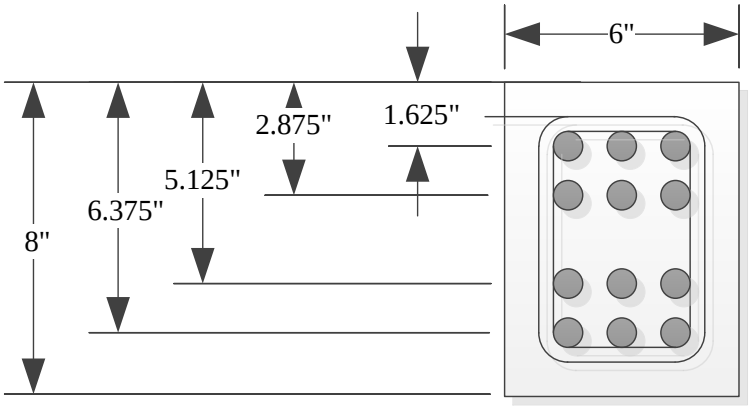

Figure 8- 2 Cross section of GFRP Beam (UHP-FRC #2)

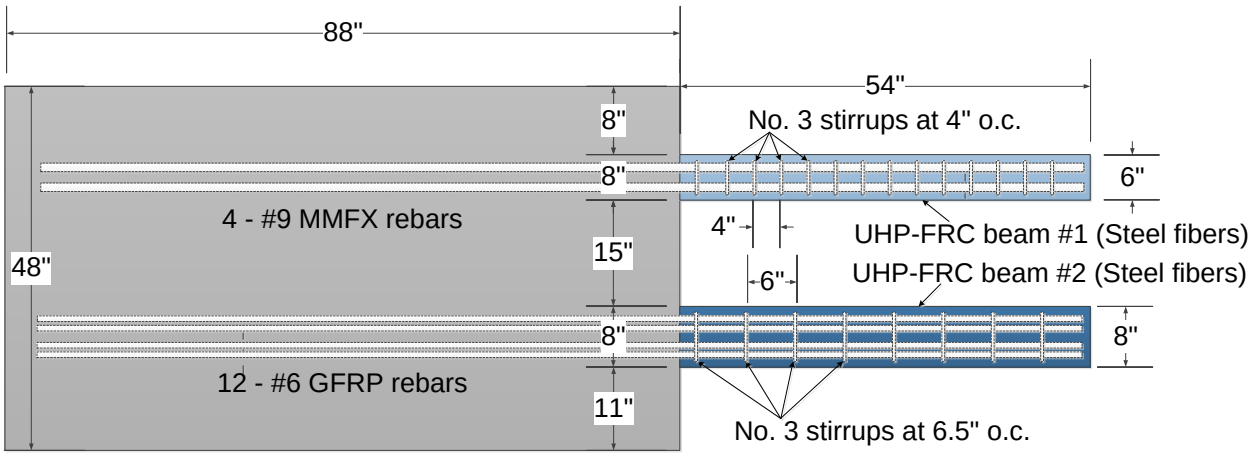

Figure 8- 3 Detailed side view of the specimen showing specimens UHP-FRC #1 and #2

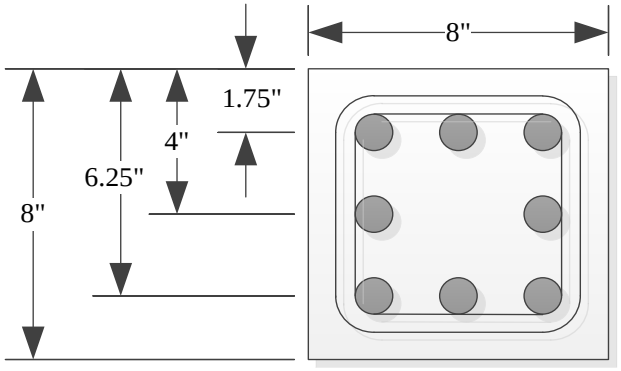

Figure 8- 4 Cross section of BFRP Beam (UHP-FRC #3 and #4)

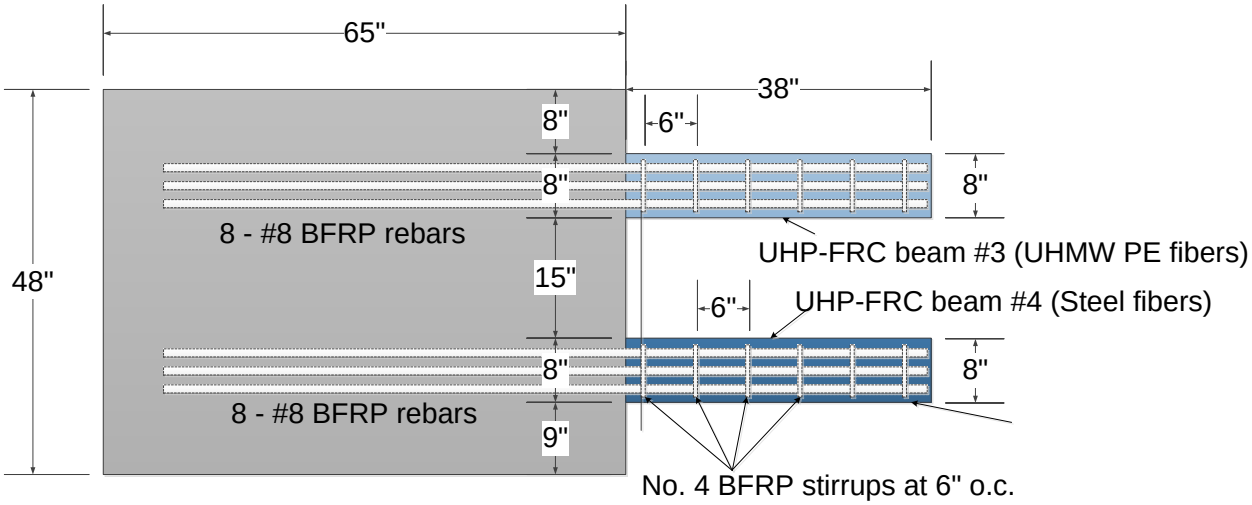

Figure 8- 5 Detailed side view of the specimen showing specimens UHP-FRC #3 and #4

8.2 Design calculations

The detailed design of the four specimens is presented in this section.

8.2.1 Notation and terminology

The following list defines the notation and terminology used in the design.

$a =$ Depth of equivalent rectangular stress block.

$A_{sc} =$ Total area of non-prestressed compression longitudinal reinforcement.

$A_{st} =$ Total area of non-prestressed tension longitudinal reinforcement.

$b =$ Width of compression face.

$c =$ Distance from extreme compression fiber to neutral axis.

$c_c =$ Clear cover of reinforcement.

$C_{concrete} =$ Compression force provided by concrete.

$C_{reinforcement} =$ Compression force provided by reinforcement.

$d =$ Distance from extreme compression fiber to centroid of longitudinal tension reinforcement.

$d_c =$ Distance from extreme compression fiber to centroid of longitudinal compression reinforcement.

$E_s =$ Modulus of elasticity of reinforcement

$f_c^{'} =$ Compressive strength.

$f_{fu} =$ Tensile stress at rupture.

$f_y =$ Reinforcement yield stress.

$\beta_1 =$ Factor relating depth of equivalent rectangular compressive stress block to depth of neutral axis.

ε_{st} = Ultimate compressive strain of concrete

$\varepsilon_{rupture}$ = Ultimate reinforcement rupture strain

ε_t = Net tensile strain in extreme layer of longitudinal tension reinforcement at nominal strength.

ε_{ty} = Value of net tensile strain in the extreme layer of longitudinal tension reinforcement used to define a compression-controlled section.

8.2.2 UHP-FRC #1

The first beam was design with UHP-FRC with micro short steel fibers. The fiber content for the UHP-FRC beam was 3% by volume. High strength MMFX bars confirming to ASTM A1035/A10355M was used as flexural reinforcements. The design calculations are presented below:

$f_c^{'} = 22ksi$, $\beta_1 = 0.65$

$f_y = 100ksi$

$E_s = 29,000ksi$

$\varepsilon_y = 0.009$

$b = 6in.$

$d = 4.311in.$

$d_c = 1.689in.$

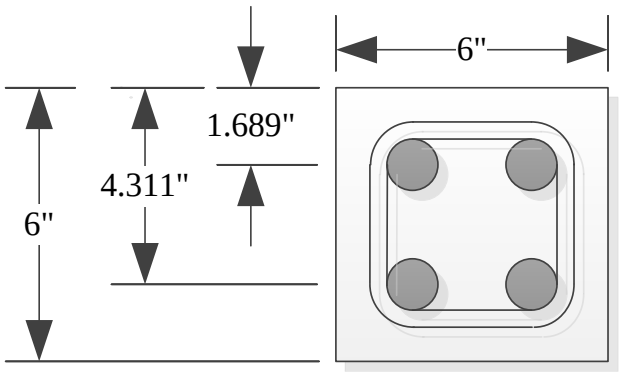

Figure 8- 6 Cross section of UHP-FRC #1

Taking 4 #9 Grade 100 MMFX rebars,

Based on strain compatibility,

- $a = \beta_1 c$; $c = \dfrac{a}{\beta_1}$
- $\dfrac{\varepsilon_{sc}}{\varepsilon_{cu}} = \dfrac{c - d_c}{c}$ or, $\varepsilon_{sc} = \dfrac{c - d_c}{c} * \varepsilon_{cu}$
- $\dfrac{\varepsilon_{st}}{\varepsilon_{cu}} = \dfrac{d - c}{c}$ or, $\varepsilon_{st} = \dfrac{d - c}{c} * \varepsilon_{cu}$

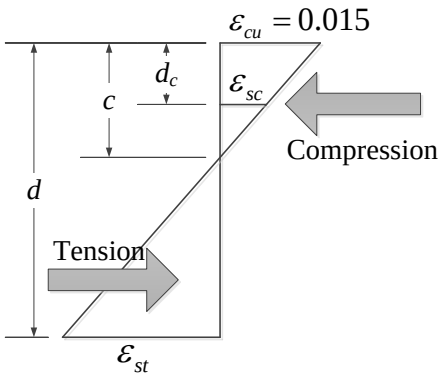

Figure 8- 7 Strain compatibility diagram

Compression force, $C = C_{concrete} + C_{reinforcement}$

$$C_{concrete} = 0.85 f_c^{'} ab$$

$$C_{reinforcement} = A_s f_{sc}$$

Where, $$f_{sc} = \min \begin{Bmatrix} f_{fu} \\ E_s * \varepsilon_{sc} \end{Bmatrix}$$

Tension force, $T = A_{st} f_{st}$

Where, $$f_{st} = \min \begin{Bmatrix} f_{fu} \\ E_s * \varepsilon_{st} \end{Bmatrix}$$

Assuming that the MMFX rebars yield in tension but do not yield in compression,

- $f_{sc} = E_s * \varepsilon_{sc} = E_s * \dfrac{c - d_c}{c} * \varepsilon_{cu}$
- $f_{st} = 100 ksi$

Now,

Compression force, $C = C_{concrete} + C_{reinforcement}$

$$C = 0.85 f_c^{'} ab + A_s f_{sc}$$

$$C = 0.85 f_c^{'} ab + A_s * E_s * \left(\frac{c - d_c}{c} \right) * \varepsilon_{cu}$$

$$C = 0.85 f_c^{'} ab + A_s * E_s * \left(\frac{\frac{a}{\beta_1} - d_c}{\frac{a}{\beta_1}} \right) * \varepsilon_{cu}$$

Tension force, $T = A_{st} * f_{st} = A_{st} * 100$

Based of equilibrium of forces,

Compression force (C) = Tension force (T)

or, $C_{concrete} + C_{reinforcement} = T$

or, $0.85 f_c^{'} ab + A_s * E_s * \left(\frac{\frac{a}{\beta_1} - d_c}{\frac{a}{\beta_1}} \right) * \varepsilon_{cu} = A_{st} * 100$

or, $0.85 * 22 * a * 6 + (2 * 1) * 29000 * \left(\frac{\frac{a}{0.65} - 4.311}{\frac{a}{0.65}} \right) * 0.015 = (2 * 1) * 100$

Solving for a,

- $a = 1.238 in.$
- $c = \frac{a}{\beta_1} = \frac{1.238}{0.65} = 1.905 in.$

Strain in tension longitudinal reinforcement,

- $\varepsilon_{st} = \frac{d - c}{c} \varepsilon_{cu} = \frac{4.311 - 1.905}{1.905} * 0.015 = 0.019 > 0.009 (Yielded)$ *(Tension reinforcement has yielded.)*

Strain in compression longitudinal reinforcement,

- $\varepsilon_{sc} = \frac{c - d_c}{c}\varepsilon_{cu} = \frac{1.905 - 1.689}{1.905} * 0.015 = 0.0017 < 0.009$ *(Compression reinforcement has not yielded.)*

Stress in tension longitudinal reinforcement,

- $f_{st} = 100 ksi$

Stress in compression longitudinal reinforcement,

- $f_{sc} = E_s \varepsilon_{sc} = 29000 * 0.0017 = 49.3 ksi$

For the compression and tension forces,

- $C_c = 0.85 f_c^{'} \left(ab - A_{sc} \right) = 0.85 * 22 * \left(1.238 * 6 - 2 * 1 \right) = 101.5 kips$
- $C_s = A_{sc} f_{sc} = \left(2 * 1 \right) * 49.3 = 98.6 kips$
- $T = A_{st} f_{st} = 2 * 1 * 100 = 200 kips$

Nominal Moment,

$$M_n = C_c \left(d - \frac{a}{2} \right) + C_s \left(d - d_c \right)$$

$$M_n = 101.5 * \left(4.311 - \frac{1.238}{2} \right) + 98.6 * \left(4.311 - 1.689 \right)$$

- $M_n = 633.27 kip - in. = 52.77 kip - ft$

Considering the strain hardening of the reinforcement,

- $M_{nF} = 1.25 * M_n = 1.25 * 633.27 = 791.59 kip - in. = 65.97 kip - ft$

For development length, *(ACI 318-14:25.4.2)*

- $l_d = \left(\frac{3 f_y \Psi_t \Psi_e}{40 \lambda \sqrt{f_c^{'}}} \right) d_b$ for No. 7 and larger bars

$$l_{bhf} = \left(\frac{3*100000*1*1}{40*1*\sqrt{22000}} \right) *1.125 = 56.9in.$$

Effective span of the beam considered,

- $L = 49.5in.$
- Shear span to depth ratio $= \frac{49.5}{6} = 8.25$

Ultimate shear,

- $V_u = \frac{M_n}{L} = \frac{65.97kip - ft}{\frac{49.5}{12}\ ft} = 16kips$

Nominal shear strength provided by concrete,

- $\phi V_c = 0.75*600\,psi*bd = 0.75*600*6*4.311 = 11.64kips$

For the shear reinforcements, No. 3 Grade 60 deformed rebars are used where,

Area of shear reinforcements,

- $A_v = 2*0.11 = 0.22in.^2$

For spacing (s) of shear reinforcements,

- $s = \frac{0.75*A_v*f_y*d}{V_u - \phi V_c} = \frac{0.75*0.22*60*4.311}{16-11.64} = 9.79in.$

According to ACI 318-14; Table 9.7.6.2.2 for maximum spacing of shear reinforcement,

- $4\sqrt{f_c^{'}}b_w d = 4*\sqrt{22000}*6*4.311 = 15.35kips$
- $V_s = \frac{V_u - \phi V_c}{\phi} = \frac{16-11.64}{0.75} = 5.81kips < 4\sqrt{f_c^{'}}b_w d = 15.35kips$

Hence, maximum spacing,

- $s_{\max} = \frac{d}{2} = \frac{4.311}{2} = 2.16in. < 24in.$

However, as the cross-sectional dimensions of the beam was small, a transverse reinforcement spacing of 4 in. was considered.

Therefore, for transverse reinforcements #3 Grade 60 deformed stirrups @ 4 in. o.c. was taken.

8.2.3 UHP-FRC #2

The first beam was design with UHP-FRC with micro short steel fibers. The fiber content for the UHP-FRC beam was 3% by volume. High-strength GFRP (Glass, 104 ksi) rebars was used as flexural reinforcements. The design calculations are presented below:

$f_c^{'} = 22ksi\ ,\ \beta_1 = 0.65$

$f_{fu} = 104ksi$

$\varepsilon_{rupture} = 0.018$

$E_f = 5800ksi$

$b = 6in.$

$d = 5.75in.$

$d_c = 1.625in.$

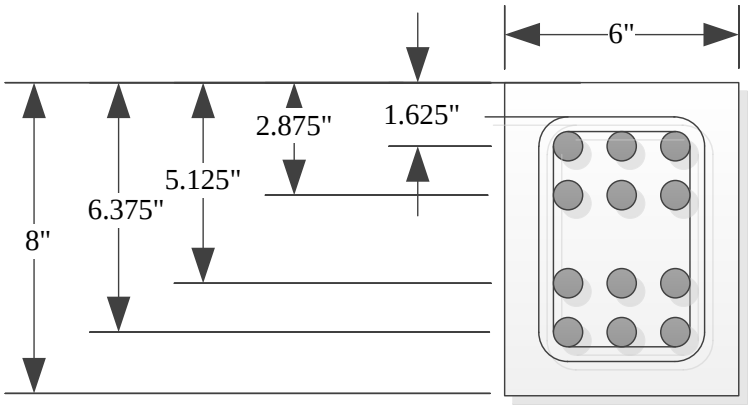

Figure 8- 8 Cross section of UHP-FRC #2

For the balanced reinforcement ratio, *(ACI 440.1R-15: 7.2.1b)*

- $$\rho_{fb} = 0.85\beta_1 \frac{f_c^{'}}{f_{fu}} \frac{E_f \varepsilon_{cu}}{E_f \varepsilon_{cu} + f_{fu}} = 0.85 * 0.65 * \frac{22000}{91000} * \frac{5800 * 0.015}{5800 * 0.015 + 91}$$

  $$\rho_{fb} = 0.0653$$

For compression control,

- $\rho_f > \rho_{fb} = 0.0653$

Taking #12 GFRP rebars in a section as shown in the cross section,

- $\rho_f = \frac{A_{st}}{bd} = \frac{6 * 0.442}{6 * 5.75} = 0.077 > \rho_{fb}$ [Compression controlled]

Based on strain compatibility,

- $a = \beta_1 c$; $c = \dfrac{a}{\beta_1}$
- $\dfrac{\varepsilon_{sc}}{\varepsilon_{cu}} = \dfrac{c - d_c}{c}$ or, $\varepsilon_{sc} = \dfrac{c - d_c}{c} * \varepsilon_{cu}$
- $\dfrac{\varepsilon_{st}}{\varepsilon_{cu}} = \dfrac{d - c}{c}$ or, $\varepsilon_{st} = \dfrac{d - c}{c} * \varepsilon_{cu}$

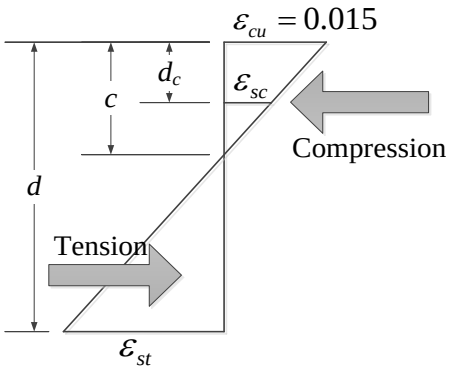

Figure 8- 9 Strain compatibility diagram

Compression force, $C = C_{concrete} + C_{reinforcement}$

$C_{concrete} = 0.85 f_c^{'} ab$

$C_{reinforcement} = A_s f_{sc}$

Where, $f_{sc} = \min \begin{Bmatrix} f_{fu} \\ E_s * \varepsilon_{sc} \end{Bmatrix}$

Tension force, $T = A_{st} f_{st}$

Where, $f_{st} = \min \begin{Bmatrix} f_{fu} \\ E_s * \varepsilon_{st} \end{Bmatrix}$

Assuming that the GFRP rebars do not rupture in both tension and compression,

- $f_{sc} = E_s * \varepsilon_{sc} = E_s * \dfrac{c - d_c}{c} * \varepsilon_{cu}$
- $f_{st} = E_s * \varepsilon_{st} = E_s * \dfrac{d - c}{c} * \varepsilon_{cu}$

Now,

Compression force, $C = C_{concrete} + C_{reinforcement}$

$C = 0.85 f_c^{'} ab + A_s f_{sc}$

$$C = 0.85 f_c^{'} ab + A_s * E_s * \left(\frac{c - d_c}{c} \right) * \varepsilon_{cu}$$

$$C = 0.85 f_c^{'} ab + A_s * E_s * \left(\frac{\frac{a}{\beta_1} - d_c}{\frac{a}{\beta_1}} \right) * \varepsilon_{cu}$$

Tension force, $$T = A_{st} * \varepsilon_{st} = A_{st} * E_s * \left(\frac{d - c}{c} \right) * \varepsilon_{cu}$$

$$T = A_{st} * E_s * \left(\frac{d - \frac{a}{\beta_1}}{\frac{a}{\beta_1}} \right) * \varepsilon_{cu}$$

Based of equilibrium of forces,

Compression force (C) = Tension force (T)

or, $$C_{concrete} + C_{reinforcement} = T$$

or, $$0.85 f_c^{'} ab + A_s * E_s * \left(\frac{\frac{a}{\beta_1} - d_c}{\frac{a}{\beta_1}} \right) * \varepsilon_{cu} = A_{st} * E_s * \left(\frac{d - \frac{a}{\beta_1}}{\frac{a}{\beta_1}} \right) * \varepsilon_{cu}$$

Or,

$$0.85 * 22000 * a * 6 + (3 * 0.442) * 5800 * \left(\frac{\frac{a}{0.65} - 1.625}{\frac{a}{0.65}} \right) * 0.015 = (6 * 0.442) * 5800 * \left(\frac{5.75 - \frac{a}{0.65}}{\frac{a}{0.65}} \right) * 0.015$$

Solving for a,

- $a = 1.921 in.$
- $c = \frac{a}{\beta_1} = \frac{1.921}{0.65} = 2.955 in.$

Now,

Strain in tension longitudinal reinforcement,

- $\varepsilon_{st} = \frac{d-c}{c}\varepsilon_{cu} = \frac{5.75-2.955}{2.955} * 0.015 = 0.014 < 0.018$

Strain in extreme tension longitudinal reinforcement,

- $\varepsilon_{st,\max} = \frac{d_t - c}{c}\varepsilon_{cu} = \frac{6.325-2.955}{2.955} * 0.015 = 0.0171 < 0.018$ *(Tension reinforcement has not ruptured.)*

Strain in compression longitudinal reinforcement,

- $\varepsilon_{sc} = \frac{c-d_c}{c}\varepsilon_{cu} = \frac{2.955-2.25}{2.955} * 0.015 = 0.0036 < 0.018$ *(Compression reinforcement has not ruptured.)*

Stress in tension longitudinal reinforcement,

- $f_{st} = E_s\varepsilon_{st} = 5800 * 0.014 = 81.2 ksi$

Stress in extreme tension longitudinal reinforcement,

- $f_{st,\max} = E_s\varepsilon_{st,\max} = 5800 * 0.0171 = 99.18 ksi$

Stress in compression longitudinal reinforcement,

- $f_{sc} = E_s\varepsilon_{sc} = 5800 * 0.0036 = 20.88 ksi$

For the compression and tension forces,

- $C_c = 0.85 f_c^{'}\left(ab - A_{sc}\right) = 0.85 * 22 * \left(1.921 * 6 - 3 * .442\right) = 190.74 kips$
- $C_s = A_{sc} f_{sc} = \left(3 * 0.442\right) * 20.88 = 27.69 kips$
- $T = A_{st} f_{st} = 6 * 0.442 * 81.2 = 215.34 kips$

Nominal Moment,

$$M_n = C_c\left(d - \frac{a}{2}\right) + C_s\left(d - d_c\right)$$

$$M_n = 190.74*\left(5.75 - \frac{1.921}{2}\right) + 27.69*\left(5.75 - 1.625\right)$$

- $M_n = 1027.77 kip - in. = 85.65 kip - ft$

For development length, *(ACI 440.1R-15:10.2b)*

- $l_{bhf} = \frac{f_{fu}}{37.5}\frac{d_b}{\sqrt{f_c'}}$ for $75000\,psi < f_{fu} < 150{,}000\,psi$

$$l_{bhf} = \frac{104000}{37.5}\frac{0.75}{\sqrt{22000}} = 14.02 in.$$

Effective span of the beam considered,

- $L = 49.5 in.$
- Shear span to depth ratio $= \frac{49.5}{6} = 8.25$

Ultimate shear,

- $V_u = \frac{M_n}{L} = \frac{85.65 kip - ft}{\frac{49.5}{12}\,ft} = 20.76 kips$

Nominal shear strength provided by concrete,

- $\phi V_c = 0.75*600\,psi*bd = 0.75*600*6*5.75 = 15.53 kips$

For the shear reinforcements, No. 3 BFRP rebars are used where,

Area of shear reinforcements,

- $A_v = 2*0.11 = 0.22 in.^2$

For spacing (s) of shear reinforcements,

- $s = \frac{0.75*A_v*f_y*d}{V_u - \phi V_c} = \frac{0.75*0.22*60*5.75}{20.76 - 15.53} = 10.88 in.$

According to ACI 318-14; Table 9.7.6.2.2 for maximum spacing of shear reinforcement,

- $4\sqrt{f_c^{'}}b_w d = 4*\sqrt{22000}*6*5.75 = 20.47kips$
- $V_s = \frac{V_u - \phi V_c}{\phi} = \frac{20.76 - 15.53}{0.75} = 6.97kips < 4\sqrt{f_c^{'}}b_w d = 20.47kips$

Hence, maximum spacing,

- $s_{\max} = \frac{d}{2} = \frac{5.75}{2} = 2.88in. < 24in.$

However, as the cross-sectional dimensions of the beam was small, a transverse reinforcement spacing of 6.5 in. was considered.

Therefore, for transverse reinforcements #3 steel stirrups @ 6.5 in. o.c. was taken.

8.2.4 UHP-FRC #3

The first beam was design with UHP-FRC with ultra-high molecular weight polyethylene fiber. The fiber content for the UHP-FRC beam was 0.75% by volume. High-strength GFRP (Glass, 104 ksi) rebars was used as flexural reinforcements. The design calculations are presented below:

$f_c^{'} = 20ksi$, $\beta_1 = 0.65$

$f_{fu} = 145.8ksi$

$\varepsilon_{rupture} = 0.024$

$E_f = 6141ksi$

$b = 8in.$

$d = 5.35in.$

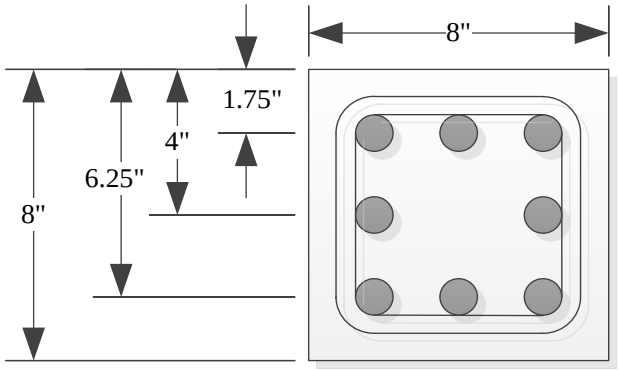

Figure 8- 10 Cross section of UHP-FRC #3

For the balanced reinforcement ratio, *(ACI 440.1R-15: 7.2.1b)*

- $\rho_{fb} = 0.85\beta_1 \frac{f_c^{'}}{f_{fu}} \frac{E_f \varepsilon_{cu}}{E_f \varepsilon_{cu} + f_{fu}} = 0.85 * 0.65 * \frac{20000}{145800} * \frac{6141 * 0.015}{6141 * 0.015 + 145.8}$

$$\rho_{fb} = 0.0293$$

For compression control,

- $\rho_f > \rho_{fb} = 0.0293$

Taking #8 BFRP rebars in a section.

- $\rho_f = \frac{A_{st}}{bd} = \frac{5 * 0.79}{8 * 5.35} = 0.0923 > \rho_{fb}$ [Compression controlled]

Based on strain compatibility,

- $a = \beta_1 c$; $c = \frac{a}{\beta_1}$
- $\frac{\varepsilon_{sc}}{\varepsilon_{cu}} = \frac{c - d_c}{c}$ or, $\varepsilon_{sc} = \frac{c - d_c}{c} * \varepsilon_{cu}$
- $\frac{\varepsilon_{st}}{\varepsilon_{cu}} = \frac{d - c}{c}$ or, $\varepsilon_{st} = \frac{d - c}{c} * \varepsilon_{cu}$

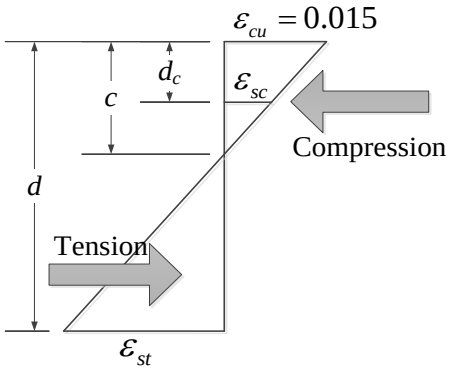

Figure 8- 11 Strain compatibility diagram

Compression force, $C = C_{concrete} + C_{reinforcement}$

$$C_{concrete} = 0.85 f_c^{'} ab$$

$$C_{reinforcement} = A_s f_{sc}$$

Where, $f_{sc} = \min \begin{Bmatrix} f_{fu} \\ E_s * \varepsilon_{sc} \end{Bmatrix}$

Tension force, $T = A_{st} f_{st}$

Where, $f_{st} = \min \begin{Bmatrix} f_{fu} \\ E_s * \varepsilon_{st} \end{Bmatrix}$

Assuming that the BFRP rebars do not rupture in both tension and compression,

- $f_{sc} = E_s * \varepsilon_{sc} = E_s * \frac{c - d_c}{c} * \varepsilon_{cu}$
- $f_{st} = E_s * \varepsilon_{st} = E_s * \frac{d - c}{c} * \varepsilon_{cu}$

Now,

Compression force, $C = C_{concrete} + C_{reinforcement}$

$$C = 0.85 f_c^{'} ab + A_s f_{sc}$$

$$C = 0.85 f_c^{'} ab + A_s * E_s * \left(\frac{c - d_c}{c} \right) * \varepsilon_{cu}$$

$$C = 0.85 f_c^{'} ab + A_s * E_s * \left(\frac{\frac{a}{\beta_1} - d_c}{\frac{a}{\beta_1}} \right) * \varepsilon_{cu}$$

Tension force, $T = A_{st} * \varepsilon_{st} = A_{st} * E_s * \left(\frac{d - c}{c} \right) * \varepsilon_{cu}$

$$T = A_{st} * E_s * \left(\frac{d - \frac{a}{\beta_1}}{\frac{a}{\beta_1}} \right) * \varepsilon_{cu}$$

Based of equilibrium of forces,

Compression force (C) = Tension force (T)

or, $C_{concrete} + C_{reinforcement} = T$

or, $$0.85 f_c^{'} ab + A_s * E_s * \left(\frac{\frac{a}{\beta_1} - d_c}{\frac{a}{\beta_1}} \right) * \varepsilon_{cu} = A_{st} * E_s * \left(\frac{d - \frac{a}{\beta_1}}{\frac{a}{\beta_1}} \right) * \varepsilon_{cu}$$

or,

$$0.85*20*a*8 + (3*0.79)*6141* \left(\frac{\frac{a}{0.65} - 1.75}{\frac{a}{0.65}} \right) * 0.015 = (5*0.79)*6141* \left(\frac{5.35 - \frac{a}{0.65}}{\frac{a}{0.65}} \right) * 0.015$$

Solving for a,

- $a = 1.893"$
- $c = \frac{a}{\beta_1} = \frac{1.893}{0.65} = 2.91"$

Now,

Strain in tension longitudinal reinforcement,

- $\varepsilon_{st} = \frac{d - c}{c} \varepsilon_{cu} = \frac{5.35 - 2.91}{2.91} * 0.015 = 0.0126 < 0.024$

Strain in extreme tension longitudinal reinforcement,

- $\varepsilon_{st,\max} = \frac{d_t - c}{c} \varepsilon_{cu} = \frac{6.25 - 2.91}{2.91} * 0.015 = 0.0172 < 0.024$ *(Tension reinforcement has not ruptured.)*

Strain in extreme compression longitudinal reinforcement,

- $\varepsilon_{sc} = \frac{c - d_c}{c} \varepsilon_{cu} = \frac{2.91 - 1.75}{2.91} * 0.015 = 0.006 < 0.024$ *(Compression reinforcement has not ruptured.)*

Stress in tension longitudinal reinforcement,

- $f_{st} = E_s \varepsilon_{st} = 6141 * 0.0126 = 77.38 ksi$

Stress in extreme tension longitudinal reinforcement,

- $f_{st,\max} = E_s \varepsilon_{st} = 6141 * 0.0172 = 105.63 ksi$

Stress in compression longitudinal reinforcement,

- $f_{sc} = E_s \varepsilon_{sc} = 6141 * 0.006 = 36.85 ksi$

For compression and tension forces,

- $C_c = 0.85 f_c^{'} \left(ab - A_{sc} \right) = 0.85 * 20 * \left(1.893 * 8 - 3 * .79 \right) = 217.16 kips$
- $C_s = A_{sc} f_{sc} = \left(3 * 0.79 \right) * 36.85 = 87.33 kips$
- $T = A_{st} f_{st} = 5 * 0.79 * 77.38 = 305.65 kips$

Nominal Moment,

$$M_n = C_c \left(d - \frac{a}{2} \right) + C_s \left(d - d_c \right)$$

$$M_n = 217.16 * \left(5.35 - \frac{1.893}{2} \right) + 87.33 * \left(5.35 - 1.75 \right)$$

- $M_n = 1270.65 kip - in. = 105.89 kip - ft$

For development length, *(ACI 440.1R-15:10.2b)*

- $l_{bhf} = \frac{f_{fu}}{37.5} \frac{d_b}{\sqrt{f_c^{'}}}$ for $75000 psi < f_{fu} < 150,000 psi$

$$l_{bhf} = \frac{105630}{37.5} \frac{1}{\sqrt{20000}} = 19.92 in.$$

Considering a shear span to depth ratio of 4. For the effective length of the beam,

- $L = 4 * 8'' = 32 in.$

Taking the effective span as:

- $L = 34 in.$

Ultimate shear,

- $$V_u = \frac{M_n}{L} = \frac{105.89 kip - ft}{\frac{34}{12} ft} = 37.37 kips$$

Nominal shear strength provided by concrete,

- $$\phi V_c = 0.75 * 600 psi * bd = 0.75 * 600 * 8 * 5.35 = 19.26 kips$$

For the shear reinforcements, No. 4 BFRP rebars are used where, $f_{rupture} = 126 ksi$

Area of shear reinforcements,

- $$A_v = 2 * 0.196 = 0.392 in.^2$$

For spacing (s) of shear reinforcements,

- $$s = \frac{0.75 * A_v * f_y * d}{V_u - \phi V_c} = \frac{0.75 * 0.392 * 126 * 5.35}{37.37 - 19.26} = 10.94 in.$$

According to ACI 318-14; Table 9.7.6.2.2 for maximum spacing of shear reinforcement,

- $$4\sqrt{f_c'} b_w d = 4 * \sqrt{20000} * 8 * 5.35 = 24.21 kips$$
- $$V_s = \frac{V_u - \phi V_c}{\phi} = \frac{37.37 - 28.8}{0.75} = 11.43 kips < 4\sqrt{f_c'} b_w d = 24.21 kips$$

Hence, maximum spacing,

- $$s_{\max} = \frac{d}{2} = \frac{5.35}{2} = 2.675 in. < 24 in.$$

However, as the cross-sectional dimensions of the beam was small, a transverse reinforcement spacing of 6 in. was considered.

Therefore, for transverse reinforcements #4 BFRP stirrups @ 6 in. o.c. was taken.

8.2.5 UHP-FRC #4

The first beam was design with UHP-FRC with micro short steel fibers. The fiber content for the UHP-FRC beam was 3% by volume. High-strength GFRP (Glass, 104 ksi) rebars was used as flexural reinforcements. The design calculations are presented below:

$f_c^{'} = 22ksi\ ,\ \beta_1 = 0.65$

$f_{fu} = 145.8ksi$

$\varepsilon_{rupture} = 0.024$

$E_f = 6141ksi$

$b = 8in.$

$d = 5.35in.$

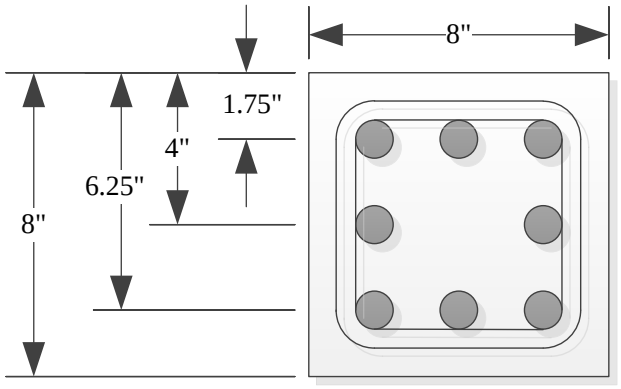

Figure 8- 12 Cross section of UHP-FRC #4

For the balanced reinforcement ratio, *(ACI 440.1R-15: 7.2.1b)*

- $\rho_{fb} = 0.85\beta_1 \frac{f_c^{'}}{f_{fu}} \frac{E_f \varepsilon_{cu}}{E_f \varepsilon_{cu} + f_{fu}} = 0.85 * 0.65 * \frac{22000}{145800} * \frac{6141 * 0.015}{6141 * 0.015 + 145.8}$

  $\rho_{fb} = 0.0323$

For compression control,

- $\rho_f > \rho_{fb} = 0.0323$

Taking #8 BFRP rebars in a section as shown:

- $\rho_f = \frac{A_{st}}{bd} = \frac{5 * 0.79}{8 * 5.35} = 0.0923 > \rho_{fb}$ [Compression controlled]

Based on strain compatibility,

- $a = \beta_1 c$; $c = \dfrac{a}{\beta_1}$
- $\dfrac{\varepsilon_{sc}}{\varepsilon_{cu}} = \dfrac{c - d_c}{c}$ or,

  $\varepsilon_{sc} = \dfrac{c - d_c}{c} * \varepsilon_{cu}$
- $\dfrac{\varepsilon_{st}}{\varepsilon_{cu}} = \dfrac{d - c}{c}$ or,

  $\varepsilon_{st} = \dfrac{d - c}{c} * \varepsilon_{cu}$

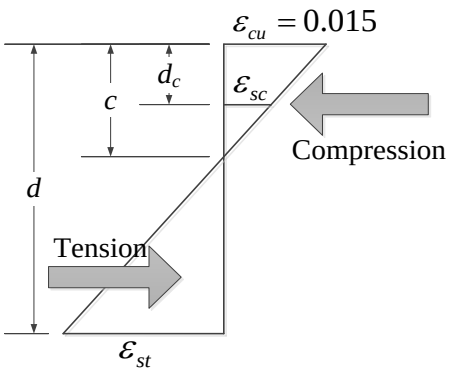

Figure 8- 13 Strain compatibility diagram

Compression force, $C = C_{concrete} + C_{reinforcement}$

$C_{concrete} = 0.85 f_c^{'} ab$

$C_{reinforcement} = A_s f_{sc}$

Where, $f_{sc} = \min \begin{Bmatrix} f_{fu} \\ E_s * \varepsilon_{sc} \end{Bmatrix}$

Tension force, $T = A_{st} f_{st}$

Where, $f_{st} = \min \begin{Bmatrix} f_{fu} \\ E_s * \varepsilon_{st} \end{Bmatrix}$

Assuming that the BFRP rebars do not rupture in both tension and compression,

- $f_{sc} = E_s * \varepsilon_{sc} = E_s * \dfrac{c - d_c}{c} * \varepsilon_{cu}$
- $f_{st} = E_s * \varepsilon_{st} = E_s * \dfrac{d - c}{c} * \varepsilon_{cu}$

Now,

Compression force, $C = C_{concrete} + C_{reinforcement}$

$$C = 0.85 f_c^{'} ab + A_s f_{sc}$$

$$C = 0.85 f_c^{'} ab + A_s * E_s * \left(\frac{c - d_c}{c} \right) * \varepsilon_{cu}$$

$$C = 0.85 f_c^{'} ab + A_s * E_s * \left(\frac{\frac{a}{\beta_1} - d_c}{\frac{a}{\beta_1}} \right) * \varepsilon_{cu}$$

Tension force, $T = A_{st} * \varepsilon_{st} = A_{st} * E_s * \left(\frac{d - c}{c} \right) * \varepsilon_{cu}$

$$T = A_{st} * E_s * \left(\frac{d - \frac{a}{\beta_1}}{\frac{a}{\beta_1}} \right) * \varepsilon_{cu}$$

Based of equilibrium of forces,

Compression force (C) = Tension force (T)

or, $C_{concrete} + C_{reinforcement} = T$

or, $0.85 f_c^{'} ab + A_s * E_s * \left(\frac{\frac{a}{\beta_1} - d_c}{\frac{a}{\beta_1}} \right) * \varepsilon_{cu} = A_{st} * E_s * \left(\frac{d - \frac{a}{\beta_1}}{\frac{a}{\beta_1}} \right) * \varepsilon_{cu}$

or,

$$0.85 * 22 * a * 8 + (3 * 0.79) * 6141 * \left(\frac{\frac{a}{0.65} - 1.75}{\frac{a}{0.65}} \right) * 0.015 = (5 * 0.79) * 6141 * \left(\frac{5.35 - \frac{a}{0.65}}{\frac{a}{0.65}} \right) * 0.015$$

Solving for a,

- $a = 1.856"$

- $c = \frac{a}{\beta_1} = \frac{1.856}{0.65} = 2.855"$

Now,

Strain in tension longitudinal reinforcement,

$$\varepsilon_{st} = \frac{d-c}{c}\varepsilon_{cu} = \frac{5.35-2.855}{2.855} * 0.015 = 0.0131 < 0.024$$

Strain in extreme tension longitudinal reinforcement,

- $\varepsilon_{st,\max} = \frac{d_t - c}{c}\varepsilon_{cu} = \frac{6.25-2.855}{2.855} * 0.015 = 0.0178 < 0.024$ *(Tension reinforcement has not ruptured.)*

Strain in extreme compression longitudinal reinforcement,

- $\varepsilon_{sc} = \frac{c-d_c}{c}\varepsilon_{cu} = \frac{2.855-1.75}{2.855} * 0.015 = 0.0058 < 0.024$ *(Compression reinforcement has not ruptured.)*

Stress in tension longitudinal reinforcement,

- $f_{st} = E_s\varepsilon_{st} = 6141 * 0.0131 = 80.45ksi$

Stress in extreme tension longitudinal reinforcement,

- $f_{st,\max} = E_s\varepsilon_{st,\max} = 6141 * 0.0178 = 109.31ksi$

Stress in compression longitudinal reinforcement,

- $f_{sc} = E_s\varepsilon_{sc} = 6141 * 0.0058 = 35.62ksi$

For compression and tension forces,

- $C_c = 0.85 f_c^{'}\left(ab - A_{sc}\right) = 0.85 * 22 * \left(1.856 * 8 - 3 * .79\right) = 233.34kips$
- $C_s = A_{sc} f_{sc} = \left(3 * 0.79\right) * 35.62 = 84.42kips$
- $T = A_{st} f_{st} = 5 * 0.79 * 80.45 = 317.78kips$

Nominal Moment,

$$M_n = C_c\left(d - \frac{a}{2}\right) + C_s\left(d - d_c\right)$$

$$M_n = 233.34*\left(5.35 - \frac{1.856}{2}\right) + 84.42*\left(5.35 - 1.75\right)$$

- $M_n = 1335.74 kip - in. = 111.31 kip - ft$

For development length, *(ACI 440.1R-15:10.2b)*

- $l_{bhf} = \frac{f_{fu}}{37.5}\frac{d_b}{\sqrt{f_c^{'}}}$ for $75000\,psi < f_{fu} < 150,000\,psi$

$$l_{bhf} = \frac{109310}{37.5}\frac{1}{\sqrt{22000}} = 19.65 in.$$

Considering a shear span to depth ratio of 4. For the effective length of the beam,

- $L = 4*8'' = 32 in.$

Taking the effective span as:

- $L = 34 in.$

Ultimate shear,

- $V_u = \frac{M_n}{L} = \frac{111.31 kip - ft}{\frac{34}{12}\,ft} = 39.29 kips$

Nominal shear strength provided by concrete,

- $\phi V_c = 0.75*600\,psi*bd = 0.75*600*8*5.35 = 19.26 kips$

For the shear reinforcements, No. 4 BFRP rebars are used where, $f_{rupture} = 126 ksi$

Area of shear reinforcements,

- $A_v = 2*0.196 = 0.392 in.^2$

For spacing (s) of shear reinforcements,

- $$s = \frac{0.75 * A_v * f_y * d}{V_u - \phi V_c} = \frac{0.75 * 0.392 * 126 * 5.35}{39.29 - 19.26} = 9.89 in.$$

According to ACI 318-14; Table 9.7.6.2.2 for maximum spacing of shear reinforcement,

- $$4\sqrt{f_c'} b_w d = 4 * \sqrt{22000} * 8 * 5.35 = 25.39 kips$$
- $$V_s = \frac{V_u - \phi V_c}{\phi} = \frac{39.29 - 28.8}{0.75} = 13.99 kips < 4\sqrt{f_c'} b_w d = 25.39 kips$$

Hence, maximum spacing,

- $$s_{\max} = \frac{d}{2} = \frac{5.35}{2} = 2.675 in. < 24 in.$$

However, as the cross-sectional dimensions of the beam was small, a transverse reinforcement spacing of 6 in. was considered.

Therefore, for transverse reinforcements #4 BFRP stirrups @ 6 in. o.c. was taken.

8.3 Fiber type and volume fraction of fibers

Two different fiber type are used in this research namely micro short steel fibers (Dramix OL 13/0.20) and ultra-high molecular weight polyethylene (UHMW PE) fibers as shown in *Figure 8-14*. A fiber content of 3% and 0.75% by volume was used for micro short steel and UHMW PE fibers respectively. The mechanical properties of the fibers are presented in *Figure 8-3*.

Figure 8- 14 Micro short steel fiber (left) and ultra-high molecular weight polyethylene fiber (right)

Table 8- 3 Mechanical properties of the fibers

	Length in.(mm)	Diameter in.(mm)	Tensile strength ksi (MPa)
Micro short steel fiber	0.51 (13)	0.008 (0.21)	399 (2750)
UHMW Polyethylene fiber	0.5 (13)	0.00006 (0.0015)	375 (2580)

8.4 Concrete mix design

UHP-FRC used for the specimens was developed at UT Arlington (Aghdasi et al., 2015) based on high packing density theory (Willie et al., 2012). Materials which were locally available in the Unites States were used to develop the mix. The properties of the mix ingredients are presented in the Table 8-4. The target compressive strength for UHP-FRC mix with micro short steel fibers was 22,000 psi (150 MPa) and for UHP-FRC mix with UHMW polyethylene fiber was 20,000 psi (140 MPa).

Table 8- 4 Mix proportion by weight for UHP-FRC (Developed at UT Arlington)

Components	Micro short steel fibers (V_f=3%)	UHMW Polyethylene fiber (V_f=0.75%)
Silica sand 1	0.43	0.43
Silica sand 2	0.37	0.37
Portland type I cement	1	1
Fly ash	0.2	0.2
Glass powder	0.25	0.25
Silica fume	0.25	0.25
Water	0.29	0.29
Superplasticizer	0.021	0.021
Fibers	0.276	0.0085

8.5 Specimen construction

All the specimens were constructed at the UT Arlington Civil Engineering Laboratory Building (CELB) by the author with the help of Dr. Shih-Ho (Simon) Chao's research group.

8.5.1 Strain gauge installation

For the specimens, strain gauges were installed (*Figure 8-15*) on the flexural reinforcements near the interface of the reinforced concrete support block and the cantilever UHP-FRC specimens. The exact location of the strain gauges is depicted in the *Figures 8-16 to 8-19*. The installation process includes marking, grinding and sanding of the longitudinal reinforcements at the locations predetermined to obtain a flat, smooth surface for the strain gauges. A 400 grit sandpaper was used for sanding process. After that the strain gauges were glued to the surface and three layers of coating, polyurethane, nitrile, rubber mastic electrical tape and electric liquid, were applied to seal the moisture.

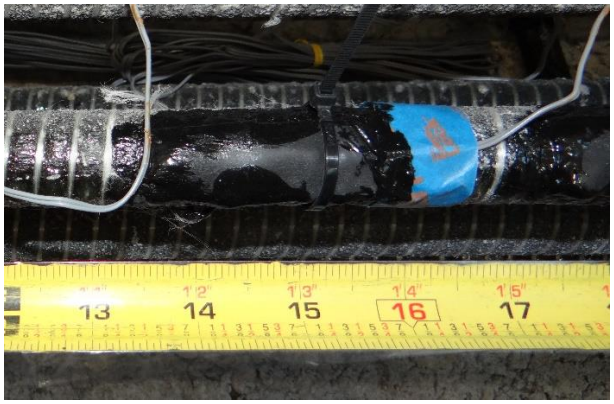

Figure 8- 15 Strain gauge installed on a flexural reinforcement (BFRP)

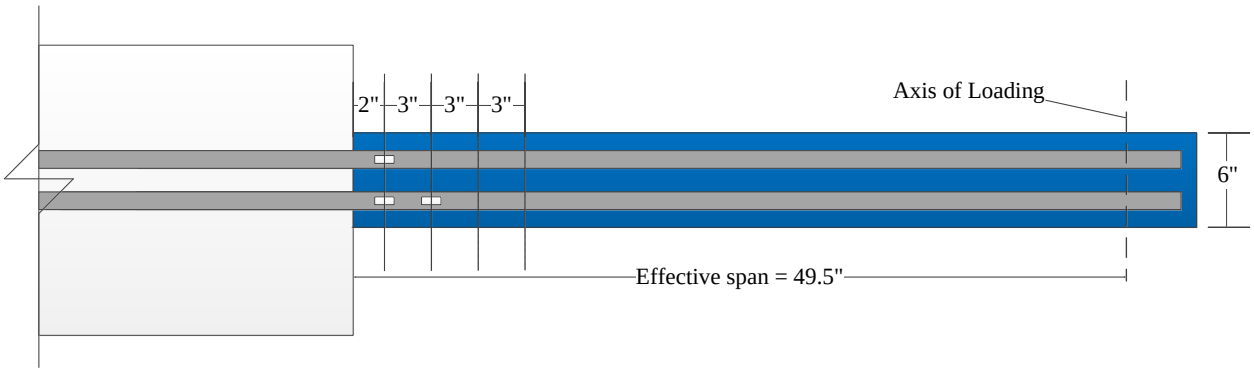

Figure 8- 16 Strain gauge location for UHP-FRC #1

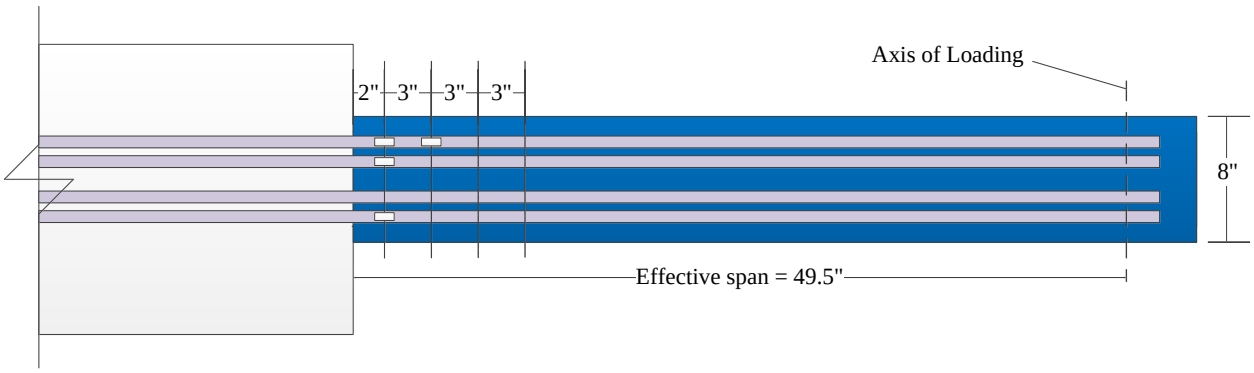

Figure 8- 17 Strain gauge location for UHP-FRC #2

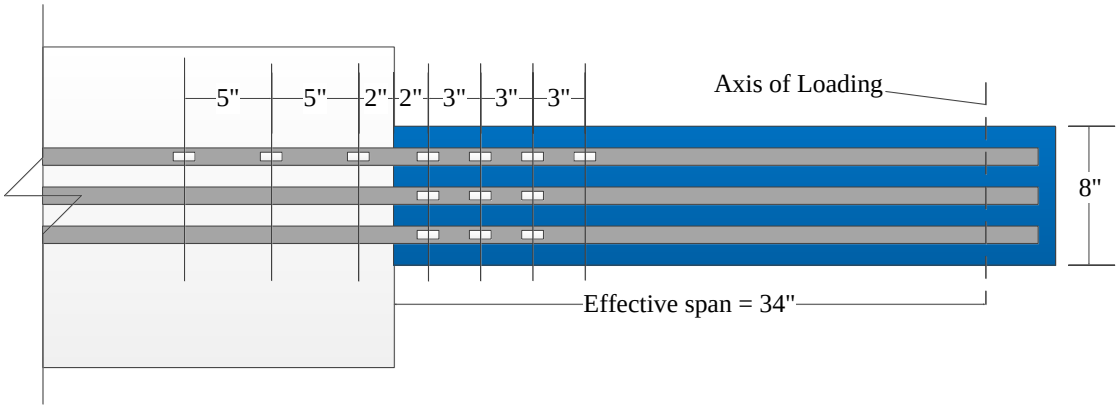

Figure 8- 18 Strain gauge location for UHP-FRC #3

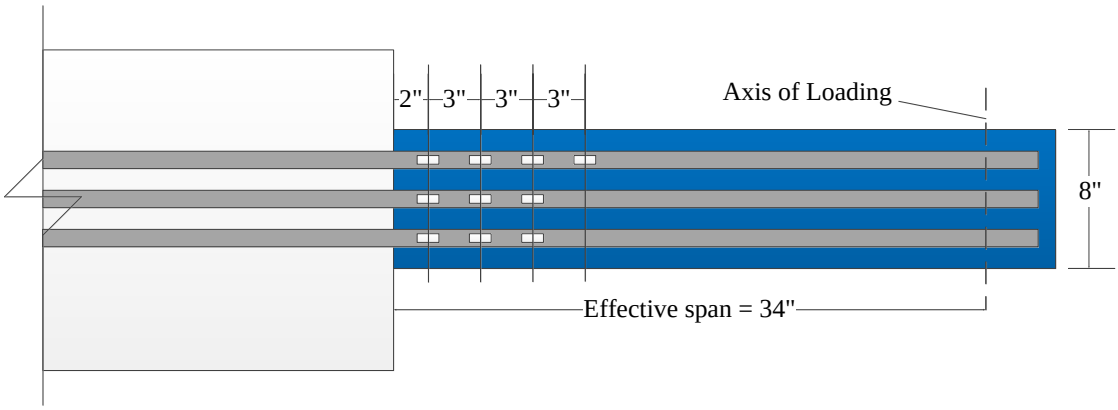

Figure 8- 19 Strain gauge location for UHP-FRC #4

8.5.2 Caging and formwork fabrication

Reinforcing bar cage for the UHP-FRC beam specimens as well as their supporting reinforced concrete block was prepared in the UT Arlington CELB. The preparation of the four specimens was

conducted along with the preparation of a total of two support blocks (two specimens per support block). The reinforcement cage for the support block was prepared and placed in the formwork as shown in *Figure 8-20*. Additional reinforcements (*Figure 8-21*) were provided at the beam-block interface to prevent compression failure of the concrete of the support block. The reinforcements for the beam specimens were prepared (*Figure 8-22*). The prepared specimen reinforcements were inserted in the support cage as shown in *Figure 8-23 and 8-24*.

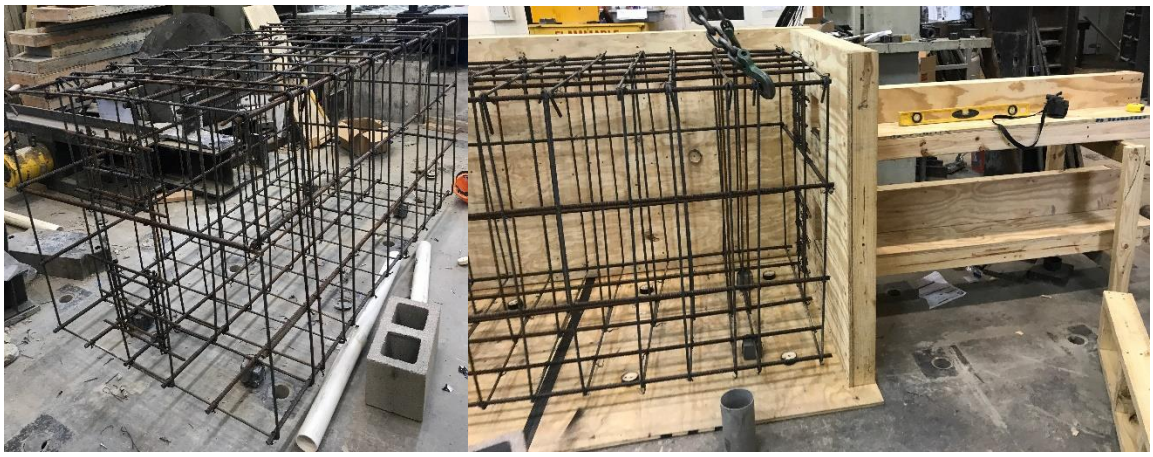

Figure 8- 20 Preparation of support block cage and positioning inside the formwork

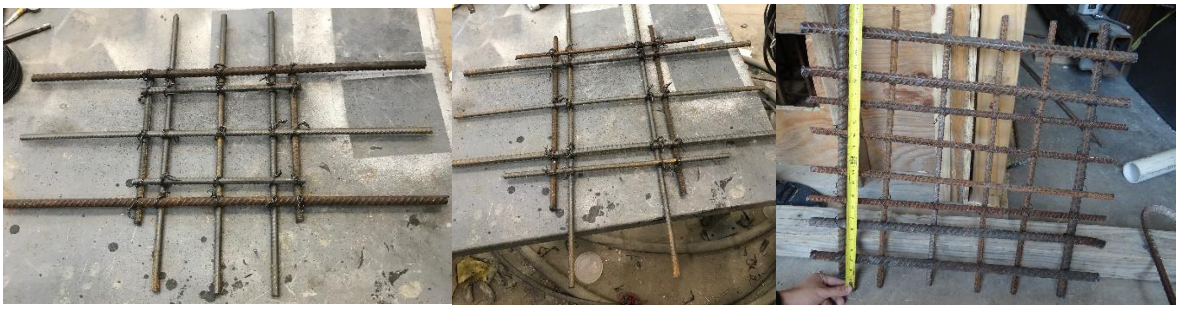

(a) (b) (c)

Figure 8- 21 Additional reinforcements provided at the beam-block interface for (a) UHP-FRC #1 **(b) UHP-FRC #2 (c) UHP-FRC #3 and #4**

(a) (b)

Figure 8- 22 Reinforcement for specimens (a) UHP-FRC #1 and UHP-FRC #2 (b) UHP-FRC #3 and UHP-FRC #4

Figure 8- 23 Reinforcement for specimens UHP-FRC #1 (left) and UHP-FRC #2 (right)

Figure 8- 24 Reinforcements for the specimens inserted in the support reinforcement cage

8.5.3 Mixing of concrete, casting and curing of the UHP-FRC specimens

8.5.3.1 Reinforced concrete support block

A concrete of target compressive strength of 5 ksi was poured in the support reinforced concrete block (*Figure 8-25 and 8-26*). The concrete was obtained from a local ready-mix truck with a specified slump of 5 inches. The concrete was initially poured on a wheelbarrow to check for consistency and slump prior to pouring concrete into the support block formwork. The concrete was then poured into the formwork and vibrated with a needle vibrator for compactness.

Figure 8- 25 Concrete pouring of the support block

Figure 8- 26 The hardened concrete of the support block shown with the specimen (UHP-FRC #3 and UHP-FRC #4 specimen BFRP reinforcements)

8.5.3.2 UHP-FRC specimens

The dry component materials of the UHP-FRC were weighed in pounds and collected as per the required proportion. It was then transferred to the pan mixer (*Figure 8-27*) for mixing and dry mixed initially. The water was added in gradual portions in order to get a good paste. After a uniform paste was ready, the fibers as per the required proportion were added and was mixed again for a few minutes till a consistent mix (*Figure 8-28*) was obtained. The UHP-FRC was then transferred from the mixer into the specimens (*Figure 8-29*) by using buckets. The specimen was cured in the strong floor room at a temperature of 77°F (25°C) and a relative humidity of 100% until the day of testing. *Figure 8-30* shows the prepared final specimens UHP-FRC #3 and UHP-FRC #4 after the removal of the formwork.

(a) (b)

Figure 8- 27 (a) Rotating pan mixer used for UHP-FRC (b) UHP-FRC preparation

(a) (b)

Figure 8- 28 (a) UHP-FRC preparation using a pan mixer (b) Consistent UHP-FRC mix (c) Uniform distribution of fibers

Figure 8- 29 UHP-FRC pouring for the specimens

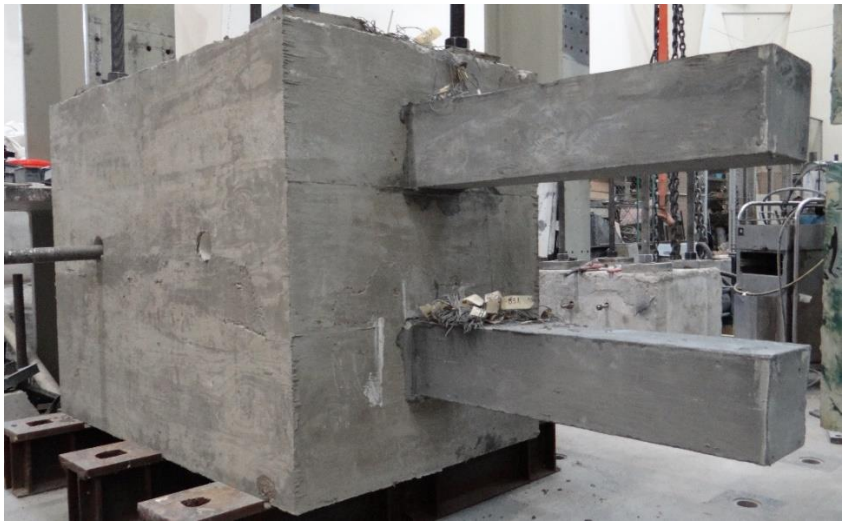

Figure 8- 30 Prepared specimens UHP-FRC #3 and UHP-FRC #4

8.5.4. Test setup and instrumentation

The loading of the specimen is achieved using a Material Testing System (MTS) hydraulic actuator in the Civil Engineering Laboratory Building (CELB) at UTA using the loading protocol as shown in *Figure 8-31***.** Displacement control was used for the loading of the specimens. The beams were loaded in the loading axis between two bearing plates of 6 in. wide along the length of the beam and 1 in. thick. The plates were spread along the entire width of the beam. A layer of grout was used at the contact surface between the UHP-FRC specimen and the loading plate to ensure a uniform interface contact. Lateral stiffeners were used on the lateral sides of the beam to prevent any torsional movement.

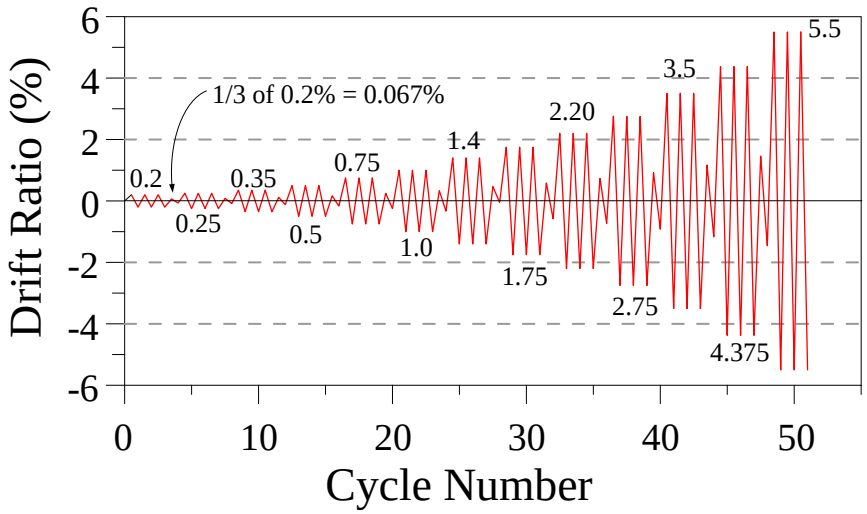

Figure 8- 31 Loading protocol for reversed cyclic loading

The test setup consists of a load application mechanism as shown in *Figure 8-32 and Figure 8-33*, four linear variable differential transformers (LVDTs) along with a string pot. The LVDTs and string pot was used to measure the vertical displacement and the strain gauges provide the strain value of the flexural reinforcements in the specimen. All sensors were connected to the DAQ box and the data was recorded.

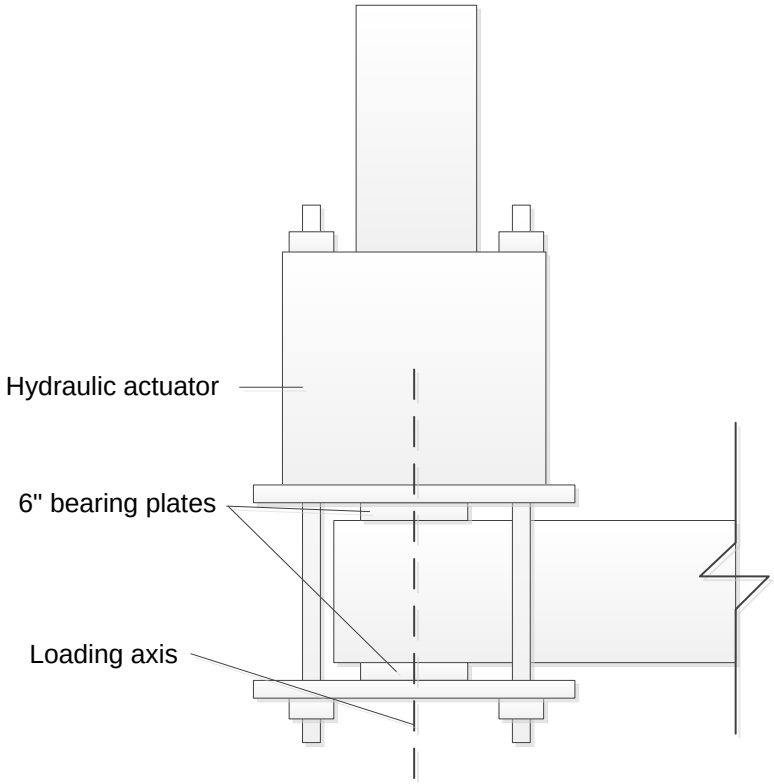

Figure 8- 32 Cyclic load application mechanism on the cantilever specimen

The drift was calculated using the formula shown below. The shear stress was obtained from the recorded peak's longitudinal load using the formulae presented below:

$$D = V/S \times 100\% \quad [1]$$

where:

D = Drift ratio (%)

V = Net vertical displacement of the specimen (in.)

S = Effective span (in.)

$$M = P \times S/1000 \quad [2]$$

where:

$M =$ Applied moment (kips-in.)

$P =$ Applied load (lbf)

$S =$ Effective span (in.)

Figure 8- 33 Figure showing the loading head setup of the cantilever specimen

8.5.5 Material testing

8.5.5.1 UHP-FRC compressive strength

The compressive strength is often determined by testing cylinders. However, using this method for very high strength concrete is difficult because of higher loading capacity of the machines and the need for the cylinders to have their ends prepared (Graybeal and Davis, 2008). In this research, 2.78 in. (70.7 mm) cubes are used to determine the compressive strength and its properties. These are an

acceptable alternative to the standard 4 in. (102 mm) cylinders. The main objective of the compressive strength is to obtain the compressive strength of UHP-FRC at the time of specimen testing.

Chapter 9

Part II: Experimental results

9.1 UHP-FRC #1

A maximum moment of 840 kip-in. (95 kN-m) was recorded at a drift of 8%. Moment versus drift ratio relationship of beam UHP-FRC #1 showed large cyclic deformation up to a drift of 8% without significant damage to the UHP-FRC material. The specimen exhibited stable cyclic behavior up to very large drift ratios. From the *Figure 9-1*, it can be seen that there is minor residual deformation. Flexural cracking was seen to be the primary mode of cracking during the test. From the strain data, it is observed that the MMFX rebars have crossed the yield strain at the interface. The moment and reinforcement strain relationship can be viewed in *Figure 9-2*. The test pictures of the specimen for different values of drift can be viewed from *Figure 9-3 to 9-17*.

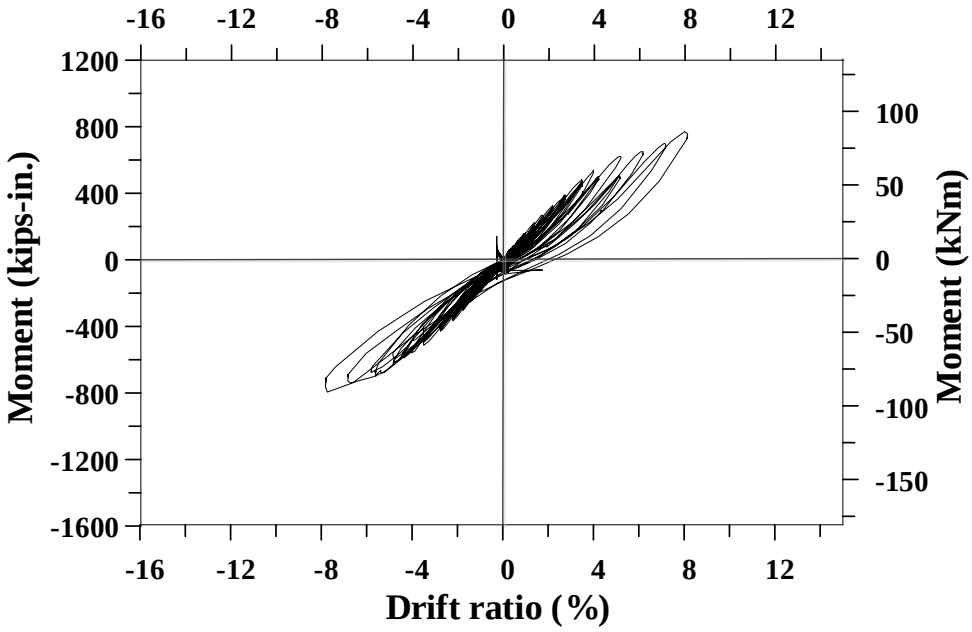

Figure 9- 1 Moment vs Drift ratio for UHP-FRC #1 with steel fibers (MMFX bars)

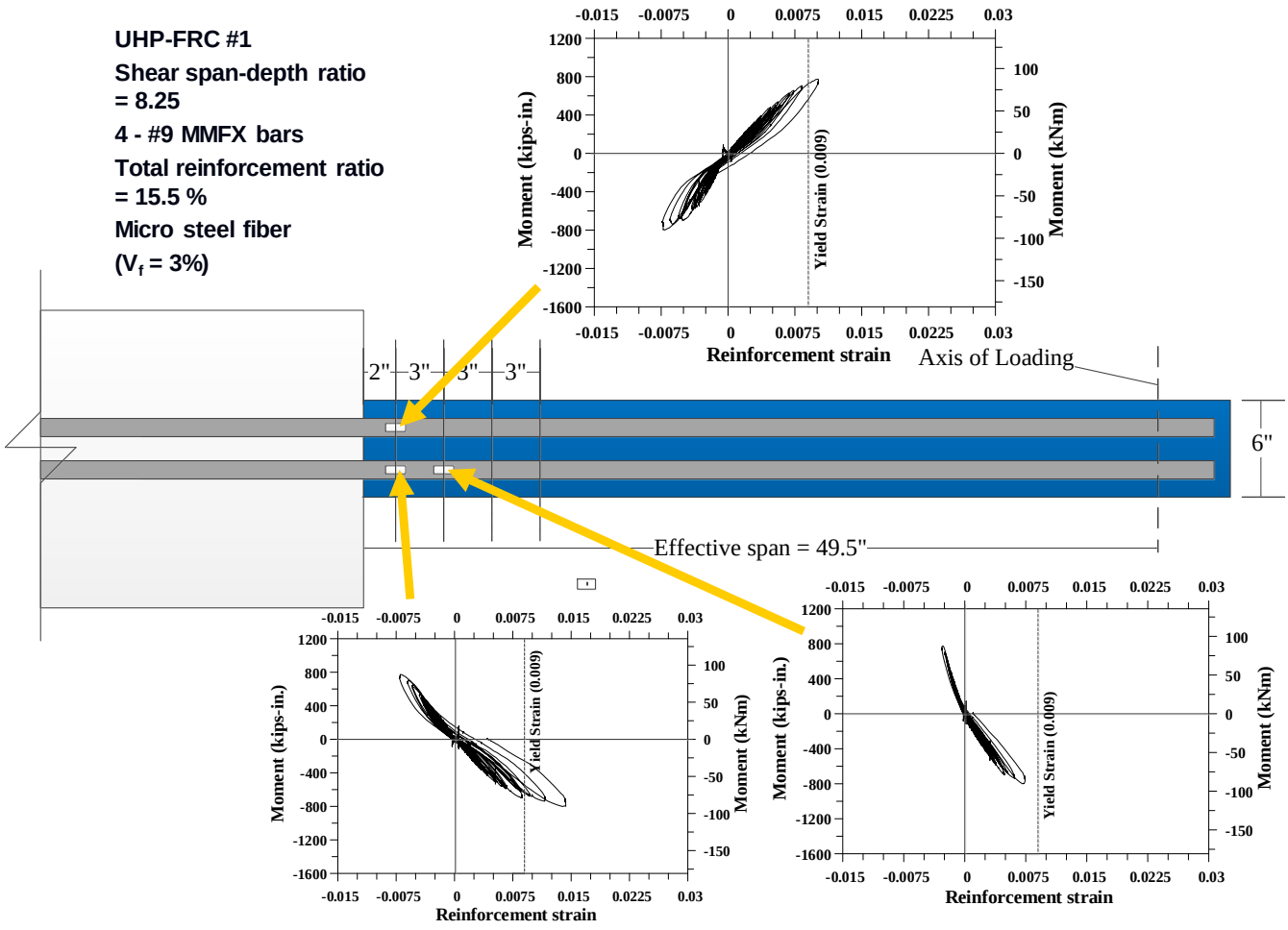

Figure 9- 2 Moment vs reinforcement strain for UHP-FRC #1

Figure 9- 3 UHP-FRC #1 at 0.2% drift

Figure 9- 4 UHP-FRC #1 at 0.25% drift

Figure 9- 5 UHP-FRC #1 at 0.35% drift

Figure 9- 6 UHP-FRC #1 at 0.5% drift

Figure 9- 7 UHP-FRC #1 at 0.75% drift

Figure 9- 8 UHP-FRC #1 at 1.0% drift

Figure 9- 9 UHP-FRC #1 at 1.4% drift

Figure 9- 10 UHP-FRC #1 at 1.75% drift

Figure 9- 11 UHP-FRC #1 at 2.2% drift

Figure 9- 12 UHP-FRC #1 at 2.75% drift

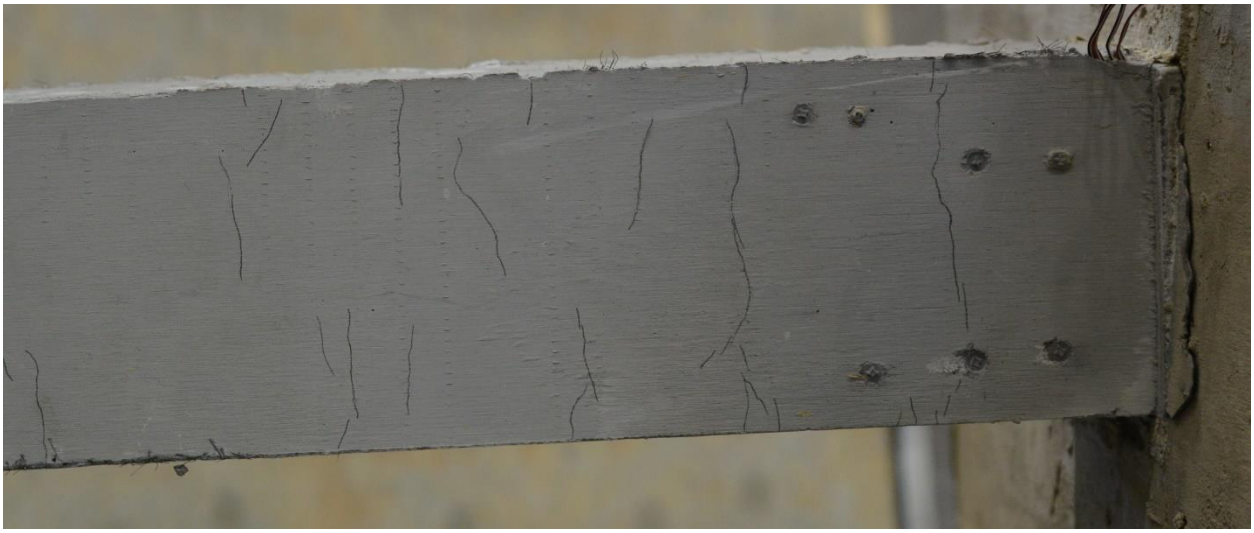

Figure 9- 13 UHP-FRC #1 at 3.5% drift

Figure 9- 14 UHP-FRC #1 at 4.0% drift

Figure 9- 15 UHP-FRC #1 at 5.0% drift

Figure 9- 16 UHP-FRC #1 at 7.0% drift

Figure 9- 17 UHP-FRC #1 at 8.0% drift

9.2 UHP-FRC #2

A maximum moment of 1050 kip-in. (119 kN-m) was recorded at a drift of 13%. Moment versus drift ratio relationship of beam UHP-FRC #2 showed large cyclic deformation up to a drift of 10% without significant damage to the UHP-FRC material. Stable cyclic behavior was observed up to 13% drift after which the moment started to decrease. From the *Figure 9-18*, it can be seen that there is minor residual deformation. Flexural cracking was seen to be the governing mode of cracking during the test. Strain data of flexural reinforcements (*Figure 9-19*) indicate that the rebars are elastic during the testing. The test pictures of the specimen for different values of drift can be viewed from *Figure 9-20 to 9-40*.

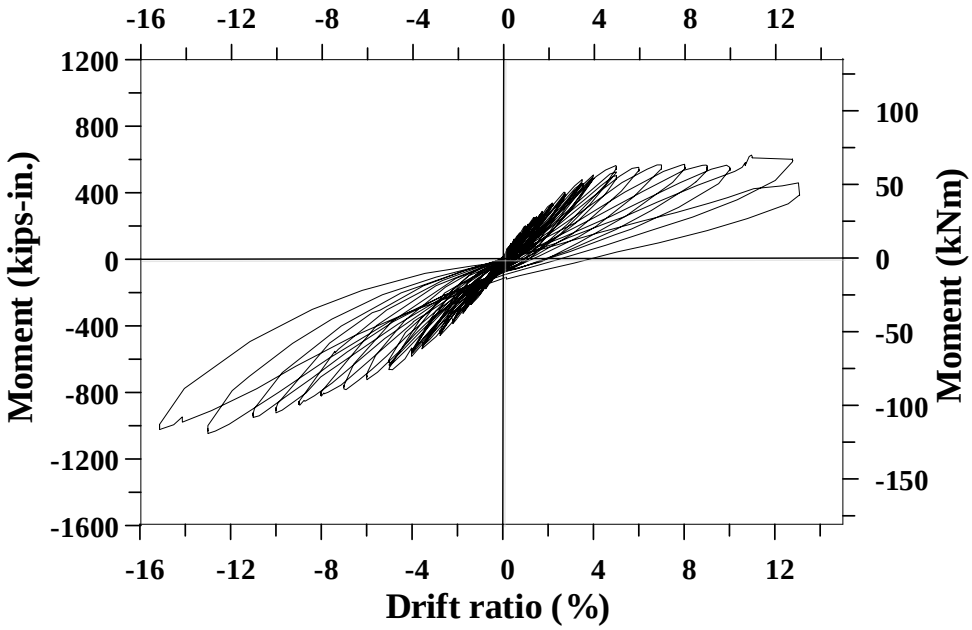

Figure 9- 18 Moment vs Drift ratio for UHP-FRC #2 with steel fibers (GFRP bars)

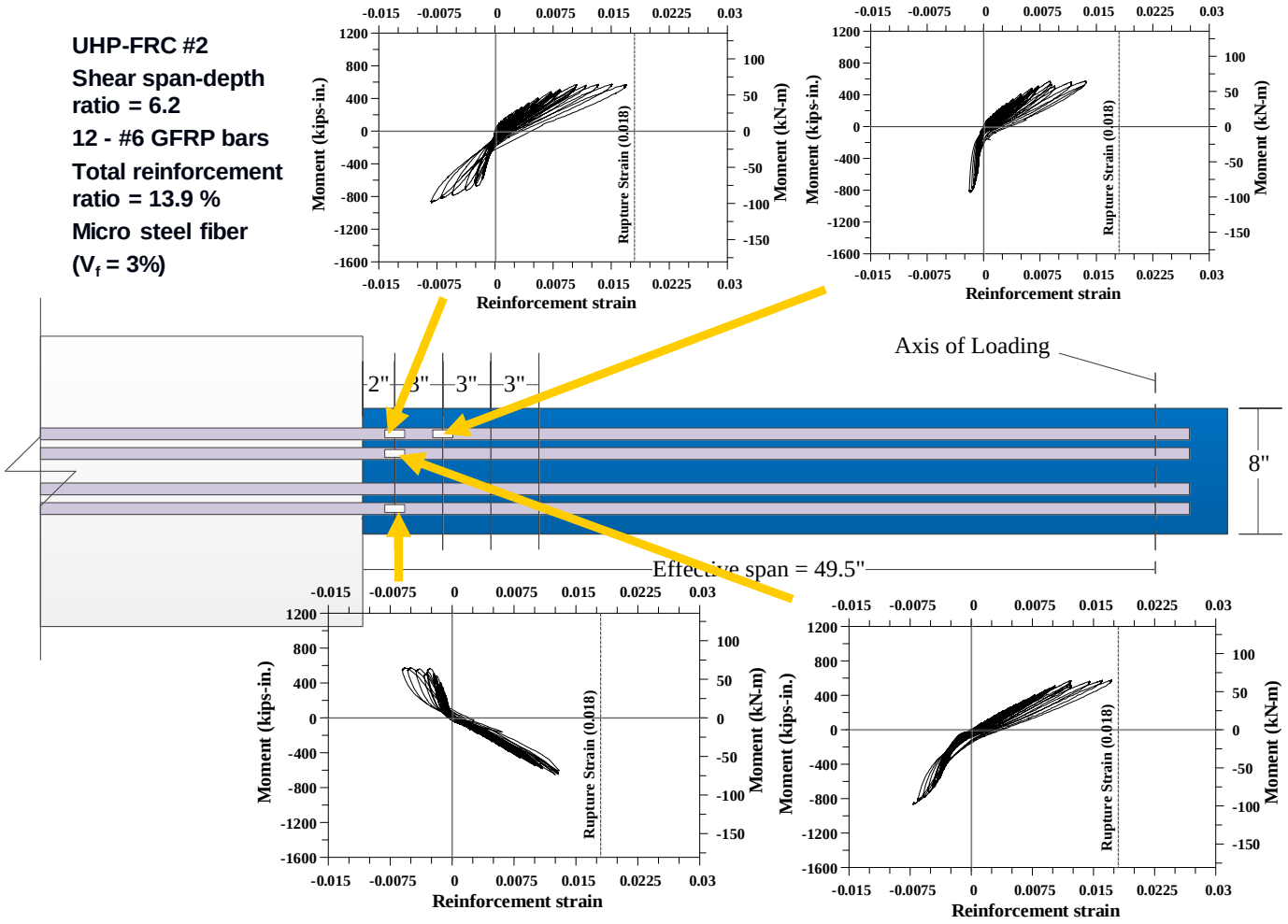

Figure 9- 19 Moment vs reinforcement strain for UHP-FRC #2

Figure 9- 20 UHP-FRC #2 at 0.2% drift

Figure 9- 21 UHP-FRC #2 at 0.25% drift

Figure 9- 22 UHP-FRC #2 at 0.35% drift

Figure 9- 23 UHP-FRC #2 at 0.5% drift

Figure 9- 24 UHP-FRC #2 at 0.75% drift

Figure 9- 25 UHP-FRC #2 at 1.0% drift

Figure 9- 26 UHP-FRC #2 at 1.4% drift

Figure 9- 27 UHP-FRC #2 at 1.75% drift

Figure 9- 28 UHP-FRC #2 at 2.2% drift

Figure 9- 29 UHP-FRC #2 at 2.75% drift

Figure 9- 30 UHP-FRC #2 at 3.5% drift

Figure 9- 31 UHP-FRC #2 at 4.0% drift

Figure 9- 32 UHP-FRC #2 at 5.0% drift

Figure 9- 33 UHP-FRC #2 at 6.0% drift

Figure 9- 34 UHP-FRC #2 at 7.0% drift

Figure 9- 35 UHP-FRC #2 at 8.0% drift

Figure 9- 36 UHP-FRC #2 at 9.0% drift

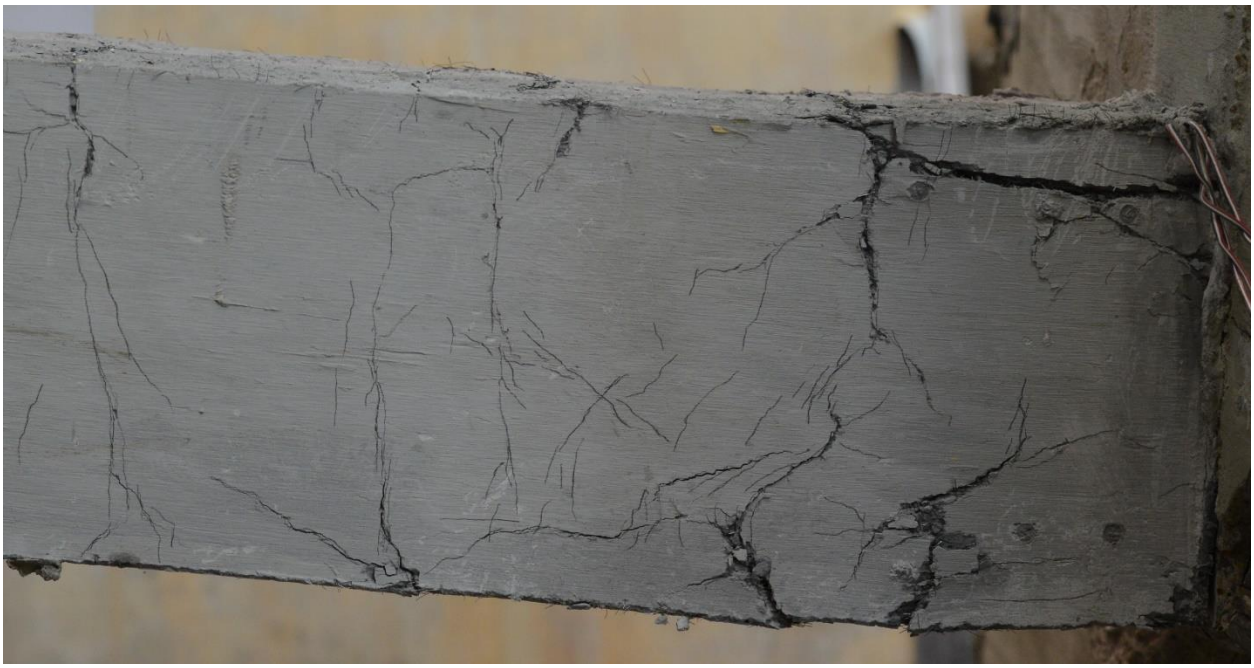

Figure 9- 37 UHP-FRC #2 at 10.0% drift

Figure 9- 38 UHP-FRC #2 at 10.0% drift

Figure 9- 39 UHP-FRC #2 at 13.0% drift

Figure 9- 40 UHP-FRC #2 at 15.0% drift

9.3 UHP-FRC #3

A maximum moment of 1470 kip-in. (166 kN-m) was recorded at a drift of 10%. Moment versus drift ratio relationship of beam UHP-FRC #3 showed large cyclic without significant damage to the UHP-FRC material. Stable cyclic behavior was observed up to 9% drift after which the moment started to decrease. From the *Figure 9-41*, it can be seen that there is minor residual deformation. Despite having a shear span to depth ratio of 4.25, flexural cracking was seen to be the governing mode of cracking during the test. It was seen that the flexural reinforcements had ruptured at the interface of the support block and the specimen resulting to excessive drifts. Strain data of flexural reinforcements are presented from *Figure 9-42 to 9-43***.** The test pictures of the specimen for different values of drift can be viewed from *Figure 9-44 to 9-63*.

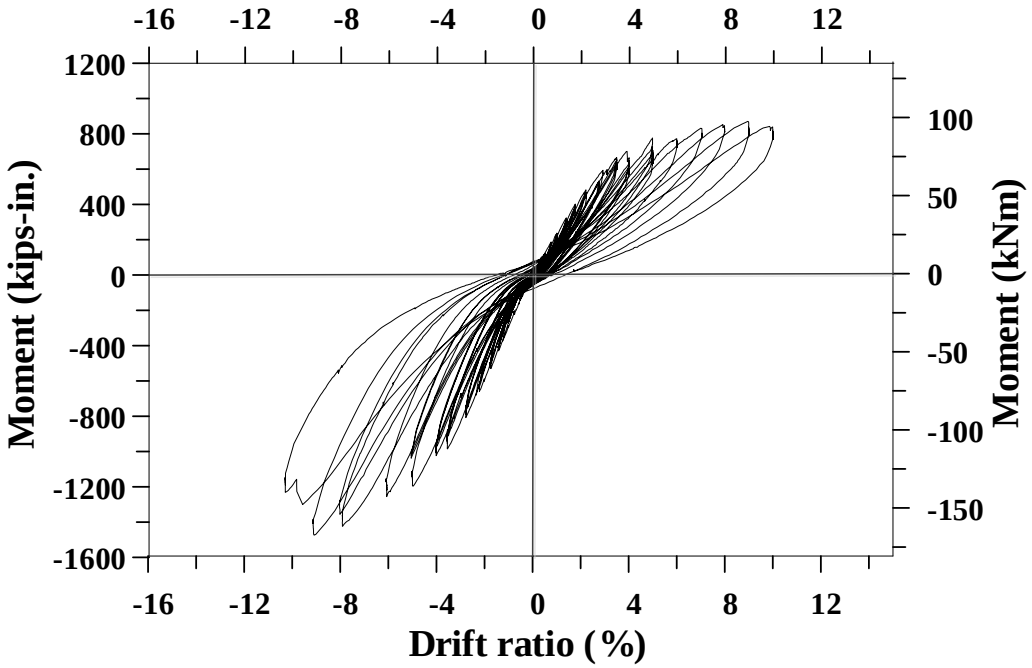

Figure 9- 41 Moment vs Drift ratio for UHP-FRC #3 with PE fibers (BFRP bars)

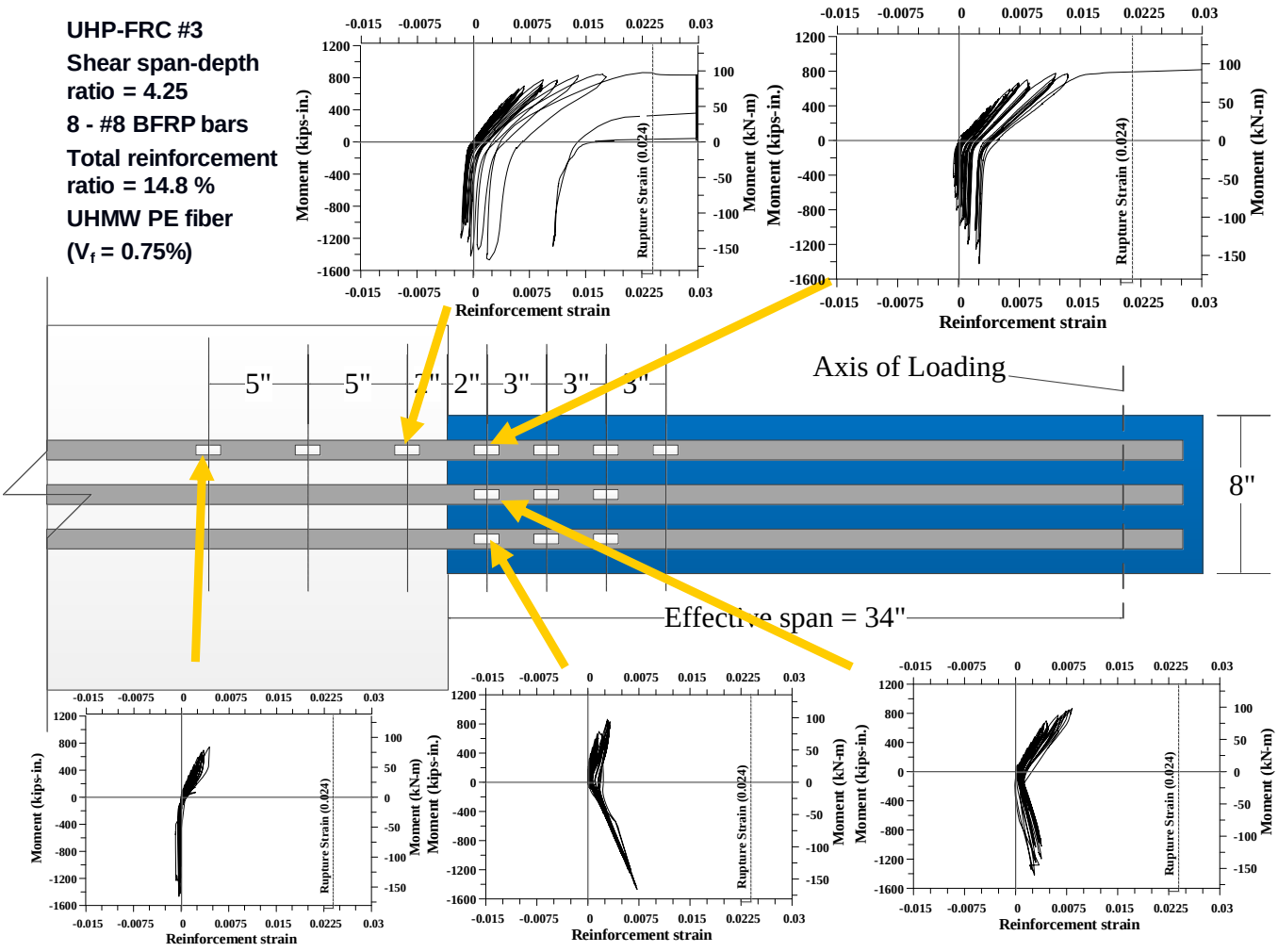

Figure 9- 42 Moment vs reinforcement strain for UHP-FRC #3

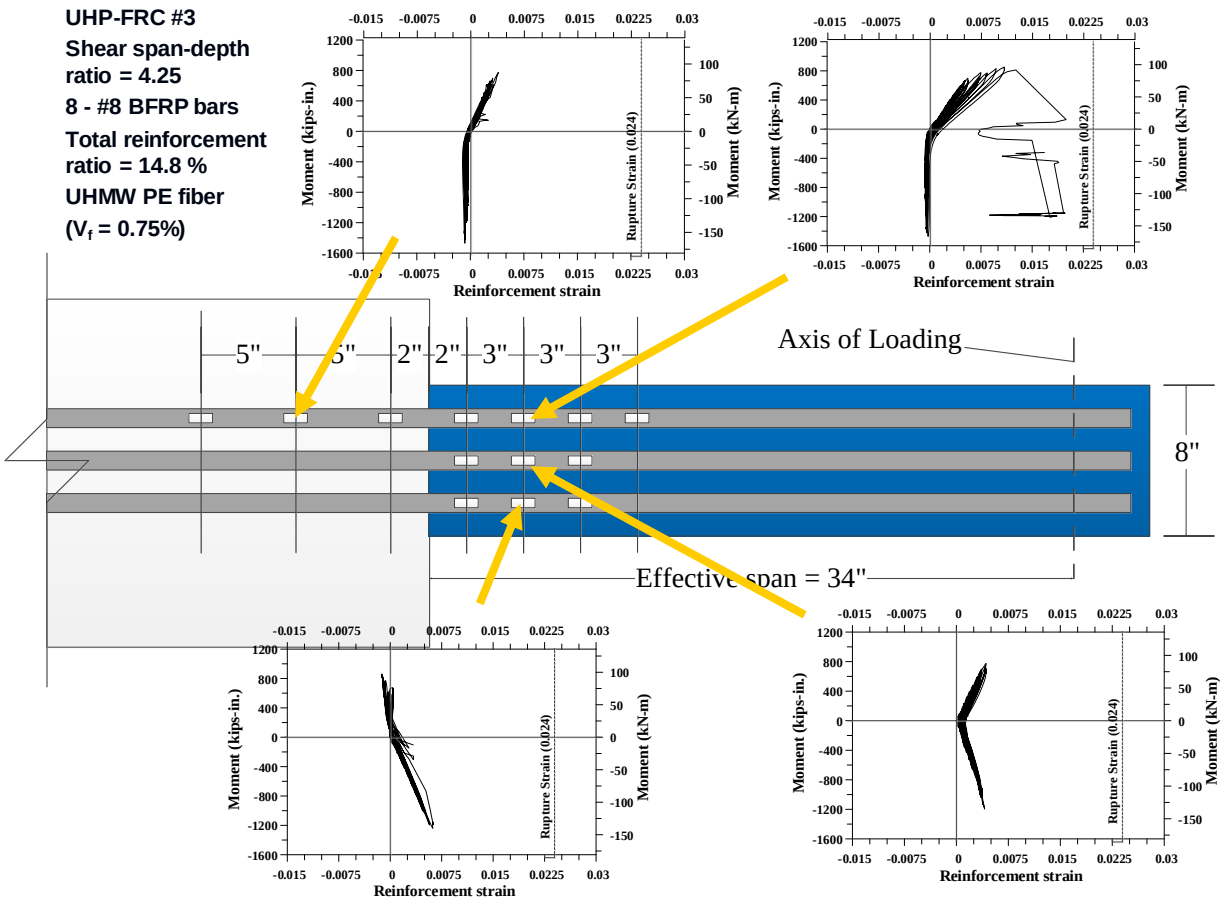

Figure 9- 43 Moment vs reinforcement strain for UHP-FRC #3

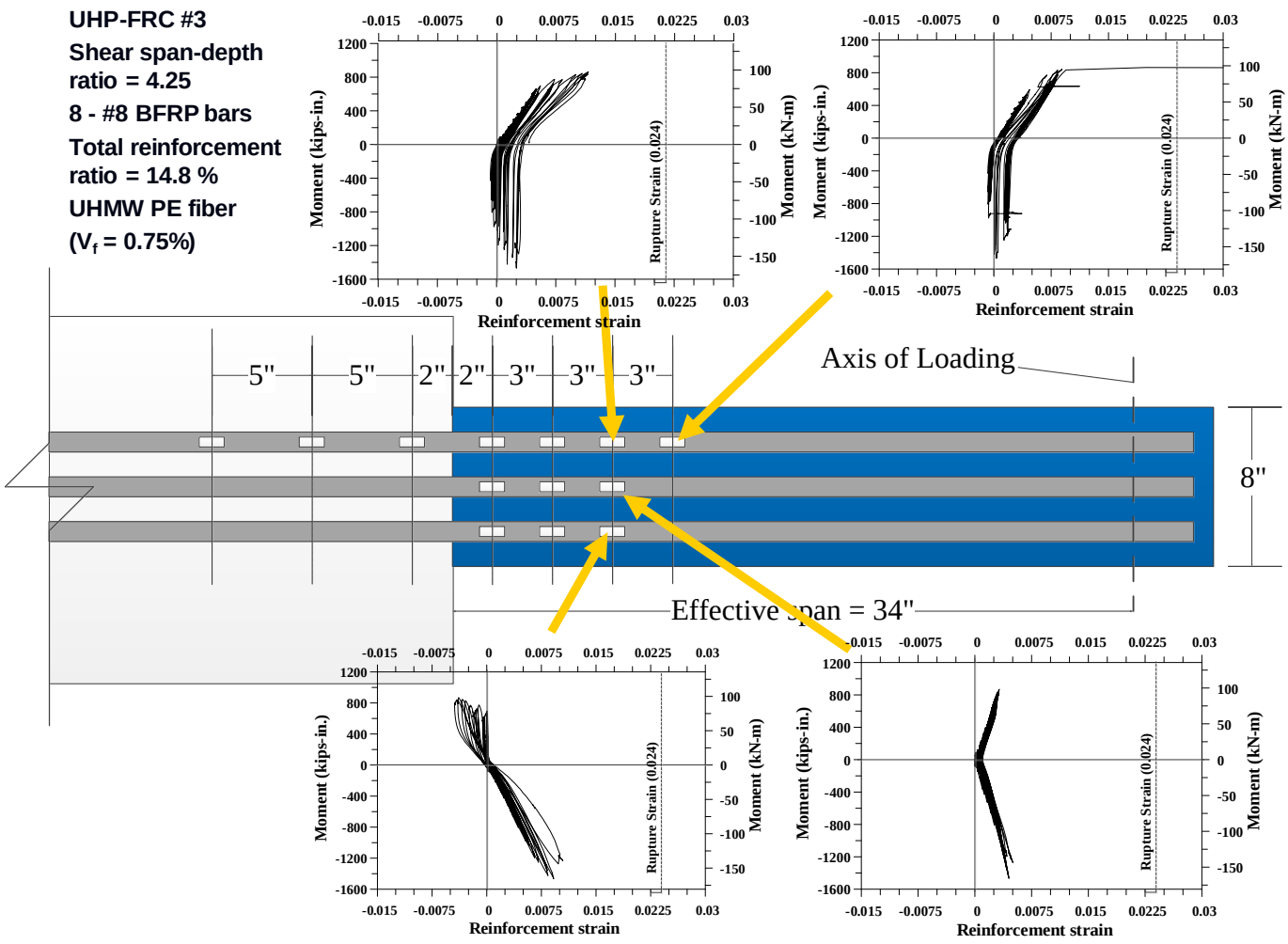

Figure 9- 44 Moment vs reinforcement strain for UHP-FRC #3

Figure 9- 45 UHP-FRC #3 at 0% drift

Figure 9- 46 UHP-FRC #3 at 0.2% drift

Figure 9- 47 UHP-FRC #3 at 0.25% drift

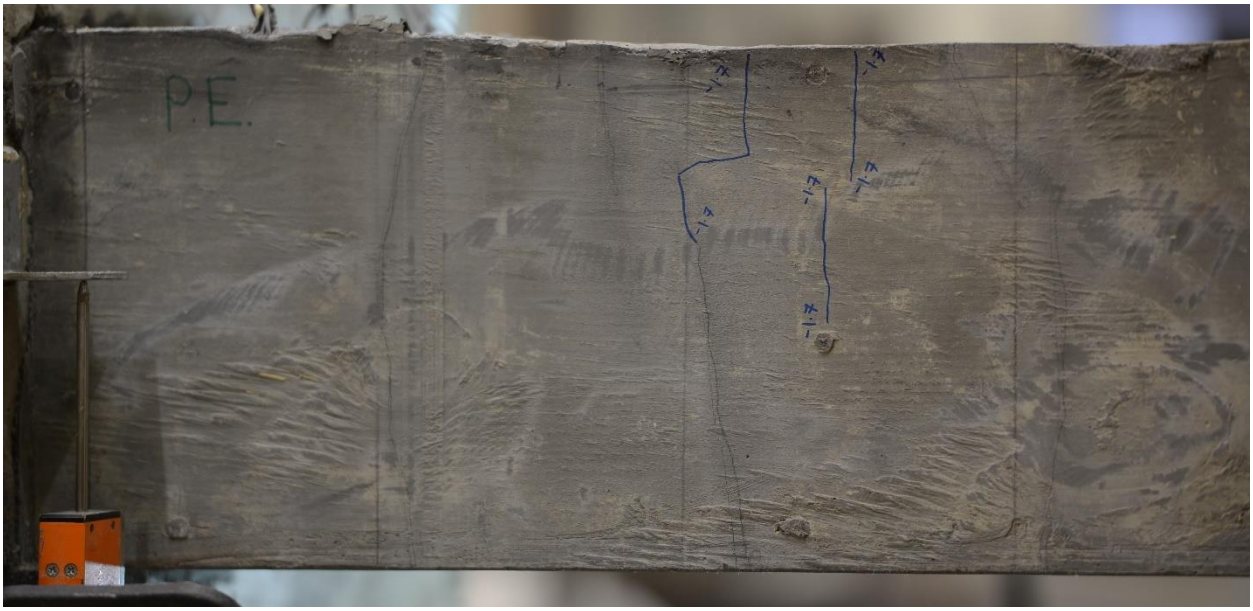

Figure 9- 48 UHP-FRC #3 at 0.35% drift

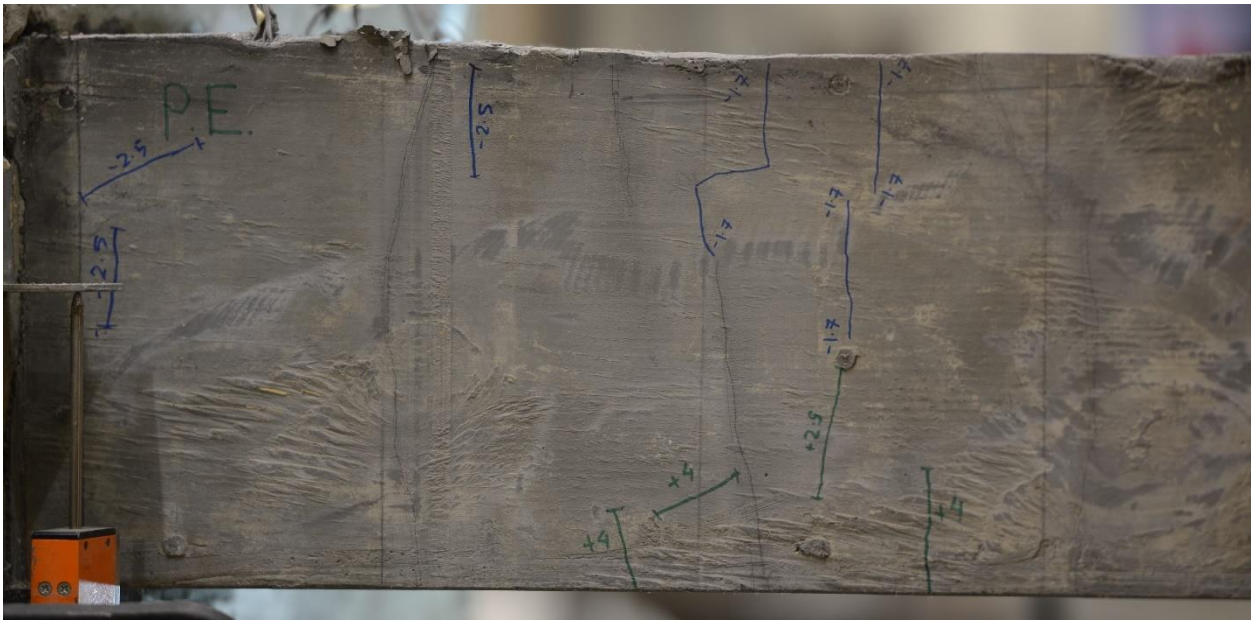

Figure 9- 49 UHP-FRC #3 at 0.5% drift

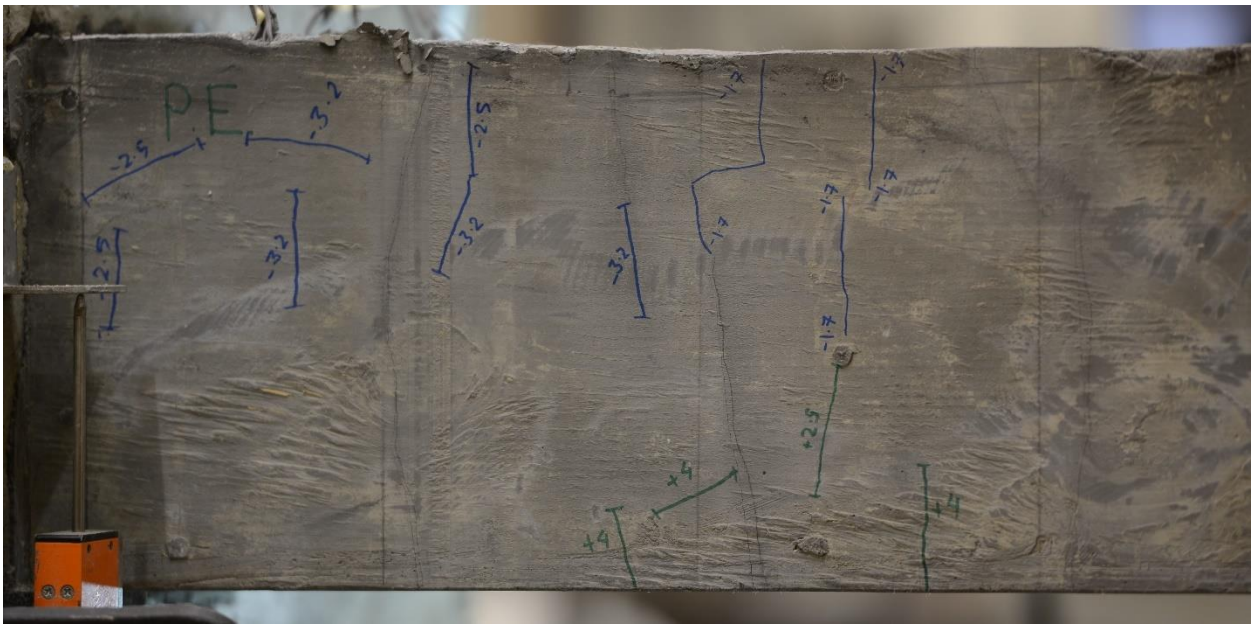

Figure 9- 50 UHP-FRC #3 at 0.75% drift

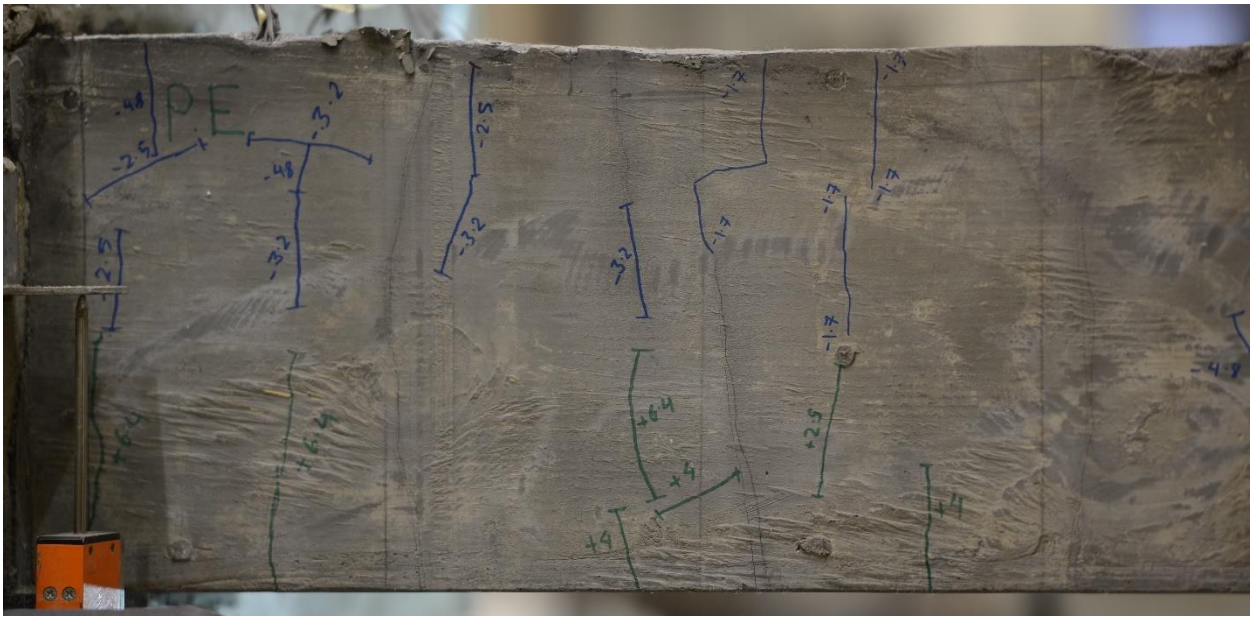

Figure 9- 51 UHP-FRC #3 at 1.0% drift

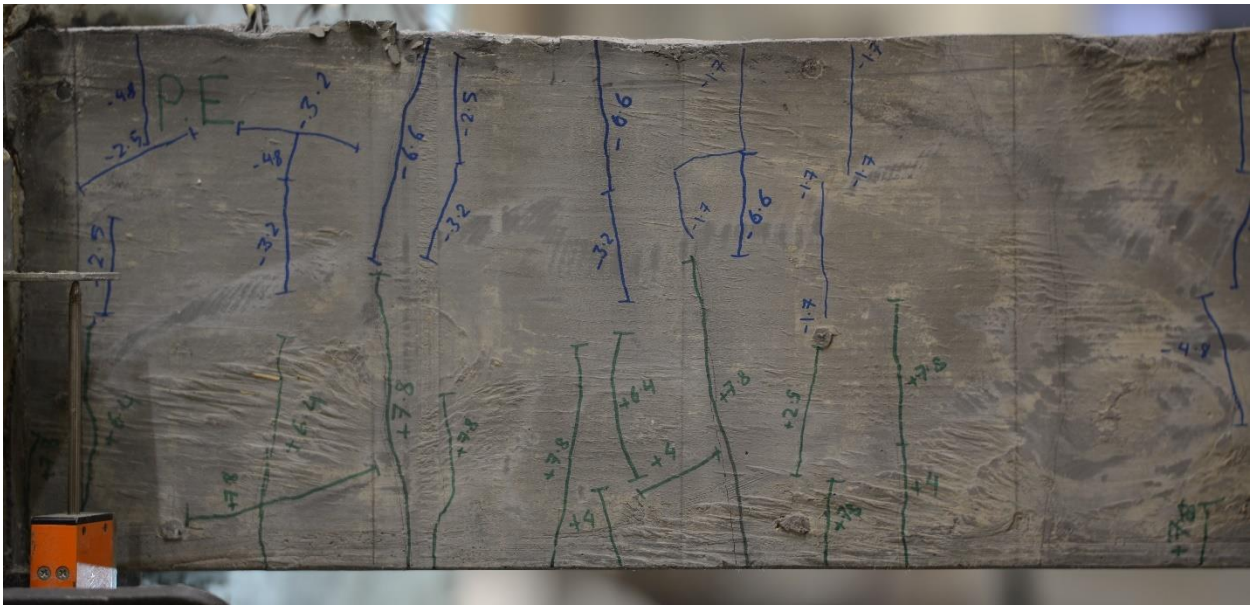

Figure 9- 52 UHP-FRC #3 at 1.4% drift

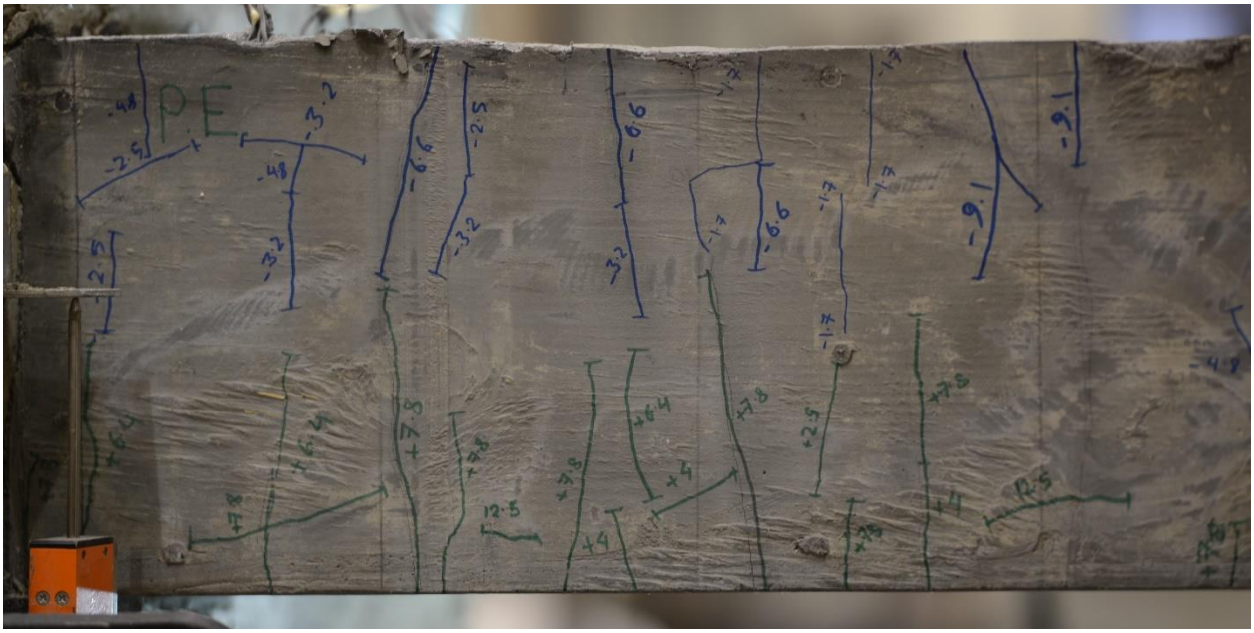

Figure 9- 53 UHP-FRC #3 at 1.75% drift

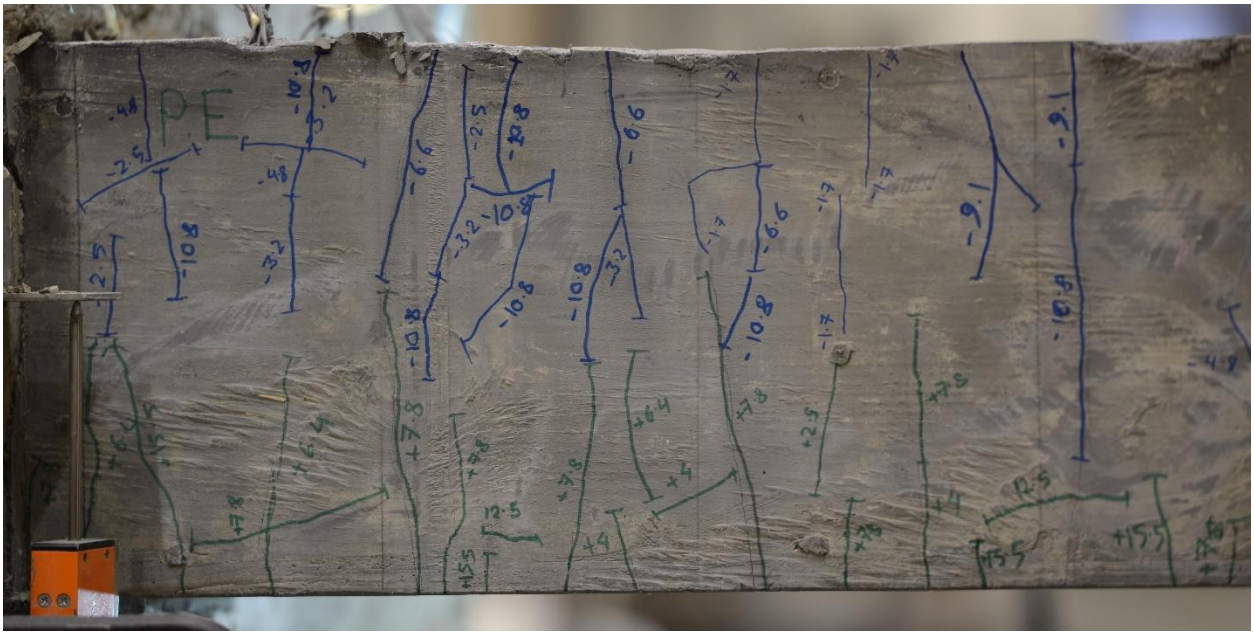

Figure 9- 54 UHP-FRC #3 at 2.2% drift

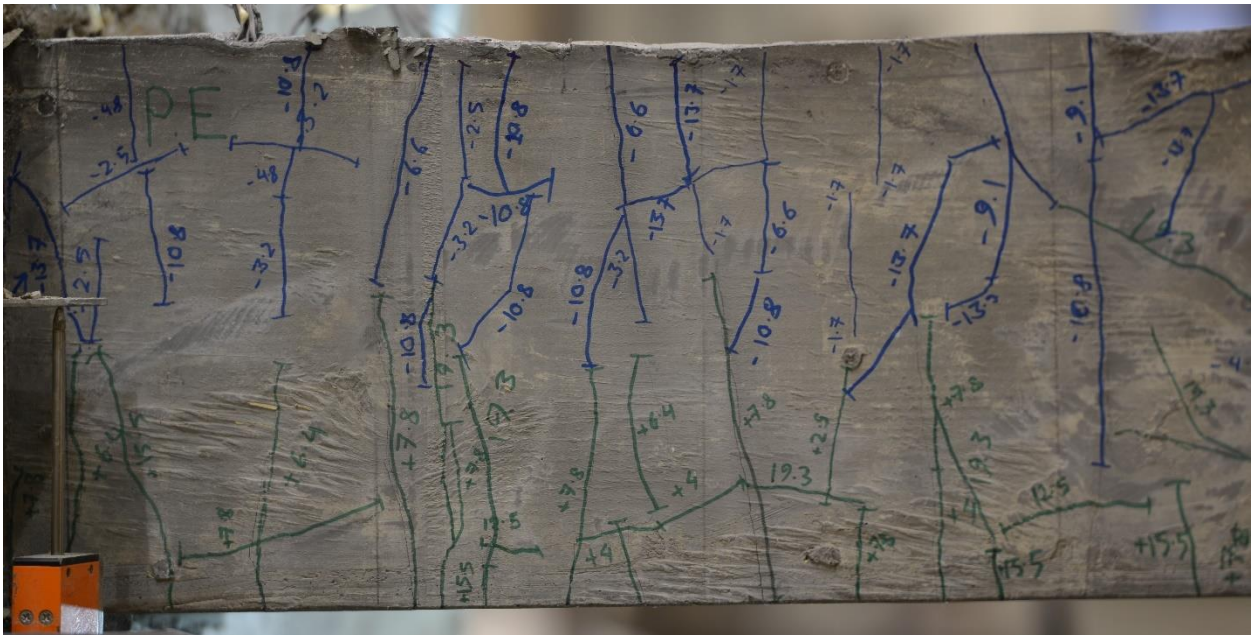

Figure 9- 55 UHP-FRC #3 at 2.75% drift

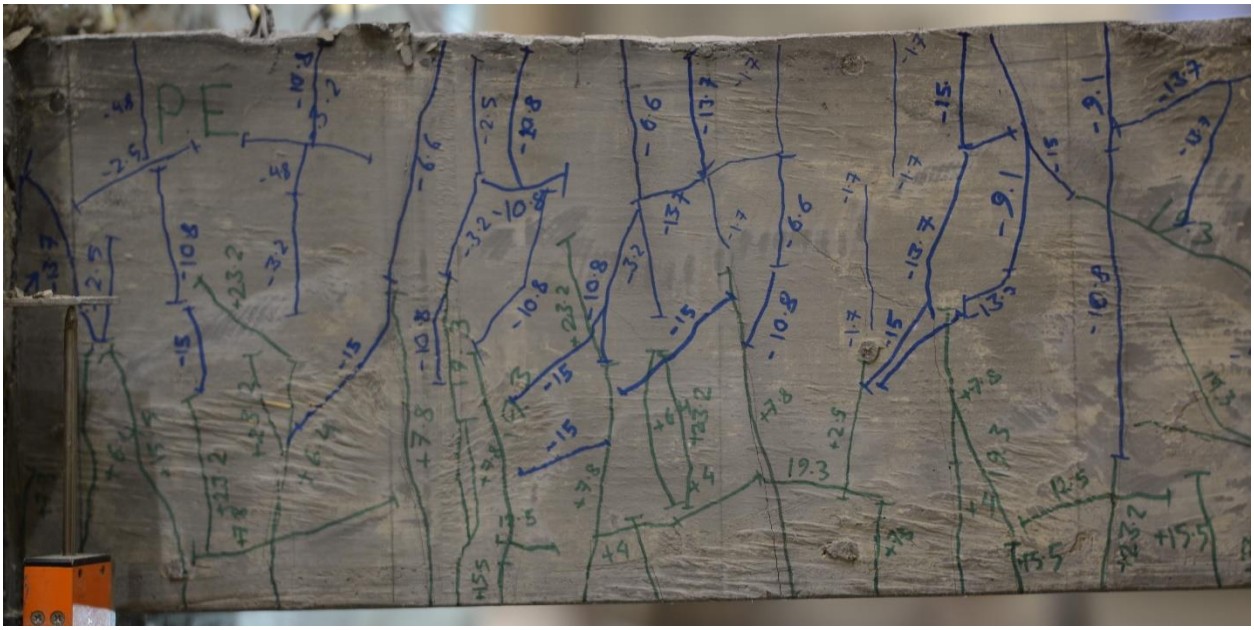

Figure 9- 56 UHP-FRC #3 at 3.5% drift

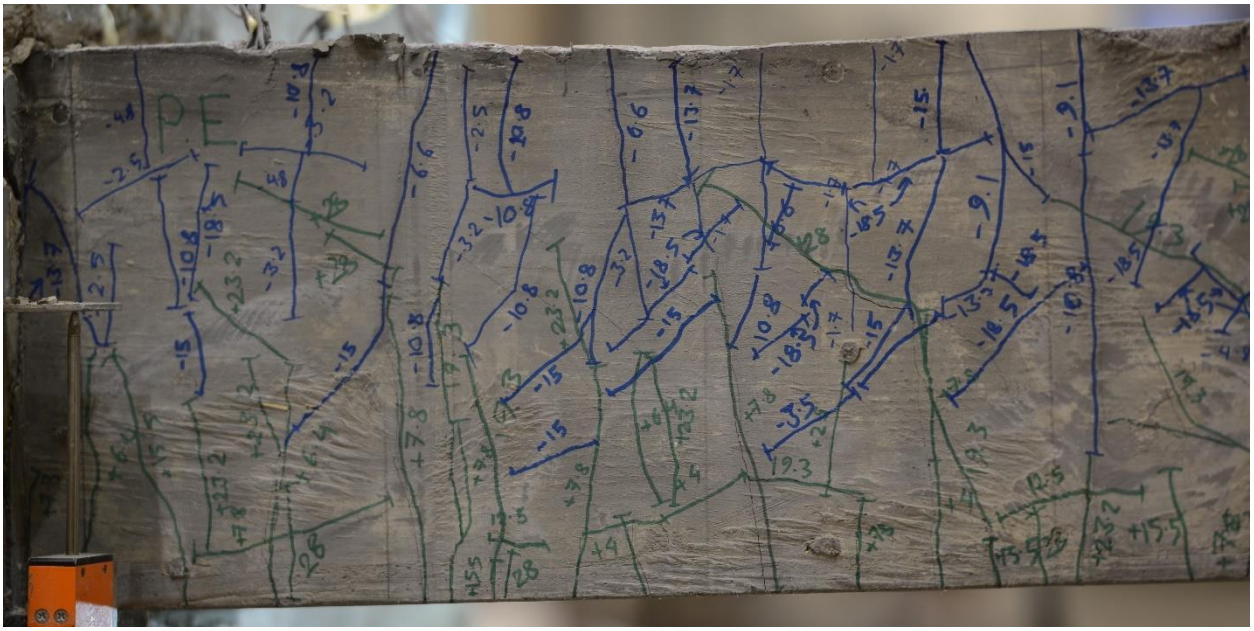

Figure 9- 57 UHP-FRC #3 at 4.0% drift

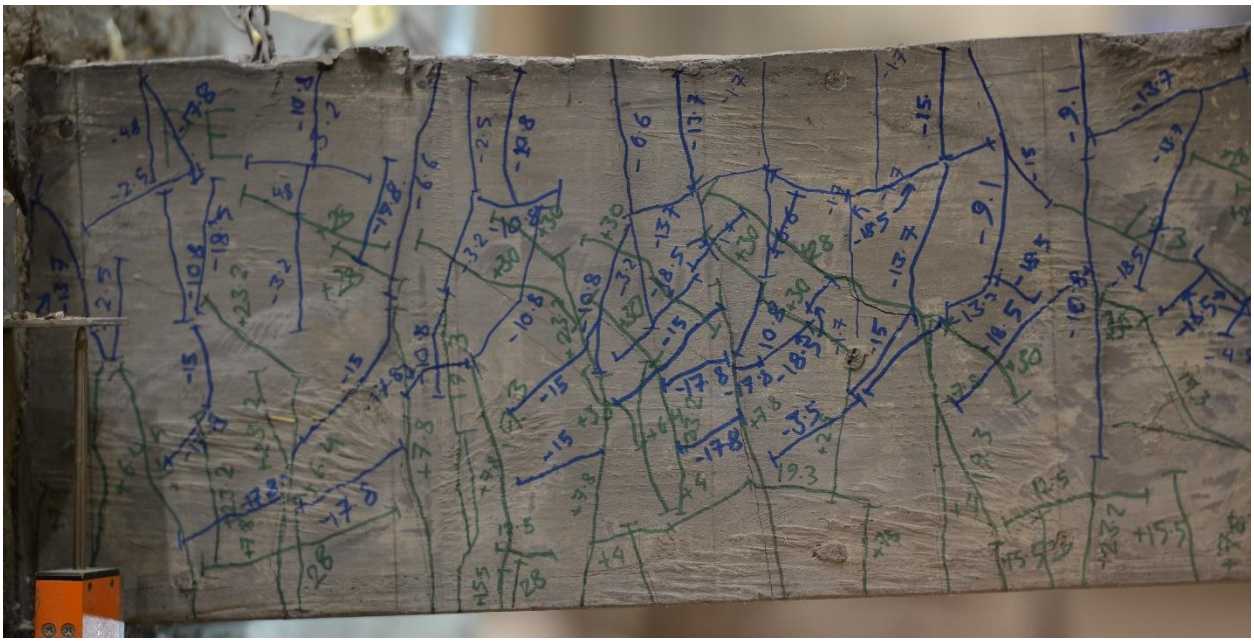

Figure 9- 58 UHP-FRC #3 at 5.0% drift

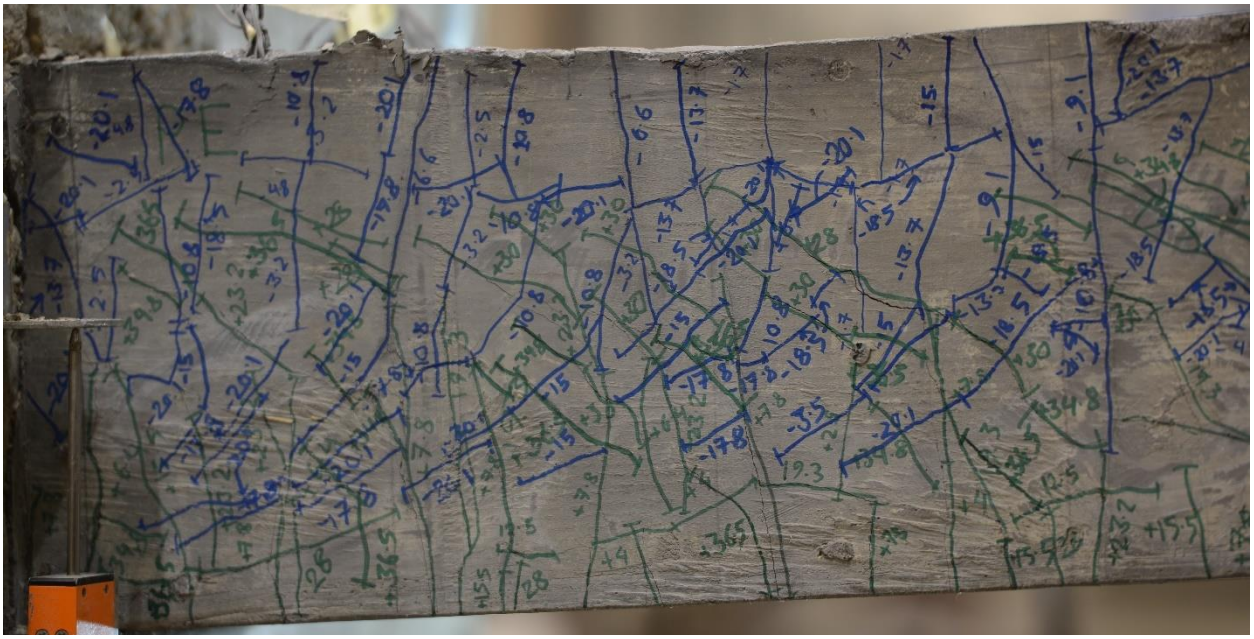

Figure 9- 59 UHP-FRC #3 at 6.0% drift

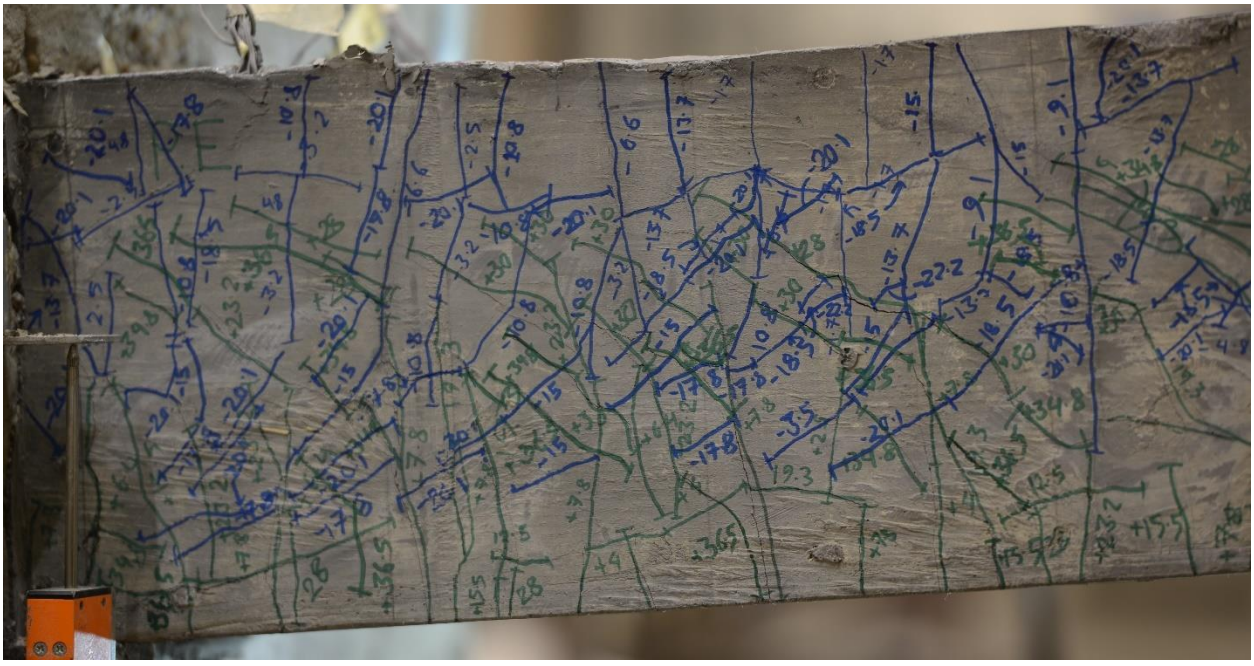

Figure 9- 60 UHP-FRC #3 at 7.0% drift

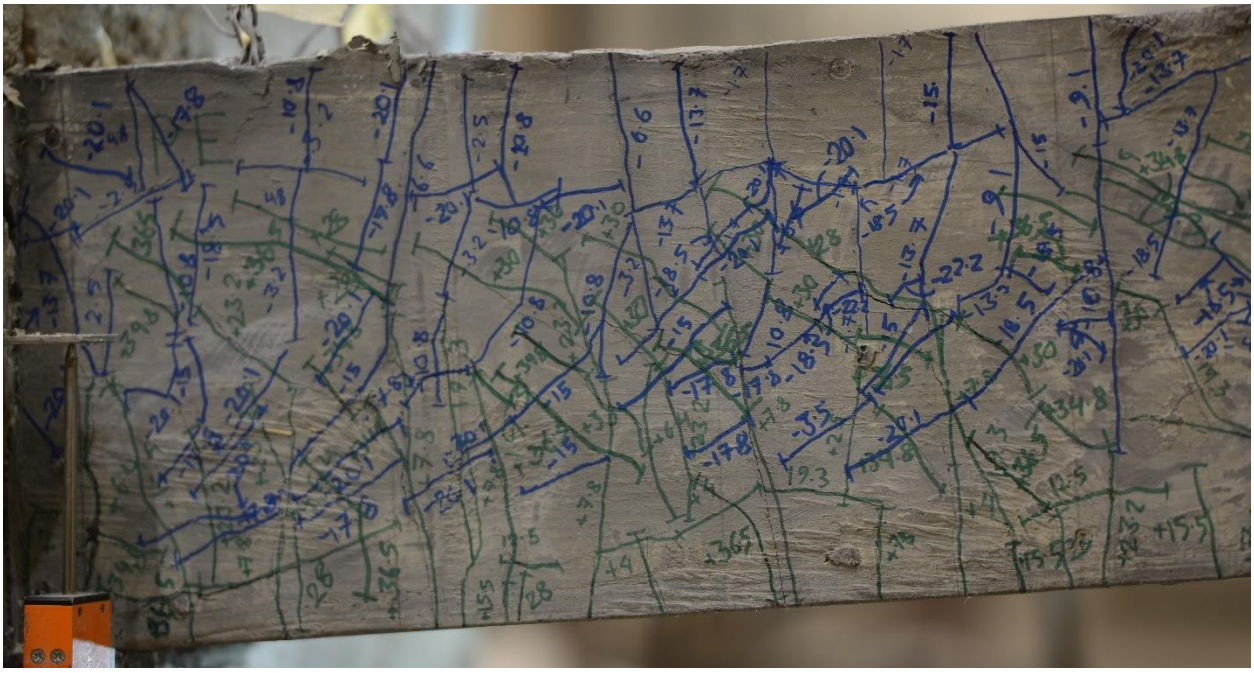

Figure 9- 61 UHP-FRC #3 at 8.0% drift

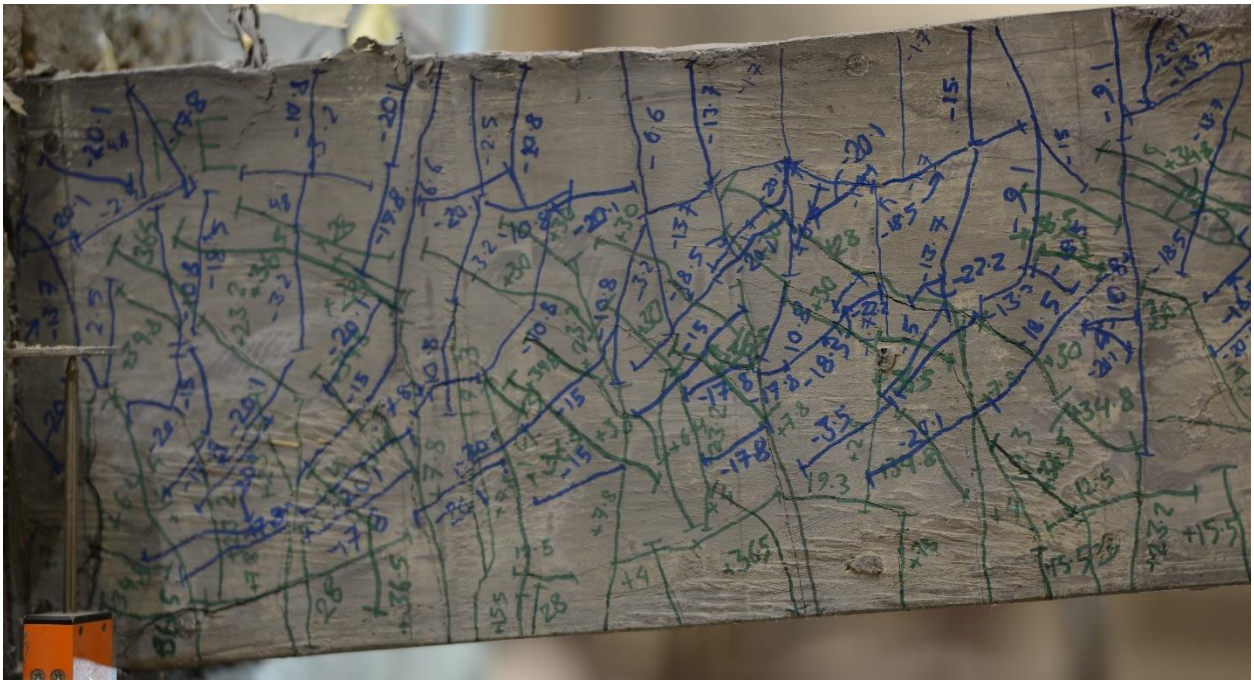

Figure 9- 62 UHP-FRC #3 at 9.0% drift

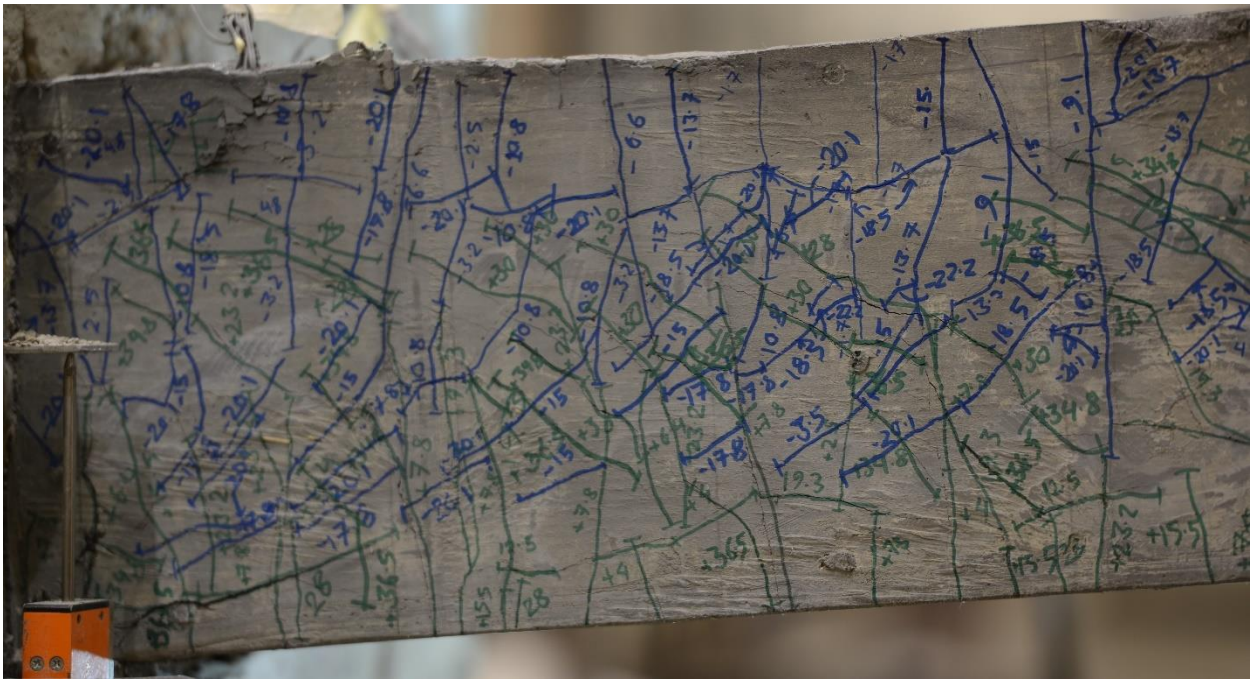

Figure 9- 63 UHP-FRC #3 at 10.0% drift

9.4 UHP-FRC #4

A maximum moment of 1430 kip-in. (162 kN-m) was recorded at a drift of 8%. Moment versus drift ratio relationship of beam UHP-FRC #4 showed large cyclic without significant damage to the UHP-FRC material. Stable cyclic behavior was observed up to 8% drift after which the moment started to decrease. From the *Figure 9-64*, it can be seen that there is minor residual deformation. Despite having a shear span to depth ratio of 4.25, flexural cracking was seen to be the governing mode of cracking during the test similar to specimen UHP-FRC #3. Flexural reinforcements remained elastic throughout the testing. Strain data of flexural reinforcements are presented from *Figure 9-65 to 9-66***.** The test pictures of the specimen for different values of drift can be viewed from *Figure 9-67 to 9-85*.

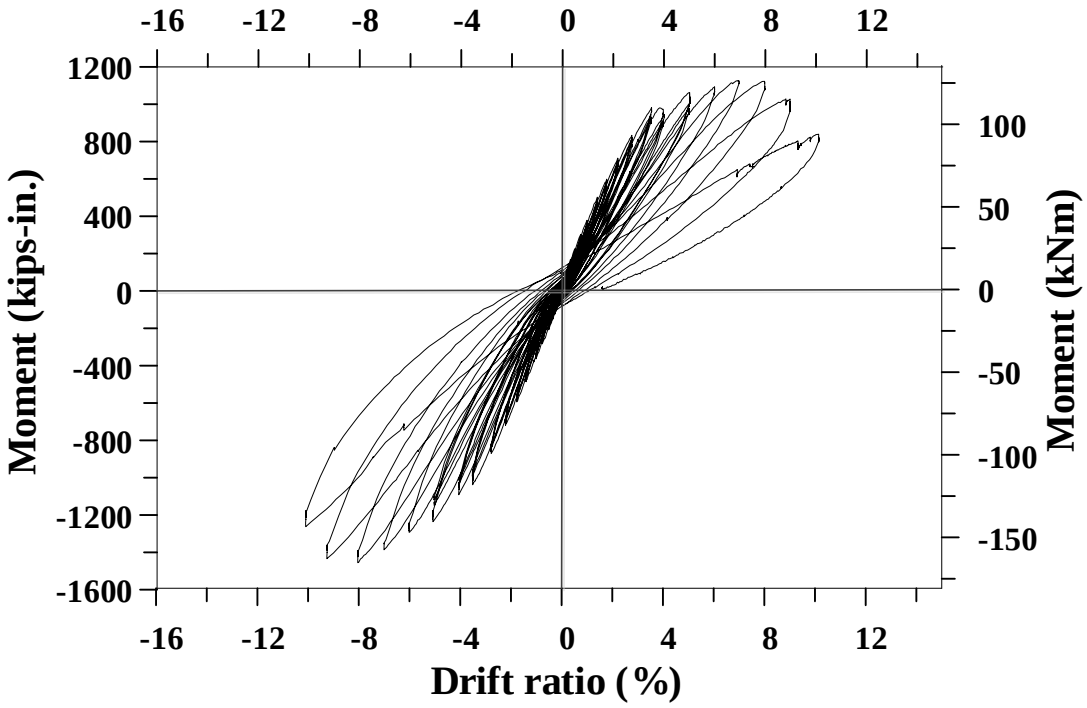

Figure 9- 64 Moment vs Drift ratio for UHP-FRC #4 with steel fibers (BFRP bars)

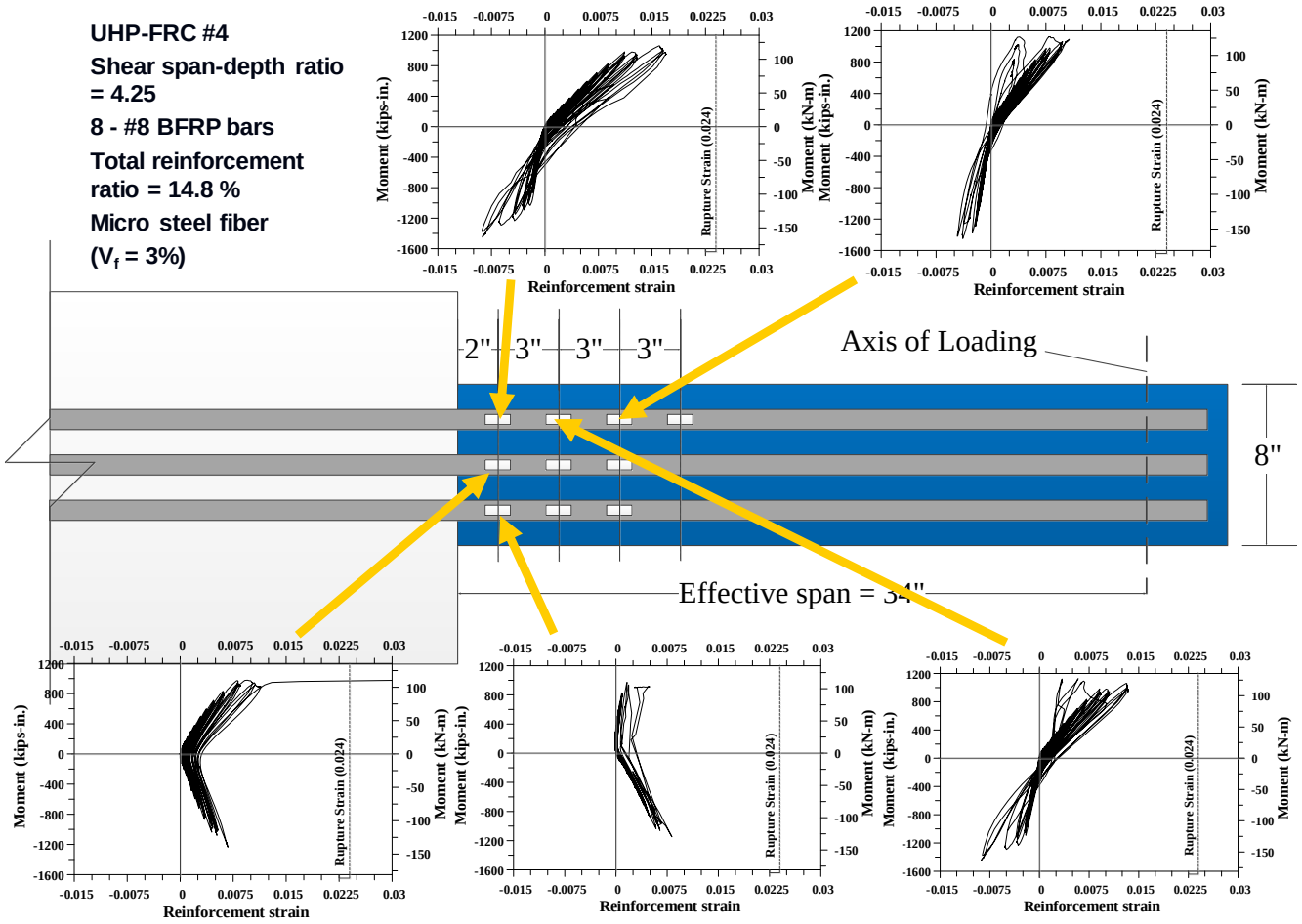

Figure 9- 65 Moment vs reinforcement strain for UHP-FRC #4

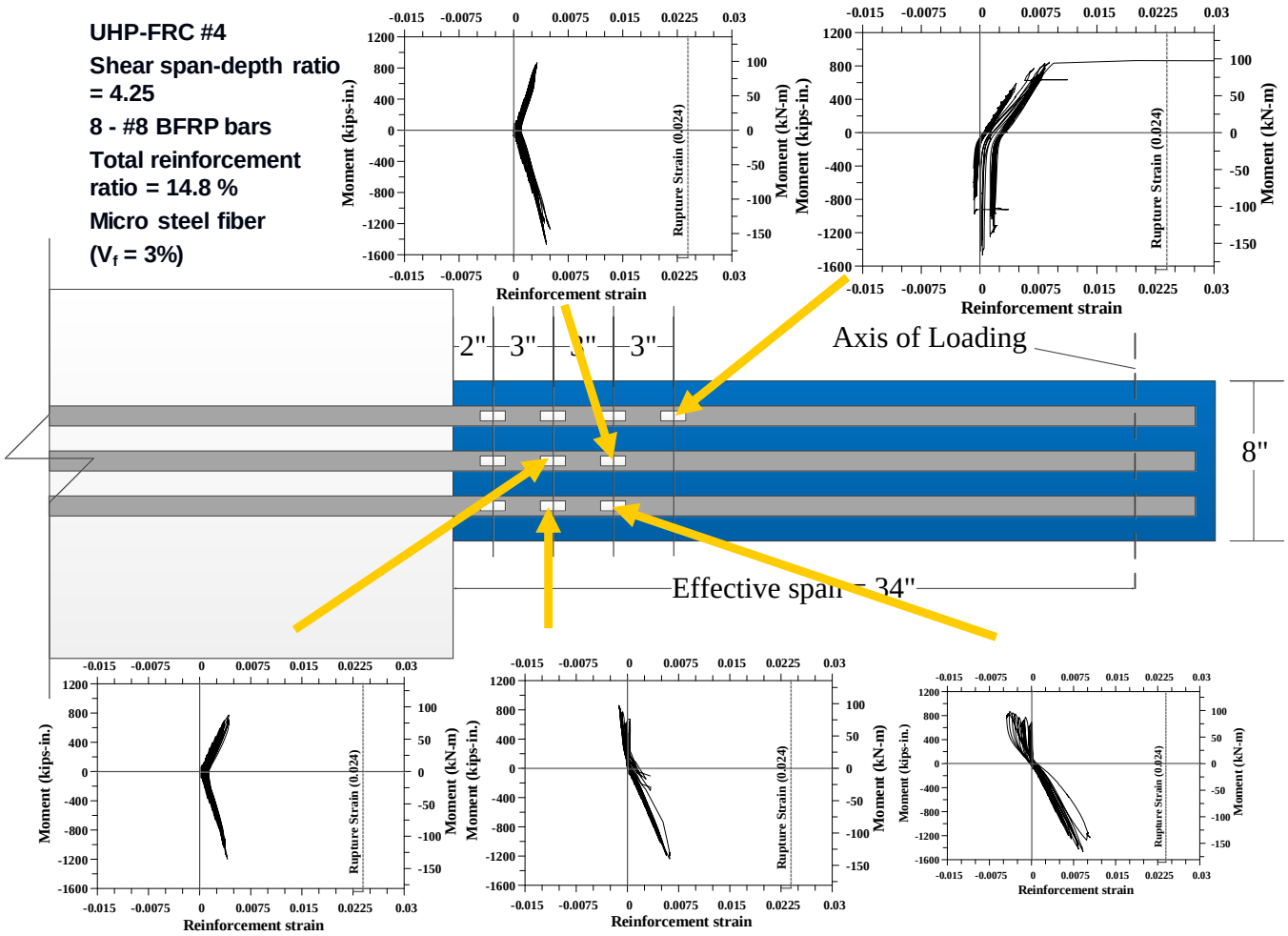

Figure 9- 66 Moment vs reinforcement strain for UHP-FRC #4

Figure 9- 67 UHP-FRC #4 at 0% drift

Figure 9- 68 UHP-FRC #4 at 0.2% drift

Figure 9- 69 UHP-FRC #4 at 0.25% drift

Figure 9- 70 UHP-FRC #4 at 0.35% drift

Figure 9- 71 UHP-FRC #4 at 0.5% drift

Figure 9- 72 UHP-FRC #4 at 0.75% drift

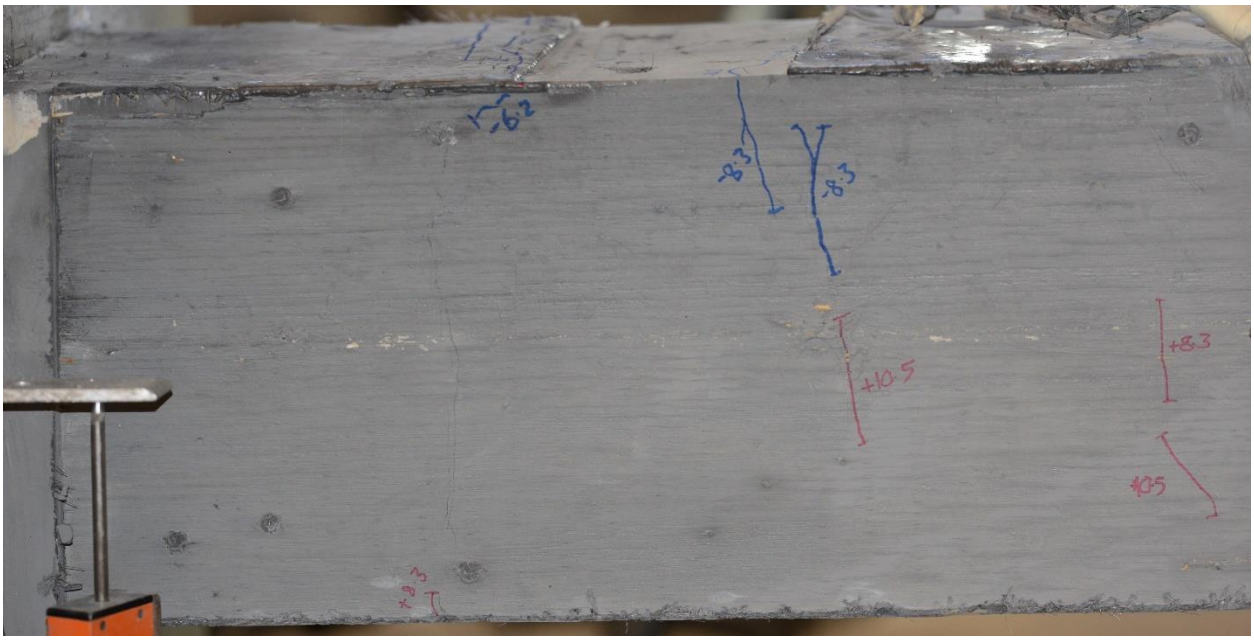

Figure 9- 73 UHP-FRC #4 at 1.0% drift

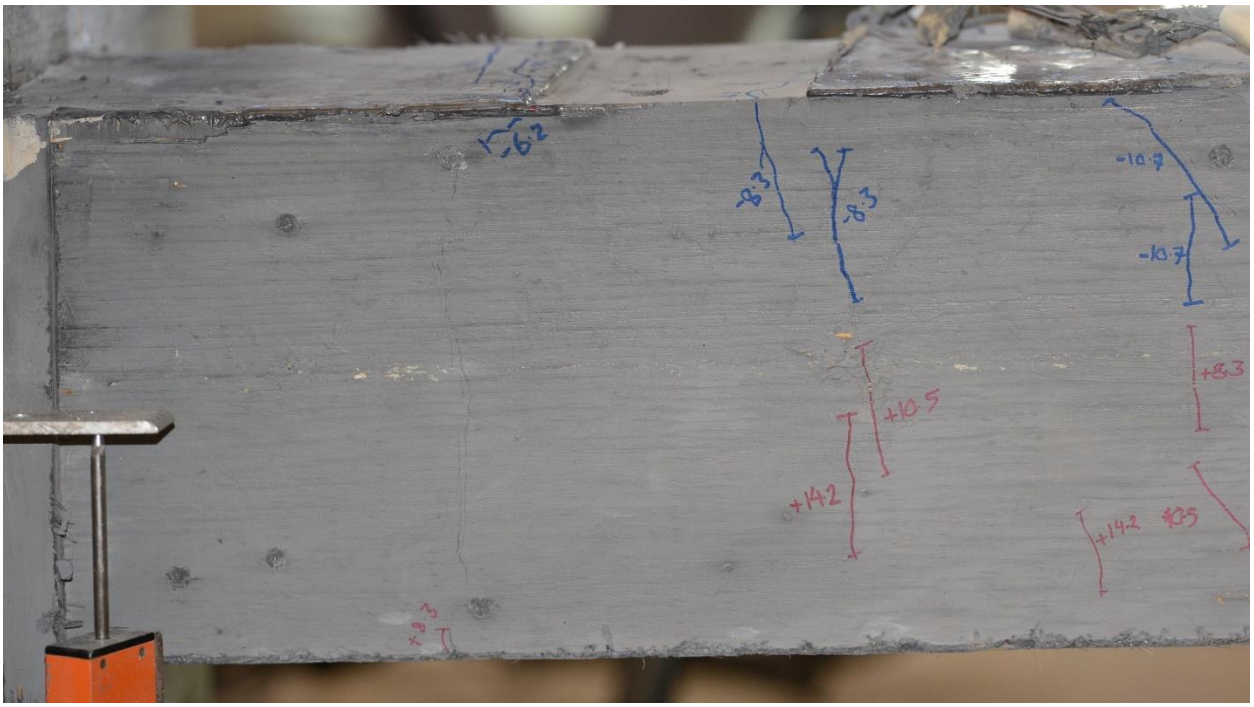

Figure 9- 74 UHP-FRC #4 at 1.4% drift

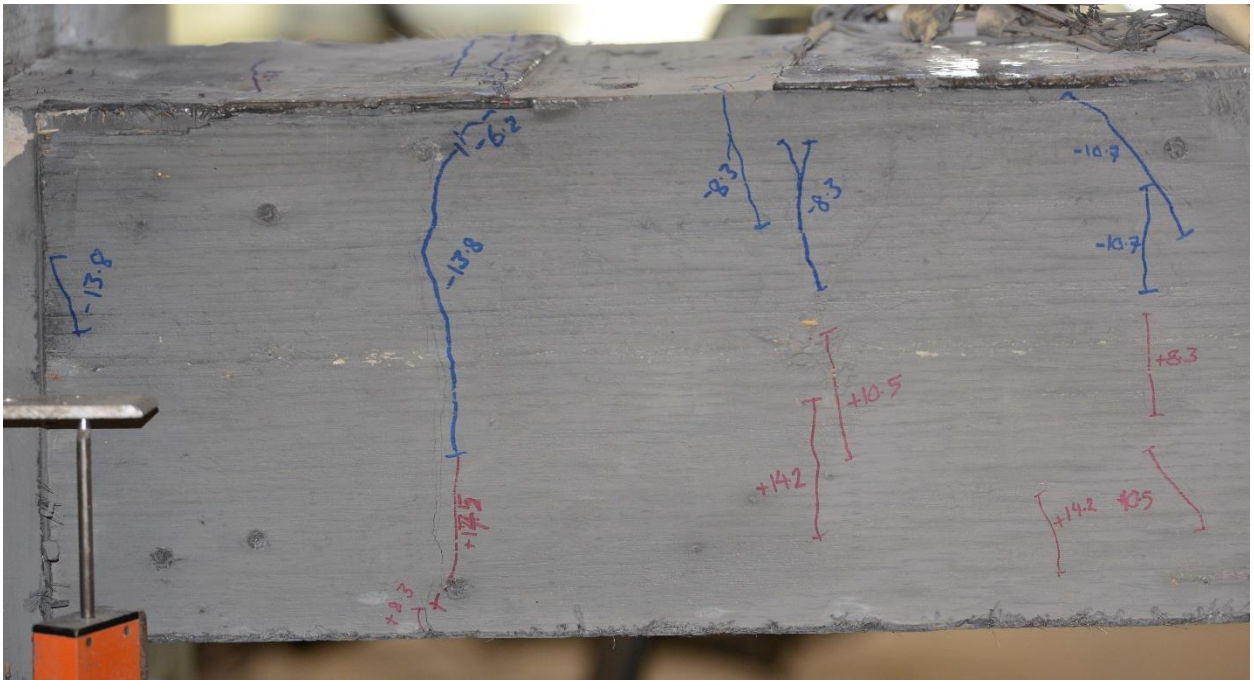

Figure 9- 75 UHP-FRC #4 at 1.75% drift

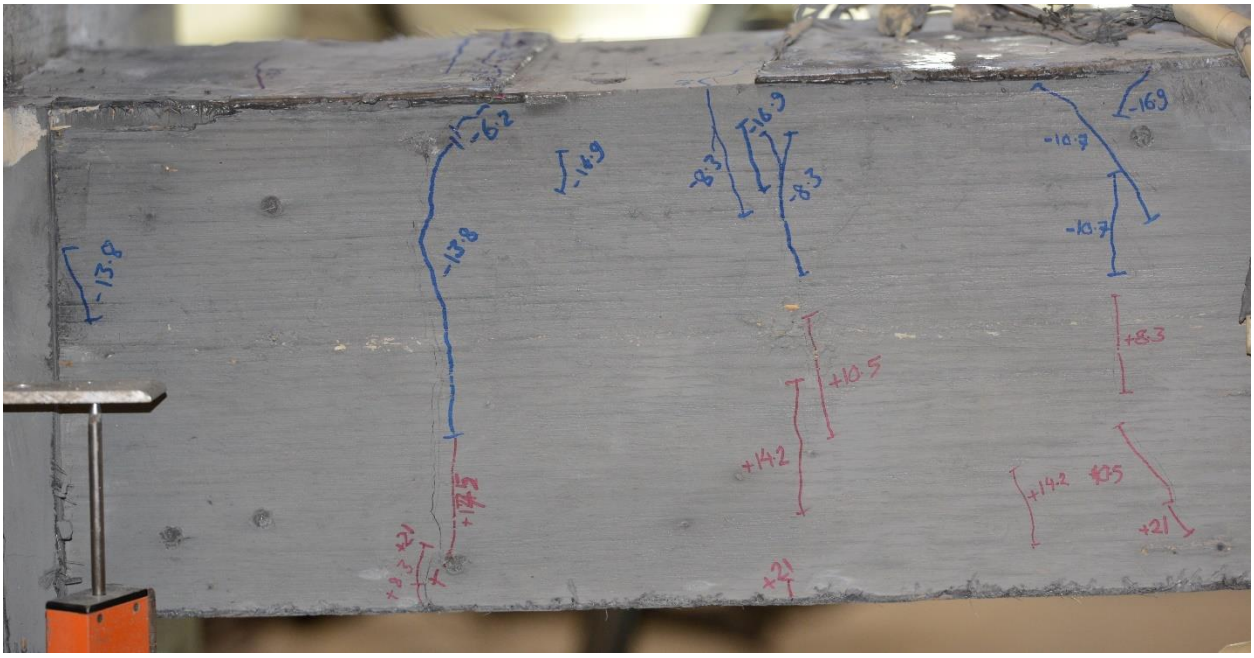

Figure 9- 76 UHP-FRC #4 at 2.2% drift

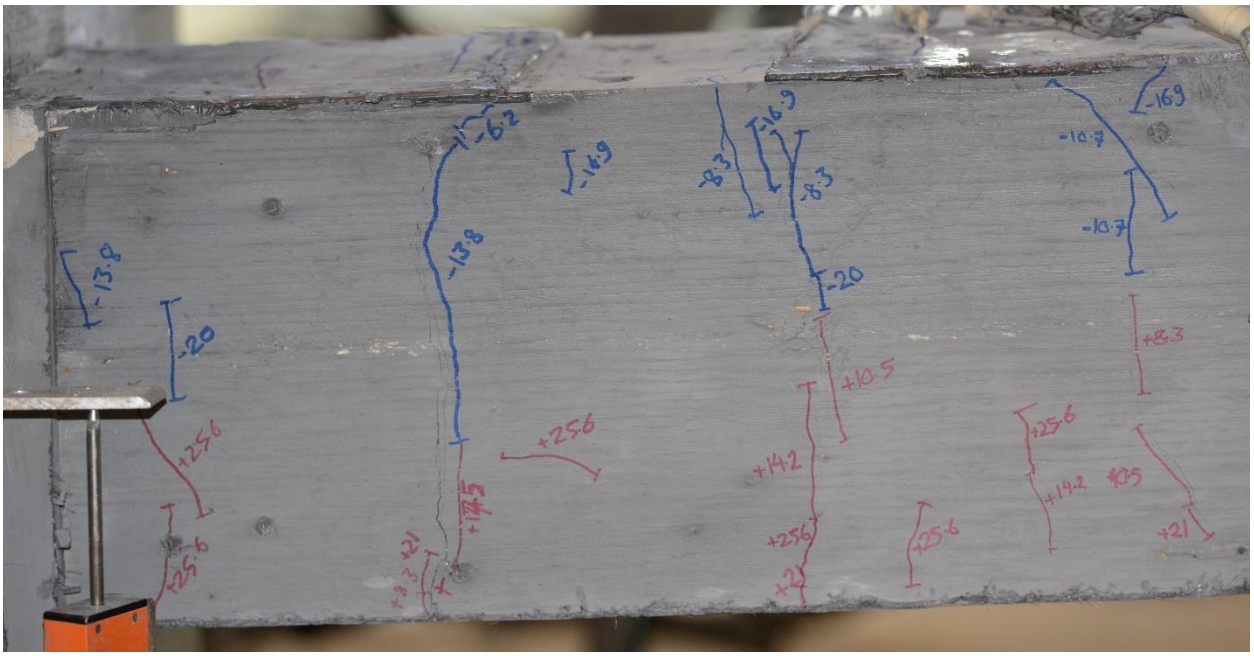

Figure 9- 77 UHP-FRC #4 at 2.75% drift

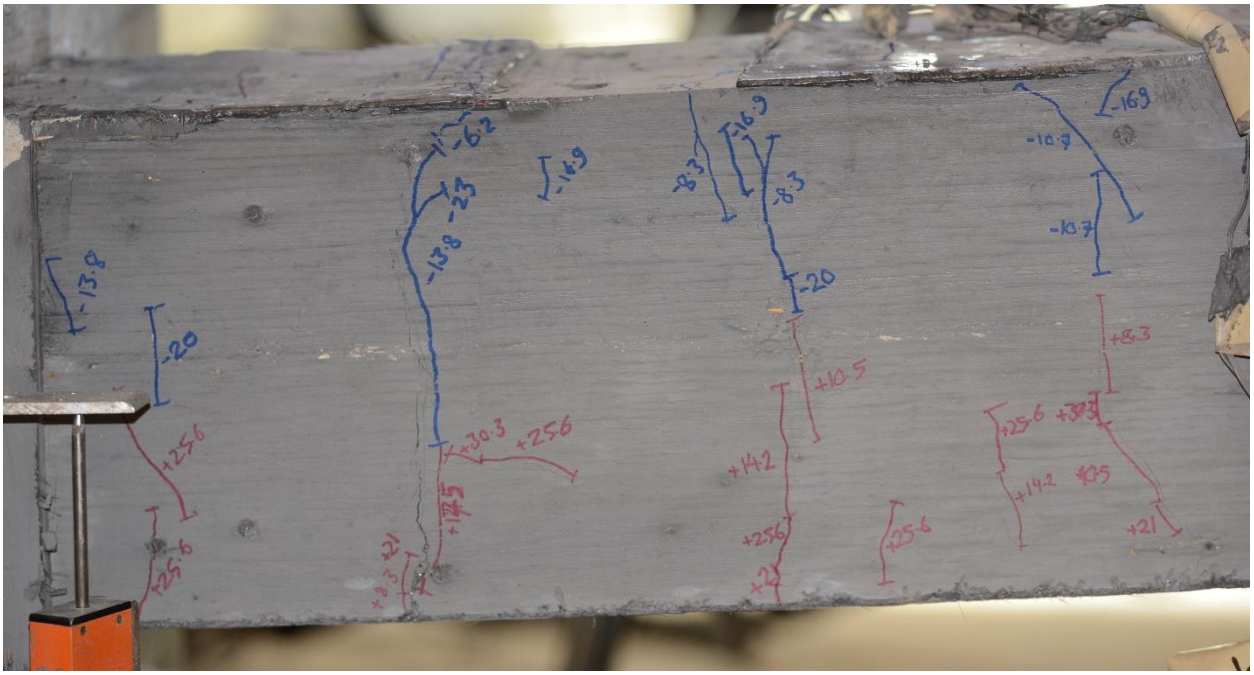

Figure 9- 78 UHP-FRC #4 at 3.5% drift

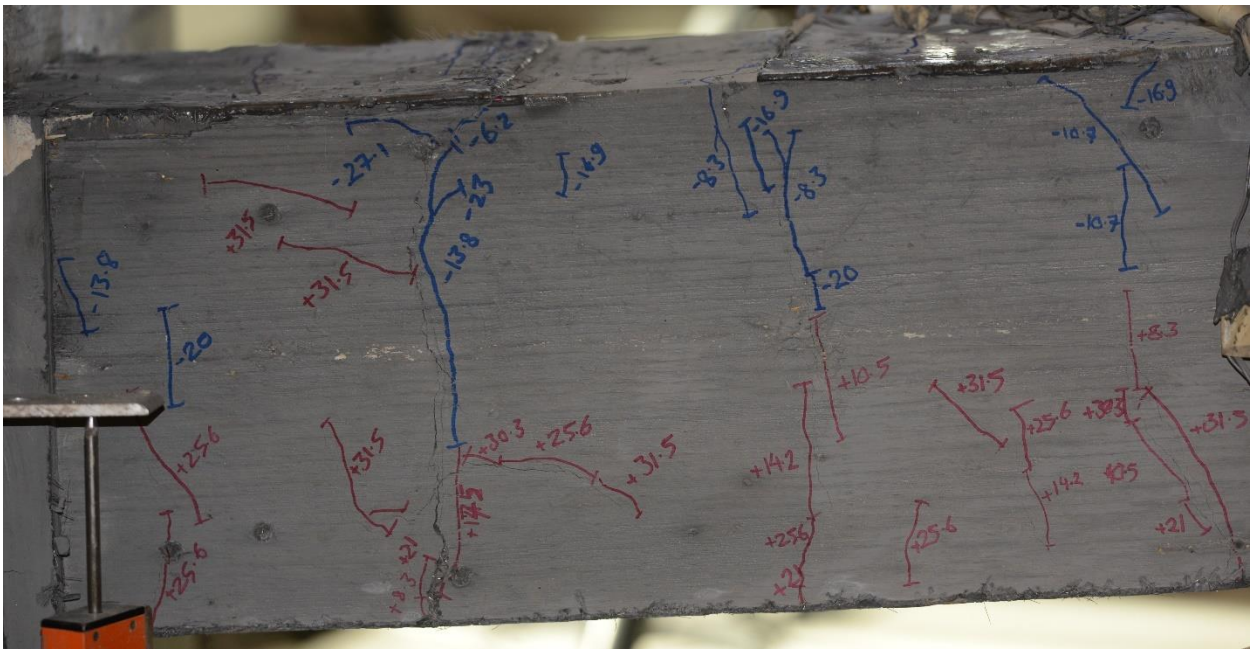

Figure 9- 79 UHP-FRC #4 at 4.0% drift

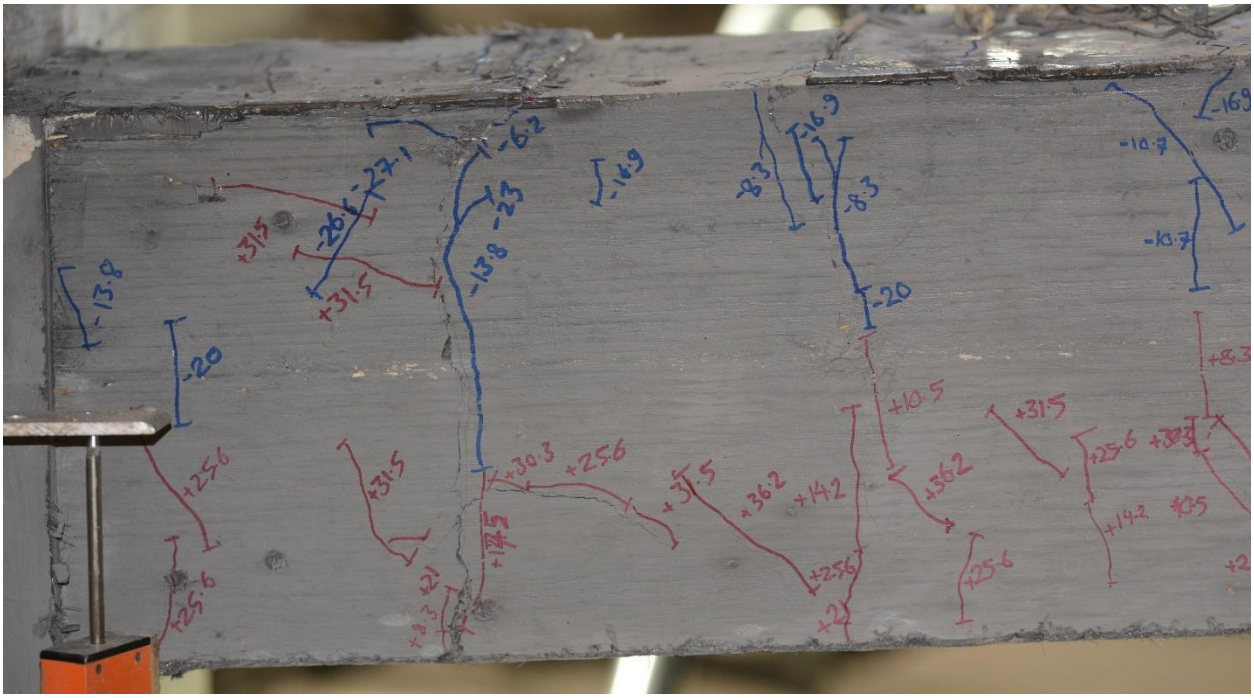

Figure 9- 80 UHP-FRC #4 at 5.0% drift

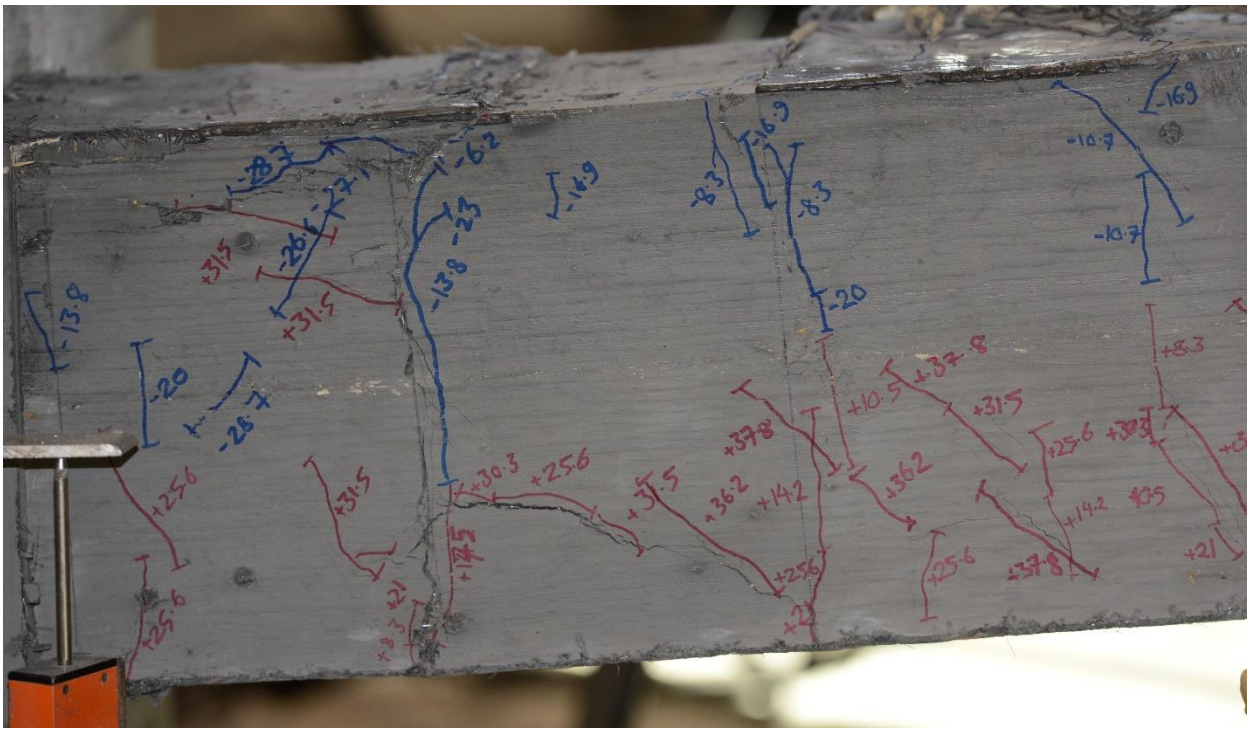

Figure 9- 81 UHP-FRC #4 at 6.0% drift

Figure 9- 82 UHP-FRC #4 at 7.0% drift

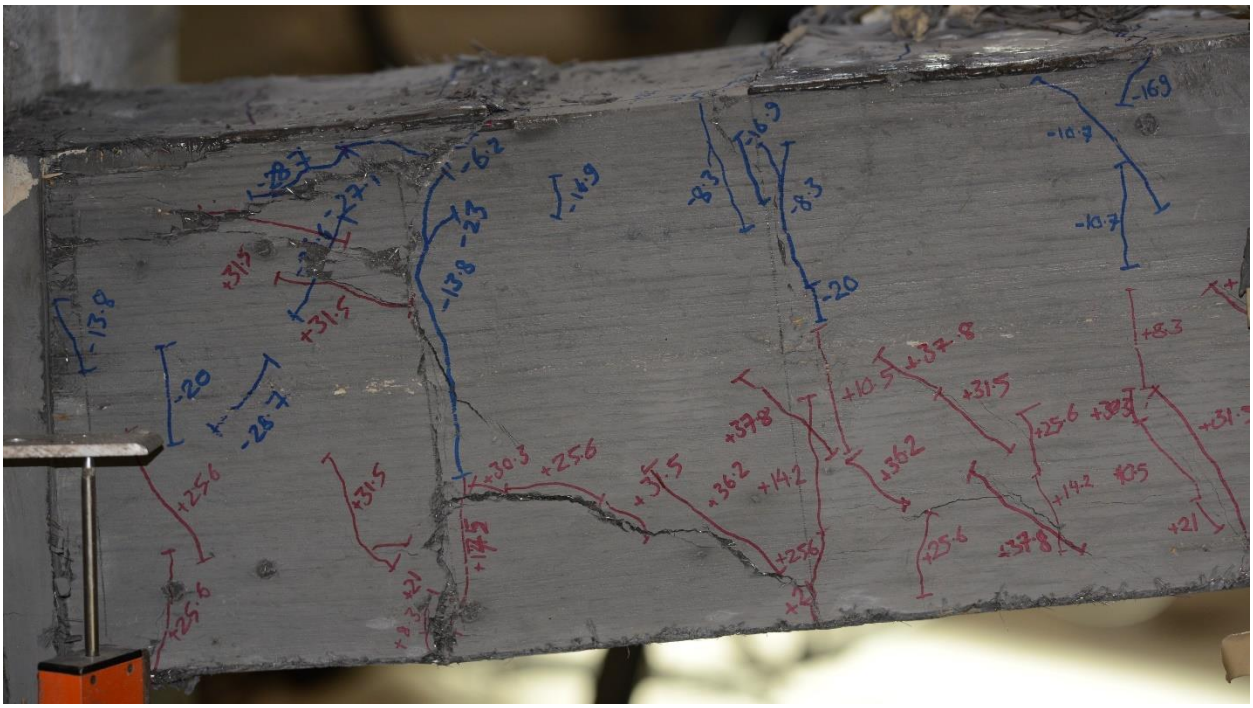

Figure 9- 83 UHP-FRC #4 at 8.0% drift

Figure 9- 84 UHP-FRC #4 at 9.0% drift

Figure 9- 85 UHP-FRC #4 at 10.0% drift

The test pictures of the specimens at different values of drift can be viewed from *Figure 9-86 to Figure 9-88*.

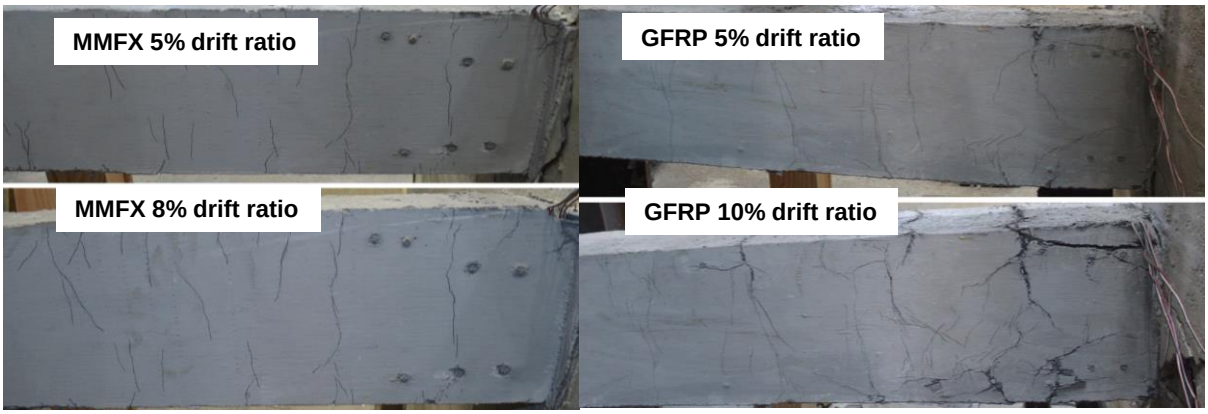

Figure 9- 86 Cracking in UHP-FRC #1 and #2 specimens with high-strength steel (left) and GFRP bars (right)

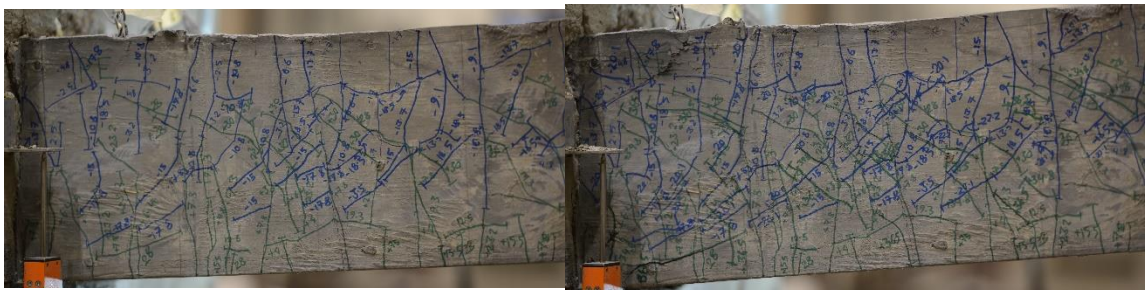

Figure 9- 87 Cracking in UHP-FRC #3 specimen (PE fibers) with BFRP bars at 5% drift(left) and 10% drift (right)

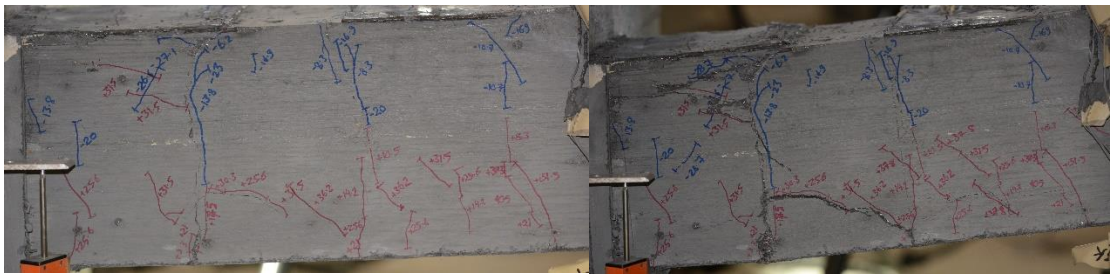

Figure 9- 88 Cracking in UHP-FRC #4 specimen (steel fibers) with BFRP bars at 5% drift (left) and 9% drift (right)

A comparison between the recorded moment and the designed nominal moment is presented in Table 9-1 below.

Table 9- 1 Comparison between the calculated design nominal moment and the maximum recorded moment values

Specimen	Design nominal moment kip-in. (kN-m)	Maximum moment recorded kip-in. (kN-m)	Remarks
UHP-FRC #1	792 (89)	840 (95)	6% higher
UHP-FRC #2	1028 (116)	1050 (119)	2% higher
UHP-FRC #3	1271 (144)	1470 (166)	15% higher
UHP-FRC #4	1336 (151)	1430 (162)	7% higher

Chapter 10

Part II: Summary, Conclusions and Recommendations

10.1 Summary

The research objective was to develop highly sustainable and efficient reinforced concrete structural members for future infrastructure by utilizing emerging high-performance materials. These materials include ultra-high-performance fiber-reinforced concrete (UHP-FRC) and corrosion resistant high-strength fiber-reinforced polymer (FRP) bars and high-strength steel rebars (MMFX). The new type of UHP-FRC flexural members were designed based on a newly developed design concept, ductile-concrete strong-reinforcement (DCSR), in which the ductile component was the concrete and the elastic component was the reinforcement. The advantages of using such design was to fully utilize the high compressive strength and ductility of UHP-FRC and minimize the cracking by reducing the elongation of reinforcement, thereby maintaining high stiffness of the members. Four specimens were tested under reversed cyclic loading.

The results showed that the UHP-FRC beams have much large stiffness and strength than conventional reinforced concrete members and can sustain very large drift ratios under reversed cyclic loading without major damage in the material.

Because of the DCSR design concept, the reinforcement remains elastic thus providing a self-centering capability. This allows a very sustainable and resilient future structures subjected to extreme loadings.

10.2 Conclusion

This research investigated a new type of structural members made with ultra-high-performance materials including ultra-high-performance fiber-reinforced concrete (UHP-FRC), high-strength noncorrosive FRP rebars, and high-strength high corrosion resistant MMFX steel rebars.

1. The proposed flexural members can also sustain very large cyclic displacements without major damage in the UHP-FRC material, which provided ample shear strength and confinement to the reinforcement throughout the testing.
2. Even with the high amount of reinforcement, UHP-FRC's superior ductility provided a very stable cyclic behavior up to very large drift ratios.

3. The specimens also exhibited self-centering ability, which considerably reduces the residual displacement after being subject to large displacements.
4. The test results also showed that the high damage resistant and self-centering characteristics of the proposed UHP-FRC columns can provide excellent resilience for future infrastructures.

10.3 Recommendation

The following is the recommendation from this study.

In the UHP-FRC specimens with BFRP stirrups, shrinkage cracks were observed at the location of the stirrups before the loading (*Figure 10-1*). Further testing resulted in the increase of the preformed cracks. Further research is required to study the effect of BFRP stirrups with UHP-FRC structures.

Figure 10- 1 Shrinkage cracks developed at the location of the BFRP stirrups prior to testing

References

AASHTO Guide for Design of Pavement Structures, 1993, (vol. 1), ISBN-13: 978-1560510550. American Association of State Highway and Transportation Officials, Washington, D.C., 1993

AASHTO Guide for Design of Pavement Structures. American Association of State Highway and Transportation Officials, 1993, Washington, D.C., pp. III-59 – III-78.

AASHTO. (2017). LRFD Bridge Design Specifications. 7th edition, American Association of State Highway and Transportation Officials (AASHTO), Washington, D.C.

ACI Committee 318, 2013, "Building Code Requirements for Structural Concrete (ACI 318-14) and Commentary (ACI 318R-14)," American Concrete Institute, Farmington Hills, MI, 519 pp.

ACI Committee 318, 2013, "Building Code Requirements for Structural Concrete (ACI 318-14) and Commentary (ACI 318R-14)," American Concrete Institute, Farmington Hills, MI, 519 pp.

ACI Committee 318, 2014, “Building Code Requirements for Reinforced Concrete and Commentary (ACI318-14/ACI318R-14),” American Concrete Institute Farmington Hills, MI.

ACI Committee 440, 2015, “ACI 440.1R-15Guide for the Design and Construction of Structural Concrete Reinforced with Fiber-Reinforced Polymer Bars”, American Concrete Institute, Farmington Hills, MI

AFGC, 2013, “Béton fibrés à ultra-hautes performances, (Ultra high performance fiber-reinforced concretes)”, recommendations, France.

Aghdasi, P., Heid A. E., and Chao, S.-H. ,2016, "Developing Ultra-High-Performance Fiber-Reinforced Concrete for Large-Scale Structural Applications,” ACI Materials Journal, V. 113, No. 5, September-October 2016, pp. 559-570.

Aghdasi, P.; Palacios, G.; Heid, A.E.; and Chao, S.-H., 2015, 'Mechanical properties of a highly flowable ultra-high-performance fiber-reinforced concrete mixture considering large-size effects,' High Performance Fiber Reinforced Cement Composites (HPFRCC 7), International Workshop, Stuttgart, Germany.

Ahlborn, T., Harris, D., Misson, D., and Peuse, E. , 2011, “Characterization of Strength and Durability of Ultra-High-Performance Concrete Under Variable Curing Conditions,” Transportation Research

Record: Journal of the Transportation Research Board, No. 2251, 2011, Transportation Research Board of the National Academies, Washington, D.C., pp. 68–75. DOI: 10.3141/2251-07.

American Concrete Pavement Association. Guidelines for Full-Depth Repair. Technical Bulletin TB002.0[4]2P. ACPA, Skokie, IL.

ASTM, 2013, “Standard Test Method for Bond Strength of Epoxy-Resin Systems Used with Concrete by Slant Shear1.” C882/C882M − 13a, ASTM International, 4 pp.

Buitelaar, P., 2004, “Heavy Reinforced Ultra High-Performance Concrete,” Proceedings of the International Symposium on Ultra High-Performance Concrete, Ed., Schmidt, M., Fehling, E., and Geisenhanslüke, C., Kassel University Press, Kassel, Germany, pp. 25–35.

Chao, S. ,2018, Use of Ultra-High-Performance Fiber-Reinforced Concrete (UHP-FRC) for Fast and Sustainable Repair of Pavements Use of Ultra-High-Performance Fiber- Reinforced Concrete (UHP-FRC) for Fast and Sustainable Repair of Pavements. Baton Rouge, LA.

Chao, S.-H., October 3rd, 2008, “Achieving “Green” Concrete through the Use of High-Performance Fiber Reinforced Concrete," ASCE Texas Section Fall Meeting, Addison, Dallas.

Concrete Pavement Rehabilitation and Preservation Treatments. TechBrief. No. FHWA-IF-06-005. FHWA, , 2005, US Department of Transportation.

Davila, R. S., 2007, “Recommendations for the design of ultra-high-performance concrete structures.” Doctoral dissertation, Massachusetts Institute of Technology.

Federal Highway Administration (FHWA), 2011, “Ultra-High-Performance Concrete,” TechNote, FHWA-HRT-11-038, Federal Highway Administration, 8 pages.

Fehling, E.; Bunje, K.; and Leutbecher, T., 2004, “Design relevant properties of hardened Ultra High Performance Concrete,” Proceedings of the International Symposium on Ultra High Performance Concrete, University of Kassel, pp. 327-338, Kassel, Germany.

Glotzbach, C., Fröhlich, S., and Piotrowski, S., Kassel University Press, Kassel, Germany, 2012, pp. 937–944.

Gordian, 2019, RSMeans Heavy Construction Costs Book. Gordian, Rockland, MA.

Graybeal, B., and Tanesi, J., 2007, “Durability of an Ultra-High-Performance Concrete,” Journal of Materials in Civil Engineering, Vol. 19, No. 10, pp. 848-854.

Hadl, P., Pietra R. D., Hoang, K. H., Pilch, E., Tue, N. V., 2015, “Anwendung von UHPC als direkt befahrener Aufbeton bei der Integralisierung eines bestehenden Brückenbauwerks in Österreich.” Ernst & Sohn Verlag für Architektur und technische Wissenschaften GmbH & Co. KG, Berlin. Beton- und Stahlbetonbau 110, Heft 2.

Horii, H. and Nemat-Nasser, S., “Compression-Induced Microcrack Growth in Brittle Solids: Axial Splitting and Shear Failure,” Journal of Geophysical Research, Vol. 90, No. B4, pp. 3105-3125, 1985.

Kaka, V. B., 2017, “Applications of Ultra-High Performance Fiber-Reinforced Concrete on Flexural Structural and Architectural Members.”, Master Thesis, Department of Civil Engineering, University of Texas at Arlington, TX, 348 pp.

Khayat, K. H. and Valipour, M., 2014, “Design of Ultra High-Performance Concrete as an Overlay in Pavements and Bridge Decks,” Center for Transportation Infrastructure and Safety/NUTC program, Missouri University of Science and Technology, funded by U.S. Department of Transportation Research and Innovative Technology Administration, 2014.

McNerney, M. T., and Harrison, R., 1998, “Enhanced Pavement Management Systems for Airports: A Full Cost Analysis of Operational Impacts.” Airport Facilities: Innovation for the Next Century, 1–15.

Mehta, P. K. and Monteiro, P. J. M., 2014, Concrete—Microstructure, Properties, and Materials, Fourth edition, McGraw-Hill.

Menard, R., May. 2010, Why Precast Costs Less. Precast Magazine, National Precast Concrete Association, https://precast.org/2010/05/why-precast-costs-less/. Accessed November 05, 2018.

Muñoz, M. A. C., 2012 “Compatibility of Ultra High-Performance Concrete as Repair Material: Bond Characterization with Concrete under different Loading Scenarios.” Master Thesis, Department of Civil Engineering, Michigan Technological University.

Nagasaka, T.; Fukuyums, H.; and Tanigaki, M., 1993, "Shear Performance of Concrete Beams Reinforced with FRP Stirrups,” Fiber-Reinforced -Plastic Reinforcement for Concrete Structures-International Symposium, SP-138, American Concrete Institute, Farmington Hills, MI, pp. 789-811.

Nanni, A., 1993, “Flexural behavior and design of RC members using FRP reinforcement,” Journal of Structural Engineering, V.119, No.11, pp. 3344–3359.

National Cooperative Highway Research Program (NCHRP)., 2017, Use of Fiber-Reinforced Polymers in Highway Infrastructure. NCHRP Synthesis 512. 159 pages.

Palacios, G., 2015, “Performance of Full-Scale Ultra-High-Performance Fiber-Reinforced Concrete Column Subjected to Extreme Earthquake-Type Loading and Effect of Surface Preparation on the Cohesion and Friction Factors of the AASHTO Interface Shear Equation.” Master Thesis, Department of Civil Engineering, University of Texas at Arlington, TX, 625 pp.

Pavement Tools Consortium; “pavementinteractive.org”, 2018.

Pennsylvania Department of Transportation, Publication 242 Pavement Policy Manual, February 2018.

Rapid Construction of Rigid (Portland Cement Concrete) Airfield Pavements. Advisory circular No: 150/5370-16. FAA, U.S. Department of Transportation, September 28, 2007.

Roesler, J. R., Hiller J. E., Brand, A.S., August 2016, Continuously Reinforced Concrete Pavement Manual Guidelines for Design, Construction, Maintenance, and Rehabilitation. Report FHWA-HIF-16-026. FHWA, U.S. Department of Transportation.

Russell, H. G., Graybeal, B. A., June 2013 Ultra-High Performance Concrete: A State-of-the-Art Report for the Bridge Community. Report FHWA-HRT-13-060. FHWA, U.S. Department of Transportation.

Sajna, A., Denarié, E., and Bras, V., 2012, “Assessment of a UHPFRC Based Bridge Rehabilitation in Slovenia, Two Years After Application,” Proceedings of Hipermat 2012 3rd International Symposium on UHPC and Nanotechnology for High Performance Construction Materials, Ed., Schmidt, M., Fehling, E.,

Santos, P. M. D., July. 2009, “Assessment of the Shear Strength between Concrete Layers.” Ph.D. Dissertation, University of Coimbra. 338 pp.

Sarkar, J., 2010, “Characterization of the Bond Strength between Ultra High-Performance Concrete Bridge Deck Overlays and Concrete Substrates.” Master Thesis, Department of Civil Engineering, Michigan Technological University.

Shann, S. V., 2012, “Application of Ultra High Performance Concrete (UHPC) as a Thin Bonded Overlay for Concrete Bridge Decks.” Master Thesis, Department of Civil Engineering, Michigan Technological University.

"SP Systems Guide to Composites," Composite Engineering Materials – Systems

Stacks, D. L, May 07,2018. Pavement Manual. Manual Notice 2018-1. TxDOT Online Manual, May 01, 2018. http://onlinemanuals.txdot.gov/txdotmanuals/pdm/full_depth_repair.htm.

Switzer, W. J., Fischer, A., Fuselier, G. K., Smith, P. J. and Verfuss, W., 2003, "Overnight Pavement Replacement Using Precast Panels and Conventional Subgrade Material, Washington Dulles International Airport Case Study," Airfield Pavement Specialty Conference (ASCE), pp. 259 – 278.

Tayabji, S., Ye, D., and Buch, N., Winter 2013, "Precast concrete pavements: Technology overview and technical considerations", PCI Journal, Vol. 58, Issue 1, pp. 112-128.

Van Dam, T. J.,Peterson, K. R., Sutter, L. L., Panguluri A., Sytsma, J., Buch, N., Kowli, R., and Desaraju, 2005, P. Early-Opening-to-Traffic Portland Cement Concrete for Pavement Rehabilitation. NCHRP Web Document 76. National Cooperative Highway Research Program, Washington, DC.

Walls III, J. and Smith, September 1998, M. R. Life-Cycle Cost Analysis in Pavement Design-Interim Technical Bulletin.FHWA-SA-98-079. FHWA, U.S. Department of Transportation.

Waweru, R. N., 2015, "Strength of Horizontal Shear Reinforcement with Limited Development." Ph.D. Dissertation, University of Texas at Arlington, Arlington, TX. 305 pp.

Wille, K.; Naaman, A.E.; El-Tawil, S.; and Parra-Montesinos, G.J., 2012, "Ultra-High Performance Concrete and Fiber Reinforced Concrete: Achieving Strength and Ductility without Heat Treatment," Materials and Structures, V. 45, No. 3, pp. 309-324.

Wille, K.; Naaman, A.E.; El-Tawil, S.; and Parra-Montesinos, G.J., 2012, "Ultra-High Performance Concrete and Fiber Reinforced Concrete: Achieving Strength and Ductility without Heat Treatment," Materials and Structures, V. 45, No. 3, pp. 309-324.

Yuguang, Y., Walraven, J., and den Uijl, J., 2008, "Study on Bending Behavior of an UHPC Overlay on a Steel Orthotropic Deck," Proceedings of the Second International Symposium on Ultra High Performance Concrete, Ed., Fehling, E., Schmidt, M., and Stürwald. S., Kassel University Press, Kassel, Germany, pp. 639–646.

Biographical information

Ashish Karmacharya was born in Kathmandu, Nepal on May 15, 1992. After obtaining a Bachelor of Science in Civil Engineering from Pulchowk Engineering College, IOE, Lalitpur, Nepal in 2015, he worked as a Civil Engineer in for a year. In the August of 2016, he enrolled for Structural Engineering in the Graduate School at The University of Texas at Arlington.

During his Graduate studies at University of Texas at Arlington working with Dr. Shih-Ho Chao, he was involved in several projects including Use of Ultra-High-Performance Fiber-Reinforced Concrete for Fast and Sustainable Repair of Pavement and a New Sustainable Structural member with Ultra-High-Performance Fiber-Reinforced Concrete and Fiber-Reinforced Polymer Reinforcement.

After receiving his M.S in Structural Engineering and Applied Mechanics, Ashish plans to work as a Structural Engineer and gain design experience working towards his P.E. license. Due to his qualification and dedication, he has secured a position as a Graduate Engineer at Martinez Moore Engineers and plans to utilize his knowledge and experience gained at UTA through this research further ahead.